From the sublime to the ridiculous: Top physics and Minimum Bias events in the ATLAS detector at the LHC.

Kenneth Wraight

University of Glasgow
Department of Physics and Astronomy

Submitted in fulfilment of the requirements
for the degree of Doctor of Philosophy

Spring 2011

Abstract

This thesis is comprised of two separate physics themes, both of which involve the ATLAS detector situated at the LHC at CERN. The first constituent is a study of the top quark signal in the fully-leptonic channel for proton-proton collisions at a centre-of-mass energy of $10\ \mathrm{TeV}$. Here an event counting analysis is performed based on Monte Carlo simulation. This is supplemented by a study into one of the sources of systematic error. The second component is forward-backward correlations in minimum bias events. For this, there is a Monte Carlo hadron-level comparison of the correlation for $900\ \mathrm{GeV}$ centre-of-mass collisions, followed by a comparison of Monte Carlo predictions to data for $900\ \mathrm{GeV}$ and $7\ \mathrm{TeV}$ collisions.

Top Physics

A measurement of the fully-leptonic $t\bar{t}$ cross-section in the three decay channels ee, $\mu\mu$ and $e\mu$ is performed on ATLAS produced fully simulated pseudo-event data-samples. Selection rates for signal and background events consistent with ATLAS results are found along with the kinematic distributions of selected events. A calculation of the non-hadronic $t\bar{t}$ cross-section, based on the measured cross-sections, will then return the theoretical value of $217.06pb$ used to generate the original samples, showing the closure of the pseudo-analysis process.

A more detailed study is made of the systematic uncertainty arising from variations in the initial (ISR) and final (FSR) state showering models, based on the Pythia event generator. A fast simulation of the ATLAS detector is used with similar object and event selection to the fully simulated case. The effect of ISR variations on the signal is found to be negligible as it is washed out in the subsequent decays of the $t\bar{t}$ system. However, the effect of FSR is found to cause 5% uncertainty in the selected signal events. In addition, in the main background of each of the selection channels the effect of FSR is found to produce variations of up to 30% in well populated channels. The variations in signal and background measurements will then be used to calculate a new estimate of the systematics on the measured $t\bar{t}$ cross-section for each channel.

Minimum Bias

A detailed study of the forward-backward (FB) correlation and event shapes of a selection of Pythia tunes for pp collisions with $\sqrt{s} = 900\,\mathrm{GeV}$ is performed. This includes an investigation into the sources of particle production in generated minimum bias events as well as the component sub-processes in generated minimum bias events. The tunes are found to be practically degenerate (within $10 - 20\%$ variation) for the "standard" distributions. The inclusion of a new observable, namely the forward-backward correlation, to the "standard" set is recommended. The study finds that the FB-correlation and its $\mathrm{p_T}$ and ϕ dependent variations are able to discern differences between the selected tunes to a greater degree than the usual inclusive distributions. Further, the FB-correlation is found to be sensitive to the particle production processes within the tunes, an invaluable property for the purposes of generator tuning.

A measurement of the forward-backward correlation for pp collision of $\sqrt{s} = 900\,\mathrm{GeV}$ and $7\,\mathrm{TeV}$ at the LHC using the ATLAS detector is made. The measured correlation is compared to the predicted correlation of several ATLAS centrally produced generator tunes. A correction procedure is developed and validated on the generator samples to correct the generated correlation to the hadron-level correlation. This is then applied to the measured correlation and a comparison of corrected data to the hadron-level predictions of the generated tunes made. The corrected correlations at the two collision energies are compared as well as the calculation of a global correlation at both energies. The measured and corrected correlations are found to lie above the predicted distributions at both energies and across the η-range. Further investigation of measured correlation using augmented FB-correlations is recommended.

Acknowledgements

The first and biggest thanks for this monolith goes to Craig Buttar who has been extremely approachable and encouraging throughout my Ph.D. A co-starring role was played by Sarah Allwood-Spiers in introducing me to the ATLAS software and the basics of particle physics analysis. Other department members who deserve some recognition are Chris Collins-Tooth, for extra ATLAS help, and Andy Pickford, for all his general software aid.

From my times at CERN I'd like to thank Saverio D'Auria for introducing me to the campus; Samir Ferrag who's probably the best statistician I know; and Peter Skands for all his help and guidance during my MCnet Studentship.

Less formal gratitude (in no particular order) is due to Andrew Laing, the second best Tertis player I know; Laurence "Lauro" Carson, an Irvine legend; and Dima Maneuski, the Belarusian tycoon. Also thanks for the jovial pub quizzes.

To the office-mates, I recognise the not wholly detrimental effects of Aaron Mac Raighne, who is good craic when he isn't on holiday; Graeme Stewart and Dimka (again). A special mention should also be made of Daniel Clements, wherever he is now.

Traditional thanks go to my Mum and Dad for their continual support throughout *all* my studies. And to the clique of flatmates who have shared my abode over the past few years: Lorraine, Cat, Grant, Sam and the ever brown Tony "Bryan" Brown. And a special thanks to Siobhan.

Declaration

I declare that except where explicit reference is made to the work of others, this dissertation is the result of my own work. This work has not been submitted for any other degree at the University of Glasgow or any other institution.

Kenneth Wraight

Contents

List of Tables

List of Figures

Chapter 1

Preface

Chapter 2 describes the relevant theory of top quark production and decay. After a concise introduction to the Standard Model, various features of hadron-hadron collisions are introduced and briefly discussed. The discussion then focuses on QCD top pair production and subsequent final states. Current measurements of top quark properties are reviewed and the strategy for a cross-section measurement introduced. Also described are the basic features and concerns of pseudo-event generation, in particular multi-jet event simulation.

Chapter 3 provides a brief overview of the LHC accelerator at CERN and gives a non-comprehensive description of the ATLAS experiment. The LHC and experiments are introduced and a short summary of their purpose and design is given. The ATLAS experiment is described in more detail with emphasis on the detector technology and expected performance. The sub-detectors and their responsibilities are explained and the LHC distributed analysis framework introduced.

Chapter 4 gives an account of a top pair production cross-section measurement performed using ATLAS produced fully simulated data for proton-proton collisions at a centre-of-mass energy of $10\ \mathrm{TeV}$. The construction of event objects is discussed and the recipe of event selection for three of the di-leptonic final states is given. Significant background processes are also introduced and included in the pseudo-analysis. The relevance of each background to the appropriate channel is remarked upon and techniques for their removal are discussed and implemented. The result of the pseudo-analysis is presented along with estimates of statistical and main systematic uncertainties for each selection channel. The results are compared to the theoretical prediction.

Chapter 5 describes a more detailed study into one of the sources of systematic error, namely, initial and final state radiation. The main features relevant in each channel are described before an evaluation of the effects of varying the initial and final state contributions to the signal and main background in each channel. The results, based on fast simulation, give an estimation of the importance in pseudo-event analysis. The results of the cross-section analysis are then revised and the new estimates compared to the original measurement. This

work of this chapter was undertaken while on an MCnet Studentship under the supervision of Peter Skands.

Chapter 6 introduces a second physics theme of minimum bias. The main components of minimum bias events are described from the point of view of event simulation. This perspective is used to distinguish various sources of particle production. A Pythia based comparison of various generator tunings and production sources is made using a selection of observables at the hadron-level for simulated $900\ \mathrm{GeV}$ centre-of-mass proton-proton collisions. One observable in particular is used extensively to assess its capacity to isolate sources of particle production, much desired by event generator developers. Much of the work in this chapter comes from the guidance and help of Peter Skands.

Chapter 7 uses ATLAS produced minimum bias simulated events of various tunings to compare to data found in the first year of LHC operation at $900\ \mathrm{GeV}$ and $7\ \mathrm{TeV}$ collision energies. The track and event selection is described, a detailed explanation of the correction procedure given and a systematics study presented. The final results, comparing data to generated hadron-level predictions, are then presented with full treatment of systematic and statistical errors. The work in this chapter was done with the help and guidance of Craig Buttar and Samir Ferrag.

Chapter 8 gives a final conclusion. The work of the preceding chapters is summarised, the main results restated and concluding remarks made.

Chapter 2

Theory

After a brief introduction to the Standard Model, this chapter describes the theoretical concepts used in the calculation and prediction of hadron-hadron interactions. This is followed by the basic theory of top quark production and decay relevant to the work of later chapters. The main focus is on QCD top pair production and subsequent final states. Current measurements of top quark properties are reviewed and the general strategy for a cross-section measurement introduced. Also described are the basic features and concerns of pseudo-event generation, in particular multi-jet event simulation.

2.1 Preamble

Particle physics is a relatively modern development in the physical sciences. It requires state-of-the-art technologies from other fields to perform experiments, develop theories and make predictions. Drawing on engineering and material sciences, some of the world's most complicated machines have been built. Mathematical and statistical resources help develop theories and interpret data. Computational software and hardware are essential in storing and processing the vast quantities of data harvested in modern experiments. The goal of this enterprise is to construct a theory by which to explain the physical phenomena found at microscopic scales. The modern understanding of this behaviour is an elementary model of particle physics, consisting of a collection of simple particles and fundamental forces. These basic constituents comprise the reductive basis of the physical sciences.

2.2 Forces

Modern physics recognises four forces: Gravity, Electromagnetism, the Weak force and the Strong force[1]. The strength and range of these forces are defining characteristics, granting them significance at different physical magnitudes. Although the forces are distinct in nature they have competing effects on matter at various scales. To unfold these convolutions experiments are designed where one force dominates over all others thereby allowing scrutiny of a single compulsion. The latter two forces are the interest of experimental particle physics, though the unification of all four is the quarry of many a theoretical physicist.

Gravity is apparent at the levels of everyday life and larger. It is manifest in the pull of objects to the earth and the movement of the celestial bodies. This force has resided longest in human consciousness and the history of its understanding closely corresponds to the development of science itself through the ages. Electromagnetism as a co-joined entity is relatively new in comparison. It has only been understood as a single force, thanks to Maxwell, for around a century. However before this the effects were apparent in the technology of the compass and the advent of electricity. Deeper examination of the material world reveals the ubiquity of this force. All common matter is held in its grasp. It is the essence of chemistry, transforming atoms to molecules and elements to compounds. Both these forces appear to have limitless range and diminish over space in accordance with an inverse-square law.

The other two forces are not obviously manifest on the macroscopic scale. They are hidden in the microcosm of atoms and require the resolution of high energy physics experiments to reveal their character. The Weak force has the shortest range, captured in the diameter of a nucleon. It is responsible for beta-decay, but without further understanding of the world (e.g. stellar theory), its effect in everyday experience is easily neglected. The Strong force, is just as elusive in common life but underpins all physical objects. It binds quarks to form hadrons, without which there would be no centre to construct the atom around. Moreover, at the limits of its range, it has enough strength to hold the nucleus together despite electromagnetic repulsion. Unlike their macroscopic cousins these forces are not described by an inverse-square law which gives them more complicated characteristics.

The strength of a force is measured by its coupling constant. This is a somewhat misleading name as the strength of a force will depend on the energy of the interaction. The range is a reflection of the type of intermediate particle involved. Massive mediators limit the distance the force can be propagated across, in accordance with Heisenberg's uncertainty

[1] It is worth a passing remark that through the history of physics the nomenclature of the forces has lost its quaint aesthetic. Gravity has a long history in general language, including a popular meaning. Electromagnetism, though truncated, is made from two linguistic elements with similar etymological richness. The most recent additions have little romance to their names. Rather than adding to common language they have simply been cropped from it in an efficient but unimaginative fashion.

principle. In addition, self-interaction of a mediator checks the extent to which the force can be felt. Consequently, unlike electromagnetism and gravity, the strong and weak forces do not extend infinitely and are relatively confined. Table 2.1 lists the four forces with some attributes and table 2.2 lists the force carrying particles, bosons, with some properties.

Forces	charge	strength	range(m)	mediating particle
Strong	$color$	~ 1	10^{-15}	$gluon(, pion)$
Electromagnetic	$electric$	$\sim 10^{-2}$	$infinite$	$photon$
Weak	$weak$	$\sim 10^{-5}$	10^{-18}	$W^{\pm}, Zbosons$
Gravity	$mass$	$\sim 10^{-38}$	$infinite$	$graviton?$

Table 2.1: Fundamental forces and characteristics. Strength is given in terms of relative coupling, i.e. ratio to the strong coupling. N.B. no mediating particle has been discovered for the gravitational force.

Boson	symbol	EM charge(e)	spin($h/2\pi$)	mass(GeV)
gluon	g	0	1	$0(theoretical)$
photon	γ	$< 5 \times 10^{-30} e$	1	$< 1 \times 10^{-27}$
W-boson	$W^{\pm}$	± 1	1	80.399 ± 0.025
Z-boson	Z	0	1	91.1876 ± 0.0021

Table 2.2: Bosons with associated properties[1].

2.3 Particles

Studying the mechanics of standard processes not only elucidates the nature of the force but also the nature of matter as well. The interaction of each force with matter varies depending on the characteristics of the material. The feature of an object which is susceptible to a force is called *charge*. The combination of charges an object possesses distinguishes it from others and provides the basis, along with other properties, for a codification of matter.

The quantum numbers of an object involve its *charge* and *spin* properties, these features can be used to distinguish individual particles from one another and group them by common attributes. For fermions, no two objects can possess identical quantum numbers[2]. Tables 2.3 & 2.4 list the fermions in two groups, quarks and leptons. Three generations are shown here, only the first is required for the purposes of chemistry, the second and third generations require high energy environments to generate them, e.g. accelerated particle collisions. Hence, these heavier particles are only observed in high energy physics experiments or cosmic rays.

A consequence of combining the Quantum Mechanical description of sub-atomic particles with Special Relativity is that each particle has a corresponding anti-particle[5], hence for each of the quarks and leptons listed there is a particle of equal mass but opposite charge

[2]See [4], for a recent debate of the relationship of Pauli's Exclusion Principle to Leibniz's Identity of Indiscernibles.

(for neutral particles the anti-particle can have the same properties as the particle). The overall particle content of the modern physics includes fermions, bosons and their corresponding anti-particles.

The fermions and four bosons described above are assumed to be simple, i.e. they have no further structure. As a consequence of the color-charge quarks group themselves into mesons, a quark-antiquark pairing, or (anti-)baryons, a three (anti-)quark triplet. These bound states (hadrons) have no net color. The strong force is exceptional because as two color-charges are separated the energy in the field between them increases. Once enough potential energy is contained in the field to create a quark-antiquark pair the field separates resulting in two quark-antiquark pairs. Hence, quarks are never found unbound and their existence is inferred from the behaviour of hadronic matter. In contrast leptons, which are not governed by the strong force, are observed singly.

Quark	symbol	EM charge(e)	spin($h/2\pi$)	mass(GeV)
up	u	$2/3$	$1/2$	~ 0.003
down	d	$-1/3$	$1/2$	~ 0.006
strange	s	$-1/3$	$1/2$	~ 0.1
charm	c	$2/3$	$1/2$	~ 1.3
bottom	b	$-1/3$	$1/2$	~ 4.2
top	t	$2/3$	$1/2$	~ 171

Table 2.3: Quarks with associated properties[1], paired by generation.

Lepton	symbol	EM charge(e)	spin($h/2\pi$)	mass(GeV)
electron	e	-1	$1/2$	0.000511
electron neutrino	ν_e	0	$1/2$	$< 2 \times 10^{-9}$
muon	μ	-1	$1/2$	0.1
muon neutrino	ν_μ	0	$1/2$	$< 2 \times 10^{-9}$
tauon	τ	-1	$1/2$	1.8
tauon neutrino	ν_τ	0	$1/2$	$< 2 \times 10^{-9}$

Table 2.4: Leptons with associated properties[1], paired by generation.

2.4 Standard Model and Beyond

The Standard Model (SM) builds on the smaller gauge theories concerning electromagnetic, weak and strong interactions to create a comprehensive description of sub-atomic particle behaviour. Electro-weak theory is a non-Abelian (operations in the group do not commute) $SU(2) \times U(1)$ gauge theory describing electromagnetic and weak interactions. It was first corroborated by the Gargamelle bubble chamber experiment in 1974 at CERN and later with the prediction and measurement of the W and Z bosons at Super proton anti-proton Synchrotron, again, at CERN. QCD is also a non-Abelian theory with $SU(3)$ symmetry. Its

description of the strong force was first corroborated by deep inelastic scattering experiments at SLAC and DESY.

The Standard model combines both sub-theories to create a $SU(3) \times SU(2) \times U(1)$ gauge theory and implies[3] there are twelve bosons[4] (8 for the strong force, 3 for the weak force and 1 for electromagnetism). It has succeeded in describing the experimental results of the past decades with some important additions: the theory was augmented to include CP violation and can be adjusted to include neutrino masses. Its explanatory power is limited by a number of free parameters which must be fed in to the theory after experimental measurement. These include the particle masses, force couplings and mixing angles.

Theories wishing to supersede this are known as Beyond the Standard Model (BSM) theories. They seek to supplant the SM by invoking additional fields and particles to account for the free parameters input into the SM. So far there have been no observations which go beyond the descriptive limits of the SM, such observations are colloquially called "new physics". An important feature of the formalism of groups is that they lend themselves well to hierarchical structures. Hence, some theories seek to include the elements of the SM into a larger system which includes each sub-group. These Grand Unifying Theories (GUTs) argue from symmetry considerations that each SM gauge theory is the manifestation of a greater super-theory whose symmetry is broken at the high energies, known as the GUT-scale. The "new physics" signals of BSM theories are sought at the world's largest particle physics experiment at CERN, the Large Hadron Collider.

2.5 Hadron-Hadron interactions

The theoretical account of particle interactions in high energy particle physics is based on the exchange of force carrying particles between elementary charged particles (i.e. fermions). Therefore the theoretical description of hadronic scattering reduces the process to the interaction of fundamental component quarks and gluons (collectively known as partons). When the constituents collide they have some fraction of the total hadron momentum. Hence, the picture of hadron bunches with a fixed momentum is transformed into beams of quarks and gluons with varying momenta. The probability of a constituent quark having a certain fraction can be measured. The theory then allows for the interaction of the simple colliding particles to be split into two computationally independent parts. The high momentum part is calculated to a chosen accuracy using perturbative quantum chromodynamics (pert.QCD), while the rest is approximated using tuned phenomenological models.

[3] In general, a gauge group with $SU(n)$ symmetry has $n^2 - 1$ gauge bosons.

[4] Technically the gauge bosons from the fields involved in the theory do not correspond to the physical bosons in experiment. Instead a linear combination of gauge bosons become physical force carriers. An analogous situation arises in classical electromagnetism where the vector and axial potentials do not map directly to the electrostatic and magnetic potentials.

The nature of the colliding particles is the essential difference between hadron-hadron scattering and lepton-lepton scattering. In the latter case the centre of mass energy of the interaction can be tuned to a relatively precise value since the colliding particles are simple objects. In contrast, the centre of mass energy of colliding partons is only probabilistically related to the hadronic beam energy. In addition, the complex nature of hadrons entails hadronic collisions are much more "messy" since several interactions can occur per hadronic scatter.

This complicates hadronic event identification as there are then several signatures to disentangle in the detector at once. In addition, in order to produce a particular event (e.g. di-top production), which requires a certain centre of mass energy, other collisions will inevitably occur, as the partons probabilistically collide with energies around the production threshold. If these "extra" events also have similar signatures in the detector this can lead to the misidentification of the *signal* process. Hence, hadronic collisions produce *background* events which must be filtered from the events of interest.

2.5.1 Hard Event Calculation

This section describes the basic mathematical concepts used to calculate parton-parton scatterings. These constitute the formal description of hadron-hadron collisions.

Modern particle scattering cross-sections are calculated using Feynman diagrams and rules, fig.2.1 shows two Feynman diagrams. Feynman diagrams give a space-time picture of possible particle histories between the initial state of the incoming particles and the final state of the outgoing products. Any particles occurring only within the confines of the diagram (i.e. not part of the initial or final state) are virtual. Such particles are not limited by energy-momentum conservation and can have a 4-vector magnitude not equal to the particle mass. These "off-shell" particles contribute to the interaction amplitude but are not directly observable in experiment.

As this physical picture is based on particles, to include quantum mechanical aspects, all possible histories must be summed in accordance with the principle of superposition. This is interpreted as particles interacting in every way possible at once but to varying extents, i.e. some histories have a greater contribution to the calculation than others. The number of vertices involved in a history gives its order. Typically, the higher the order of the diagram the less it contributes to the overall amplitude and the more convoluted the calculation. This is because each vertex entails a factor, less than unity, squared. Hence each increase in order decreases the relative contribution of the diagram to the final calculation. This fact means QCD calculations are well-suited to perturbative calculation techniques.

An individual diagram's contribution is calculated using free field equations for incoming and outgoing particles and Hamiltonian operators to describe particle interactions. The total

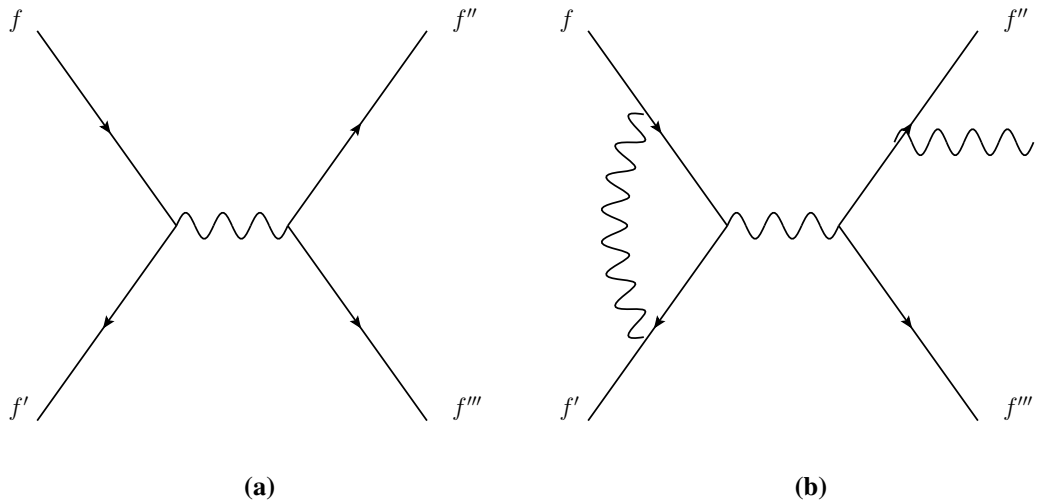

Figure 2.1: a) Tree-Level fermion scattering; b) Higher-order fermion scattering.

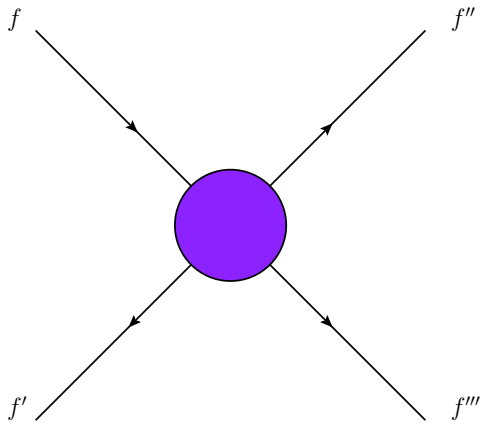

Figure 2.2: Generic fermion scattering. The purple blob at the centre represents all possible scatterings.

scattering cross-section amplitude is the sum of each possible interaction history over all possible interaction states. Fig.2.2 represents all possible Feynman diagrams for a fermionic scattering. This weights the individual contributions from different diagrams, giving greater import to more probable (usually lower order) particle histories.

The amplitude is calculated using Feynman rules: internal lines of virtual particles contribute a factor for the particle's propagator; vertices, where bosons are exchanged, contribute a factor from the interaction term of the Lagrangian; incoming or outgoing lines carry the energy, momentum and spin contributions of the process. These rules automate the calculation procedure such that computers can be employed to produce the final result.

There are an infinite number of processes which may be calculated and an infinite order of complexity available to each one (as internal loops can always be added to a diagram). Since all possible histories must be superimposed for the final result, this introduces a computa-

tion limitation due to finite resources. Though the effect of higher orders to the calculation is expected to diminish as the order increases, i.e. the calculations will converge around a value, there is no guarantee these contributions are negligible in all regions of phase-space. Hence, to avoid infinite tasks of perturbative calculation, a limited number of terms are calculated precisely while higher-order effects are approximated by additional mathematical techniques.

2.5.2 Hard Shower: Radiative Corrections

QCD calculations involve cancellations relating to infrared (IR) and collinear splitting. Collinear splitting involves the emission of a quark or gluon at a small angle to the initial parton trajectory and IR splitting is the emission of low energy radiation from a parton. Partons emit radiation (gluons in the case of QCD or photons in the case of QED) isotropically, producing a cone of radiation around the hard parton. The first splitting happens relatively soon after the hard scatter, with subsequent emission occurring about a factor of ten later, in what ever emission ordering scheme is used (e.g. $\mathrm{p_T}$, Q^2, etc.) for each radiative generation. Collinear (IR) splittings become asymptotically more likely as the angle with respect to the parent trajectory of the emitted parton decreases. This introduces a potential divergence, i.e. the calculations to higher-orders will not converge, as more and more splittings must be considered in order to gain a precise picture of the hard shower. Fig.2.3 shows an example of fermionic showering.

Delicate mathematical manipulation results in the cancellation of computational infinities arising from infra-red divergences i.e. virtual loop corrections added in higher-order calculations and soft and collinear splittings. This gives finite values for calculated quantities which can then be usefully compared with experiment.

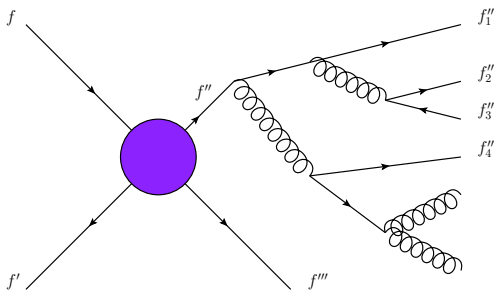

Figure 2.3: Generic fermion scattering with one fermion strongly showering to six daughters.

2.5.3 Renormalisation

Since precise pert.QCD calculations are usually computed to only the first two or three orders, commonly known as next-to-leading (NL) and next-to-next-to-leading order (NNL), respectively, higher-orders must be considered by other means. Renormalisation accounts for the quantum fluctuations at scales lower than an energy cut-off μ_R^2, while eliminating the physical details below the scale. Hence, radiative corrections are taken into account for radiation with $\mathrm{p_T} < \mu_R^2$, without the individual diagrams being calculated and summed.

These effects are accounted for by introducing running couplings (and masses etc.) to calculations which are dependent on the energy (equivalently, time or distance) scale of the calculation (i.e. $\alpha_s \rightarrow \alpha_s(\mu)$). This sums the effects of short-time fluctuations of the fields involved at the cost of introducing some scale dependence to the calculations. Scale dependence means different choices of μ_R^2 can lead to variations in calculated physical quantities. The extent of discrepancy can be mitigated by a reasonable choice of μ_R^2, where slight variations do not lead to large changes in predicted quantities. This is usually around the energy scale of the event.

Any remaining fluctuations in observables around μ_R^2 (e.g. $\mu_R^2/2$ to $2\mu_R^2$) are characterised by a systematic error in the theoretical calculation. As higher-order terms are included in the perturbative calculation the scale dependence diminishes. However, anomalies can appear in the higher-order descriptions which lead to infinities in calculation that are a limitation of the mathematical tools available without physical meaning.

2.5.4 Factorisation and Soft Physics

Pert.QCD is used to calculate the high momentum (hard) part of the interaction and can be calculated a priori for a particular process using the tools outlined above. In contrast, the low momentum (soft) part of the interaction is modelled by non-perturbative methods modelled on previous experimental results. This formal separation is known as factorisation and the computational independence of the hard and soft parts of the partonic interaction is provable to all perturbative orders[6], for a selection of processes such as Drell-Yan and Deep Inelastic Scattering. However, the success of factorisation as a predictive tool has made it ubiquitous in theoretical calculations. Factorisation distills the particular Feynman calculation from the general features of the theory, which apply to experiment. General features include the soft initial state physics, jet structure, infrared-safe observables and the underlying event.

As in the case of renormalisation, factorisation introduces an arbitrary but necessary scale dependence in splitting the description of the interaction into hard and soft aspects according to some scale μ_F^2. This dependence on μ_F^2 is an artefact of the finite order of the computation and can be mitigated by the inclusion of higher-order terms. μ_F^2 is usually chosen such that the scale dependence of the calculated quantities is limited. Often the same scale is used for

both factorisation and renormalisation i.e. $\mu_F^2 = \mu_R^2 = Q^2$.

The following sections give some detail pertaining to the soft aspects of event calculation.

2.5.5 Initial State and PDFs

As mentioned, in contrast to incident hadrons, the particular partonic constituents involved in the collision are not well-defined. Parton distribution functions (PDFs) are used to probabilistically predict the flavor and momentum fraction, x, of the colliding partons. The PDFs are extracted a posteriori from the partonic distributions found in previous scattering experiments (e.g. deep inelastic scattering data). These data are fitted to provide a reasonable estimate of which type of parton with what associated longitudinal momentum is likely to interact for a given set of initial conditions, e.g. hadronic type and CoM energy.

Exactly which data is included/excluded from previous experiments and how much importance it is given in the global fit affects the PDFs. This is essentially the difference between the various PDF groups' parameterisations e.g. CTEQ[5] and MRST[6]. Different choices in the factorisation scale for an event can also provide alternative PDFs, which in turn can lead to discrepancies in calculation.

2.5.6 Underlying Event

The underlying event (UE) is composed of several relatively low energy components which can contaminate measurements of the hard scatter. It is therefore important to understand and limit these effects. The UE is nebulously described as all physics processes occurring during a bunch crossing except for the hard scatter. This can be separated into several sub-processes: initial and final state radiation, color reconnection, multi-parton interactions, multi-proton interactions and remnant fragmentation. Initial and final state radiation have been outlined above. Color reconnection pertains to the effects of the strong force on final state particles which are colored. Multiple interactions can occur when either more than one proton interacts per bunch crossing (also known as pile-up) or more than one parton interacts in the same proton scattering. Remnant fragmentation concerns the subsequent break up of the proton after the hard scatter. The physical origins of these processes are not precisely understood so non-perturbative phenomenological assumptions are used to estimate their contributions.

In order to measure the contribution of UE to measurements of hadronic processes, a good control region is defined. Here, little signal is expected so UE effects can be studied. The method of CDF[7] is to investigate the energy deposited in the central detector region perpendicular to the hardest jet for di-jet events. The hard process of di-jet production creates

[5]CTEQ: Coordinated Theoretical-Experimental Project on QCD, see http://www.phys.psu.edu/ cteq/ .
[6]Martin, Roberts, Stirling and Thorne, see http://durpdg.dur.ac.uk/hepdata/mrs.html .

jets "back-to-back" in the centre-of-mass frame. These high momentum jets are expected to leave detector deposits separated by $\sim 180^\circ$ in ϕ. This leaves the transverse region $60^\circ < \phi < 120^\circ$ from the hardest jet relatively free of jets from the hard scatter or subsequent radiation. Hence, activity in this area can be associated with the underlying event.

2.5.7 Hadronisation and Jet Formation

Most of the particles resulting from primary collisions are observed in the detector as a multitude of secondary particles (e.g. pions, photons, etc.). The multi-particle state comes as a consequence of quark confinement. After the initial collision of the color-charged partons inside hadrons, the colored final state particles move apart increasing the strong potential between them until there is enough energy to produce a quark-anti-quark pair from the vacuum. This process is iterated through generations of particles until the partons form bound states when they can no longer move apart. This process it known as hadronisation, illustrated in fig.2.4.

As the particles result from a common ancestor, they form a collimated bundle of hadrons which are then deposited across and throughout the detector. Hence, high-energy final state partons result in a spray of particles in the detector systems. In event analysis these particles are associated within and across adjacent detector elements to construct the spray of particles into a jet.

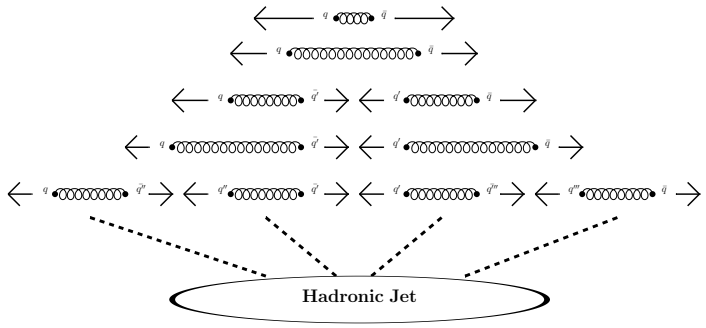

Figure 2.4: Hadronisation of quark pair.

Jets are interpreted as the observable manifestation of partons resulting from hadronic collisions. While jet definitions and the corresponding algorithms are well-defined and understood, the partonic information they contain is much more ambiguous. This reflects the incomplete understanding of the physical mechanism by which partons hadronise. Although the perturbative process by which partonic radiation is generated is understood and modelled, the non-perturbative process of hadronisation is much more complex and difficult to precisely predict. Hence matching hadrons to partons is an ambiguous process.

Jet algorithms attempt to simplify and project the information from several hadronic sprays (i.e. the plethora of calorimeter information) onto a few parton-like objects. Jets can

then be used as a theoretical tool to predict and interpret the final state hadrons as evidence of the partonic structure of the event which came to generate them (e.g. to infer the decay of a massive particle $t \rightarrow 3jets$). Fig.2.5 shows a schematic diagram of the differing stages of jet production.

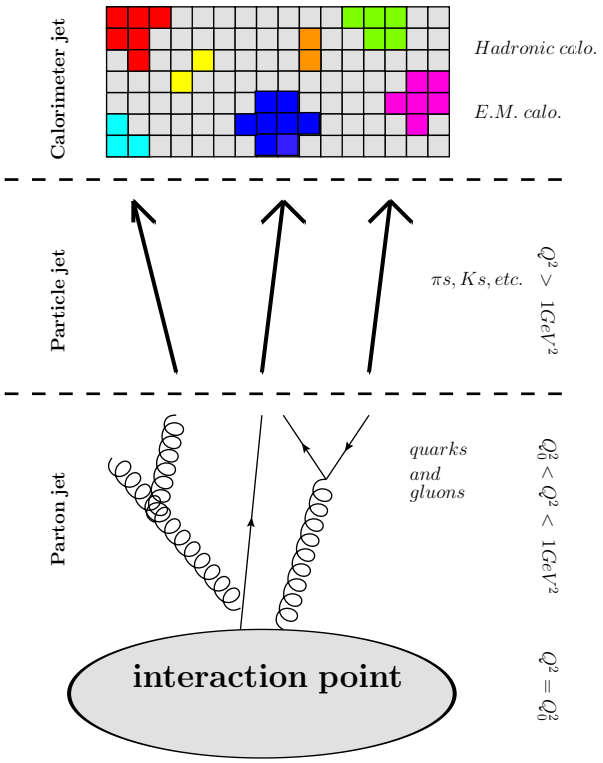

Figure 2.5: Schematic diagram of jet production stages. Q^0 refers to energy scale of hard scatter.

2.5.7.1 Jet Algorithm Safety

Various algorithms have different approaches as to how jet reconstruction is done, with some consequences for the theoretical consistency and computational efficiency of the algorithm itself. This section outlines the primary concerns for jet algorithm stability and gives a brief description of several jet algorithms which are used for analysis of ATLAS data, along with some comments regarding their safety.

There are two sources of ambiguity in jet construction. The first comes when deciding which particles should be included in the jet. The details of how this is decided lie in the jet algorithm specifics and the values of the parameters chosen. The second source comes from choosing how the constituent information should be combined. The usual choice of recombination scheme is a direct 4-vector sum of the included particles (E-scheme).

Once the two issues are settled a jet definition has been specified. Since jet definitions are well-defined they can be included in phenomenological predictions. An important point

is that the choice of jet definition should be appropriate to the analysis. Any derived physics conclusions that come from jet construction should be independent of the jet definition, however, in practice this is not always the case leading to various reconstructions of the event depending on the jet definition. Further, if the jet algorithms are not theoretically sound divergences can arise leading to unphysical predictions as real-virtual correction cancellations cannot be performed in certain QCD calculations. Hence it is imperative for prediction and analysis purposes that variations in the jet construction should not affect results.

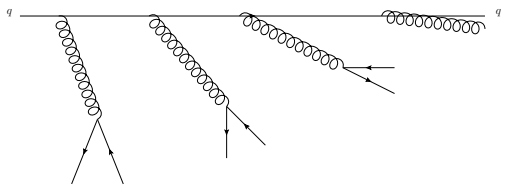

Figure 2.6: Schematic of soft and collinear gluon radiation from a quark.

Infrared safety is affected by the coverage and response of the detector. In the former case, the imperfect coverage of the detector, due to cracks and the beam pipe, and the finite resolution mean the full collinear and IR structure of all events is unobtainable. In the latter case, the response of the detector can be affected by the choice of threshold value and noise present in calorimetry, as well as the effect of magnetic fields on the deposited hadron energy. High beam luminosity will add extra jet seeds by adding soft particles to hard events in event pile-up. And, in addition, the contributions from the calorimeter towers themselves can vary with jet structure e.g. when multiple incident hadrons hit the same tower or one hadron showers across multiple towers.

Both these factors can lead to shifts in the measured energy scales. In general, inclusive quantities, e.g. jet multiplicity spectrum, are less susceptible to detector influence. Jet algorithms which are sensitive to collinear and IR effects can construct event structures which differ from insensitive jet definitions. IR safety means the information of the reconstructed event, which combines hadrons, can give approximately and consistently the same result as the actual event before reconstruction.

2.5.7.2 Jet Algorithms

There are two kinds of jet algorithm: the first is the cone algorithm which is a "top down" approach, using centres of *invariant* energy-flow as seeds (e.g. ATLAS Cone and SIS Cone algorithms, see sec.3.2.3.4 for details); the second type is a "bottom up" method which attempts to undo the branching of QCD radiation by sequential recombination (e.g. k_t and anti-k_t algorithms, see sec.3.2.3.4). The former case is based on the idea that collinear emission will not greatly affect the momentum flow of the parent parton, hence a cone shape

centred around hard particles in the detector is used to collect surrounding collinear radiation. The latter definition type is insensitive to collinear splitting as a necessary corollary of the k_t -style jet building procedure is the inclusion of showered hadrons around a central point, providing they pass some threshold cut. The threshold removes potential collinear problems.

Although jets can be helpfully thought of as the products of partonic hadronisation, the nature of the jet definition (i.e. the information sought and the applicability of the algorithm) implies a variable mapping between partonic and hadronic levels. A small jet radius, R, is preferable in cases where many jets are expected to be resolved, and in cases where pile-up and underlying event influences may be important. Contrastingly, large radius values are appropriate for minimising loss of jet energy from QCD radiation and hadronisation. For example, in the case of measuring the top mass, small R values can lower the observed top mass by omitting radiative contributions, while large R can increase the measured mass by including pile-up and UE effects. Differences such as cone size and $\mathrm{p_T}$ cut-off can optimise an algorithm for a specific purpose. The sensitivity of an algorithm to collinear or IR splitting does not render it universally invalid. The appropriateness of a jet algorithm depends on the purposes and context of analysis.

2.6 Top Physics

Although the top quark was discovered in 1995 [8, 9], and predicted long before, it remains the most enigmatic part of the standard model. The large mass of the top quark makes its lifetime and subsequent decay chains unique and hence the top sector is a particularly interesting area of particle physics for study as it includes aspects which have no analogue in other flavor sectors such as b-physics. This section gives a brief history of top quark searches, followed by theoretical and experimental evidence for the top, then a short review of some of the distinctive features of the top sector i.e. top-quark production, decay and properties.

2.6.1 Short History

After the discovery of the bottom quark in the late seventies at Fermilab [10] the search for a third generation partner began based on theoretical motivations (see section 2.6.2.1). At the time electron-positron colliders were favoured, such as PETRA at DESY, TRISTAN at KEK, SLC at SLAC and LEP at CERN. The strategy throughout the late seventies and eighties was to search for a top-antitop bound state, $e^+e^- \rightarrow t\bar{t}$ (just as in the case of the bottom and charm quarks before). The energy available to pair produce top quarks at threshold is half the CoM energy. Hence, by 1990, the lack of any experimental evidence for "toponium" increased the experimental lower limit of the top mass to above $45.8GeV/c^2$. This was based on the data

from SLC and LEP, with centre-of-mass (CoM) energies of around the Z-pole ($91.19\ \mathrm{GeV}$). Further increases to the collision CoM energy was prohibited by synchrotron radiation from the accelerated electron beams.

However, throughout the 1980s hadron-hadron collider technology became more popular. This increased the CoM energy and hence the production range of particle colliders far above the earlier e^+e^- colliders. Hadron colliders also offered the opportunity to study top production via EW single W-boson decay, $W \rightarrow tb$, see fig. 2.7, unavailable at e^+e^- colliders as only Z production is available. This mechanism was expected for $m_{top} \simeq 77\ \mathrm{GeV}/c^2$. Heavier quark production comes via the strong di-top production, with EW top decays, $t \rightarrow Wb$, almost exclusively (see section 2.6.4). The $Sp\bar{p}S$ at CERN and the TEVATRON at Fermilab had collision energies of $\sqrt{s} = 630\ \mathrm{GeV}$ and $\sqrt{s} = 1.8TeV$, respectively. Although CoM energy was no longer an immediately limiting factor, the interaction luminosity and the expected rate of the resulting top production became inhibiting. In 1989 the $Sp\bar{p}S$ experiments UA1 and UA2 increased the lower top mass limit to $m_{top} > 60\ \mathrm{GeV}/c^2$ and $m_{top} > 69\ \mathrm{GeV}/c^2$, respectively [11, 12], in single W-decay searches.

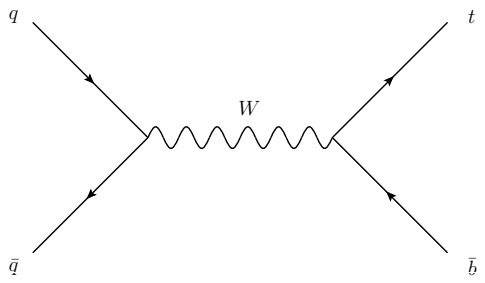

(a) s-channel gluon fusion

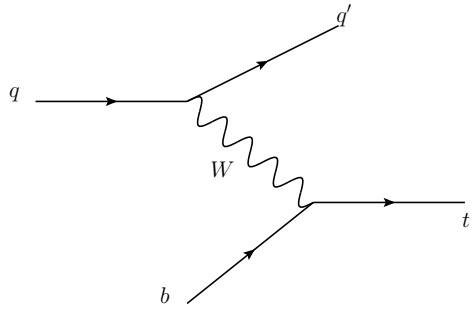

(b) t-channel gluon fusion

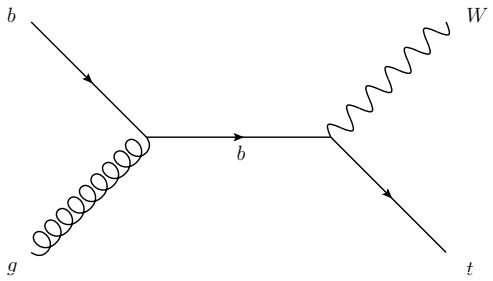

(c) t-channel gluon fusion

Figure 2.7: Lowest order single top production via strong interaction from hadron-hadron collisions.

Data taken by the Collider Detector at Fermilab (CDF) from TEVATRON collider between 1988 and 91 raised the limit of $m_{top} > 72\ \mathrm{GeV}/c^2$ for single W production. In 1992

this was further increased above the W threshold to $m_{top} > 91\ \mathrm{GeV}/c^2$. In 1992 the $D\emptyset$ experiment began data taking at the TEVATRON, with comparable sensitivity to CDF. $D\emptyset$ placed a limit of $m_{top} > 131\ \mathrm{GeV}/c^2$ (later corrected to $128\ \mathrm{GeV}/c^2$ with a recalibration of the luminosity measurement). In 1994 CDF claimed the first evidence for di-top quark production at the TEVATRON[7] with some discrepancy from the SM prediction (a cross-section 2.5 times larger than the expected). This was later revised after an improved background normalisation brought the $t\bar{t}$ cross-section to within SM limits but reduced the significance of the potential signal. In 1995 CDF and $D\emptyset$ jointly announced the discovery of the top quark, marking the end of a search lasting nearly two decades and spanning a much larger energy range than had been anticipated.

2.6.2 Motivation for the Top Quark

The discovery of the top quark in 1995 was the end of a search which began after the discovery of the bottom quark in the late 1970s. Though other models neglecting a sixth quark had been constructed and previous searches had failed to reveal any conclusive results, there were a number of indirect theoretical and experimental reasons to suppose the existence of a sixth quark. Below is a short synopsis of some of the main arguments for the top quark before the TEVATRON discovery, as well as a brief explanation of the constraint on the top mass based on indirect searches. This section is based on the opening chapter of [13].

2.6.2.1 Theoretical Motivation for the Top Quark

Theoretical considerations were based around the preference for three quark doublets. There were two main reasons for this. Firstly, a partner for the bottom quark is required for the GIM-mechanism[14] to be generalised to three quark generations[8].

The second reason pertains to renormalisation of the gauge theory of weak interactions itself. Renormalisability can be proven in the case that the sum of the weak hyper-charges, of all left-handed fermions is zero i.e. $\sum_{left-handed\ fermions} Y_i = 0$. If each lepton multiplet has a value y=-2 and each quark multiplet y=+2/3, then the renormalisation condition is met when every quark exists in three color versions and the number of quark and lepton generations is equal. However, the general proof of gauge theory renormalisation is only applicable if the gauge theory in question is consistent, i.e. without anomalies. In the case where there are anomalies present due to fermion loops like fig.2.8, the cancellation of potentially diver-

[7] Top pair production had previously been claimed at $Sp\bar{p}S$ in 1984 with $m_{top} > 40 \pm 10\ \mathrm{GeV}/c^2$. This was later recanted after more data and improved analysis.

[8] The GIM-mechanism was originally proposed for a quartet of fermions but is equally generalisable to a sextet. It describes how Flavor Changing Neutral Currents can be suppressed for tree-level processes in the SM (i.e. a change in quark flavor via Z-boson emission alone), as well as prohibiting processes with a change in Strangeness greater than one, neither of which have been observed in experiment.

gent diagrams becomes impossible and the proof inapplicable, even if the gauge theory is renormalisable. Anomaly freedom is guaranteed if

$$d_{abc} = \sum_{fermions} Tr[\hat{\lambda^a}, \{\hat{\lambda^b}, \hat{\lambda^c}\}] = 0, \tag{2.1}$$

where d_{abc} is the coefficient in the definition of the anomaly and $\hat{\lambda^i}$ represents the generators of the gauge group. In the SM, electroweak interactions are described by the gauge group $SU(2) \times U(1)$ with the role of the gauge generators filled by the Pauli matrices $\hat{\lambda}^i = \sum_i (i = 1, 2, 3)$ and the hyper-charge $\hat{\lambda}^4 = Y$. In the case of fig.2.8, supposing there are an equal number of lepton generations and quark doublets, such that renormalisation is possible if the theory is without anomalies, then

$$d \propto \sum_{i=1}^{N} \left[\frac{1}{2}(0)^2 - \frac{1}{2}(-1)^2 + \frac{1}{2}N_c \left(+\frac{2}{3}\right)^2 - \frac{1}{2}N_c \left(-\frac{1}{3}\right)^2 \right] = 0 \tag{2.2}$$

Where the anomalies cancel if N_c, the number of quark colors, is three. Therefore, since experimental evidence favoured (at least) three lepton generations[9], this argument implies there are three quark generations. In addition, the lack of experimental observations of the kind of processes which could produce anomalies in calculations, like fig.2.8, corroborates the theoretical mechanism outlined above. Hence, since three quark doublets were expected, SM gauge theory predicted a partner for the bottom quark in the third generation.

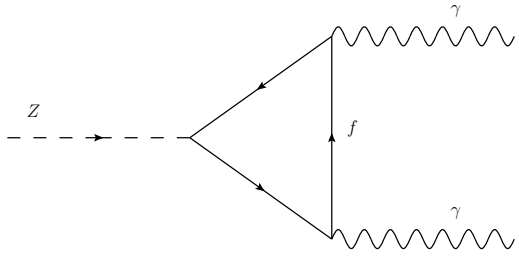

Figure 2.8: Fermion loop which could potentially produce an anomaly in calculation.

2.6.2.2 Indirect Experimental Evidence for the Top Quark

The strongest indirect evidence for the top quark comes from electron-positron collisions at LEP and SLC. Here, the b-quark isospin[10] was studied by measuring the $Z \rightarrow b\bar{b}$ vertex near

[9] Since the mid-1970s the experimental evidence was available for the tauon but only with the precision measurement of the Z mass resonance at LEP could a maximum limit of three species of lepton be set. The LEP measurement was based on measuring Z boson decay rates. It was found no further fermion generations were required to account for Z mass resonance. This rules out any other "light" (i.e. $m_f < \frac{1}{2}M_Z$) fermions in the SM.

[10] In detail, the axial-vector and vector charge components of the Z coupling to b-quarks were measured. In theory, these are dependent on the third component of the weak isospin for left- and right-handed b-quark

the Z-pole and comparing the partial decay width to the full hadronic width, $R_b = \frac{\Gamma_{Z\to b\bar{b}}}{\Gamma_{Z\to had.}}$. There is excellent agreement between the theoretical predictions and experiment in SM if top quark effects are included in the calculation[11]. In addition, the forward-backward asymmetry of $e^+e^- \to b\bar{b}$ is also sensitive to the relative size of the axial-vector and vector couplings of $Z \to b\bar{b}$,

$$A^0_{FB}(M_Z) = \frac{3}{4}\frac{2v_e a_e}{(v_e^2+a_e^2)}\frac{2v_b a_b}{(v_b^2+a_b^2)}, \tag{2.3}$$

where a_b and v_b are the axial-vector and vector charges respectively. Measurements at LEP, SLC, as well as lower energy experiments [12] suggest the third isospin component of the b-quark is -1/2, which implies it should have a weak isospin partner with a complementary isospin of +1/2, i.e. the top quark, in order that the doublet has zero combined isospin.

2.6.3 Constraints on Top Mass

In the SM, all EW quantities (mass, width, couplings of W and Z bosons) depend on five fundamental parameters. At leading order this set can be reduced to three: two boson couplings and the Higgs field vacuum expectation value. These can be related to the three best measured quantities of EW theory: the electromagnetic coupling constant α, the Fermi constant G_F and the Z-boson mass m_Z. If the EW mixing angle θ_W is defined as:

$$\sin^2\theta_W \equiv 1 - \frac{m_W^2}{m_Z^2}. \tag{2.4}$$

The W-boson mass may then be expressed as:

$$m_W^2 = -\frac{\frac{\pi\alpha}{\sqrt{2}G_F}}{\sin^2\theta_W(1-\Delta r)}, \tag{2.5}$$

where Δr is the contribution from one-loop corrections, e.g. fig.2.9.

The correction contribution from the top to W and Z boson masses can be expressed as follows:

$$(\Delta r)_{top} \simeq \frac{3G_F}{8\sqrt{2}\pi^2\tan^2\theta_W}m_t^2, \tag{2.6}$$

Hence, the top correction contribution has quadratic dependence on the top mass at lead-

fields and the electric charge of the b-quark. Since the electric charge is well measured (Q=-1/3), the weak axial-vector and vector couplings imply measurement of the b-quark isospin-spin.

[11] In fact, when the sensitivity of R_b to the top mass is investigated, a value around 175GeV/c is strongly favoured.

[12] Low energy experiments such as PEP, PETRA and TRISTAN were sensitive to the interference between neutral current and electromagnetic amplitudes. This resolves the sign ambiguity of the combined relative coupling.

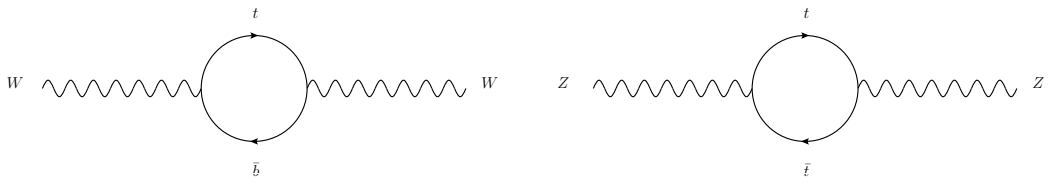

(a) **(b)**

Figure 2.9: Virtual top loops which effect W and Z boson mass predictions.

ing order. This places a strong constraint on top mass predictions as this contribution is much larger than other loop corrections. The equivalent analysis of the contribution to the one loop correction from the Higgs boson places a much weaker constraint on the top mass. The contribution

$$(\Delta r)_{Higgs} \simeq \frac{3G_F m_W^2}{8\sqrt{2}\pi^2}\left(ln\frac{m_H^2}{m_Z^2} - \frac{5}{6}\right) \tag{2.7}$$

is merely logarithmic and hence an experimental measurement would require greater precision to probe this constraint, as well as a good understanding of the contributions from other corrections of a similar magnitude. Precision measurement of parameters which are sensitive to these loop corrections and would place limits on the top contribution and hence the top mass itself. This was used to successfully predict the range of the top mass before CDF or $D\emptyset$ observed it[13].

An indirect measurement of the top mass based on Z-pole data together with measurements of the W-boson mass and total width as well as several other EW quantities gives $m_{top} = 179.4^{+12.1}_{-9.2}\ \mathrm{GeV}/c^2$ [15, 16], which coincides well with the world average of direct measurements $m_{top} = 172.7 \pm 2.9\ \mathrm{GeV}/c^2$ [17]. This corroboration between theory and experiment lends confidence to the predictive power and accuracy of radiative corrections to the SM, and hence this technique is the basis for predictions of the last remaining particle of the SM, the Higgs boson.

2.6.4 Top Sector

The following section describes the production and decay of top quarks at hadron colliders, outlining the peculiarities of this sub-sector of flavor physics at the LHC.

[13] In addition to precision measurement of W and Z masses, νN and eN deep inelastic scattering, νe elastic scattering and atomic parity violation can be used to constrain the top mass prediction within the SM.

2.6.4.1 Top Production

Top quarks can be produced by two mechanisms: the first, and most copious, is via the strong force, when tops are produced in quark-antiquark pairs; the second is via the EW force, involving W-bosons, which produces top quarks singly. Here, top pair production will be described since it is of most interest to the following analysis.

The total top quark pair production cross-section for a hadron-hadron hard scattering process with a CoM energy $\sqrt{s}$ is expressed as:

$$\sigma^{t\bar{t}}(\sqrt{s}, m_{top}) = \sum_{i,j=q,\bar{q},g} \int dx_i dx_j f_i(x_i, \mu^2) f_j(x_j, \mu^2) \times \hat{\sigma}^{ij \to t\bar{t}}(\rho, m_{top}^2, x_i, x_j, \alpha_s(\mu^2), \mu^2), \tag{2.8}$$

where $f_i(x_i, \mu^2)$ and $f_j(x_j, \mu^2)$ are the PDFs for the two incident hadrons and $\rho = 4m_{top}/\sqrt{\hat{s}}$, where $\hat{s} = x_i x_j s$ is the effective CoM squared of the incident partons. This relates the CoM energy of hadronic collision to the energy available for the partonic interaction. The summation indices run over all parton pair combinations i.e. $q\bar{q}$, qg, $\bar{q}g$ and gg. Fig.2.10 shows the tree-level di-top pair production mechanisms via quark-antiquark annihilation and gluon fusion.

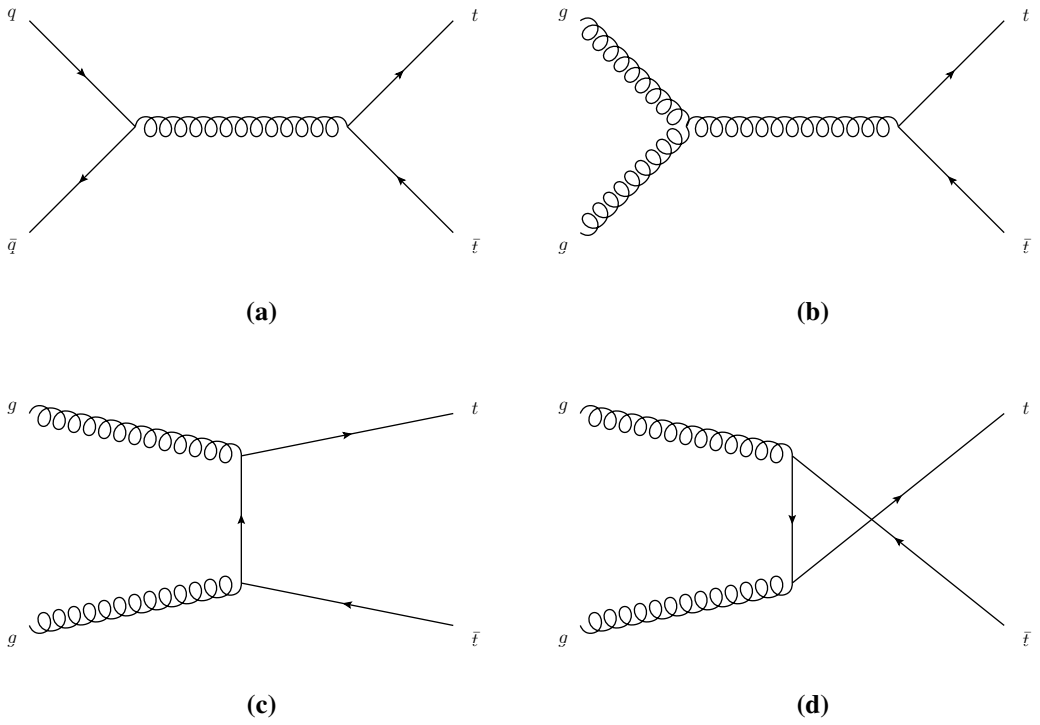

Figure 2.10: Lowest order top pair production via strong interaction from hadron-hadron collisions: a) quark-antiquark annihilation, b) s-channel gluon fusion, c) and d) t-channel gluon fusion.

For top pair production, the minimum effective CoM energy of the two incident partons is $\sqrt{\hat{s}} \geq 2m_{top}$. From the previous relation, the product of the two incident parton fractions is the ratio of the hadronic CoM squared to the partonic CoM squared , i.e. $x_i x_j = \hat{s}/s \geq 4m_{top}^2/s$. Hence, for approximately equal parton fractions $x_i \simeq x_j = x \Rightarrow x \simeq \frac{2m_{top}}{\sqrt{s}}$. From this rough calculation, top pair production requires the parton fraction of the hadron momentum to be at least equal to the ratio of twice the top mass to the hadronic CoM energy.

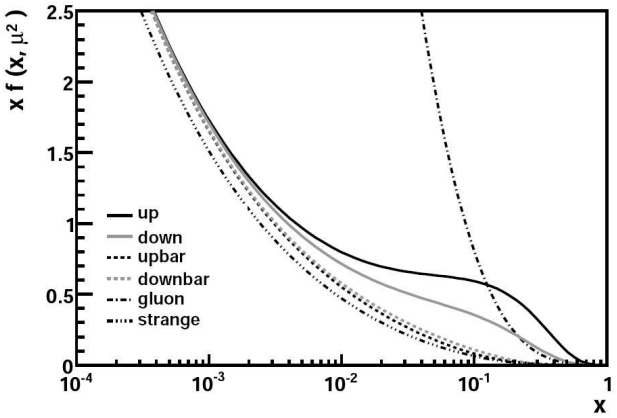

Figure 2.11: PDFs of proton constituents[18], CTEQ6.5M parameterisation[19].

At the LHC, with nominal CoM of $14TeV$, $x = 0.025$ [14]. This is an order of magnitude lower than the TEVATRON momentum fraction (Run I $x = 0.19$, Run II $x = 0.18$). Comparing these to the PDFs calculated for scales around the top mass, i.e. $Q^2 \sim 4m_{top}^2$, fig.2.11 shows that the dominant top pair production mechanism at the TEVATRON is via quark-antiquark annihilation[15], while at the LHC it is by gluon fusion (90%).

Realistically, asymmetric momenta are possible, where the momentum of one parton in the collision is much higher than the other. This effectively adds low-x gluon contributions to the total $t\bar{t}$ cross-section. Also, top pairs can be produced above the mass threshold. Though the first of these is important for calculations for the TEVATRON environment, where tops are more rarely produced, the high energies of the LHC mean low-x gluons play a smaller role in top pair production. Top pairs produced at the LHC are also more likely to have significant energy above threshold, leading to final states with higher kinematic parameters than previous observed.

Accurate measurement of the top pair production cross-section is important for reasons other than as a signal in itself. Firstly, it is an opportunity to look for the signs of new physics. This may come as an enhancement of the cross-section, implying a new production mechanism (e.g. gluino production and decay, $\tilde{g} \rightarrow \tilde{t}t$), or as a suppression, suggesting a

[14] At a CoM of 10 TeV $x = 0.035$ and for the 2010 CoM energy 7 TeV $x = 0.05$.

[15] By this argument, for Run I 10% of $t\bar{t}$ production is via gluon fusion. A small increase in $\sqrt{s}$ in Run II leads to 30% increase in production cross- section and increases the proportion of gluon fusion $t\bar{t}$ events to 15%

new top decay mode (e.g. to a stop and the lightest super-symmetric particle, $t \rightarrow \tilde{t}\tilde{\chi}^0$). A second reason is that the $t\bar{t}$ signal is also an irreducible background to any single top cross-section measurement, which itself is important in measuring the $|V_{tb}|$ CKM matrix element. In addition $t\bar{t}$ event topology is similar to the kinematics of multi-jet events such as Higgs or SUSY signatures, therefore it is a stepping stone to more complex analyses.

2.6.4.2 Top Decay

The decay of the top quark is expected to go primarily by the two-body channel $t \rightarrow Wb$. When the terms of order m_b^2/m_t^2, α_s and order $(\alpha_s^2/\pi)m_W^2/m_t^2$ are ignored in the decay amplitude, the expression for the predicted width of the top decay in the SM is:

$$\Gamma_t = \frac{G_F m_t^3}{8\pi\sqrt{2}} \left(1 - \frac{M_W^2}{m_t^2}\right)^2 \left(1 - 2\frac{M_W^2}{m_t^2}\right) \times \left[1 - \frac{2\alpha_s}{3\pi}\left(\frac{2\pi^2}{3} - \frac{5}{2}\right)\right], \tag{2.9}$$

where the G_F is the Fermi coupling constant, which contains the largest part of the one-loop EW radiative corrections. Including the correction in the expression makes the calculation theoretically accurate to better than 2%. Further QCD corrections of the order α_s^2 improve the accuracy to better than 1%. The sensitivity of the width to the large mass of the top gives an exceptionally short lifetime of $\simeq 0.5 \times 10^{-24}s$. This means that top quarks will almost always decay before hadronisation can occur, hence the extreme rarity of top-flavored bound states, making their detection practically impossible. This is a feature of quark decay peculiar to the top sector in the SM.

$t \rightarrow Ws$ and $t \rightarrow Wd$ decays are predicted to be suppressed relative to the Wb channel due to the relative strengths of the CKM matrix elements squared. The values of the matrix elements are estimated from measurement and unitarity to be $|V_{td}| = 0.004 - 0.014$, $|V_{ts}| = 0.037 - 0.044$ and $|V_{tb}| = 0.9990 - 0.9993$, though none have been measured directly thus far. $|V_{ts}|$ may be obtained indirectly from $B_s^0 - \bar{B}_s^0$ mixing, illustrated in fig.2.12. $|V_{tb}^* V_{ts}|^2$ is proportional to the frequency of oscillation, Δm_s. This was measured by CDF and found to be $\Delta m_s = 17.77 \pm 0.10(stat) \pm 0.07(syst)$ [20]. $D\emptyset$ also set a range of $17 < \Delta m_s < 21ps^{-1}$ at 90% confidence level [21]. The expected value for Δm_s from theory is $18ps^{-1}$. The theoretical uncertainty is comparable to Δm_d, implying $|V_{ts}|$ can only be obtained to within an experimental error of 20%, which is larger than the uncertainty inferred from unitarity considerations above i.e. 10%.

$|V_{ts}|/|V_{td}|$ can be extracted from the following expression:

$$\frac{\Delta m_s}{\Delta m_d} = \frac{M_{B_s}}{M_{B_d}} \xi^2 \left|\frac{V_{ts}}{V_{td}}\right|. \tag{2.10}$$

ξ^2 is the theoretical uncertainty in the ratio of hadronic matrix elements, which is smaller than the uncertainty on the hadronic matrix elements themselves. If the value of $|V_{ts}|$ from

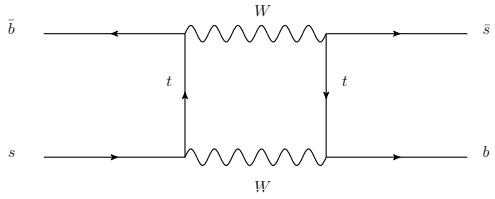

Figure 2.12: $B_s^0 - \bar{B}_s^0$ mixing via box diagram.

unitarity constraints is used then the uncertainty on $|V_{td}|$ is less than the uncertainty on Δm_d itself. Δm_d is already an object of investigation as it represents one of the constraints on the CKM unitarity triangle which is of importance in precision b-physics measurements.

$|V_{tb}|$ is one of the most precisely known (0.02%), though never directly measured, CKM matrix elements, assuming there are three generations of quarks such that the unitarity constraint can be used. Since the theoretical accuracy is much greater than the experimental, it is only worthwhile investigating this value to see if there is any evidence for a fourth generation i.e. relax the unitarity constraint. When this is done $|V_{tb}| = 0.08 - 0.9993$. In this case $|V_{tb}|$ can be directly measured by observing top decays $t \to Wq$ and comparing decays involving a b-quark to all top decays i.e.

$$R = \frac{B(t \to Wb)}{B(t \to Wq)} = \frac{|V_{tb}|^2}{|V_{tb}|^2 + |V_{ts}|^2 + |V_{td}|^2}, \tag{2.11}$$

where q is any down-type SM quark (d, s or b). In the case that the assumption of three generations is relaxed the denominator, $|V_{tb}|^2 + |V_{ts}|^2 + |V_{td}|^2$, will not be unity. Measurements of the fraction tending to one would imply $|V_{tb}| \gg |V_{ts}|\&|V_{td}|$ without providing results as to the absolute magnitude of $|V_{tb}|$. To measure the $|V_{tb}|$ directly without assuming the number of quark generations, single top production by EW interaction must be studied. The cross-section for the three single top production mechanisms provide direct measurement as each is proportional to $|V_{tb}|$[16]. $|V_{tb}|$ could also be determined from the top width observation at a lepton-antilepton collider with CoM energy at the $t\bar{t}$ production threshold. This would provide much greater experimental accuracy on ($\Delta|V_{tb}|$ $\Delta\Gamma/2$), owing to a much cleaner event environment[17].

[16]The measurement of single top production offers the best opportunity to measure the $|V_{tb}|$ CKM matrix element at a hadron collider since all three production processes involve a top quark charged current such that the cross-section calculation is proportional to $|V_{tb}|^2 g_W^2(tb)$. Each channel has different systematic uncertainties allowing for useful cross-checks across analyses.

[17]An accuracy of $30\ \mathrm{MeV}$ i.e. 2% on the top width would limit the uncertainty on $|V_{tb}|$ to 1%. This is an improvement on the single top production uncertainties at the LHC. For example the t-channel W-gluon fusion process is limited by the gluon distribution function uncertainty, $\Delta|V_{tb}|$ $\Delta g(x)/2$, where a reasonable estimation of $\Delta g(x)$ is of the order of 10%. Measuring fundamental parameters at hadron colliders typically requires input from several sources e.g. deep-inelastic scattering for PDFs, theory for precise QCD calculations, not to mention the experiment itself.

2.6.5 $t\bar{t}$ Final States

Since the top quark decays almost exclusively to a W-boson and a bottom quark in the SM, the final states of top pair decays can be split into three classes based on the decay modes of the W-boson. The W-boson can decay leptonically, $W \rightarrow l\nu_l$ to the three possible leptons or hadronically $W \rightarrow q\bar{q}'$ to the four lightest quarks- b-quarks are suppressed due to their larger mass, while the high mass of top quarks prohibits them completely. The universality of decay rate across the possible daughters means the W-boson has 9 (3 leptons plus two quarks with three possible color states) potential decay modes. Hence, 2/3 of the time the W-boson decays hadronically with the remaining third leptonic.

Fig.2.13 shows the three possible lowest-order top pair decay schemes for gluon-gluon initial states (the initial state is irrelevant to the decay mechanism): (a) is called the fully hadronic or all hadronic channel, since the outgoing quarks hadronise to jets before they reach the detector, occurs in 46.2% of events[13]; (b) is the semi-leptonic or lepton+jets channel, occurring in 43.5% of events; and, (c) is the fully leptonic channel, accounting for 10.3% of events. Each of the decay classes has been observed.

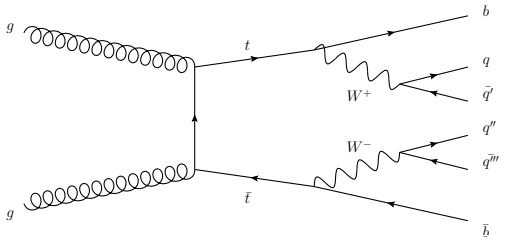

(a) fully hadronic $t\bar{t}$ decay

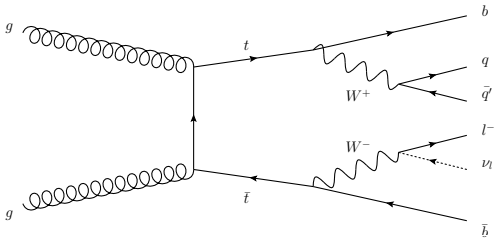

(b) semi-leptonic $t\bar{t}$ decay

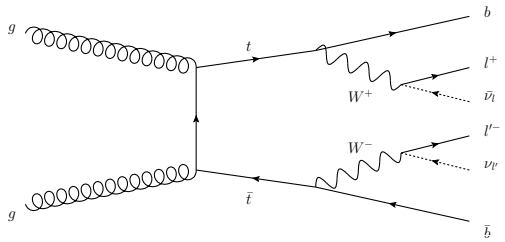

(c) fully leptonic $t\bar{t}$ decay

Figure 2.13: Lowest-order top pair final states from gluon-gluon collisions. All final state quarks (q) are u, d, s, c or corresponding anti-quark. All final state leptons (l) are either e, μ, τ with the corresponding neutrino.

2.6.6 Top Properties

Though the top quark was discovered in 1995 most of its fundamental parameters are not yet measured to high precision or confidence. The following is a list of top parameters currently under investigation.

2.6.6.1 Mass

Given the mass of the top its relative precision (1.7%) is the most accurate of all quarks. The experimental technique used to obtain the top mass measurement, i.e. obtaining a peak in the invariant mass distribution of top decay production W-boson and b-quark, suggests this value should be interpreted as the top *pole mass*. Like any other quark mass measurement, this has an inherent ambiguity of $\Lambda_{QCD} \sim 200\ \mathrm{MeV}$, originating from fragmentation effects occurring in hadronisation. The theoretical top quark precision is determined from the relation of masses between the W-boson, top quark and Higgs boson. If the Higgs boson is observed, a rough measurement of its mass would improve the top mass accuracy, as precision EW measurements are sensitive only to the logarithm of the Higgs boson mass. The relation of masses can also be used to test the consistency of the SM, by comparing a derived top mass value from a precision measurement of the W-boson with a direct top mass measurement [18] The current top mass measurement and precision from combined TEVATRON analyses is $m_{top} = 172.6 \pm 1.4\ \mathrm{GeV}/c^2$[19][22].

It will be difficult to improve on this accuracy at the LHC[20], however, new analysis techniques will offer important crosschecks. Complementing the hadronic top reconstruction of the semi-leptonic channel is the measurement of the b-quark decay length and top pair production cross-section. In the former case the transverse decay length depends on the boost the b-quark received, γ_b, from the top decay, which in turn depends on the parent top mass, like so:

$$\gamma_b = \frac{1}{2}\frac{m_{top}^2 + m_b^2 - M_W^2}{m_b^2(\sqrt{m_{top}^2 + |\vec{p_t}|^2} - |\vec{p_t}|\cos\theta_{tb})}. \tag{2.12}$$

Hence, from the measurement of the b-quark boost, given the masses of the b-quark and W-boson, a top mass value can be derived. As this method relies mainly on the tracking performance (and not directly on the jet energy scale) of the detector to identify b-quarks from secondary vertices, the uncertainties are uncorrelated to the hadronic top reconstruction

[18] For example, an uncertainty of $\Delta M_W = 20\ \mathrm{MeV}/c^2$ gives a corresponding derived top mass uncertainty of $\simeq 3\ \mathrm{GeV}/c^2$. Hence, a direct top mass measurement of equivalent precision or better is required to ascertain any discrepancies between SM theory and experimental observation.

[19] As of July 2010.

[20] A current estimate of the top mass accuracy of ATLAS is $1 - 3.5\ \mathrm{GeV}$ from $1fb^{-1}$ of data using the lepton+jets decay channel[23]. The main systematic error comes from the jet energy scale

technique.

The latter method exploits an uncertainty relationship of the SM, $\frac{\Delta\sigma_{t\bar{t}}}{\sigma_{t\bar{t}}} \sim \frac{5\Delta m_{top}}{m_{top}}$. The precision of this technique is limited by the theoretical uncertainty of 2%, which is dominated by scale dependence. Although these methods are not competitive at the LHC with current precision, they provide valuable crosschecks. Further improvements to precision is achievable at a lepton-lepton collider around threshold energy.

2.6.6.2 Electric Charge

The electric charge of the top quark, q_{top}, has yet to be measured, hence it is still possible the observed quark is not the SM partner for the b-quark. For instance, the charge correlation between W-bosons and b-quarks in $p\bar{p} \rightarrow t\bar{t} \rightarrow W^+W^-b\bar{b}$ events has not been measured at the TEVATRON experiments. A consistent alternative to the SM quark, with $q_{top} = +2/3$, is the an exotic heavy quark, Q_4, with charge $-4/3$ decaying via $Q_4 \rightarrow W^-b$. To determine the parent quark charge, the charge of the decay products must be measured, in particular the b-jet, or a study of photonic radiation in $t\bar{t}$ events undertaken[24][21]. The latter method is best applied to LHC environment where gluon-fusion dominates $t\bar{t}$ production. Contrastingly, at the TEVATRON $q\bar{q}$ annihilation is the main production mechanism and photonic ISR constitutes an irreducible background thereby limiting sensitivity. In either case, the electric charge would be much more easily ascertained at a lepton-lepton collider where the ratio $R = \frac{\sigma(l^+l^- \rightarrow hadrons)}{\sigma(l^+l^- \rightarrow l'^+l'^-)}$ can be measured at the top production threshold.

2.6.6.3 W-boson Helicity in Top Decay

In the SM all fermions have the same vector-minus-axial-vector (V-A) charged current weak interaction expression, $\left(-i\frac{g}{\sqrt{2}}V_{tb}\gamma^\mu\frac{1}{2}(1-\gamma_5)\right)$. In the top case, this means that the the W-boson in decay cannot have positive helicity i.e. be right-handed. The expression dictates that in the massless b-quark limit the b-quark must always be left-handed. To conserve angular momentum along the decay axis (there is no component of orbital angular momentum along this axis) the W-boson must always be left- handed. Hence top quarks couple to W-bosons of negative (left-handed) or zero (longitudinal) helicity. The latter coupling is enhanced with respect to the weak coupling

$$B(t \rightarrow W_0 b) = \frac{m_{top}^2}{m_{top}^2 + 2M_W^2} \simeq 0.70. \tag{2.13}$$

[21] More accurately, this method measures the combination of the electromagnetic coupling strength and the charge quantum number of the top quark. Therefore a combination of the two methods mentioned would yield both parameters to compare with SM predictions.

2.6.6.4 Spin Correlation in Strong $t\bar{t}$ Production

One of the effects of the strong interaction on the lighter quarks is the loss of spin information. The forming of bound states depolarises the constituent quarks thereby obscuring their initial spin state. In contrast, the short lifetime of the top quark, on average decaying before the strong interaction can take effect, means the information is passed to the decay products. Although the spin of the decay products is lost in subsequent hadronisation the distribution of these products is indicative of the initial top spin. At the LHC and TEVATRON where the tops are produced unpolarised, the spins of the top pair are correlated.

The reason for the correlation comes from QCD effects near the threshold of top production. Here, the $t\bar{t}$ pair, is predominantly produced in ${}^3S_1$ or ${}^1S_0$ state for $q\bar{q}$ annihilation and gluon-gluon fusion, respectively. In the former case both tops have parallel spin (i.e. opposite helicities) and in the latter anti-parallel spin (i.e. same helicity). At energies well above the production threshold conservation of chirality determines the top pair to be produced with opposite helicity. At threshold energies, where the top pair are produced with no angular momentum, the spin of the colliding partons is conserved. For $q\bar{q}$ there is a basis which interpolates at all energies between the extremes, where the $t\bar{t}$ spins are always opposite. Hence, for this aptly chosen axis, $t\bar{t}$ spin correlation can be up to 100%[22] Hence the spin correlation can be used to study the top $t\bar{t}$ production mechanism. In addition the weak decay properties can be observed by measuring the angular distributions between the decay products from each top.

At leading order, single top production at hadron colliders results in the top being left-hand polarised along the direction of motion of the d-quark in the top rest frame [23]. Both the single top polarisation and top pair correlations are verifiable SM predictions which will be useful observables by which to look for evidence of new physics.

2.6.6.5 Asymmetry in $t\bar{t}$ Production

Strong production of $t\bar{t}$ pairs are produced with a slight asymmetry in the distribution of quarks creating a forward-backward asymmetry. At the TEVATRON this effect was too small (5%) to measure. Perhaps the LHC will be able to measure this so far undetected effect.

[22]The spins are also almost totally uncorrelated in unpolarised lepton-lepton collisions (though a small amount of polarisation (2%) perpendicular to the scattering plane is inherent due to QCD interactions in the final state, and a smaller contribution again comes from mixed QCD/weak interactions in the scattering plane). Polarised beam collisions would produce polarised top pairs. This would be the ideal case to study the weak decay products of top production and hence the top spin properties; however, this is most easily achieved at lepton colliders.

[23]This is only strictly true in the leading-order case with massless quarks. Initial state radiation of gluons effects the CoM of the initial partons and therefore the helicity on the massive top quark.

2.6.6.6 Rare Top Decays

Rare top decays are difficult to produce with significant statistics and very difficult to identify in data. Flavor changing neutral current decays, $t \to Zq$ and $t \to \gamma q$ are suppressed to the extent that that the branching ratios can be neglected in the SM. Less suppressed, but still rare due to small CKM matrix elements, are the decays $t \to Ws$ and $t \to Wd$. Though these have small branching fractions (0.1% and 0.01%, respectively) the copious production of top events at the TEVATRON and especially the LHC mean there will be a significant number produced. Unfortunately, the similarity of their decays to $t \to Wb$ events make identification extremely difficult, hence there are currently no strategies for direct measurement of $|V_{ts}|$ or $|V_{td}|$.

2.6.6.7 Top Yukawa Coupling

The Yukawa coupling relates the source of mass generation in the SM, the Higgs coupling, to the fermionic matter content of the SM. The Yukawa coupling of the top quark is described by $y_t = \sqrt{2}m_t/v$, where $v \simeq 246$ GeV is the vacuum expectation value, and is close to unity. Associate Higgs production, $t\bar{t}H$, is expected to be directly observable at the LHC and through this channel y_t[24]. Complementary indirect measurements rely on precision measurement of the top quark mass. Given accurate knowledge of the vacuum expectation value, the SM expression above can be used to determine a y_t value.

2.7 Multi-Jet Event Simulation

Monte Carlo (MC) event simulation is a necessary tool in modern particle physics experiments. In essence they provide the phenomenological predictions of high energy collisions derived from theoretical principles. Many signal and background processes at the LHC will involve multi-jet event signatures. However, perturbative QCD predictions of event topologies and kinematics describe multi-parton final states. Pseudo-event generation is a complicated procedure involving several subprocesses. Although not all parts are derived strictly from first principles (e.g. parton showering and hadronisation) all have sound mathematical or phenomenological foundations. The following section describes the general features of MC pseudo-event generation.

[24]The most accurate determination of y_t would come at a linear collider. A CoM of 500 GeV would make a precision measurement possible with 33% uncertainty (with a possible improvement to 10% precision with polarised beams). An enhanced cross-section at $\sqrt{s} = 800$ GeV could potentially provide an accuracy of 5% for unpolarised e^-e^+ collision.

2.7.1 Event Simulation

The simulation of hadron-hadron interactions in MC uses factorisation explicitly to separate the "short range" hard scattering process, where QCD calculation is apt, from the "long range" soft interactions. The hard process (next-to-)leading order matrix element is calculated (Pythia[25] (LO), ALPGEN[26] (LO), HERWIG[27] (LO), MC@NLO[28] (NLO)) based on the set of parton distribution functions. The high energy environment of the LHC implies a tendency for final state partons of the hard scatter to radiate. This then requires phenomenological models based on well understood processes and assumptions with sound mathematical foundations to take into account ISR and FSR effects. Partons go through a hadronisation model such that the end products of the simulation are jets of colorless mesons and baryons. Different phenomenological models are available for this process, such as the Lund model (used by Pythia), which treats the gluons as $q\bar{q}$ pairs and hadronises them according to the string fragmentation model, and the cluster fragmentation model (used by HERWIG), which forms hadrons from colorless clusters made of quarks and gluons with low invariant mass.

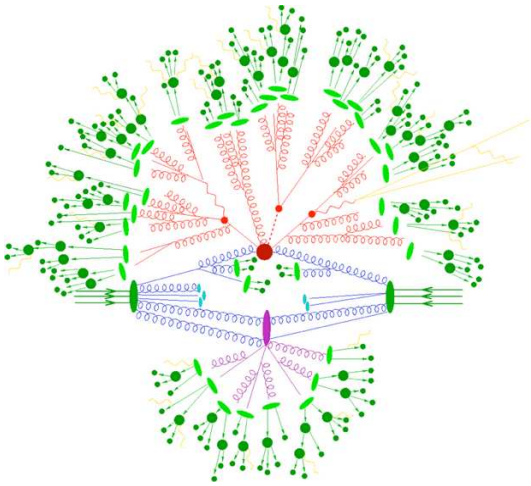

Figure 2.14: Schematic diagram of a pseudo-event: initial state (blue), hard scatter (red), parton shower (dark red), fragmentation (green), hadron decays (dark green), beam remnants (light blue) and underlying event (pink).

The inherent messiness of hadronic collisions means additional soft components of the underlying event must be simulated: multiple parton interactions (MPIs), when more than one parton-parton scatter takes place during the hadronic collision; hadron remnant fragmentation, where the remaining spectator partons produce soft radiation; and, color reconnection where the remnants of the hadronic collision(s) and interacting partons continue to influence each other via the strong force. The precise role and extent of each of these processes is not well-understood and the phenomenological models used to approximate their effect in simulation do not have the theoretical basis of ISR/FSR models.

High beam luminosity requires event simulation should include multiple proton interactions and pile-up. Multiple proton interactions occur when more than one hadronic interaction occur per bunch crossing. These are modelled in simulation by superimposing the data from minimum bias events onto the generated event. Minimum bias events are defined as events that have not been triggered by a high $\mathrm{p_T}$ lepton, jet or by missing transverse energy. Since multiple proton interactions occur per colliding bunch, the number of minimum bias events added is dependent on the luminosity of the colliding beams. Hence, LHC simulations are much more dependent on this phenomenological model than those for the TEVATRON where the luminosity is lower. A related event feature is when interactions from consecutive bunch crossings overlap in the detector, called pile-up. These can be reconstructed in a single event. This is modelled by adding randomly recorded data (called zero bias events) to hard pseudo-event signatures.

This is the end of the event generation process but for an accurate prediction of hadron collider event topologies and kinematic distributions the effects of the detector itself must be included. Particles will shower as they traverse the detector bulk leading to wide sprays of particles incident on detecting elements as well as "punch through" effects, where particle showers pass through a detector volume and deposit their energies on adjacent elements. In addition, any magnetic fields present will deflect the tracks of charged particles. At the LHC simulation of these effects is based on GEANT 4[29] software. Full simulation of the detector geometry and material distribution can be computationally taxing so in addition fast simulations are also used which are based on parameterisations of the detector response. These parameters are optimised to give reasonable approximations to full simulation. At this point the complete event and detector simulation is finished and digitisation and reconstruction software can be applied, as would be the case in real experiments.

2.7.2 Tree-Level and Beyond

The recipe of tree-level matrix element (ME) calculations is to calculate all possible Feynman diagrams for the process at a set multiplicity, sum and square them. A set of phase-space points are then calculated and weighted by the process cross-section (with the events unweighted for subsequent sampling). The procedure can be automated to cover a range of multiplicities but is limited to processes with less than 6 final state partons due to the computational complexity. A cut is made on the scale of radiative corrections to avoid soft and collinear poles. Importantly the matrix elements are inclusive (involving contributions from lower multiplicities) so samples with differing multiplicities cannot simply be added together without making provision for double-counting.

An alternative approach to calculation is the parton shower (PS) method. Here, algorithms attempt to calculate all event multiplicities approximately, using parameterisations

for radiative corrections applied to lowest-order ME calculations,

$$C_n^{PS} = C_0^{ME} \times splitting functions \simeq C_n^{ME}. \tag{2.14}$$

The splitting functions used are Sudakov form factors [30], which are interpreted as the probability of an outgoing particle not emitting radiation. This strategy works to good approximation within soft and collinear limits for strongly ordered emission ($\mathrm{p_T}$, virtuality Q^2, angle θ). Strongly ordered emission follows the rule that according to some splitting parameter, ρ, each splitting results in a decrease in the parameter i.e. $\rho_{max} = \rho_0 > \rho_1 > ... > \rho_n$. Different parton shower algorithms[25] use different ordering parameters to characterise the coupling strength of each splitting. The purpose of the ordering variable is to isolate soft and collinear poles. The parton shower does not effect the lowest-order prediction.

Comparing the two techniques, each has positive and negative aspects. The matrix element is cut-off dependent with restricted multiplicities, but is observable independent and gives accurate cross-section calculations. The assessment is slightly modified for NLO calculations, which are limited to certain channels and observables but are cut-off independent and give accurate cross-sections to a higher multiplicity than LO ME calculations. Contrastingly, parton showers are inexact and limited to the soft and collinear regions of phase-space, giving good kinematic distributions. However, within these limits PSs are cut-off and observable independent. In the light of the complementary strengths a combination of both methods in appropriate areas of phase-space would provide a more powerful and accurate predicting tool. Hence, a prescription for marrying the two is required.

2.7.3 Matching

As the hard scatter and parton shower parts of the calculation are calculated separately, a problem arises that some event configurations may be double-counted in event generation. The (N)LO matrix element calculation ends with a number of final state particles. These are then passed to the parton shower algorithm to approximate the radiative QCD corrections to all higher orders by adding a number of jets to the final state. There are then two possible sources where double-counting may occur. The first is when there is a n-parton final state passed to the shower algorithm which transform each to a jet. The same final state could also have been obtained if a $(n-1)$-parton final state was then showered with the addition of a jet. In both cases n jets would be reconstructed in the detector, hence double-counting of this n jet observable state has occurred[26]. The second source comes when events with a different number of hard partons are identified in the detector with the same final states

[25] ARIADNE uses $\mathrm{p_T}$, Pythia and SHEPRA use Q^2 with angular ordering imposed separately, HERWIG uses θ with additional cuts needed to avoid soft poles.

[26] To generalise the argument $(n-m)$ partons with m jets added in the parton step, where $0 \leq m \leq n$, can give identical final states in the detector.

due to some of the jets being lost due to momentum or geometrical cuts. To avoid double counting a matching of partons to reconstructed jets is used. The matching procedure also has the benefit of protecting the parton-level cross-section, calculated from the fixed-order matrix element, from any generation cuts (e.g. $\mathrm{p_T}$ or η).

Two matching procedures are used. The first, called $CKKW$ matching[31, 32], reweights the matrix element weights with Sudakov form factors and vetoes shower emissions in phase-space regions already covered by the ME configurations. This avoids double counting. Below a cut-off emissions are passed straight to the PS algorithm. For ME events generated with the maximum multiplicity (N) the PS is allowed to produce emissions above the cut-off so long as they are softer than the the softest ME emission. This avoids under-counting of N+1 multiplicity events. The cut-off scale introduces a dependence which is of the order of the accuracy of the PS.

The second method is MLM matching[33, 34]. In this, outgoing particles from the ME are passed to the PS and the resultant partons clustered at some resolution scale, μ (similar to making jets)

$$k^2_{t,ij} = min(E^2_i, E^2_j)(1 - \cos\theta_{ij}). \tag{2.15}$$

Any parton combinations above a cut-off, $k^2_{t,ij} = \mu$ remain unclustered. Usually the cluster cut-off is set to be the same as the cut-off used in the ME generation. Events are rejected where there are additional or insufficient clusters compared to the original multiplicity. The end result of the procedure is equivalent to Sudakov reweighting [27]. For the maximum multiplicity the matching criteria is relaxed and higher multiplicity clusters are allowed so long as the the N hardest clusters are matched. The rejection is ignored in the case of heavy flavor partons, where two partons may be merged into one jet due to the parton mass. Though double-counting is minimised in this procedure, a new systematic uncertainty is introduced, which depends on the cluster definition and matching criteria.

Most remaining discrepancies between ME and PS regions of phase-space are smoothed out after hadronisation models are applied to the outgoing partons. However, some observables sensitive to specific regions of phase-space may still be affected. Matching procedures are of great import at the LHC where the high rate of multi-jet events, for both signal and background in the case of $t\bar{t}$ analyses, make matching an essential tool in pseudo-event generation.

[27] The probability that no extra clusters were produced and that they match the directions of the original partons is equivalent to the probability that the parton shower did not produce any emissions above the cluster resolution, μ. Vetoing events which fail this requirement has the same effect as reweighting by the Sudakov form factors above the cut-off μ.

Chapter 3

Detector

In this chapter a short overview of the ATLAS experiment based at the LHC accelerator at CERN is given. The LHC and experiments are introduced and a short summary of their purpose and design is given. The ATLAS experiment is described in more detail with particular emphasis on the detector technology and expected performance. The sub-detectors and their responsibilities are explained and the LHC distributed analysis framework introduced.

3.1 LHC

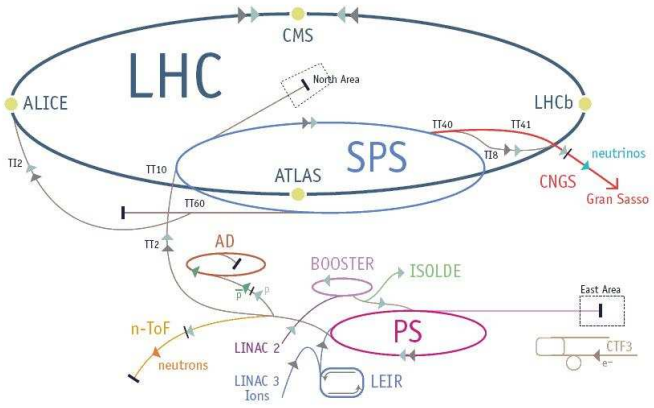

Figure 3.1: LHC accelerators.

The LHC is a proton-proton synchrotron collider, $27\mathrm{km}$ in circumference, built in a subterranean tunnel $100\mathrm{m}$ under the Swiss/French countryside which once housed the Large Electron Position (LEP) collider at CERN. The synchrotron will accelerate and collide beams of around 3×10^{14} protons at an energy of $7\ \mathrm{TeV}$ and luminosity of $10^{34}\mathrm{cm}^{-2}\mathrm{s}^{-1}$. Superconducting magnets create a $8.34\mathrm{T}$ magnetic field to bend the proton beams round the ring at velocities approaching the speed of light. Super-fluid helium is used to cool the copper clad

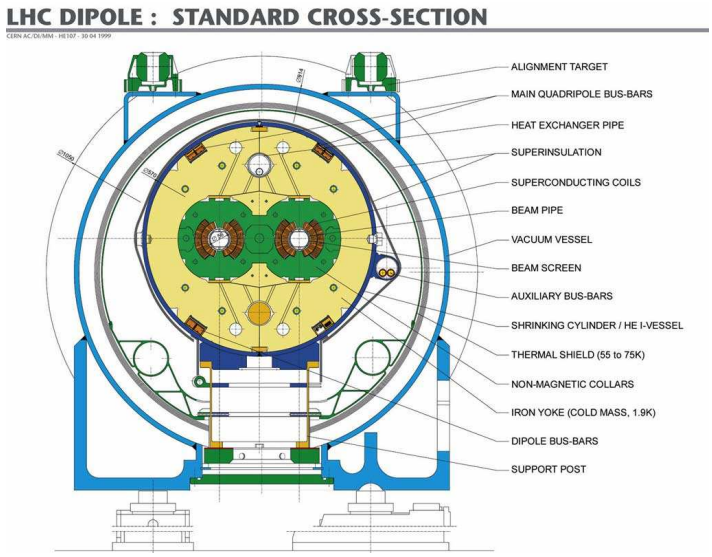

Figure 3.2: Cross-section of LHC dipole.

niobium-titanium coils which comprise the magnets to an operating temperature of $1.9\mathrm{K}$ to permit the required current of $15,000\mathrm{A}$ necessary to generate the magnetic field of the collider.

Several additional accelerators, once experiments in their own right, are used to ramp the protons up to the high energies of the LHC, see fig.3.1. Protons from a hydrogen source are first accelerated to an energy of $50\ \mathrm{MeV}$ by the Linac, then to $1.4\ \mathrm{GeV}$ by the Booster, $25\ \mathrm{GeV}$ is achieved by the proton-synchrotron(PS), and finally $450\ \mathrm{GeV}$ by the super-proton-synchrotron before they enter the LHC ring. The ring itself is composed of 8 linear insertion sections, which are used for collisions, injection, dumping, cleaning and acceleration purposes, and 8 curved arc sections, where the bending dipoles are housed.

Once inside, a radio-frequency (RF) system is used to accelerate the proton beams. The energy of the RF photons is transferred to the protons in a series of cavities. The RF system operates at a temperature of $4.5K$ with a frequency of $400.8\mathrm{MHz}$. This uses $16\mathrm{MV}$ per beam to achieve a bunch spacing of $25\mathrm{ns}$ (or 10 RF periods) and a bunch length of $7.5\mathrm{cm}$. As both beams are composed of protons, unlike the Tevatron, two independent magnetic channels are required. In the LHC these share a common yoke and cryostat, fig.3.2 shows the dipole cross-section. There are 1232 dipoles and 392 main quadrupoles on the ring. During ramping these experience forces of hundreds of tonnes per metre as the field is so strong. The stored energy of the beams must be disposed of safely in the event of a problem. In the case of quenching (rapid cooling) the energy of the beams is absorbed by $8\mathrm{tonnes}$ of steel resistors which are heated to $300^{\circ}\mathrm{C}$. The increased luminosity and energy of the LHC, see table 3.1, offer a step change in collider physics.

The proton beams are brought together at four points around the LHC ring. The four main LHC detectors coincide with the collision points. ATLAS (A Toroidal LHC ApparatuS)

attribute	$Sp\bar{p}S$(1981)	TeVatron(1987)	LHC(2009)
Particle type	$p+\bar{p}$	$p+\bar{p}$	$p+p$
Circumference(km)	6.9	6.28	26.7
No. dipoles	232	774	1232
Peak Magnetic field(T)	1.4	4.4	8.3
CoM energy(TeV)	0.62	1.96	14
Luminosity($10^{30}\mathrm{cm}^{-2}\mathrm{s}^{-1}$)	6	$50-100$	$0.1-1.0\times10^{4}$
Luminosity($fb^{-1}year^{-1}$)	0.05	0.5	100
Particles per bunch*(10^{10})	$15+8$	$24+3$	11.5
Bunches*	$6+6$	$36+36$	$2808+2808$
Bunch spacing(ns)	3800	396	25

Table 3.1: Comparison of recent hadronic accelerators.*numbers shown for each beam.

and CMS (Compact Muon Spectrometer) are omni-purpose detectors with physics programs covering the full lifetime of the LHC. From the first day measurement of particle flow to statistics based searches for SUSY particles using several years' worth of data, both SM and BSM physics will be investigated. Complementing the general purpose detectors, ALICE (A Large Ion Collider Experiment) and LHCb (LHC beauty) are dedicated experiments. LHCb has a single spectrometer arrangement optimised to study flavor-physics and CP violation. ALICE is designed to investigate the behaviour of quark-gluon plasma created in heavy ion collisions. Hence, an additional function of the LHC is heavy-ion collisions. Lead nuclei will collide with a CoM energy of 5.5 TeV and a luminosity of $10^{27}\mathrm{cm}^{-2}\mathrm{s}^{-1}$.

3.2 The ATLAS General Purpose Experiment

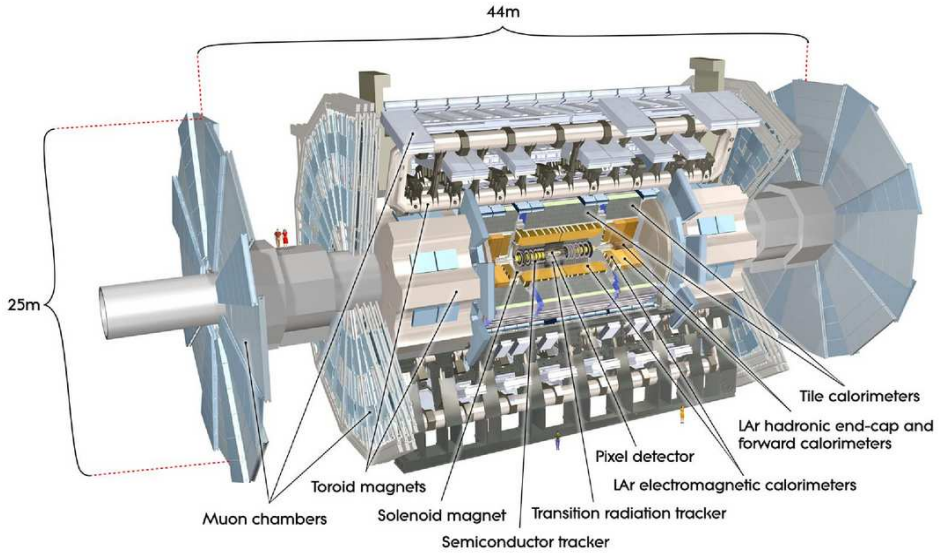

Figure 3.3: ATLAS detector.

The ATLAS collaboration involves over 3000 scientists from around the globe from 174

universities and 38 countries. The goals cover the whole physics range of the LHC including precision measurement of SM parameters and a robust search for new physics signals. The ATLAS detector is situated at point one on the LHC ring. It is $25\mathrm{m}$ in diameter and $44\mathrm{m}$ long weighing around $7000\mathrm{tonnes}$, see fig.3.3. It has several sub-detectors for triggering and full event reconstruction: inner detector for tracking; calorimetry for energy and momentum reconstruction; and an independent muon spectrometer. The detector is forward-backward symmetric around the interaction point. The magnetic field in which the detector is immersed has two sources. The first is a thin superconducting solenoid surrounding the inner detector cavity. The second surrounds the calorimeter and is comprised of three large superconducting toroids with eight-fold azimuthal symmetry. The orientation of the magnetic field is the basis for the structure of the other detector sub-systems.

At nominal design luminosity there will be bunches of 10^{11} protons circulating the LHC rings 40 million times a second. Protons will collide with centre-of-mass energies of $14\ \mathrm{TeV}$ every $25\mathrm{ns}$. Elastic $p-p$ collisions will escape detection in the central region of the ATLAS detector as they will disappear down the beam pipe (into the detection region of the forward detectors). Inelastic collisions, however, will be prolific having a comparatively large cross-section, $\sigma^{pp}_{inel.} = 80\mathrm{mb}$ ($\sigma^{pp}_{el.} = 20\mathrm{mb}$)[35]. This translates to a rate of 10^9 inelastic events per second at nominal luminosity, $\mathcal{L} = 10^{34}\mathrm{cm}^{-2}\mathrm{s}^{-1}$. This far outnumbers the rate of signal production, for instance only of the order of 10 top pairs will be produced every second from the same luminosity. The experimental upshot of this is that every potential event of interest will come with an average of 23 inelastic events per bunch-crossing. In addition to the large rate of inelastic collisions at design luminosity, QCD jet production is expected to dominate over rarer signal physics processes. For example, the event rate for di-jet events with $\mathrm{E}^{jet}_{\mathrm{T}} > 100\ \mathrm{GeV}$ is 1000 times greater than the top pair production rate, see fig. 3.4. In order to identify and study rarer processes, event signatures based on object kinematics must be accurately measured. Therefore the particle identification and event reconstruction (e.g. missing transverse energy, $miss$ and secondary vertices) place heavy demands on the ATLAS detector.

Fast and radiation-hard electronics and sensors are required with high granularity to avoid overlap of particle signals. This is needed over a broad acceptance region; almost hermetic in azimuthal coverage and large pseudo-rapidity. The inner detector will require good charge and momentum resolution and precise reconstruction of tracks to identify displaced or secondary vertices. The EM calorimeter must have good energy and position reconstruction for electrons and photons as must the hadronic calorimeter for jets and $\not\!\!E_T$. Accurate muon identification and precision momentum and charge resolution must also feature. Two final requirements are for a highly efficient trigger for high-$\mathrm{p_T}$ objects, to identify events of interest from the plethora of mundane collisions, and adequate background rejection, to distinguish between similar event signatures.

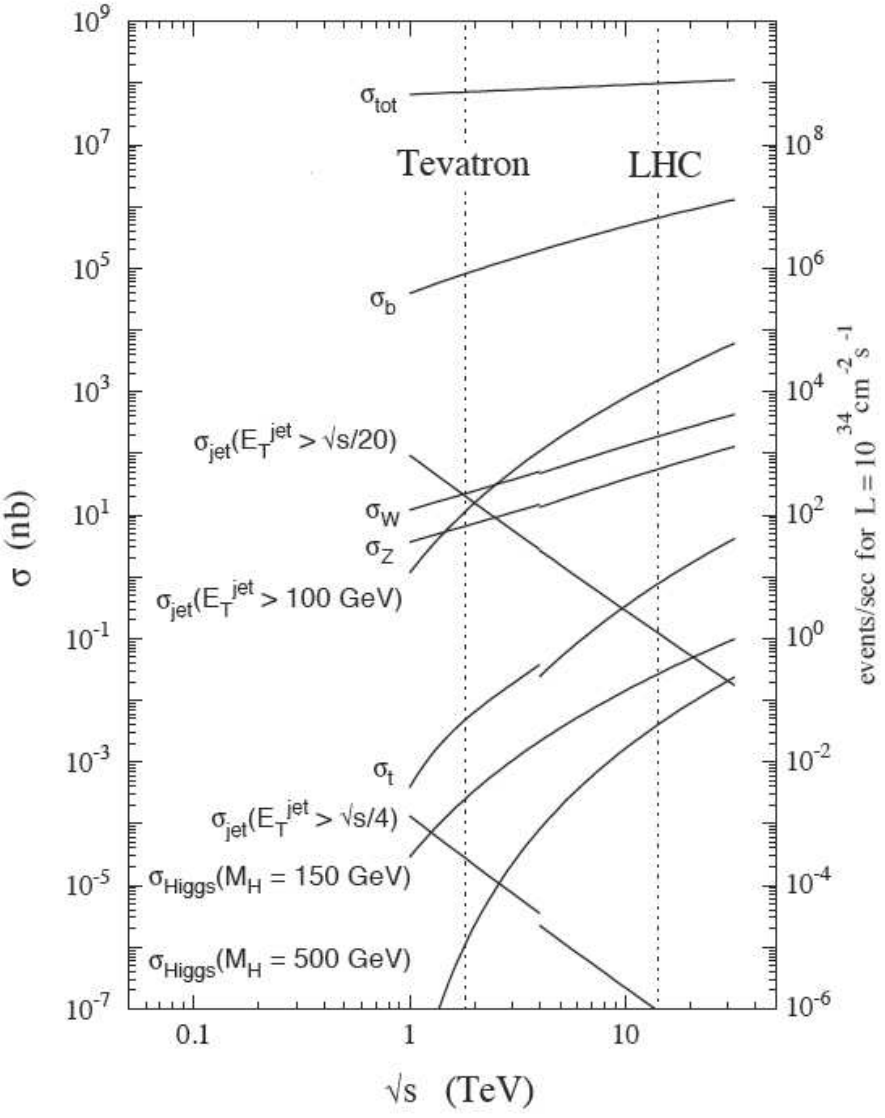

Figure 3.4: Expected production cross-sections and event rates as a function of collision energy [2].

The Inner Detector has high resolution semi-conductor pixel and strip detectors surrounded by straw-tube tracking detectors. The EM Calorimeter is based on liquid argon technology, giving high granularity electromagnetic sampling calorimeters. The Hadronic Calorimeter has coarser granularity but is sufficient to meet the demanding criteria of jet reconstruction and $\not\!\!E_T$ measurements. Forward calorimeters extend electromagnetic and hadronic measurement to $|\eta| < 4.9$. A dedicated muon spectrometer system is employed, which is independent of the inner detector for high $\mathrm{p_T}$ muons. All this is immersed in a strong magnetic field which helps to compensate for multiple-scattering effects by separating the trajectories of tracks before they enter the material. The combined performance should give accurate object reconstruction of jets, leptons and neutrinos, the latter being conspicuous by $\not\!\!E_T$ in the calorimeter systems. Table 3.2 shows the expected resolution of each sub-detector.

Detector component	Required resolution	η coverage	
		Measurement	Trigger
Tracking	$\sigma_{p_T}/p_T = 0.05\%\ p_T \oplus 1\%$	± 2.5	
EM calorimetry	$\sigma_E/E = 10\%/\sqrt{E} \oplus 0.7\%$	± 3.2	± 2.5
Hadronic calorimetry (jets)			
barrel and end-cap	$\sigma_E/E = 50\%/\sqrt{E} \oplus 3\%$	± 3.2	± 3.2
forward	$\sigma_E/E = 100\%/\sqrt{E} \oplus 10\%$	$3.1 < \lvert\eta\rvert < 4.9$	$3.1 < \lvert\eta\rvert < 4.9$
Muon spectrometer	σ_{p_T}/p_T=10% at p_T = 1 TeV	± 2.7	± 2.4

Table 3.2: ATLAS sub-detector performance goals. E and $\mathrm{p_T}$ are measured in GeV.

3.2.1 ATLAS Co-ordinates

The ATLAS geometry coordinate system is centred around the nominal interaction point. This defines the origin with the beam line defining the z-axis and the x-y plane transverse to the beam. The positive z-direction is defined as positive in the anti-clockwise beam direction, as viewed from above the LHC. The positive x-direction points toward the centre of the LHC ring and the positive y-direction points up. The detector is split into two sides around the interaction point. Side-A is defined on the positive z-axis and side-B on the negative. The azimuthal angle, ϕ, is defined around the beam axis, with zero pointing upward. The polar angle, θ, is measured from the positive beam axis and is positive in positive z. Derived from this, pseudo-rapidity is defined as $\eta = -ln\tan(\theta/2)$ which is used to define a kinematic property of massless particles. Other properties such as $\mathrm{p_T}$, $\mathrm{E_T}$ and $\not{E}_T$ are defined in the x-y plane. For massive particles, the rapidity is defined as $y = \frac{1}{2}ln[(E+p_z)/(E-p_z)]$. The separation distance, ΔR in $\eta - \phi$ space is defined as $\Delta R = \sqrt{(}\Delta\eta^2 + \Delta\phi^2)$.

Common geometric parameters are:

- $\theta = \cos^{-1}(\frac{z}{\sqrt{x^2+y^2+z^2}})$
- $\eta = -ln\tan(\frac{\theta}{2}) = -\frac{1}{2}ln(\frac{p+p_z}{p-p_z})$
- $y = -\frac{1}{2}ln(\frac{E+p_z}{E-p_z})$
- $\phi = \tan^{-1}(\frac{y}{x}) = \arctan(\frac{p_y}{p_x})$
- $m^2 = E^2 - |\vec{p}|^2$, $|\vec{p}|^2 = p_x^2 + p_y^2 + p_z^2$
- $\Delta R = \sqrt{\Delta\phi^2 + \Delta\eta^2}$

3.2.2 Inner Detector

The LHC beam pipe extends for $38\mathrm{m}$ inside the ATLAS experimental area. There are seven parts connecting to form the ultra-high vacuum system. The central chamber of the seven is centred on the interaction point and is integrated and installed with the pixel detector.

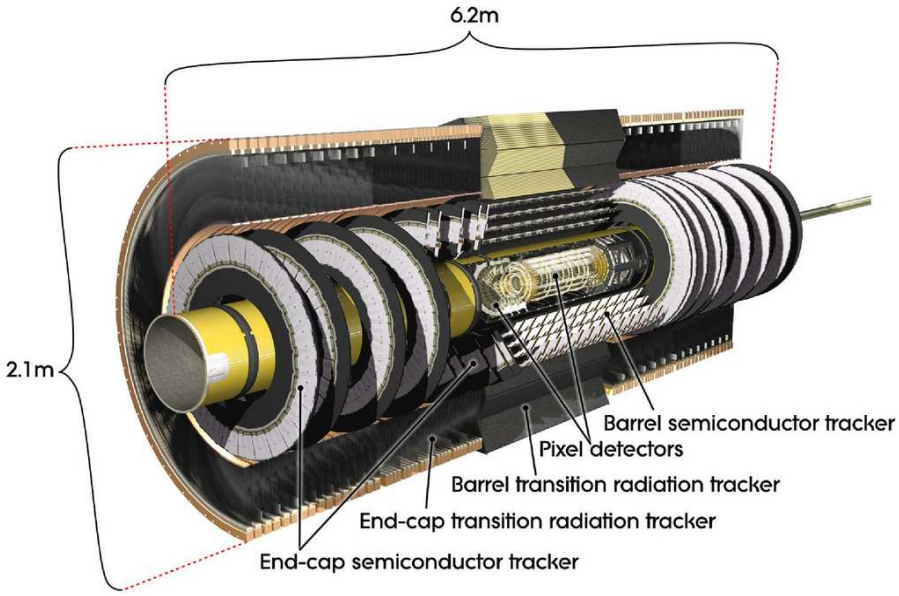

Figure 3.5: ATLAS inner detector.

The inner radius of the beam pipe is $58\mathrm{mm}$ with a thickness of $0.8\mathrm{mm}$ beryllium. The remaining sections straddle the interaction point, three each side, supported by the end-cap LAr cryostats, end-cap toroids and forward shielding.

The ATLAS Inner Detector (ID) is designed around particle trajectory identification based on small charge deposits in minimally deflecting material close to the beam line. "Hits" of deposited charge are left in the material layers and joined together to construct a particle path. The ID is designed to handle the high particle flux during the unprecedented luminosities of the LHC's nominal running. At $10^{34}\mathrm{cm}^{-2}\mathrm{s}^{-1}$ an order of 1000 particles per collision (every $25\mathrm{ns}$) are expected within the range of the ID. The ID is comprised of several sub-detectors: Pixel layers, Semi-Conductor Tracker (SCT) and Transitions Radiation Tracker (TRT). The first two have high precision accuracy and cover an η-range of $|\eta| < 2.5$. The latter has poorer granularity but an increased number of hits per track over a greater distance. The combination of the three provide robust pattern recognition by allying high precision measurement at small radii with a large number of measurements across the ID. This improves both high accuracy vertexing and flavor-tagging measurements, essential for accurate secondary vertex measurement used in identifying tau and b-quark decays, and as momentum measurements which require multiple hits. The combined dimensions of the ID comprise a cylinder of radius of $1.05\mathrm{m}$ and a length of $6.2\mathrm{m}$. The ID is immersed in a $2\mathrm{T}$ magnetic field extending over $6.2\mathrm{m}$ with a diameter of $2.1\mathrm{m}$. This is used to deflect charged particles and identify the charge sign and value relative to the $\mathrm{p_T}$ of particles i.e. $\frac{q}{p}$. Figure 3.5 shows the ATLAS ID layout.

Each of the sub-detectors are composed of a barrel and two end-cap regions. For the

precision sub-detectors the barrel region is made of concentric cylinders, with discs perpendicular to the beam line either side comprising the end-caps. The highest granularity is achieved by the silicon (Si) pixels around the vertex region at the centre of the detector. Each pixel cell is $50\mu\mathrm{m} \times 400\mu\mathrm{m}$ in $\phi \times R$ with a total area of $2.3\mathrm{m}^2$ covered. There are three pixel layers with the first layer at $51\mathrm{mm}$ from the centre of the beam pipe and the other two at $89\mathrm{mm}$ and $123\mathrm{mm}$. On average each track will traverse all three layers. Accuracies of $10\mu\mathrm{m}$ in $R-\phi$ and $115\mu\mathrm{m}$ in z in the barrel region and $10\mu\mathrm{m}$ in $R-\phi$ and $115\mu\mathrm{m}$ in R in the end-cap regions are expected. There are around 80.4 million readout channels.

The SCT is comprised of four layers each made of two strips of $6.4\mathrm{cm}^2$ silicon wafer bonded pairs offset at a small angle of $40\mathrm{mrad}$, covering an area of $6.1\mathrm{m}^2$ in total. The layers are positioned 30, 37, 44.7 and $52\mathrm{cm}$ from the beam line. The $R-\phi$ coordinate is measured in each layer by a strip parallel to the beam axis. These are two $6.4\mathrm{m}$ long daisy-chained sensors with a strip pitch (centre-to-centre distance) of $80\mu\mathrm{m}$. The expected accuracy is $17\mu\mathrm{m}$ in $R-\phi$ and $580\mu\mathrm{m}$ in z in the barrel region and $17\mu\mathrm{m}$ in $R-\phi$ and $580\mu\mathrm{m}$ in the end-caps. The end-caps are composed of radially orientated sets of stereo-strips with $40\mathrm{mrad}$ offset and mean pitch of $80\mu\mathrm{m}$. The number of SCT readout channels is around 6.3 million.

The TRT is made of $4\mathrm{mm}$ diameter aluminium tubes filled with a xenon based gas mixture. Transition radiation is emitted by particles as they move through media with varying dielectric properties. The electromagnetic radiation emitted as particles traverse the gas in a tube is detected by a wire running through the centre of the each tube. Although the TRT covers a smaller $\eta-$range than the precision layers, $|\eta| < 2.0$, it has 36 layers to build tracks from. In the barrel region the $144\mathrm{cm}$ straw tubes are parallel to the beam axis with the wire divided in two halves at $\eta = 0$. In the end-cap $37cm$ long straws are arranged radially into wheel structures. The straw tubes only allow for $R-\phi$ measurement and have an accuracy of $130\mu\mathrm{m}$. The approximate number of readout channels is $351,000$. The hits can be used to contribute to momentum measurements due to the large number of hits inside the magnetic volume. In addition electron identification is improved by the detection of photons coming from electrons showering in the gas of the straw tubes. Radiated photons pass a higher threshold than charge deposited from minimum ionising particles[1]. This can be used to cross-check and complement EM calorimetry for electron energies below $25\ \mathrm{GeV}$. The combined ID performance is expected to give precision measurement of the transverse impact parameter to $10\mu\mathrm{m}$. Charge measurements of electrons and muons are expected up to $1\ \mathrm{TeV}$ with a misidentification rate of no more than a few percent. Table 3.3 shows the physical dimensions of the ID.

[1]The energy lost as a particle passes from one dielectric medium to another is proportional to $\gamma = E/mc^2$. For a given energy, this is greatest for lower mass particles, such as electrons. Hence, minimum ionising particles radiate less energy than electrons via transition radiation.

Table 3.3: ATLAS inner detector dimensions.

Item		Radial extension (mm)	Length (mm)
Overall ID envelope		$0 < R < 1150$	$0 < \|z\| < 3512$
Beam-pipe		$29 < R < 36$	
Pixel	Overall envelope	$45.5 < R < 242$	$0 < \|z\| < 3092$
3 cylindrical layers	Sensitive barrel	$50.5 < R < 122.5$	$0 < \|z\| < 400.5$
2×3 disks	Sensitive end-cap	$88.8 < R < 149.6$	$495 < \|z\| < 650$
SCT	Overall envelope	$255 < R < 549$ (barrel)	$0 < \|z\| < 805$
		$251 < R < 610$ (end-cap)	$810 < \|z\| < 2797$
4 cylindrical layers	Sensitive barrel	$299 < R < 514$	$0 < \|z\| < 749$
2×9 disks	Sensitive end-cap	$275 < R < 560$	$839 < \|z\| < 2735$
TRT	Overall envelope	$554 < R < 1082$ (barrel)	$0 < \|z\| < 780$
		$617 < R < 1106$ (end-cap)	$827 < \|z\| < 2744$
73 straw planes	Sensitive barrel	$563 < R < 1066$	$0 < \|z\| < 712$
160 straw planes	Sensitive end-cap	$644 < R < 1004$	$848 < \|z\| < 2710$

Track reconstruction involves several factors including material corrections, track extrapolation and fitting and vertex fitting. Various algorithms are available for these processes and an optimising procedure will occur when event data arrives. Track building consists of three main parts. Firstly, the raw data of the ID are clustered and processed into space-points. Then a track finding algorithm is applied based on the space-points of the three pixel layers and the first SCT layer where the granularity is highest around the interaction point. Next, the remaining SCT information is added and quality cuts are applied. TRT data is added to the surviving tracks and a final refit is performed including information from all three sub-detectors. The final fit is compared to the Si pixel only fit and the best extrapolation chosen as the track (though all TRT information is kept). Lastly, vertex finding algorithms are applied to identify the interaction point, secondary vertices and photon conversions. In tandem, a back-tracking algorithm is used beginning with TRT information unassociated with Si pixel layers. It attempts to link unassociated hits to tracks as conversion or particle decays.

Electrons and pions are affected most severely in traversing the detector material. After traversing the SCT, electrons are expected to lose $20 - 50\%$ of their energy. Conversion of electrons to photons (and vice versa) is only weakly dependent on the energy of the electron with $10 - 50\%$ of electrons converting within the pixel layers. Conversions are identified using tracks which have no pixel layer hits, no associated primary or secondary vertex and pass a "loose" electron quality cut. Fitting electron tracks to include Bremsstrahlung effects improves identification by mitigating the effects of material. This is done by allowing changes in track curvatures due to photon radiation, thus including more space-points in the track, therefore improving the reconstruction of particle information. The specifics of Bremsstrahlung algorithms depends on the analysis, with factors like energy, pseudo-rapidity and running time to be considered. For electrons which have lost a large fraction of their en-

ergy in the pixel and SCT layers, the TRT helps to reconstruct conversions down to $1\,\mathrm{GeV}$. Though overall reconstruction performance is worse in the end-caps, due to the greater bulk of material to pass through, TRT performance is best in this region. The TRT end-caps are composed of an efficient and regular radiating foil, while in the barrel is a matrix of radiating fibres.

The combined performance of the ID allows a reconstruction efficiency above 98% for muons with $\mathrm{p_T} \geq 1\,\mathrm{GeV}$. Electrons and pions are more affected by material and hence the reconstruction efficiency is somewhat lower, $70 - 95\%$. These efficiencies increase for higher transverse momenta. Reconstruction algorithms help to identify kaons, vertices and conversions. Electron reconstruction algorithms reduce the bias of $\mathrm{p_T}$ measurement, while the EM calorimeters are required for high-η tracks crossing the end-caps. The parameters of such algorithms can be optimised for specific analyses. For example, simulated $t\bar{t}$ analyses were performed where the primary vertex was identified with 99% efficiency with low luminosity pile-up, i.e. the expected overlap of events in the initial running of the LHC, taken into account.

3.2.3 Calorimetry

Calorimeter depth provides adequate containment of EM and hadronic showers for signal sampling and limiting punch-through. The showering of an incident EM particle in a material depends on the general features of the material i.e. the radiation length, X_0, and the Molière radius[2], R_M. The radiation length of EM radiation is the average distance travelled in a medium before the electron (photon) radiates (converts). These material characteristics along with the space available inside the detector determine which calorimeter constituents are physically appropriate i.e. materials with smaller R_M make jets less diffuse and reduce overlap, therefore improving event resolution. Figure 3.6 illustrates the ATLAS calorimetry system.

In hadronic calorimetry the significant parameter is the interaction length λ_0. This is the average distance travelled by a hadron before it interacts via the strong force. Typically λ_0 is an order of magnitude greater than X_0 which implies hadronic calorimeters must be thicker than EM calorimeters if the same containment is expected. Hadronic calorimetry is generally poorer than EM as material response is complicated by several factors. Nuclear binding effects and detecting neutrons are problematic[3]. A further complication comes from spal-

[2]The Molière radius is a characteristic parameter of a material relating the transverse scale of fully contained EM showers from incident electrons/photons to the radiation length: $R_M = 0.0265 X_0(Z + 1.2)$, where Z is the atomic number of the material. By definition the radius defines a cylinder containing 90% of a shower's energy.

[3]Neutron detection can be compensated for by introducing unstable nuclei in the calorimeter material which will leave detectable remnants after fission induced by the capture of slow neutrons. Such detectors are known as 'compensating'. The ATLAS hadronic calorimeter is not compensating.

lation in hadronic calorimeters where an incident particle not only interacts with a nucleus but destroys it by causing it to emit nucleons (including neutrons) and decrease its atomic number. A final factor is the production of π_0s inside the hadronic calorimeter volume which decay electromagnetically to photons, which can escape detection.

Calorimetry in ATLAS has three main parts: electromagnetic, hadronic and forward. The combined calorimeter has over 200,000 cells combined into larger objects with physically meaningful 4-momentum. It is based on energy sampling so, although not all energy is of an incident jet is absorbed, an indicative measure will be collected and the rest reconstructed. This introduces a sampling error to jet energy measurements.

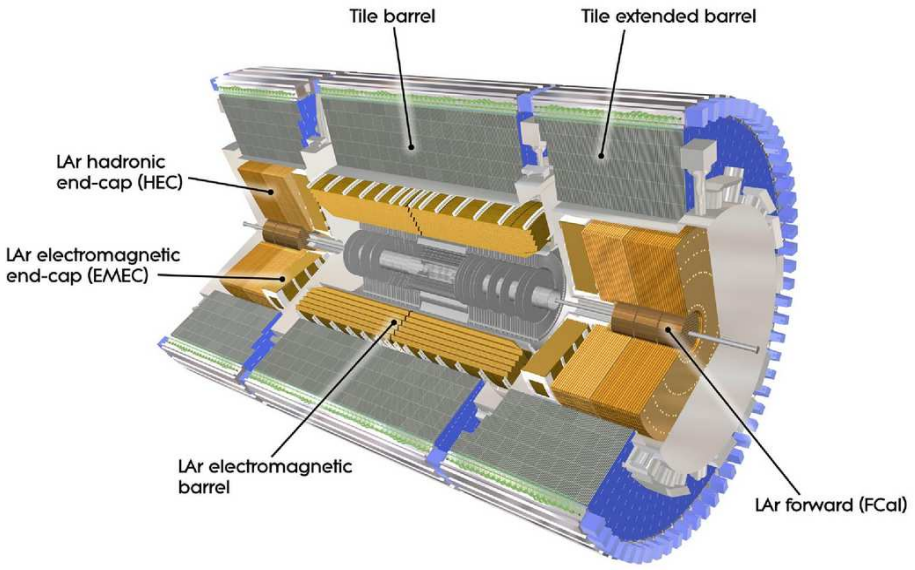

Figure 3.6: ATLAS electromagnetic and hadronic calorimeters.

3.2.3.1 Electromagnetic Calorimeter

The electromagnetic calorimeter is designed to measure the energy and position of electrons and photons to an energy of 0.5% over the range $5\ \mathrm{GeV} - 5\ \mathrm{TeV}$. It covers a η-range of $|\eta| < 3.2$, with precision measurement inside $|\eta| < 2.5$. There are three elements; a barrel calorimeter ($|\eta| < 1.475$) and two end-cap calorimeters ($1.375 < |\eta| < 3.2$). The barrel is composed of two halves separated at $z = 0$ by $4\mathrm{mm}$. The central solenoid and liquid argon (LAr) calorimeter share a common vacuum vessel to limit dead material from vessel walls. The end-caps have two coaxial wheels. The outer wheel covers $1.375 < |\eta| < 2.5$ and the inner $2.5 < |\eta| < 3.2$. Each EM calorimeter element is comprised of three longitudinal layers: front/strips, middle and back. Lead induces particle showers while LAr absorbs the energy deposits. Periodically the collected charge is read out sampling the particle energy from the shower shape. In addition there is a pre-sampler closer to the beam, over $\eta < 1.8$

used to correct for material effects upstream. The pre-sampler is an active LAr layer, $1.1cm$ thick in the barrel and $0.5\mathrm{cm}$ in the end-cap. The EM calorimeter is projective in η and designed such that all particles originating from the centre of the detector strike each of the calorimeters at the same η. The bulk thickness is designed to maximise electron and photon energy collection hence the barrel is more than 22 X_0s and more than 24 X_0s in the end-caps. There is complete ϕ-coverage without any azimuthal cracks. Gaps in η-coverage between barrel and end-caps ($1.4447 < \eta < 1.55$) are mitigated by scintillation tiles to recover energy. The whole EM calorimeter is surrounded and cooled to an operating temperature of $89\mathrm{K}$ by cryostats.

At high luminosities the ID alone cannot accurately determine the interaction point due to the high occupancy from additional interactions. However, the EM calorimeter can augment this information to help establish the primary vertex for certain events. The angle of incidence of particles impinging on the calorimeter can be found by comparing impact points. Reconstruction of η-depth information in the two layers closest to the beam, including shower barycentres, allows projection of particle paths back to the origin. The intersection of the particle trajectories will give position of the primary vertex.

A 'sliding window' algorithm is used to identify and reconstruct energy clusters. This uses a fixed size rectangular window to scan across the calorimeter cells. The point where the maximum energy falls within the window is chosen as the cluster centre. The optimum window size depends on the particle type and region of the sub-detector. Electrons tend to deposit larger clusters than photons because of their greater probability of interaction in upstream material and emission of soft photons as they are deflected in the magnetic field. Photons travel on average $9/7X_0$ before depositing energy in the calorimeter, while electrons shower immediately. The difference in optimum window size means several collections of cluster objects are built from the same raw data by the reconstruction software. For each object, tracks are sought within a $\Delta\eta \times \Delta\phi$ region of 0.05×0.1. Any tracks found have their momentum compared to the cluster energy and a check for conversions made. If a cluster is matched to a track with suitable momentum, $E^{cluster}/\mathrm{p_T}^{track} < 10$, without conversions then the cluster becomes part of an electron object, otherwise the cluster becomes a photon object. Once the object category has been assigned, different corrections can be applied based on shower shapes in the calorimeter. There are four standard quality cuts used for electrons: loose, medium, tight and tight without isolation. Photon selection corresponds to the tight electron quality but with no associated track.

Before any reconstruction algorithms are applied to the calorimetry data several processes prepare the data for analysis. After the energy in each cell has been calculated from raw data it is summed and weighted into space-points in each layer. Most of the incident particle energy is collected in the calorimeter absorbers i.e. lead with LAr in the gaps. A small amount is lost in the ID, cryostats, solenoid and cables, and some energy passes through the

calorimeter material. The energy of a cluster is calculated from a linearly weighted sum of the deposits in the 3 layers of the calorimeter and the pre-sampler. The longitudinal weighting factors are applied to correct for energy loss between the different particle deposits. Information from the front and middle layers is combined to reconstruct a shower impact point. The $\eta - \phi$ position is calculated as the energy weighted barycentres of all cluster cells in a layer. Only the second layer is used to establish the ϕ-coordinate, where the granularity is best. The front and middle layers are averaged to determine the η-coordinate, with the front given three times the weight for its greater resolution. Next corrections are applied for resolution and response of the calorimeter material.

3.2.3.2 EM Calorimeter Corrections

In order to accurately determine the energy and position of particles incident on the calorimeter several corrections are required: corrections for position; corrections for energy from lateral and longitudinal shower shapes; and, correct for $\eta - \phi$ modulations, coming from material fluctuations. Each set of corrections is determined separately for each layer and region and particle type. The process of energy and position adjustment begins with calculating the initial cluster information. The position co-ordinates are then corrected to take into account modulations in position accuracy over $\eta - \phi$. The energy correction is based on lateral and longitudinal shower shapes. Lastly, a correction is made for modulations in energy response over η and ϕ. Studies show the required level of energy correction is around 10% across the calorimeter layers, with more between barrel and end-cap regions where the cryostat sits. Strategies involving $Z \rightarrow ee$ events data are intended to derive correction parameters from data.

Each calorimeter layer requires separate corrections. In calculating the total energy deposited by a particle across the whole sub-detector the impact point is used to correct for modulations in η and ϕ. Modulations in $\eta - \phi$ come from several sources and affect both position and energy measurements. Since the initial designs for ATLAS a significant amount of material has been added upstream i.e. between the calorimeter and interaction region. Extra material encourages early showering through electromagnetic interactions upstream of the calorimeter. This means particles will suffer more energy loss as they traverse the material and are more likely to convert before they deposit charge in the calorimeter. This affects lateral shower shape which degrades resolution. Local and medium range inhomogeneities arising from temperature and voltage gradients and dead material inside the detector are expected but require full detector operation before they can be adequately appreciated.

Many aspects the detector arrangement require subsequent corrections in measurement. Firstly, the positioning of the calorimeters assumes particles originate exactly from the detector origin. The slightly non-projective geometry affects the measured cluster energy as

it affects shower depth. To adjust for z-offset from the origin the depth of each layer must be assumed in order to optimise resolution. For the barrel the depth is considered as the radial distance from the beam axis; for the end-caps it is the distance to the x-y plane passing through the origin. An accurate parametrisation of particle showering is required in each layer such that deposits across the element which share a common ancestor are correctly associated.

Over the ϕ range the accordion geometry of the calorimeters leads to varying responses. For energy measurement, ϕ-modulation of the order of $< 0.5\%$ from absorber spacing is expected at high energies. At lower energies ϕ resolution is around as accurate as the absorber spacing which washes out the effect. Over the η range measurements are biased by the finite granularity of the cells and EM showers are not fully contained in the η windows. These constraints lead to modulation and bias in η depending on the impact point within the cell. η-modulation of around 0.3% biases the measured shower to particles impacting on cell centres. Corrections vary continuously over η due to fluctuations in upstream material.

3.2.3.3 Hadronic Calorimeter

The hadronic calorimeter encloses the EM calorimeter with almost hermetic coverage of the ϕ-region over $|\eta| < 4.9$. It is designed to collect as much hadronic activity as possible, though it is non-compensating, and limit particles passing through into the muon spectrometer. The barrel is composed of steel absorbers and scintillating active readouts extending to $|\eta| = 1.7$ (further than the EM barrel region). The barrel is composed of a central region $|\eta| < 1.0$ and extended regions $0.8 < |\eta| < 1.7$. The inner radius is $2.28\mathrm{m}$ and the outer $4.25\mathrm{m}$ with three layers between. The end-caps are composed of two independent wheels over $1.5 < |\eta| < 3.2$. Each wheel has two parallel copper plates, giving a total of 4 layers per end-cap. Between the copper plates active LAr sections detect charge deposits. The inner radius of the wheel is $0.475\mathrm{m}$ (slightly less when overlapping with the forward calorimeters) and the outer $2.03\mathrm{m}$. In addition there is a forward calorimeter, composed of copper for EM signals and tungsten for hadronic measurements, each with LAr. The structure is regularly spaced longitudinal channels filled with concentric metal rods and tubes parallel to the beam axis with LAr filling the gaps between. This covers the high-η region $3.1 < |\eta| < 4.9$. The hadronic calorimetry has cells of granularity $\Delta\eta \times \Delta\phi = 0.1 \times 0.1$ and a thickness of 10 interaction lengths over the whole acceptance region (11λ at $\eta = 0$ including outer support).

3.2.3.4 Jet Building

The efficiency and quality of jet reconstruction is a significant factor in the majority of planned analyses at the LHC. The demands of accuracy in measurement of jet attributes by various analyses is unprecedented in collider experiments. For example, an absolute system-

atic uncertainty of less than 1% on the jet energy scale is required for precise measurement of the top quark mass. The individual cells of the calorimeter provide the basic elements used by software algorithms to construct larger combinations which can be interpreted as physically meaningful objects. In the hadronic calorimeter there are two possible reconstruction techniques: signal towers and topological clusters.

Signal towers begin by projecting the calorimeter cells on to a fixed grid in $\eta - \phi$ of 0.1×0.1 regions over $|\eta| < 5$ and $-\pi < \phi < \pi$, which gives 6400 towers in total. Cells which completely fall inside a grid element contribute all of their energy to a specific tower. Cells larger than the tower bin contribute a fraction of their energy to several towers depending on the cell-grid overlap. The final grid is the sum of all weighted cell signals, weighted by overlap. Tower signals are reconstructed on a basic electromagnetic energy scale: this is the basic raw signal from ATLAS, corrected for electronic and geometric factors, but without high precision corrections used in EM object reconstruction. Hadronic calibration is applied later at the level of the jet object.

Topological clusters construct 3-dimensional 'energy blobs' for each particle shower entering the calorimeter. The blobs are created from seed cells based on signal-to-noise ratios or significances above a threshold. All neighbouring cells in 3-dimensions are collected to the cluster. Next-to-nearest neighbours are used if a secondary threshold is met, lower than the first. Finally, a ring of 'guard cells', surrounding all clustered cells, satisfying another lower threshold, is added. A splitting algorithm separates any overlap between clusters. Once clusters are found, calibration is possible based on energy scale, noise, shape and location. Weights are given to the clusters by location, energy and cell-density to correct for energy loss. A further (out-of-cluster) correction for the effect of clustering itself is applied to remove bias from energy belonging to particle showers lying outside the clustered cells. Topological clusters are calibrated on electromagnetic or local energy scales with further hadronic calibration of the jet object later.

Different calorimeter signal definitions construct jet shapes differently over the regions of the calorimeter. The tower method uses all cells to populate the energy grid, while the cluster method applies a significance criterion. The latter method has the advantage of including noise suppression. Noise suppression is most effective at low-E where the contribution from noise is most prominent. Subsequent choice of jet definition will also be affected by the choice of jet signal as larger cone or cluster sizes will likely include more noise. In the forward region jets have lower $\mathrm{p_T}$ on average and are therefore affected more by fluctuations from noise and pile-up at the high luminosities. The choice of jet builder should reflect the analysis of interest as the choice of object definition does.

Jet calibration is based on cell signal weighting. Low signal densities in calorimeter cells indicate a hadronic signal in non-compensating calorimeters; therefore, signal weights are adjusted to compensate to the order of $\frac{e}{\pi}$ signal ratio. High signal densities are more

like EM showers and so do not require re-weighting. The calibration weights are based on fully simulated di-jet events. They vary according to cell position and energy density but are universal as they do not depend on specific variables related to particle kinematics. The 4-momenta are recalculated using re-weighted energy values. Local residual non-linearities in response, depending on particle $\mathrm{p_T}$, and non-uniformities over the detector range, depending on η, require further calibration from data.

Both towers and clusters signal definitions used to define massless pseudo-particle objects with $E = |\vec{p}| = \sqrt{p_x^2 + p_y^2 + p_z^2}$, where $p_x = |\vec{p}| \cdot \frac{\cos\phi}{\cosh\eta}$, $p_y = |\vec{p}| \cdot \frac{\sin\phi}{\cosh\eta}$ and $p_z = |\vec{p}| \cdot \tanh\eta$. Reconstruction of mass is difficult as shower evolution in the calorimeters washes out directions and energies of individual particles in a jet. Additional effects upstream of the hadronic calorimeters from the magnetic field and material increase signal loss.

ID tracks can be used as a cross-check for calorimeter signals using $f_{track} = \frac{\mathrm{p_T}^{track}}{\mathrm{p_T}^{calo.}}$ as a test of effectiveness. They can also be used to recover energy lost in the crack regions of the calorimeter between barrel and end-cap regions. Any improvements in jet recovery limits the contribution of fake missing energy in events, since missing energy is calculated using the imbalance of calorimeter energy distribution. Another promising use of jet tracks is in identifying primary vertices of hard jets in high occupancy pile-up events. ID kinematics pertaining to a jet can be used rather than values derived from calorimetry if the ID offers better resolution. The chapter on jets in [35] suggest that for some processes this is the case for relatively low-$\mathrm{p_T}$ jets i.e. $\mathrm{p_T} < 80\ \mathrm{GeV}$. Advantages from additional ID information are limited by the η-range as $\eta^{ID} < 2.5$.

3.2.3.5 ATLAS Jet Algorithms

Several jet algorithms are available in ATLAS - fixed cone, sequential recombination and an event shape based algorithm. There is no universal algorithm used in all analyses (see 2.5.7.2). Inclusive QCD kinematic measurements prefer wide definitions such that the proportion of jet information available is maximised. In contrast, multi-jet FS analyses, like $t\bar{t}$, tend to use narrow jets to avoid merging. Common to all ATLAS jet definitions is full 4-momentum recombination for any change in jet constituents. This generic format of jet algorithms allows the same jet building recipe to be used on various calorimeter elements, e.g. cell information, energy towers, etc.

Some theoretical and experimental issues are common to all algorithms. On the theoretical side, as previously mentioned, IR and collinear safety is important. This basically requires that any soft particles not from the hard scatter should not affect the jets reconstructed; nor should the $\mathrm{p_T}$ carried by one particle or split across several particles in jet fragmentation. In addition, order independence is demanded, such that the same hard scatter

event is reconstructed at parton, particle-jet or detector level.

Experimental factors concern detector technology and environmental independence. The first issue is that all detector contributions to the signal (signal characteristics and inefficiencies) must be calibrated out or corrected to minimise effects. For example, finite spatial/energy effects must be mitigated as well as the effects of electronic noise and signal loss. Environmental dependencies concern underlying event effects. The event shape should be consistently and stably reconstructed despite varying UE effects such that all relevant event information can be studied with high efficiency. A final concern of jet algorithms is in how easily the software can be efficiently implemented. To this end, jets must be fully defined (jet finder and configuring parameters) and the demand on computing resources limited.

3.2.3.6 Jet Algorithms

ATLAS Cone Algorithm

The ATLAS cone algorithm uses an iterative method to identify stable cones, i.e. those where the cone-axis and sum of the momenta of the constituents coincides. All particles are treated as seeds for potential jets with all surrounding particles within a cone of $\Delta R < R$, where $\Delta R^2_{i,j} = \Delta\eta^2_{i,j} + \Delta\phi^2_{i,j}$ a measure of the jet proximity in the $\eta - \phi$ plane of the detector. Since these potential jets may include parts of another, a further algorithm is required to separate or combine overlapping areas. This is known as a split-merge procedure. Some new threshold is introduced that is used to decide whether overlapping potential jets should be merged (split) if it falls below (above) some threshold. Once this has taken place the remaining clustered cones are chosen as jets. This algorithm is collinear safe but IR unsafe, as the addition of soft radiation in the proximity of hard jets can lead to stable seeds which change the jet structure of the event[4]. This is exacerbated by high jet multiplicity, where more soft deposits are probable, which will be ubiquitous at the LHC due to the high CoM and luminosity of events. This makes QCD predictions which are IR sensitive impossible to test.

SIS Cone Algorithm

The Seedless Infrared Safe (SIS) Cone method ensures IR safety by finding all possible jet seeds. A sliding cone enclosure scans over the $\eta - \phi$ plane. The stable[5] potential jets are then kept, beginning with the hardest as before and split-merging any overlaps.

k_t Algorithm

The method of the k_t algorithm is to find the smallest of $d_{i,j} = min(k^2_{t_i}, k^2_{t_j})\Delta R^2_{i,j}/R^2$ and $d_{i,Beam} = k^2_{i,Beam}$, where i and j denote jet indices, k_t is the inverse of the jet's trans-

[4] Augmentations to the cone procedure are possible which will invent additional jet seeds, e.g. mid-point algorithms, but these only push the problem back to higher jet multiplicity cases.

[5] Stability is found when the redefining the jet axis, and hence the cone centre, by summing the momenta of the constituent particles, does not introduce new particles into the cone.

verse momentum, and $d_{i,Beam}$ is the distance to the beam. $d_{i,Beam}$ acts as a maximum cut-off limiting the cluster size. The ratio $\Delta R^2_{i,j}/R^2$ ensures jets are separated by a minimum distance R. This method of hierarchical clustering is not IR safe for all soft jets near the beam but is IR safe for jets above the $\mathrm{p_T}$ cut.

Anti-k_t Algorithm

The anti-k_t procedure alters the k_t algorithm to find the smallest of $d_{i,j} = min(\frac{1}{k^2_{t_i}}, \frac{1}{k^2_{t_j}})\Delta R^2_{i,j}/R^2$ and $d_{i,Beam} = \frac{1}{k^2_{i,Beam}}$. In this case the hardest particles will cluster first such that if no other particles are in close proximity the algorithm will create perfect cones.

3.2.4 Muon Spectrometer

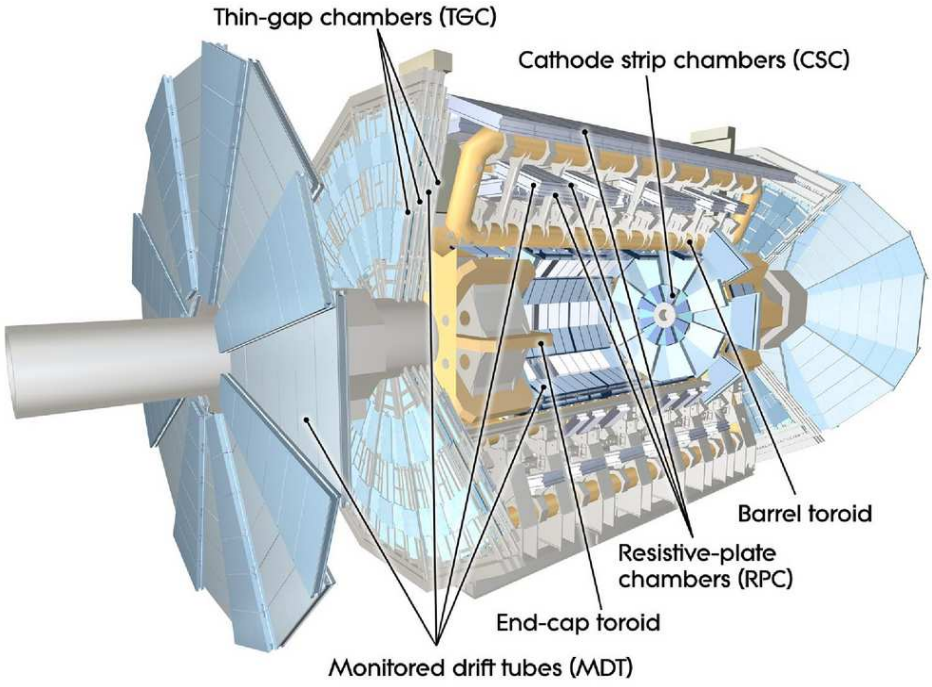

Figure 3.7: ATLAS muon spectrometer.

The muon spectrometer is the outer shell of the ATLAS detector. It is comprised of three layers of high precision tracking chambers with separate triggering to the rest of the detector. The trigger chambers have a timing resolution of $1.5 - 4\mathrm{ns}$. The layout of the spectrometer is based on the expected deflection of muon trajectories in the magnetic field. The barrel consists of three cylindrical layers around the beam axis, while the transition region and end-caps are made of three planar layers perpendicular to the beam. The barrel toroid provides the magnetic field over $|\eta| < 1.4$, in the end-caps, $1.6 < |\eta| < 2.7$, the source is two smaller magnets at either end of the barrel toroid. From $1.4 < |\eta| < 1.6$, the transition region, both barrel and end-cap magnets contribute. The field over the spectrometer is mostly orthogonal

to the muon trajectories and minimises the loss of resolution from multiple interactions. Figure 3.7 is an illustration of the ATLAS muon spectrometry system.

Each of the magnet toroids has eight coils radially orientated symmetrically around the beam axis. The end-cap toroid is rotated by 22.5° with respect to the barrel such that there is radial overlap at the interface between the two magnets to optimise bending power. In the barrel the eight coils have individual cryostats while in the end-cap they share the same. Each end-cap has eight racetrack-like coils, each coil is a twin double-pancake type windings, housed in aluminium casing. Performance of the magnets is characterised by the bending power which in turn is understood by the field integral $\int Bdl$, with B the component normal to the muon direction and l the muon trajectory. The barrel toroid has strength $1.5 - 5.5\mathrm{Tm}$ over $|\eta| < 1.4$, and the end-caps $1 - 7.5\mathrm{Tm}$ over $1.6 < |\eta| < 2.7$. The bending power in the overlap region is diminished. The magnetic field is continuously measured by $1,800$ Hall sensors over the spectrometer volume.

Precision measurement of the track coordinate is achieved by various technologies over the spectrometer. Monitored Drift Tubes (MDTs) are used over most of the η-region. In $2 < |\eta| < 2.7$ Cathode Strip Chambers (CSCs) with higher resolution are used in the innermost layer to compensate for the high rate and backgrounds conditions. In the trigger system, covering $|\eta| < 2.4$, Resistive Plate Chambers (RPCs) are used in the barrel and Thin Gap Chambers (TGCs) in the end-caps. The trigger provides bunch crossing identification, well-defined $\mathrm{p_T}$ thresholds and a measure of the muon trajectory in the orthogonal direction to the precision tracking chambers. An alignment accuracy of $30\mu\mathrm{m}$ is achieved using around $12,000$ alignment sensors, based on optical monitoring.

3.2.5 Forward Detectors

In addition to the main ATLAS sub-detectors located immediately around the interaction point there are three other smaller detectors positioned further from the primary vertices. The Luminosity measurement Using Cerenkov Integrating Detector (LUCID) straddles the main detector $17\mathrm{m}$ from the main interaction point in either direction along the beam line. LUCID detects inelastic proton-proton scattering to measure the relative luminosity for ATLAS. A second luminosity measure, this time absolute, is provided by the Absolute Luminosity For ATLAS detector (ALFA). The ALFA detectors are located either side of the main detector $240\mathrm{m}$ from the interaction point. ALFA uses scintillating fibre trackers inside "Roman pots" to measure the absolute luminosity as close as $1\mathrm{mm}$ to the beam. Finally, at $\pm 140\mathrm{m}$ from the interaction point, the Zero-Degree Calorimeter (ZDC) is positioned. ZDC uses layers of alternating tungsten plates and quartz rods to measure neutral particles at $\eta \geq 8.2$ to help determine the centrality of heavy-ion collisions.

3.2.6 Shielding

Radiation levels at the LHC will be well above those of any other particle physics experiment in the past. Hence, detector components will be severely irradiated and beam-induced backgrounds will be major obstacles to precision data-taking, and will increase over time. ATLAS shielding has been designed such that these effects will be minimised while leaving detector performance as unaffected as possible. The primary source of radiation at nominal design luminosities is expected to come from collisions at the interaction point. Charged hadrons from secondary interactions and inelastic proton-proton interactions will dominate the radiation backgrounds at small radii, i.e. the inner detector region, while neutrons will become more significant as the particles progress through the detector. The degrading effects of this environment include increased backgrounds and occupancies, radiation induced damage, ageing of the detector hardware, single event damage and increased radionuclides which impede human maintenance of the detector. Most of the energy from primary radiation is absorbed in two regions. The first is the Target Absorber Secondaries (TAS) collimators which protect the LHC quadrupole magnets and the forward calorimetry. Primary particles traversing the beam pipe at very shallow angles cross a significant number of $X_0 s$. Studies suggest this will contribute the majority of radiation backgrounds in the muon system. Table 3.4 shows the expected radiation doses in sub-detector regions for 500fb^{-1} of data, corresponding to about seven years of operation.

Inner detector					
Location	**F_{neq}** (10^{14} cm^{-2})		**Dose** (kGy)		**Charged-particle flux** above 10 MeV (Hz/cm^2)
Pixel layer 0	13.5		790		40×10^6
SCT layer 1	0.8		38		1.5×10^6
SCT disk 9	0.6		23		10^6
TRT outer radius	0.25		3.5		10^5
Calorimeters					
Location	$\lvert\eta\rvert$		**Maximum dose** (kGy)		
EM barrel	1.475		1.2		
EM end-cap	3.2		150		
Tile	1.2		0.15		
HEC	3.2		30		
FCal	4.9		1000		
Muon spectrometer					
Location	**Flux** (kHz/cm^2)		**Flux** (Hz/cm^2)		**Single-plane rates** (Hz/cm^2)
	n	γ	μ	p	
Barrel chambers	2.6–4.0	1.0–1.5	0.3–4.5	0.4–3.2	6.0–11.0
Inner edge of inner wheel	79	25	21	64	347
Inner edge of outer wheel	2.7	1.5	3	0.9	12

Table 3.4: ATLAS sub-detector doses expected after seven years of LHC operation.

To mitigate the effects of the high radiation LHC environment ATLAS has around 3000tonnes

of shielding. Like much of ATLAS, this follows a tripartite pattern. The inner layer of shielding is composed of iron and copper for their high density and is designed to stop high energy hadrons and secondary particles. The second layer is doped polyethylene, rich in hydrogen, used to slow neutrons liberated from interactions in the first layer. The low energy neutrons are captured by a boron dopant. This process creates gamma radiation and so a third layer of steel or lead is used to stop photons.

3.2.7 Detector Control System

The Detector Control System (DCS) provides comprehensive access to ATLAS operational control. It has access to all sub-detectors and the technical infrastructure of the experiment. All operational parameters are controlled, monitored and recorded. Any abnormal behaviour is flagged for automatic or manual adjustment. Communication between ATLAS sub-detectors and ATLAS with the LHC machine goes through the DCS, with dedicated hardware links for critical information. Information such as beam and bunch intensities and position is shared. The machine provides the $400.08\mathrm{Hz}$ clock of the accelerator required by the L1 trigger. ATLAS provides information on total and relative luminosity from its dedicated sub-detectors and information on when it is safe to inject or dump beams from the interlock system. This exchange of information is essential to the safe operation of the detector and the machine.

3.2.8 Triggering

The Trigger and Data AcQuisition (TDAQ) systems select and record event data. The task for the triggering system is to take all proton-proton collision data generated at a rate of the order of $1\mathrm{GHz}$ and reduce it to a practically recordable rate of about $200\mathrm{Hz}$. The rejection factor of 5×10^6 is achieved by implementing a three-level trigger. The level 1 (L1) trigger uses a subset of detector information to identify regions of interest (RoIs) on which to base the trigger decision. This reduces the data rate to $75\mathrm{kHz}$. The level 2 (L2) trigger and event filter (EF) are known as the high-level trigger and in combination reduce the information to a manageable rate of around $200\mathrm{Hz}$.

On-line event selection is specified before event runs begin by a set of trigger configurations. A trigger configuration is the combination of a trigger menu, prescale values and forced acceptance rates. A trigger menu is a series of trigger signatures which are the logical combination of trigger elements. A trigger element is specified according to object and energy, with the possible addition of shower shape or isolation criteria. For example, trigger element `e25i` requires an event to contain an electron object (e) with $\mathrm{E_T} > 25\,\mathrm{GeV}$ (25) which is isolated (i), i.e. has no other electron objects within a defined proximity. Trigger elements themselves are the logical combination of all three trigger levels. If at least one

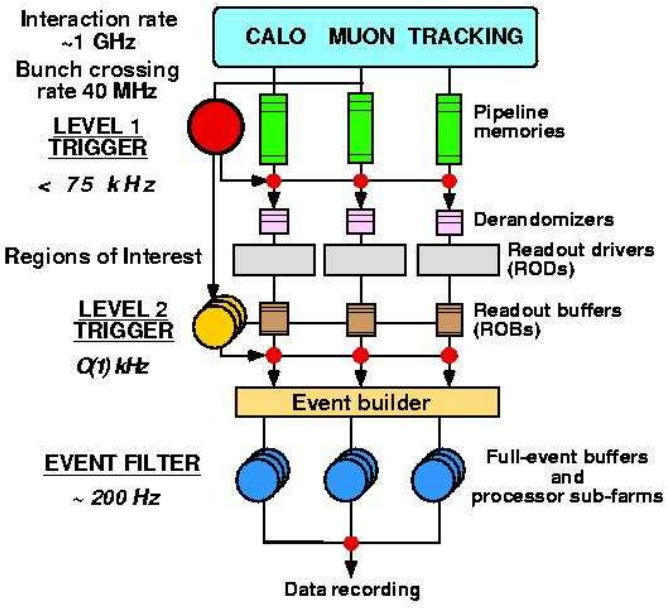

Figure 3.8: ATLAS trigger system.

trigger element is passed then the menu is passed and the event is selected. Menus allow an event to be recorded based on object kinematics in such a way that it can be retrieved by various analyses.

Trigger streams are used to filter events by trigger content based on the trigger signatures. Four streams were used for data taking in 2010: egamma (for electrons and photons), jetTauEtMiss (for jet, tau and missing $\mathrm{E_T}$), muon and minBias (for minimum bias events). By grouping events by these metadata categories, users can identify objects and events more easily.

The L1 trigger uses a subset of detector information, namely the muon triggers and calorimetry, to identify high $\mathrm{p_T}$ objects and make rough $\not\!\!E_T$ and $\mathrm{H_T}$ measurements to base the primary selection on. High $\mathrm{p_T}$ muon objects are based on information from trigger chambers of the muon spectrometer. Calorimeter information is at reduced granularity at L1. Interesting objects are located as RoIs and noted using $\eta - \phi$, type and threshold information. The central trigger processor uses combinations of trigger selections to produce a trigger 'menu', which can be optimised to reduce the use of bandwidth by prescaling as background and luminosity conditions change. Events passing L1 selection are passed to higher levels which use full detector information to assess the RoIs identified at L1. L2 selection uses full detector granularity and precision in the RoIs ($\sim$ 2% of total detector information) to make decisions in an average of $40\mathrm{ms}$ reducing the event rate to $3.5\mathrm{Hz}$. The event filter reduces the event rate to the desired rate of $200\mathrm{Hz}$ by implementing offline style procedures, such as vertexing and track fitting, with an average processing time of $4\mathrm{s}$. Figure 3.8 depicts the ATLAS trigger hierarchy.

The data acquisition system receives and buffers event data from detector-specific readout electronics at the L1 trigger acceptance rate. Without the trigger a storage rate of $40\mathrm{TBs}^{-1}$ would be required to record all ATLAS data. The first level makes decisions in $> 2.5\mathrm{ns}$ based on the limited amount of total detector information. After the higher-level triggers have reduced the rate of information to $200\mathrm{Hz}$ the approximate event size is $1.5\mathrm{Mbytes}$. An annual data rate of several PBytes is expected to be recorded. As well as moving data the DAQ configures, monitors and controls the hardware and software elements which make up the data-taking system. The DCS interacts with the DAQ to synchronise the detector state with data-taking state.

Each detector sub-system uses specific ReadOut Drivers (RODs) with standardise functionality to transfer information from front-end data streams. The L1 buffer stores information until the trigger latency allows it to be checked. The derandomising buffer stores the accepted L1 information before it is passed to higher levels. This allows the L1 trigger to function at maximum rate without significant dead-time ($\leq 1\%$). When an event is selected by L1 the data in the pipelines are passed to the RODs. Digitised signals are formatted as raw data before being passed to the DAQ system. RODs have standard ATLAS procedures for data formatting, error detection and recovery and physical interface for data transfer to the DAQ. The DAQ temporarily stores the accepted data in local buffers before it is analysed by the L2 trigger on the RoIs. L2 accepted events are passed to the event-building system and then on to the event filter for final selection. The events left are stored permanently in the CERN computer centre for offline analysis.

3.2.9 Off-Line Analysis and Monte Carlo

The data stored by the DAQ is not in analysis ready format. The raw data passing the event filter is grouped by detector run but is not ordered by time within the run or by physics selection. It is first reconstructed as Event Summary Data (ESD) from the digitised record of event data. This creates object orientated data such as tracks, vertices, jets, etc. The data processing involves a one-to-one mapping of events so the data remains unordered with respect to time or physics selection. The data is further summarised to Analysis Object Data (AOD) format which is then ready for user analysis. This step introduces ordering by physics selection into streams. After AOD processing the event size is greatly reduced from $2MB$ to $0.1MB$. Although the formatting steps create event candidate objects, like electrons, photons, jets, etc., these are not unambiguous. For instance, electron and photon objects share many of the same candidates. In addition, the object construction algorithms can be re-run by a user to tailor analyses, e.g. using topo-cluster jets rather than tower based jets.

In order to assess potential detector responses and test analysis strategies before the detector is operational, expected physics processes are simulated. This involves Monte Carlo

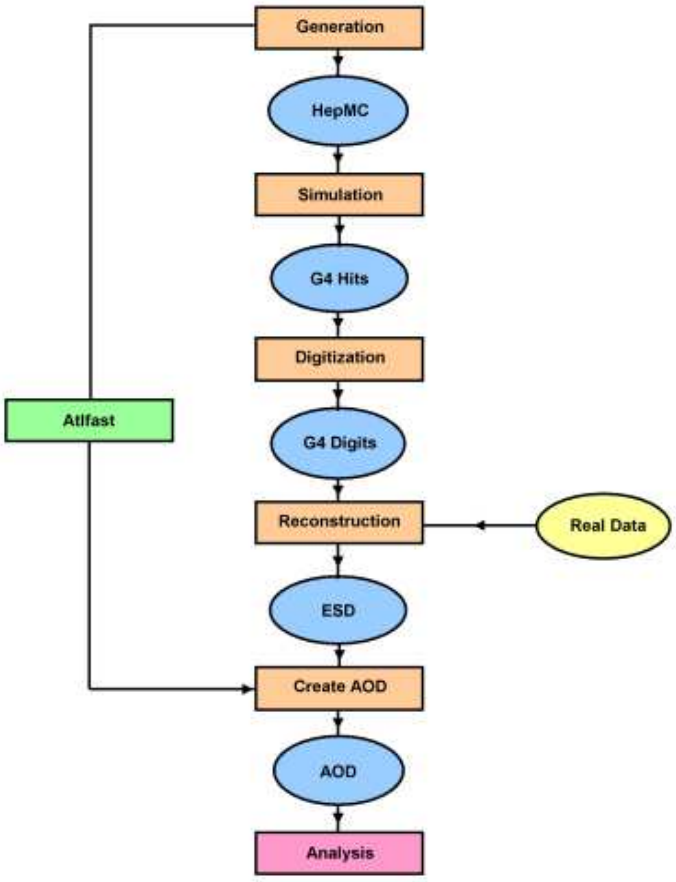

Figure 3.9: Schematic of ATLAS event chain for data and MC.

production of QCD events, which can include low-Q^2 background processes as well as high-Q^2 events of interest, and detector simulation. The simulation chain begins with the generation of a specific physics process which outputs a series of 4-vectors corresponding to the kinematics of the semi-stable particles generated. These are input to a simulation process which mimics the interaction of the incident radiation with the ATLAS detector materials using GEANT[29] to simulate the passage of particles through matter. The resultant trajectories and energy deposits are fed into a digitisation step which applies the response of the detector sub-systems to the deposited energy and outputs simulated voltages and times. At this point the simulated data is of the same format as real raw data, see fig.3.9, and therefore can be handled by the same offline procedures to create ESD and AOD files. The simulated data follows the same procedure for ease of use and in order to reflect the real data format as closely as possible so users have consistency. The major difference between simulated and real data is the inclusion of MC truth information. These data sets can then be used by collaboration groups and individual users. Further filtering of events, event objects or object attributes can be applied, as well as reconstructed objects added, tailored to the analysis needs. These Derived Physics Datasets (DPDs) reduce duplication of efforts and standardise basic analysis procedures across the collaboration.

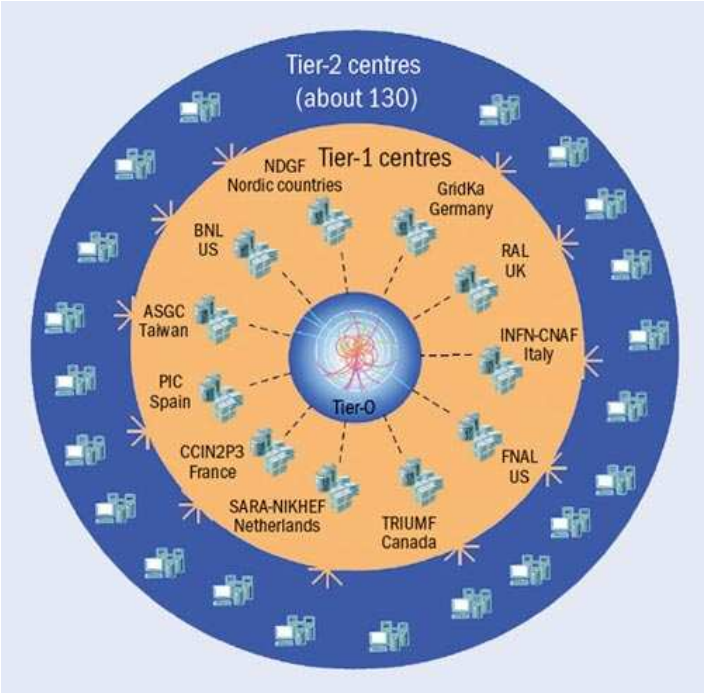

Figure 3.10: Schematic of grid network.

3.2.10 Data Storage

In previous particle physics collaborations the data collected was distributed around the world so that each institute could have access to the same event information to run separate analyses. The LHC experiments create such a volume of data that it is impractical to distribute it entirely and repeatedly around the world. Hence a different analysis model is adopted where the individual analyses developed by disparate institutes go to the data rather than vice-versa. In fact not only do the analyses run over data stored in distant repositories, they also use remote computing resources. These advantages are possible by the development of the "grid". The grid pools computing resources and storage to overcome traditional constraints of local computing. For the LHC, computing resources are organised into a hierarchy of four tiers, see fig.3.10, with each institutions role dependent on the resources at their disposal.

The primary level, tier-0, is located at CERN itself. There, raw data is collected and initially processed into ESD and AOD format, which is replicated and transferred to all tier-1 sites. There are 10 tier-1 facilities situated around the globe. Further event reprocessing is done at tier-1 and AOD files are sent on to tier-2. Tier-2 resources are clustered around tier-1 sites based on geography but in principle any tier-1 and tier-2 sites can communicate. Event simulation, analysis and calibration can take place at these institutions. Here AOD information is stored, along with a small amount of ESD and raw data. All members of the collaboration have access to tier-2 sites. The final level, tier-3, is any institution with local

clusters or desktops where event analyses will be performed. Advantages to data storage include sharing resources across member institutions and back-up of event data. Advantages for users include the ability to specify which location's computing resources are used to process the events from another specified facility, though in practice these are selected automatically. The user submits analyses to the grid which allocates it to appropriate computing sites and returns the results to the user. All the allocating infrastructure and computational duties are handled behind the scenes with the user blissfully unaware of the details.

Chapter 4

Top Physics Pseudo-Analysis

The chapter details work done in the pre-data phase of the LHC on di-leptonic top events in ATLAS. It describes a measurement performed using simulated data (on AODs) of the fully leptonic top pair production cross-section for proton-proton collisions at a centre-of-mass energy of $10\ \mathrm{TeV}$. Object and event selection is described in the three selection channels based on the three di-leptonic final states. Significant background processes were included in the pseudo-analysis and selection techniques for their removal implemented. The result of the pseudo-analysis is presented along with estimates of statistical and main systematic uncertainties for each selection channel with comparison to theoretical predictions are discussed.

Although object and event selection of this chapter comes directly from [3] the author was involved in the validation of this event selection technique. The results shown in this chapter were independently produced by the author and reproduce the results of [3]. The discussion of systematics at the end of the chapter in 7.5 reiterates the discussion in [3] and is used to motivate the following chapter.

4.1 Object Selection

The semi- and fully-leptonic di-top production channels are preferred for the initial top searches. In the initial running period many aspects of the detector and software will be commissioned in situ. While this process is carried out it is important not to rely on unvalidated techniques for results and to use conventional methods to isolate control samples on which new techniques can be tested. Hence, to begin, event searches will favour objects which are relatively easy to identify, even if their production is somewhat rarer. This is the case with the fully leptonic di-top production channel, which occurs with only a quarter the frequency of either the semi-leptonic or fully hadronic channels. Also, tauons are not reconstructed as this introduces an additional algorithm inefficiency.

With two leptons produced in the Born level diagram (and hence in all orders) the fully leptonic channel is remarkably clean. The two leptons can be used to trigger and select events with the large missing energy of the associated neutrinos, an important factor in background rejection. Event selection has limited dependence on jet reconstruction, as only two jets are required, and, importantly, no flavor-tagging dependence. Hence, the di-top production uses several basic measurements to identify signal and reject background events: electrons, muons, jets and missing energy.

This section gives details of the object definitions used in the analysis. These follow the object construction in [3].

4.1.1 Electrons

Electrons are reconstructed from a standard cluster based algorithm. This uses charge deposits in the electromagnetic calorimeter (E-cal) to make cluster seeds and match them to a track in the inner detector, first to the track origin and then to the extrapolated track position in the calorimeter. A requirement on the authorship of the electron ensures the electron was constructed using the standard cluster based algorithm (i.e. not solely `Softe` or `Forward` algorithms). A quality cut uses an electron identification algorithm with the aim of distinguishing electrons from other particles which may be detected in the E-cal (e.g. jets and pions). It is based on assessing shower shapes in the E-cal and tracks in the inner detector.

The standard algorithm separates electrons from fakes using isolation variables. Three different quality cuts are possible to allow flexibility in analysis: *loose*, *medium* and *tight*, see the chapter of [35] concerning electrons for full details of the quality definitions. The *loose* definition of an electron applies cuts on the EM shower shape in the calorimeter (second layer) and some hadronic leakage variables. The *medium* definition includes more information from the calorimeter (first and second layers), track quality requirements and track-cluster matching. The *tight* definition adds E/p, b-layer and TRT requirements. The *loose* definition has excellent electron identification efficiency, $\epsilon_{id} = 88\%$ for $Z \rightarrow ee$ events with $E_t > 17$ GeV, but does not reject fake electron signatures well having a jet rejection factor $R_{jet} = 567$. The additional cuts of the other definitions improve the rejection of fakes, $R_{jet}^{medium} = 2184$ and $R_{jet}^{tight} = 8.9 \times 10^4$, with some decrease in identification efficiency, $\epsilon_{id}^{medium} = 77\%$ and $\epsilon_{id}^{tight} = 62\%$. It depends on the analysis which definition is appropriate. For this analysis a *medium* condition was used. This improves jet rejection by a factor of 3-4 and decreases the identification efficiency by 10% compared to the *loose* definition.

Further requirements are added to reduce background contamination. A threshold limiting the transverse energy in a cone around the electron trajectory ensures the electron is isolated. This reduces the contamination from fake electron signatures. A $\mathrm{p_T}$ cut is chosen to lie on the plateau of the trigger turn-on curve where the efficiency is highest and most

stable. A p_T below the plateau would include more relatively low energy final state particles from top events but also increase contamination. The fiducial η region runs from the centre of the detector to the edge of the end-caps leaving one cell of the E-cal outer wheel to avoid inefficiencies at the edge of the material. The crack region ($1.37 <| \eta |< 1.52$) between the barrel and the end-caps of the E-cal is also removed.

The electron selection is summarised in the following table 4.1:

parameter	definition
author	`egamma` (author() == 1 or 3)
quality	`medium`
isolation	`etcone20` $\leq$ 6GeV
p_T	$\geq$ 20GeV
η	$0 \leq \mid \eta \mid \leq 1.37$ or $1.52 \leq \mid \eta \mid \leq 2.47$

Table 4.1: Electron parameters

4.1.2 Muons

Muons are reconstructed from the charge deposits in the muon spectrometer and matched to tracks in the inner detector. `Staco` muons are merged reconstructions of muons from the `Muonboy` and `MuTag` algorithms. `Muonboy` identifies regions of activity in the barrel and end-cap muon trigger chambers at the outer parts of the detector. Hits are then combined into local segments (roughly pointing to the IP). Segments are combined by 3D tracking in the B-field to make candidate tracks. Candidates are accepted if they can be back tracked to the IP. `MuTag` begins with tracks (> 3 GeV/c) found in the inner detector and associates them to Spectrometer segments based on geometric location. This complements the outside-in approach of `Muonboy`, identifying muons which might otherwise be lost.

The `isCombinedMuon` quality requirement ensures the `Muonboy` algorithm with inner detector tracks to reconstruct muon objects. A threshold limiting the transverse energy in a cone around the muon trajectory improves muon isolation. A p_T cut is chosen to lie on the plateau of the trigger turn-on curve where the efficiency is highest and most stable, similar to the electron case. The fiducial η region runs from the centre of the detector to the edge of the spectrometer. Further detail of muon definitions can be found in the chapter concerning muons in [35].

The muon selection is summarised in the following table 4.2:

4.1.3 Jets

Jets are reconstructed using the `Cone4H1Tower` algorithm. This is a seeded cone algorithm using charge deposits in the hadronic calorimeter reconstructed into towers and a cone radius

parameter	definition
author	`Staco`
quality	`isCombinedMuon`
isolation	`etcone20` $\leq$ 6GeV
$\mathrm{p_T}$	$\geq$ 20GeV
η	$\mid \eta \mid \leq 2.5$

Table 4.2: Muon parameters

$R = 0.4$. The $\mathrm{p_T}$ cut is chosen to make sure jets are well defined relatively high $\mathrm{p_T}$ final state objects coming signal decays and not soft radiation from secondary processes in background events. The value of $\mathrm{p_T} > 20$ GeV is chosen as studies of the $\mathrm{p_T}$ spectra of hadronic products from signal and background events suggest this cut will retain much of the of top decay products while rejecting jets from background events. The fiducial η region runs from the centre of the detector to the edge of the hadronic calorimeter. Further detail of jet definitions can be found in the chapter concerning jets in [35].

The jet selection is summarised in the following table 4.3:

parameter	definition
author	`Cone4H1Tower`
$\mathrm{p_T}$	$\geq$ 20GeV
η	$\mid \eta \mid \leq 2.5$

Table 4.3: Jet parameters

4.1.4 Missing Energy and Overlap Removal

The missing transverse energy ($\not\!\!E_T$) algorithm used in this analysis was `MET_RefFinal`. This calculates $\not\!\!E_T$ by beginning with the reconstructed objects (electrons, photons, muons, taus & jets) in an event. The constituent calorimeter cell information from identified objects is summed together with unassociated cells in the detector, the muon spectrometer and LAr and Tile sub-detectors (to correct for energy lost in the cryostat). The vector sum defines any imbalance in the transverse energy of an event, which is identified as $\not\!\!E_T$.

Overlap removal is done in the following fashion:

- select electrons
- select jets, removing overlap with the selected electrons ($\Delta R \leq 0.2$)
- select muons, removing overlap with jets ($\Delta R \leq 0.3$)

4.2 Trigger and Reconstruction Efficiencies

4.2.1 Trigger Efficiencies

Two single lepton triggers were used for this analysis: `EF_e15_medium`, which is an electron trigger with a lower $\mathrm{p_T}$ threshold of $15\ \mathrm{GeV}$, the *medium* requirement uses information from the electromagnetic shower; and, `EF_mu15`, which is a muon trigger with the same lower limit. Both are based on tri-level trigger chains, where the first coarse level picks out regions of interest (RoIs) in the calorimeters which are then scrutinised in greater detail by the subsequent trigger levels.

To calculate each lepton flavor trigger efficiency the proportion of reconstructed lepton objects passing selection criteria in fully leptonic same flavor events which match ($\Delta R < 0.05$) generated leptons from W decay were required to also match ($\Delta R < 0.1$) trigger RoIs, i.e.,

$$\xi_{trig} = \frac{N^{lep}_{rec \to RoI}}{N^{lep}_{rec \to tru}}, \tag{4.1}$$

where ξ_{trig} is the trigger efficiency per bin (w.r.t. reconstructed lepton), $N^{lep}_{rec \to tru}$ is the number of selected leptons matched to generated leptons and $N^{lep}_{rec \to RoI}$ is the number of selected leptons matched to generated leptons and trigger RoIs.

The following $\mathrm{p_T}$ and η trigger efficiency distributions were obtained for electrons, fig.4.1 and muons, fig.4.2. In both plots the normalised hadron-level $\mathrm{p_T}$ distribution is transposed on the efficiency plot. The errors plotted for the efficiencies in these distributions are an over estimate of the correct value as they are based on Poissonian statistics rather than the correct Binomial calculation.

Fig.4.1 shows the steep trigger turn on curve for $\mathrm{p_T}$ with a plateau for $\mathrm{p_T} > 20\ \mathrm{GeV}$. Obvious features in the η plot are the dips at either side of the hadron-level distribution. This is due to gaps in the fiducial volume of the EM calorimeter. This has been taken into account in the calculation of the efficiency distribution.

4.2.2 Reconstruction Efficiencies

To calculate each lepton flavor reconstruction efficiency the proportion of generated leptons from W and tau decays in fully leptonic same flavor events were required to match ($\Delta R < 0.05$) reconstructed lepton objects passing selection criteria, i.e.,

$$\xi_{rec} = \frac{N^{lep}_{rec \to tru}}{N^{lep}_{tru}}, \tag{4.2}$$

where ξ_{rec} is the trigger efficiency per bin (w.r.t. reconstructed lepton), N^{lep}_{tru} is the number

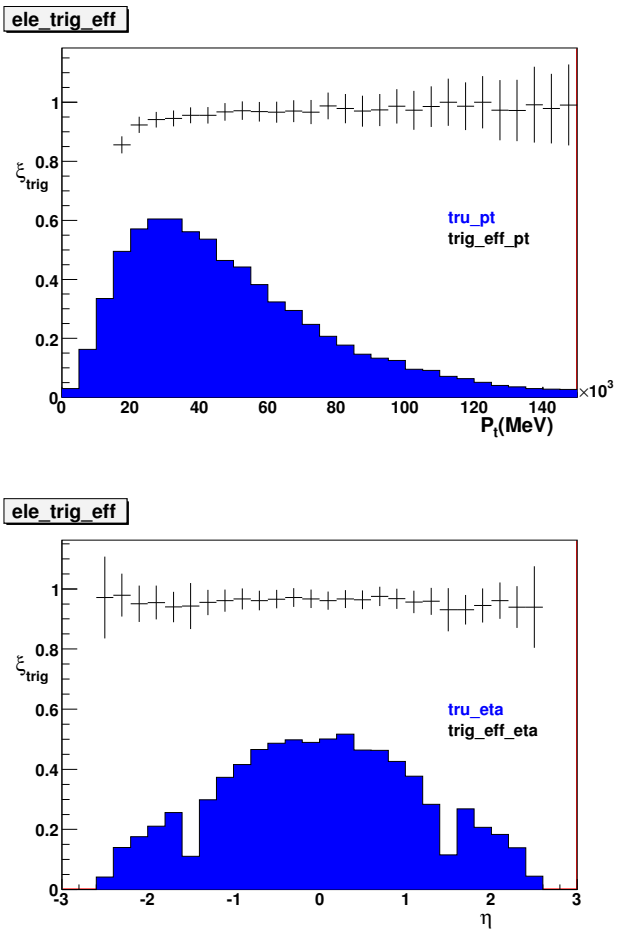

Figure 4.1: `EF_e15_medium` trigger efficiency as a function of reconstructed electron $\mathrm{p_T}$ (above) and η (below). Both sets of errors are Poissonian.

of generated leptons and $N^{lep}_{rec \to tru}$ is the number of selected leptons matched to generated leptons.

The following $\mathrm{p_T}$ and η reconstruction efficiency distributions were obtained for electrons, fig.4.3, and muons, fig.4.4. Again, the errors used for the efficiencies in these plots are an over estimate of the correct Binomial errors. The effect of the symmetric gaps in η coverage of the EM calorimeter are again noticeable in fig.4.3 with the drop in reconstruction efficiency at either end of the distribution.

4.3 Event Selection Cuts and Cut-flow

The section gives details of the event selection used in the analysis as well as the resulting cut-flow. The event selection follows [3] but all results shown are from an independent analysis.

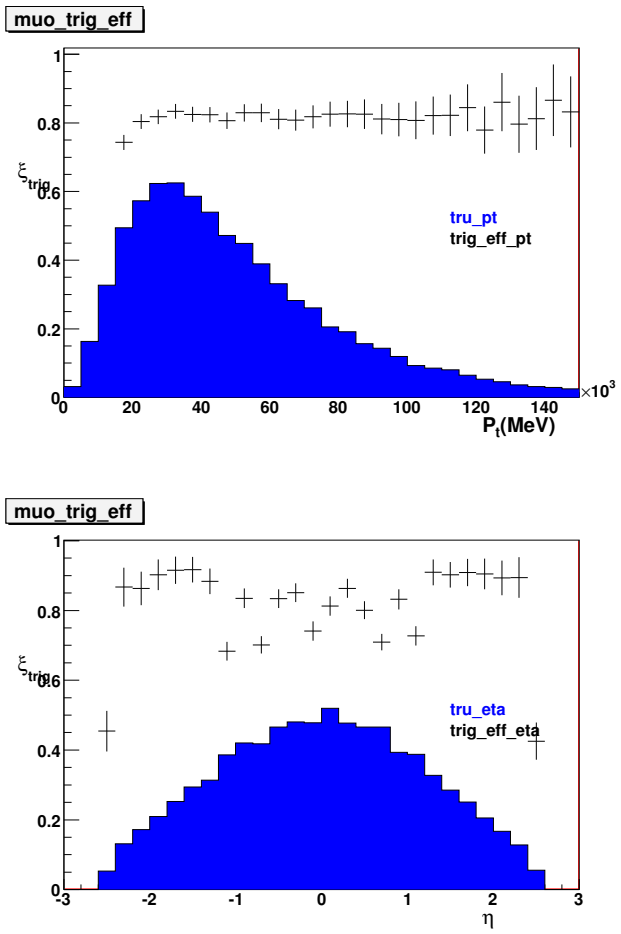

Figure 4.2: `EF_mu15` trigger efficiency as a function of reconstructed muon $\mathrm{p_T}$ (above) and η (below). Both sets of errors are Poissonian.

4.3.1 Event Selection Summary

One of the defining features of the events is the presence of two leptons. These are chosen such that they have high $\mathrm{p_T}$ and are well isolated and of opposite charge, where the isolation and charge requirements reduce background from non-prompt (i.e. not from top decay) leptons. A further necessary condition, is that at least two jets are present. These are expected to originate from the b-quarks from top-decay, with further jets possible from initial or final state radiation (ISR/FSR) from these high energy collisions.

The di-leptonic channel is then sub-divided into a di-electronic (ee) channel, a di-muonic ($\mu\mu$) channel and a mixed ($e\mu$) channel. Selection between channels differs in the $\not\!\!E_T$ threshold and the absence of a di-lepton invariant mass veto around the Z-pole for the mixed channel. Both these cuts are specific to same-flavor events where background contamination from Z→ll events is an important consideration. This is not the case in mixed-flavor events.

Table 4.4 summarises the event selection cuts. Table 4.5 lists the event processes analysed along with their corresponding cross-sections and k-factors. The latter co-efficient is used

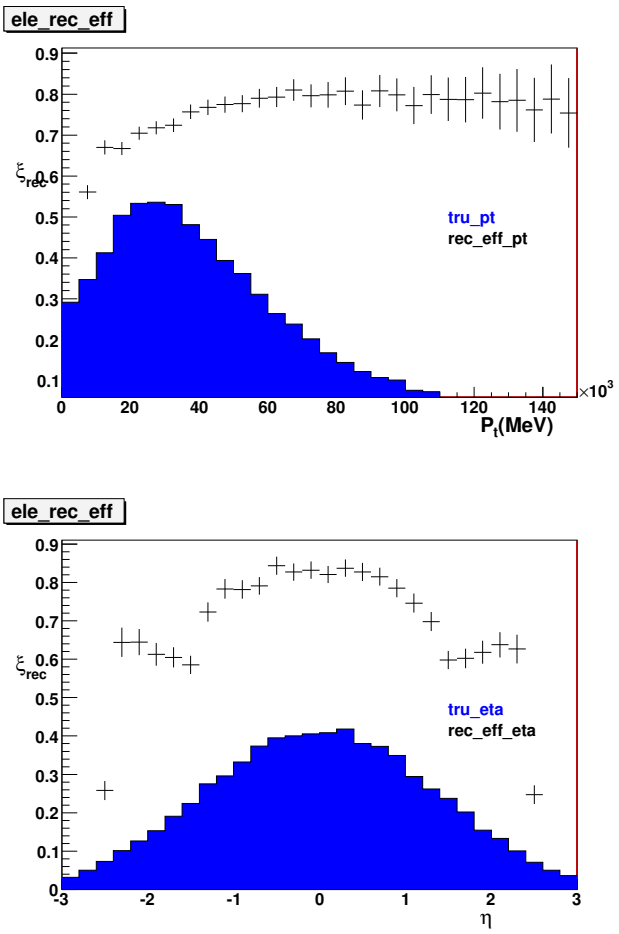

Figure 4.3: Electron reconstruction efficiency as a function of generated electron $\mathrm{p_T}$ (above) and η (below). Both sets of errors are Poissonian.

to compare predictions from different MC generators which may have differing assumptions used in calculations. These must be normalised across MC formats for accurate combination.

Cut	ee and $\mu\mu$	eμ
trigger	`EF_e15_medium`, `EF_mu15` (resp.)	`EF_e15_medium` or `EF_mu15`
lepton	two opposite charged leptons, $\mathrm{p_T} > 20$ GeV	same as ee and $\mu\mu$
$\not{E}_T$	> 35 GeV	> 20 GeV
jets	≥ 2 jets of $\mathrm{p_T} > 20$ GeV	same as ee and $\mu\mu$
invariant lepton mass	$m_{ll} < 86$ GeV or $m_{ll} > 96$ GeV	

Table 4.4: List of event cuts.

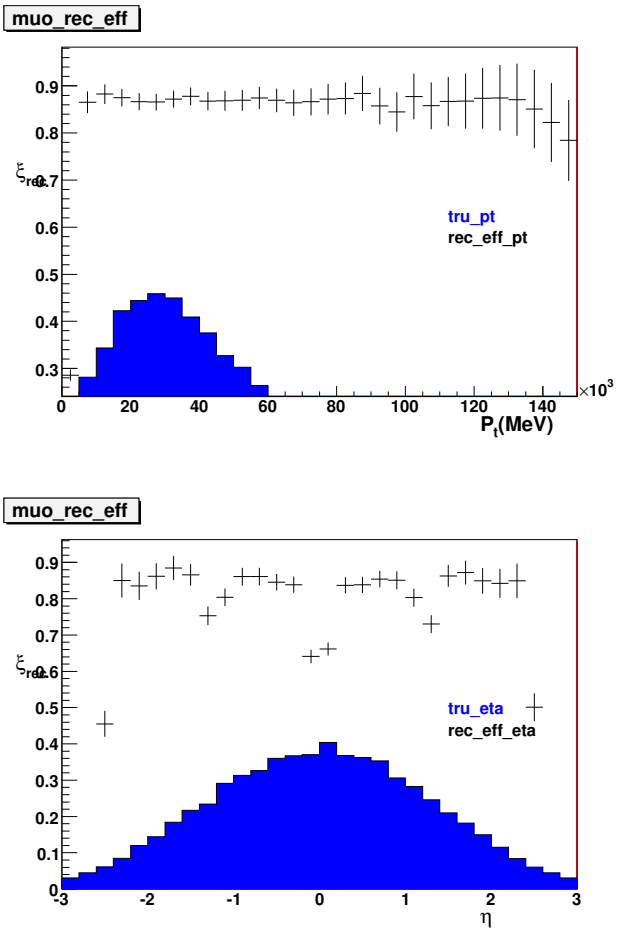

Figure 4.4: Muon reconstruction efficiency as a function of generated muon $\mathrm{p_T}$ (above) and η (below). Both sets of errors are Poissonian.

sample	$\sigma(pb^{-1})$	k-factor
$t\bar{t}$	202.86	1.07
Weν	13253.84	1.22
W$\mu\nu$	13242.22	1.22
W$\tau\nu$	13237.72	1.22
Zee	1183.66	1.22
Z$\mu\mu$	1182.41	1.22
Z$\tau\tau$	1178.57	1.22
Wbb	14.64	1.22
WW	15.62	1.69
WZ	1.37	1.42
ZZ	4.87	1.81
t-chan	41.12	1.05
W-chan	14.41	0.99

Table 4.5: Sample processes used in analysis

The following tables 4.6-4.11 summarise the selection cut-flow channel by channel over signal and background samples. Both exclusive, where one selection criterion is applied while the others are relaxed, and combined, where all selection criteria are applied cumulatively, results are presented. The results have been scaled to an integrated luminosity of 200pb^{-1}, which is of the order of data expected within the first year of LHC running. All appropriate k-factors have been included. Errors were calculated using $\sqrt{N}$ and similarly scaled.

4.3.2 Di-electron Channel Selection

The largest backgrounds in this channel come from Z→ee+jets, where two real electrons are present, along with radiative jets and $\not\!\!E_T$ can arise from the limits of fiducial volume; and W→eν+jets, where a jet from I/FSR fakes an electron and $\not\!\!E_T$ will result from the neutrino. Tables 4.6 and 4.7 show the exclusive and combined cut-flow of the ee channel analysis respectively.

sample	leps	O.S	inv. mass	$\not\!\!E_T$	≥2jets	all	trigger
$t\bar{t}$	379.0 ± 6.8	365.4 ± 6.6	345.7 ± 6.5	304.3 ± 6.1	322.5 ± 6.2	228.1 ± 5.3	221.9 ± 5.2
Weν	174.9 ± 71.0	92.8 ± 31.1	172.4 ± 70.6	117.2 ± 60.7	24.7 ± 10.6	13.8 ± 7.8	13.8 ± 7.8
W$\mu\nu$	0.0 ± 0.0	0.0 ± 0.0	0.0 ± 0.0	0.0 ± 0.0	0.0 ± 0.0	0.0 ± 0.0	0.0 ± 0.0
W$\tau\nu$	17.3 ± 11.5	11.0 ± 9.8	17.3 ± 11.5	11.0 ± 9.8	6.3 ± 3.6	0.0 ± 0.0	0.0 ± 0.0
Zee	67809.7 ± 493.4	67341.0 ± 491.7	16330.9 ± 241.6	106.1 ± 13.8	4306.5 ± 87.0	13.2 ± 2.3	12.7 ± 2.2
Z$\mu\mu$	0.0 ± 0.0	0.0 ± 0.0	0.0 ± 0.0	0.0 ± 0.0	0.0 ± 0.0	0.0 ± 0.0	0.0 ± 0.0
Z$\tau\tau$	152.7 ± 22.4	150.2 ± 22.2	152.2 ± 22.4	9.0 ± 2.9	13.8 ± 3.8	7.0 ± 2.6	6.8 ± 2.6
Wbb	0.6 ± 0.4	0.3 ± 0.2	0.6 ± 0.4	0.2 ± 0.2	0.2 ± 0.2	0.0 ± 0.0	0.0 ± 0.0
WW	48.7 ± 3.5	47.4 ± 3.5	46.4 ± 3.5	28.8 ± 2.7	3.6 ± 1.0	2.1 ± 0.7	2.1 ± 0.7
WZ	14.7 ± 0.8	12.8 ± 0.7	4.6 ± 0.4	3.3 ± 0.4	6.1 ± 0.5	0.1 ± 0.1	0.1 ± 0.1
ZZ	182.1 ± 5.7	174.2 ± 5.5	52.0 ± 3.0	33.0 ± 2.4	79.7 ± 3.7	1.4 ± 0.5	1.4 ± 0.5
t-chan	3.3 ± 1.0	1.9 ± 0.7	3.3 ± 1.0	1.9 ± 0.7	2.2 ± 0.8	1.4 ± 0.6	1.4 ± 0.6
W-chan	23.6 ± 3.9	21.7 ± 3.7	19.8 ± 3.5	18.5 ± 3.4	8.3 ± 2.3	6.4 ± 2.0	6.4 ± 2.0

Table 4.6: Selected electron events exclusive cut-flow for CoM = 10TeV, integrated Luminosity = 200pb^{-1}

sample	leps	O.S	inv. mass	$\not\!\!E_T$	≥2jets	all	trigger
$t\bar{t}$	379.0 ± 6.8	365.4 ± 6.6	334.3 ± 6.4	269.8 ± 5.7	228.1 ± 5.3	228.1 ± 5.3	221.9 ± 5.2
Weν	174.9 ± 71.0	92.8 ± 31.1	91.6 ± 30.8	54.9 ± 23.7	13.8 ± 7.8	13.8 ± 7.8	13.8 ± 7.8
W$\mu\nu$	0.0 ± 0.0	0.0 ± 0.0	0.0 ± 0.0	0.0 ± 0.0	0.0 ± 0.0	0.0 ± 0.0	0.0 ± 0.0
W$\tau\nu$	17.3 ± 11.5	11.0 ± 9.8	11.0 ± 9.8	6.8 ± 6.8	0.0 ± 0.0	0.0 ± 0.0	0.0 ± 0.0
Zee	67809.7 ± 493.4	67341.0 ± 491.7	16162.1 ± 240.3	19.7 ± 4.8	13.2 ± 2.3	13.2 ± 2.3	12.7 ± 2.2
Z$\mu\mu$	0.0 ± 0.0	0.0 ± 0.0	0.0 ± 0.0	0.0 ± 0.0	0.0 ± 0.0	0.0 ± 0.0	0.0 ± 0.0
Z$\tau\tau$	152.7 ± 22.4	150.2 ± 22.2	150.0 ± 22.2	8.7 ± 2.8	7.0 ± 2.6	7.0 ± 2.6	6.8 ± 2.6
Wbb	0.6 ± 0.4	0.3 ± 0.2	0.3 ± 0.2	0.0 ± 0.0	0.0 ± 0.0	0.0 ± 0.0	0.0 ± 0.0
WW	48.7 ± 3.5	47.4 ± 3.5	45.1 ± 3.4	26.5 ± 2.6	2.1 ± 0.7	2.1 ± 0.7	2.1 ± 0.7
WZ	14.7 ± 0.8	12.8 ± 0.7	3.6 ± 0.4	0.7 ± 0.2	0.1 ± 0.1	0.1 ± 0.1	0.1 ± 0.1
ZZ	182.1 ± 5.7	174.2 ± 5.5	49.7 ± 3.0	10.8 ± 1.4	1.4 ± 0.5	1.4 ± 0.5	1.4 ± 0.5
t-chan	3.3 ± 1.0	1.9 ± 0.7	1.9 ± 0.7	1.4 ± 0.6	1.4 ± 0.6	1.4 ± 0.6	1.4 ± 0.6
W-chan	23.6 ± 3.9	21.7 ± 3.7	17.8 ± 3.4	14.7 ± 3.1	6.4 ± 2.0	6.4 ± 2.0	6.4 ± 2.0

Table 4.7: Selected electron events combined cut-flow for CoM = 10TeV, integrated Luminosity = 200pb^{-1}

4.3.3 Di-muon Channel Selection

The largest backgrounds in this channel come from Z$\rightarrow \mu\mu$, where two real muons are present, along with radiative jets and $\not\!\!E_T$ can arise from the limits of fiducial volume; and single top W-channel, where a real leptonic top decay occurs and real non-prompt muons can come from b-jet decays. In addition, Z$\rightarrow \tau\tau$ events, where two real non-prompt leptons can result from the decay of the two τs, are also significant. Tables 4.8 and 4.9 show the exclusive and combined cut-flow of the $\mu\mu$ channel analysis respectively.

sample	leps	O.S	inv. mass	$\not\!\!E_T$	$\geq$2jets	all	trigger
$t\bar{t}$	550.5 $\pm$ 8.2	539.7 $\pm$ 8.1	507.8 $\pm$ 7.8	449.7 $\pm$ 7.4	470.2 $\pm$ 7.5	349.8 $\pm$ 6.5	339.0 $\pm$ 6.4
Weν	0.0 $\pm$ 0.0	0.0 $\pm$ 0.0	0.0 $\pm$ 0.0	0.0 $\pm$ 0.0	0.0 $\pm$ 0.0	0.0 $\pm$ 0.0	0.0 $\pm$ 0.0
W$\mu\nu$	21.2 $\pm$ 15.4	19.9 $\pm$ 14.1	21.2 $\pm$ 15.4	14.1 $\pm$ 12.5	1.3 $\pm$ 1.3	0.0 $\pm$ 0.0	0.0 $\pm$ 0.0
W$\tau\nu$	2.1 $\pm$ 2.1	0.0 $\pm$ 0.0	2.1 $\pm$ 2.1	0.0 $\pm$ 0.0	0.0 $\pm$ 0.0	0.0 $\pm$ 0.0	0.0 $\pm$ 0.0
Zee	0.0 $\pm$ 0.0	0.0 $\pm$ 0.0	0.0 $\pm$ 0.0	0.0 $\pm$ 0.0	0.0 $\pm$ 0.0	0.0 $\pm$ 0.0	0.0 $\pm$ 0.0
Z$\mu\mu$	107280.7 $\pm$ 703.4	107279.6 $\pm$ 703.4	23933.4 $\pm$ 332.2	370.4 $\pm$ 33.9	7526.2 $\pm$ 128.6	52.8 $\pm$ 7.0	49.9 $\pm$ 6.8
Z$\tau\tau$	277.3 $\pm$ 29.9	277.3 $\pm$ 29.9	276.8 $\pm$ 29.9	16.5 $\pm$ 4.3	22.8 $\pm$ 5.7	9.1 $\pm$ 1.8	8.7 $\pm$ 1.8
Wbb	1.3 $\pm$ 0.6	0.8 $\pm$ 0.5	1.2 $\pm$ 0.6	1.0 $\pm$ 0.5	0.9 $\pm$ 0.5	0.5 $\pm$ 0.4	0.4 $\pm$ 0.3
WW	70.6 $\pm$ 4.3	70.6 $\pm$ 4.3	65.4 $\pm$ 4.1	41.2 $\pm$ 3.3	5.2 $\pm$ 1.2	3.9 $\pm$ 1.0	3.9 $\pm$ 1.0
WZ	20.9 $\pm$ 0.9	18.3 $\pm$ 0.8	5.8 $\pm$ 0.5	4.7 $\pm$ 0.4	8.6 $\pm$ 0.6	0.2 $\pm$ 0.1	0.2 $\pm$ 0.1
ZZ	271.0 $\pm$ 6.9	262.3 $\pm$ 6.8	65.1 $\pm$ 3.4	50.4 $\pm$ 3.0	130.1 $\pm$ 4.8	2.6 $\pm$ 0.7	2.6 $\pm$ 0.7
t-chan	5.0 $\pm$ 1.2	2.8 $\pm$ 0.9	4.7 $\pm$ 1.1	2.8 $\pm$ 0.9	2.5 $\pm$ 0.8	0.6 $\pm$ 0.4	0.3 $\pm$ 0.3
W-chan	35.0 $\pm$ 4.7	33.1 $\pm$ 4.6	31.9 $\pm$ 4.5	28.7 $\pm$ 4.3	17.2 $\pm$ 3.3	12.7 $\pm$ 2.8	12.7 $\pm$ 2.8

Table 4.8: Selected muon events exclusive cut-flow for CoM = 10TeV, integrated Luminosity = 200pb^{-1}

sample	leps	O.S	inv. mass	$\not\!\!E_T$	$\geq$2jets	all	trigger
$t\bar{t}$	550.5 $\pm$ 8.2	539.7 $\pm$ 8.1	498.2 $\pm$ 7.8	407.0 $\pm$ 7.0	349.8 $\pm$ 6.5	349.8 $\pm$ 6.5	339.0 $\pm$ 6.4
Weν	0.0 $\pm$ 0.0	0.0 $\pm$ 0.0	0.0 $\pm$ 0.0	0.0 $\pm$ 0.0	0.0 $\pm$ 0.0	0.0 $\pm$ 0.0	0.0 $\pm$ 0.0
W$\mu\nu$	21.2 $\pm$ 15.4	19.9 $\pm$ 14.1	19.9 $\pm$ 14.1	12.8 $\pm$ 11.1	0.0 $\pm$ 0.0	0.0 $\pm$ 0.0	0.0 $\pm$ 0.0
W$\tau\nu$	2.1 $\pm$ 2.1	0.0 $\pm$ 0.0	0.0 $\pm$ 0.0	0.0 $\pm$ 0.0	0.0 $\pm$ 0.0	0.0 $\pm$ 0.0	0.0 $\pm$ 0.0
Zee	0.0 $\pm$ 0.0	0.0 $\pm$ 0.0	0.0 $\pm$ 0.0	0.0 $\pm$ 0.0	0.0 $\pm$ 0.0	0.0 $\pm$ 0.0	0.0 $\pm$ 0.0
Z$\mu\mu$	107280.7 $\pm$ 703.4	107279.6 $\pm$ 703.4	23932.4 $\pm$ 332.2	104.4 $\pm$ 18.4	52.8 $\pm$ 7.0	52.8 $\pm$ 7.0	49.9 $\pm$ 6.8
Z$\tau\tau$	277.3 $\pm$ 29.9	277.3 $\pm$ 29.9	276.8 $\pm$ 29.9	16.5 $\pm$ 4.3	9.1 $\pm$ 1.8	9.1 $\pm$ 1.8	8.7 $\pm$ 1.8
Wbb	1.3 $\pm$ 0.6	0.8 $\pm$ 0.5	0.6 $\pm$ 0.4	0.5 $\pm$ 0.4	0.5 $\pm$ 0.4	0.5 $\pm$ 0.4	0.4 $\pm$ 0.3
WW	70.6 $\pm$ 4.3	70.6 $\pm$ 4.3	65.4 $\pm$ 4.1	38.4 $\pm$ 3.1	3.9 $\pm$ 1.0	3.9 $\pm$ 1.0	3.9 $\pm$ 1.0
WZ	20.9 $\pm$ 0.9	18.3 $\pm$ 0.8	4.7 $\pm$ 0.4	1.0 $\pm$ 0.2	0.2 $\pm$ 0.1	0.2 $\pm$ 0.1	0.2 $\pm$ 0.1
ZZ	271.0 $\pm$ 6.9	262.3 $\pm$ 6.8	63.5 $\pm$ 3.3	13.4 $\pm$ 1.5	2.6 $\pm$ 0.7	2.6 $\pm$ 0.7	2.6 $\pm$ 0.7
t-chan	5.0 $\pm$ 1.2	2.8 $\pm$ 0.9	2.8 $\pm$ 0.9	2.2 $\pm$ 0.8	0.6 $\pm$ 0.4	0.6 $\pm$ 0.4	0.3 $\pm$ 0.3
W-chan	35.0 $\pm$ 4.7	33.1 $\pm$ 4.6	29.9 $\pm$ 4.4	24.2 $\pm$ 3.9	12.7 $\pm$ 2.8	12.7 $\pm$ 2.8	12.7 $\pm$ 2.8

Table 4.9: Selected muon events cumulative cut-flow for CoM = 10TeV, integrated Luminosity = 200pb^{-1}

4.3.4 Mixed Channel Selection

The largest backgrounds in this channel come from Z$\rightarrow \tau\tau$, where two real non-prompt (i.e. not from top decay) leptons can result from the decay of the two τs, along with radiative jets and $\not\!\!E_T$ will result from neutrinos; and single top W-channel, where a real leptonic top decay occurs and real non-prompt leptons can come from b-jet decays. In addition, W$\rightarrow \mu\nu$+jets are significant where a jet from I/FSR is fakes a jet and $\not\!\!E_T$ will result from the neutrino. Tables 4.10 and 4.11 show the exclusive and combined cut-flow of the $e\mu$ channel analysis respectively.

sample	leps	O.S	$\not\!\!E_T$	$\geq$2jets	all	trigger
$t\bar{t}$	975.5 ± 10.9	935.3 ± 10.6	907.1 ± 10.5	830.0 ± 10.0	739.6 ± 9.5	718.8 ± 9.3
Weν	21.6 ± 14.8	11.3 ± 10.0	19.4 ± 14.1	0.0 ± 0.0	0.0 ± 0.0	0.0 ± 0.0
W$\mu\nu$	489.2 ± 115.2	177.6 ± 68.2	447.1 ± 111.4	77.9 ± 22.7	18.8 ± 10.4	16.2 ± 9.9
W$\tau\nu$	25.7 ± 16.8	14.7 ± 12.8	24.4 ± 15.5	12.6 ± 11.9	9.1 ± 8.5	9.1 ± 8.5
Zee	0.4 ± 0.2	0.2 ± 0.2	0.1 ± 0.1	0.3 ± 0.2	0.1 ± 0.1	0.1 ± 0.1
Z$\mu\mu$	201.0 ± 30.1	99.9 ± 21.5	53.2 ± 15.3	31.3 ± 5.7	5.4 ± 1.9	5.4 ± 1.9
Z$\tau\tau$	399.7 ± 36.5	393.1 ± 36.2	96.4 ± 16.8	39.1 ± 5.3	27.1 ± 4.5	24.9 ± 4.1
Wbb	3.8 ± 1.4	2.2 ± 1.2	2.7 ± 1.2	2.2 ± 1.1	1.0 ± 0.7	1.0 ± 0.7
WW	128.8 ± 5.8	126.5 ± 5.7	106.4 ± 5.2	11.3 ± 1.7	10.3 ± 1.6	9.8 ± 1.6
WZ	6.3 ± 0.5	2.3 ± 0.3	5.2 ± 0.4	1.2 ± 0.2	0.3 ± 0.1	0.3 ± 0.1
ZZ	20.3 ± 1.9	4.9 ± 0.9	6.5 ± 1.1	4.6 ± 0.9	1.1 ± 0.4	1.1 ± 0.4
t-chan	6.6 ± 1.4	2.8 ± 0.9	5.5 ± 1.2	3.9 ± 1.0	0.8 ± 0.5	0.8 ± 0.5
W-chan	60.5 ± 6.2	56.7 ± 6.0	57.3 ± 6.0	29.3 ± 4.3	25.5 ± 4.0	24.2 ± 3.9

Table 4.10: Selected mixed events exclusive cut-flow for CoM = 10TeV, integrated Luminosity = 200pb^{-1}

sample	leps	O.S	$\not\!\!E_T$	$\geq$2jets	all	trigger
$t\bar{t}$	975.5 ± 10.9	935.3 ± 10.6	870.8 ± 10.3	739.6 ± 9.5	739.6 ± 9.5	718.8 ± 9.3
Weν	21.6 ± 14.8	11.3 ± 10.0	9.1 ± 9.1	0.0 ± 0.0	0.0 ± 0.0	0.0 ± 0.0
W$\mu\nu$	489.2 ± 115.2	177.6 ± 68.2	165.0 ± 66.2	18.8 ± 10.4	18.8 ± 10.4	16.2 ± 9.9
W$\tau\nu$	25.7 ± 16.8	14.7 ± 12.8	13.3 ± 11.4	9.1 ± 8.5	9.1 ± 8.5	9.1 ± 8.5
Zee	0.4 ± 0.2	0.2 ± 0.2	0.1 ± 0.1	0.1 ± 0.1	0.1 ± 0.1	0.1 ± 0.1
Z$\mu\mu$	201.0 ± 30.1	99.9 ± 21.5	23.0 ± 10.2	5.4 ± 1.9	5.4 ± 1.9	5.4 ± 1.9
Z$\tau\tau$	399.7 ± 36.5	393.1 ± 36.2	95.6 ± 16.8	27.1 ± 4.5	27.1 ± 4.5	24.9 ± 4.1
Wbb	3.8 ± 1.4	2.2 ± 1.2	1.5 ± 0.9	1.0 ± 0.7	1.0 ± 0.7	1.0 ± 0.7
WW	128.8 ± 5.8	126.5 ± 5.7	104.6 ± 5.2	10.3 ± 1.6	10.3 ± 1.6	9.8 ± 1.6
WZ	6.3 ± 0.5	2.3 ± 0.3	2.0 ± 0.3	0.3 ± 0.1	0.3 ± 0.1	0.3 ± 0.1
ZZ	20.3 ± 1.9	4.9 ± 0.9	3.0 ± 0.7	1.1 ± 0.4	1.1 ± 0.4	1.1 ± 0.4
t-chan	6.6 ± 1.4	2.8 ± 0.9	2.2 ± 0.8	0.8 ± 0.5	0.8 ± 0.5	0.8 ± 0.5
W-chan	60.5 ± 6.2	56.7 ± 6.0	53.5 ± 5.8	25.5 ± 4.0	25.5 ± 4.0	24.2 ± 3.9

Table 4.11: Selected mixed events cumulative cut-flow for CoM = 10TeV, integrated Luminosity = 200pb^{-1}

4.4 Results of Di-lepton Selections

This section shows the kinematic distributions from selected events without trigger. Table 4.4 lists the various definitions intended to evaluate the success of an analysis in terms of the proportions of signal and background events surviving the selection procedure, for each channel.

	S	B	S/B
ee	228.0±5.3	45.3±16.6	5.0±1.8
$\mu\mu$	349.8±6.5	82.4±14.3	4.2±0.7
$e\mu$	739.6±9.5	99.5±32.7	7.4±2.4
combined	1317.4±12.6	227.3±39.4	5.8±1.0

Table 4.12: Signal, background and S/B for each selection channel and combined for $\mathcal{L} = 200\mathrm{pb}^{-1}$. Quoted errors are statistical.

To calculate the cross-section from each channel the following procedure was used: Firstly the number of selected signal events is extracted from the total number of selected events by the following equation 4.3:

$$N_{t\bar{t}}^{sel} = \xi_1 \times N_{tot}^{sel}, \tag{4.3}$$

where $N_{t\bar{t}}^{sel}$ is the number of $t\bar{t}$ events selected, N_{tot}^{sel} is the total number of selected events (signal and background) and $\xi_1 = N_{signal} \div (N_{signal} + N_{background})$, a measure of how well the signal is selected from the background events.

A measured cross-section is then derivable from the number of selected signal events as follows:

$$\sigma_{t\bar{t},meas.} = \frac{N_{t\bar{t}}^{sel}}{\mathcal{L}}, \tag{4.4}$$

where $\sigma_{t\bar{t},meas.}$ is the measured $t\bar{t}$ cross-section and $\mathcal{L}$ is the integrated luminosity. The Luminosity for this analysis was $200\mathrm{pb}^{-1}$, with a conservative uncertainty of 20% used for the calculation.

The measured cross-section can then be related to the actual cross-section:

$$\sigma_{t\bar{t},calc.} = \frac{\sigma_{t\bar{t},meas.}}{\xi_2}, \tag{4.5}$$

where $\sigma_{t\bar{t},calc.}$ is the cross-section of non-all-hadronic $t\bar{t}$ production and $\xi_2 = N_{signal} \div N_{generated}$, the signal selection efficiency ($N_{generated}$=43412 events for this analysis), which takes account of the trigger and event selection.

The quoted value for the non-hadronic $t\bar{t}$ cross-section is $217.06\mathrm{pb}^{-1}$.

The following sections show the kinematics distributions for each selection channel. The

distributions of interest are the selected leptons (used as a sanity check for the analysis, i.e. no more than two should ever be selected), and their $\mathrm{p_T}$ and η distributions, the selected number of jets, and their $\mathrm{p_T}$ and η distributions, and the $miss$ distribution.

4.4.1 Di-electron Channel

Figures 4.5 and 4.6 show the kinematic distributions for the ee-channel. The results of di-electron analysis are summarised in table 4.13:

ξ_1	$\sigma_{t\bar{t},meas.}(pb)$	ξ_2	$\sigma_{t\bar{t},calc.}(pb)$
0.83±0.05	1.1±0.2	0.0053±0.0001	217.1±47.7

Table 4.13: Results of di-electron analysis. Quoted errors are statistical for $\mathcal{L} = 200\mathrm{pb}^{-1}$.

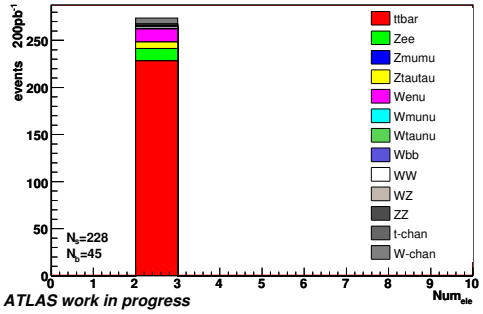

(a) Selected Electron number distribution.

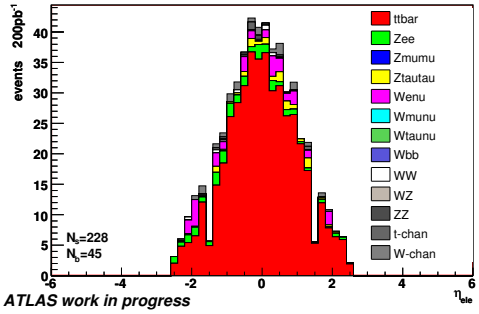

(b) Selected Electron η distribution.

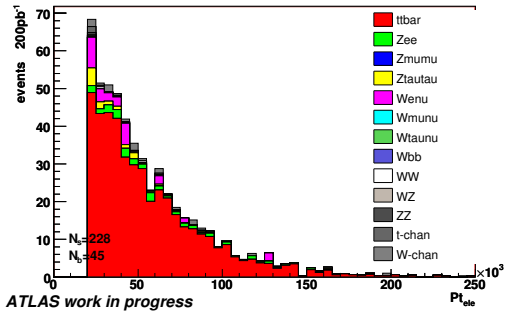

(c) Selected Electron $\mathrm{p_T}$ distribution.

Figure 4.5: Electron distributions for the di-electronic selection.

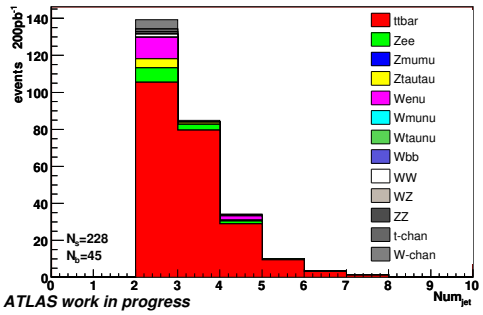

(a) Selected Jet number distribution.

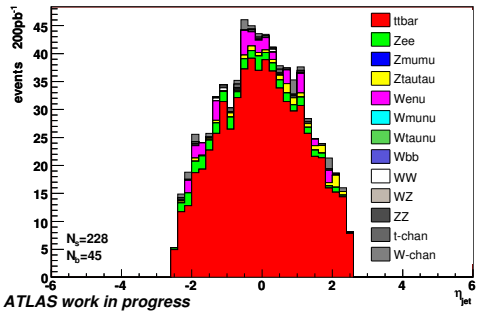

(b) Selected Jet η distribution.

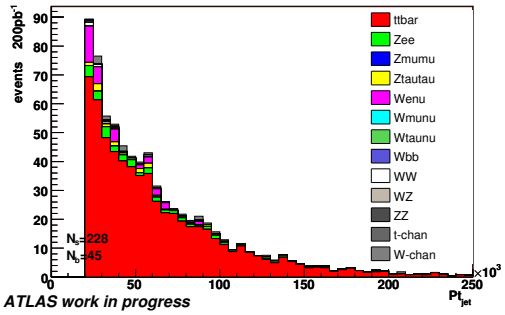

(c) Selected Jet $\mathrm{p_T}$ distribution.

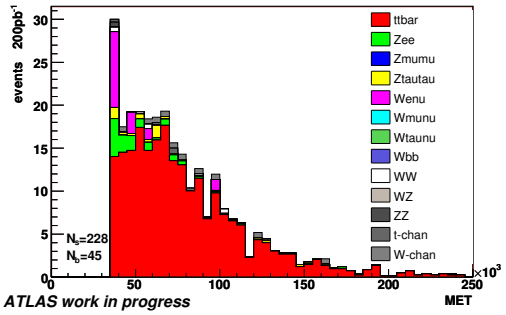

(d) Selected $E_t miss$ distribution.

Figure 4.6: Jet and $miss$ distributions for the di-electronic selection.

4.4.2 Di-muon Channel

Figures 4.7 and 4.8 show the kinematic distributions for the $\mu\mu$-channel. The results of di-muon analysis are summarised in table 4.14:

ξ_1	$\sigma_{t\bar{t},meas.}(pb)$	ξ_2	$\sigma_{t\bar{t},calc.}(pb)$
0.81±0.03	1.7±0.4	0.0081±0.0001	217.1±44.9

Table 4.14: Results of di-muon analysis for $\mathcal{L} = 200\mathrm{pb}^{-1}$. Quoted errors are statistical.

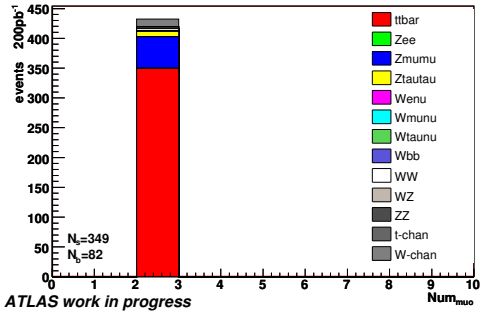

(a) Selected Muon number distribution.

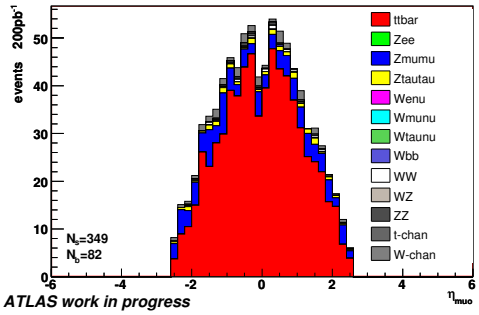

(b) Selected Muon η distribution.

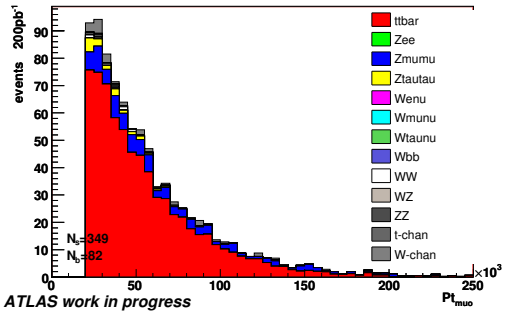

(c) Selected Muon $\mathrm{p_T}$ distribution.

Figure 4.7: Muon distributions for the di-muonic selection.

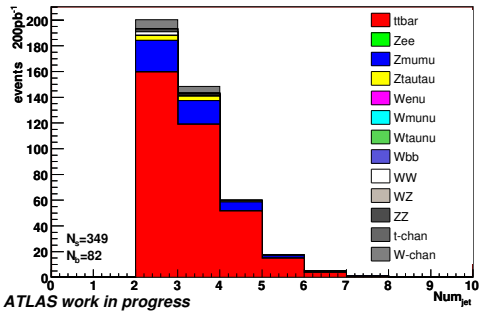

(a) Selected Jet number distribution.

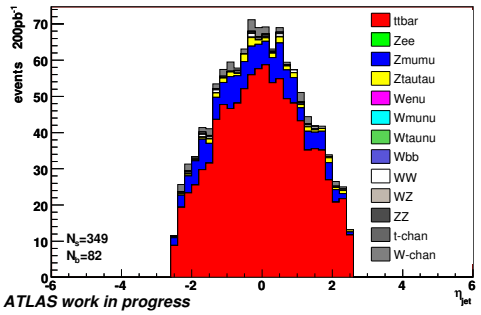

(b) Selected Jet η distribution.

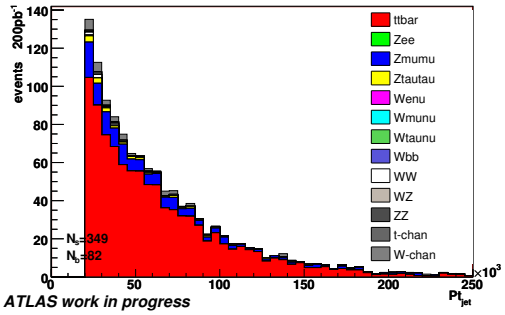

(c) Selected Jet $\mathrm{p_T}$ distribution.

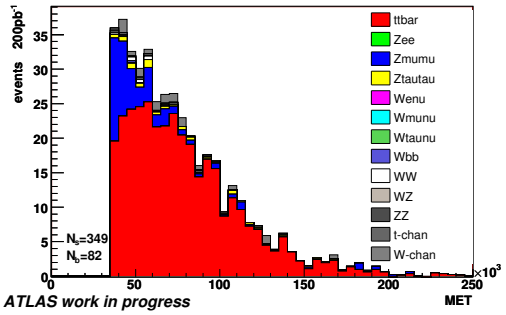

(d) Selected E_tmiss distribution.

Figure 4.8: Jet and E_tmiss distributions for the di-muonic selection.

4.4.3 Mixed Channel

Figures 4.9, 4.10 and 4.11 show the kinematic distributions for the $e\mu$-channel. The results of mixed analysis are summarised in table 4.15:

ξ_1	$\sigma_{t\bar{t},meas.}(pb)$	ξ_2	$\sigma_{t\bar{t},calc.}(pb)$
0.88±0.03	3.7±0.8	0.0170±0.0002	217.1±45.2

Table 4.15: Results of mixed analysis for $\mathcal{L} = 200\mathrm{pb}^{-1}$. Quoted errors are statistical.

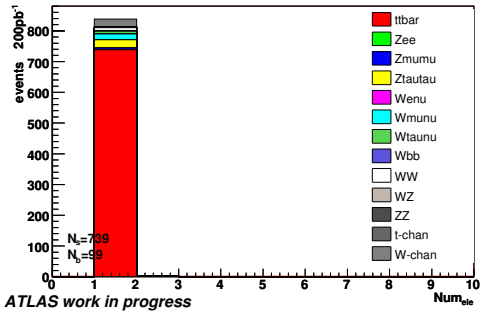

(a) Selected Electron number distribution.

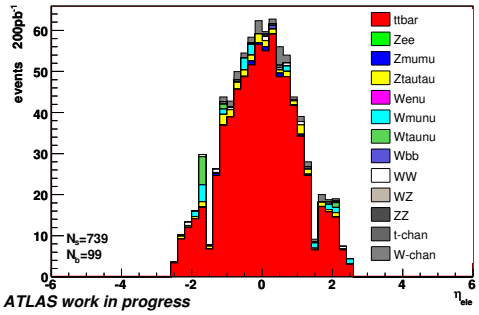

(b) Selected Electron η distribution.

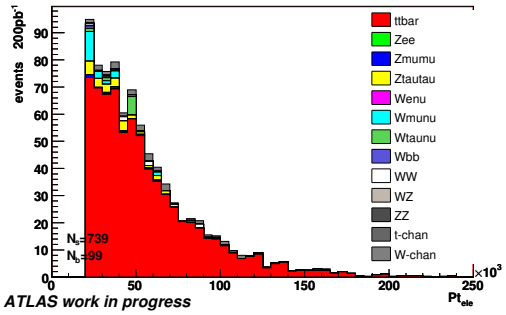

(c) Selected Electron $\mathrm{p_T}$ distribution.

Figure 4.9: Electron distributions for the di-mixed selection.

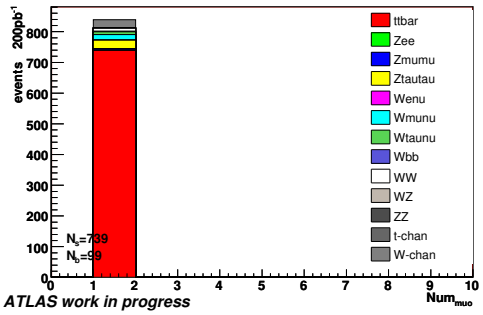

(a) Selected Muon number distribution.

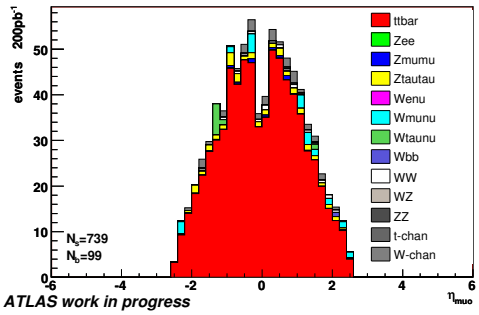

(b) Selected Muon η distribution.

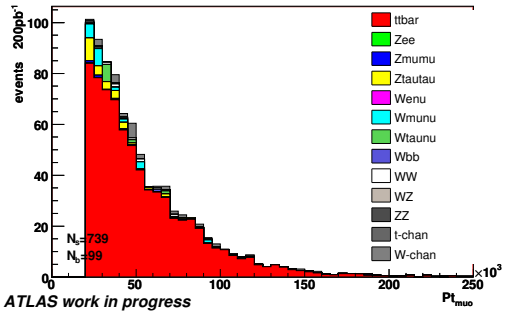

(c) Selected Muon $\mathrm{p_T}$ distribution.

Figure 4.10: Muon distributions for the di-mixed selection.

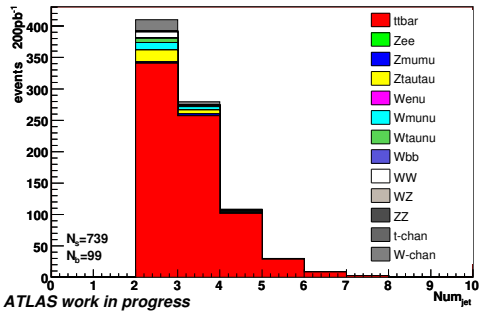

(a) Selected Jet number distribution.

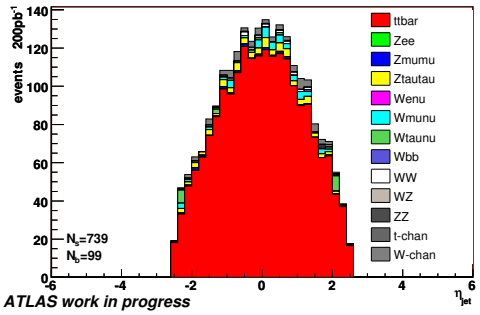

(b) Selected Jet η distribution.

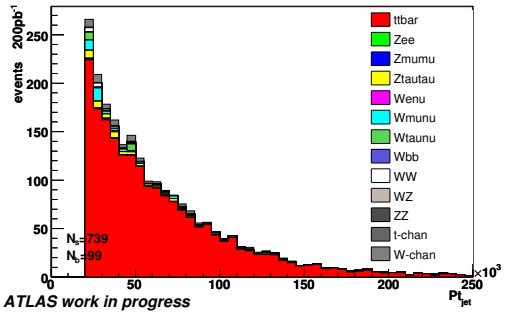

(c) Selected Jet $\mathrm{p_T}$ distribution.

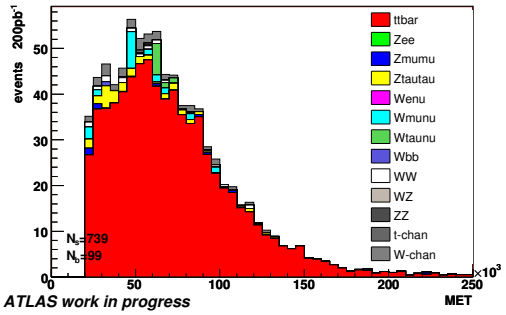

(d) Selected $E_t miss$ distribution.

Figure 4.11: Jet and $E_t miss$ distributions for the di-mixed selection.

4.4.4 Combined $t\bar{t}$ Cross-section Measurement

The result of event and object selection in each of the fully-leptonic channels is consistent with [3]. The combined results of di-lepton analysis are summarised in 4.4.4:

ξ_1	$\sigma_{t\bar{t},meas.}(pb)$	ξ_2	$\sigma_{t\bar{t},calc.}(pb)$
0.85±0.02	6.6±1.3	0.030±0.003	217.1±44.2

Table 4.16: Combined results of di-lepton analysis for $\mathcal{L} = 200\mathrm{pb}^{-1}$. Quoted errors are statistical.

In each case the $\sigma_{t\bar{t},calc.}(pb) = 217.06$ is found, proving the closure of the analytic technique.

4.5 Systematic Uncertainties

Systematic uncertainties may be understood by contrast to statistical (or random) errors. Unlike random errors, which have varied effects on an observed value over consecutive measurements, systematic errors may result in a constant or proportional bias upon iterated observations. Hence the effect of these uncertainties are evaluated by varying experimental techniques or assumptions used in calculation to assess the specific effect of each variable.

In ascertaining an experimental cross-section for fully leptonic $t\bar{t}$ events there are several possible sources of systematic error. Each source is evaluated independently, though several may be correlated to some extent. A quantitative estimate of the uncertainty on the calculated cross-section resulting from the uncertainty of a given source is obtained by varying the appropriate parameter of the calculation, within the limits of its uncertainty. Hence, the consequent change in cross-section value is the estimated uncertainty on the measured cross-section due to the source.

The following equation is used to recalculate the cross-section for each modified parameter, equation 4.6.

$$\sigma_{t\bar{t}} = \frac{N_{obs} - N_{bgd}}{A \times \xi_1 \times \mathcal{L}}, \tag{4.6}$$

where $\sigma_{t\bar{t}}$ is the fully leptonic $t\bar{t}$ cross-section, $N_{obs} - N_{bgd}$ is the number of observed signal events (with N_{bgd} the sum of data-driven background estimates, N_{bgd}^{dd}, and Monte Carlo estimates N_{bgd}^{MC}) A is the acceptance of the detector, ξ_1 is the selection efficiency and $\mathcal{L}$ is the sample luminosity.

Table 4.12 shows a list sources of systematic error. To give a feel for the relative size of the uncertainty, the ratio $\Delta\sigma\ /\sigma$ is calculated using the selected signal and background events. The following section describes each source.

$\Delta\sigma/\sigma$ (%)	ee channel	$\mu\mu$ channel	$e\mu$ channel	combined
Stat only	-7.5 / 7.8	-6.0 / 6.2	-4.0 / 4.1	-3.1 / 3.1
Luminosity	-17.3 / 26.3	-17.4 / 26.2	-17.4 / 26.2	-17.4 / 26.2
Electron Efficiency	-4.5 / 5.0	0.0 / 0.0	-2.2 / 2.4	-1.9 / 1.9
Muon Efficiency	0.0 / 0.0	-4.6 / 5.2	-2.1 / 2.2	-2.2 / 2.3
Lepton Energy Scale	-0.3 / 1.6	-2.4 / 2.0	-0.5 / 0.5	-0.8 / 0.8
Jet Energy Scale	-3.4 / 3.2	-3.0 / 4.5	-2.5 / 2.5	-2.8 / 3.0
PDF	-2.1 / 2.3	-1.4 / 1.6	-1.6 / 1.8	-1.7 / 1.8
ISR FSR	-4.0 / 4.2	-3.6 / 3.7	-3.5 / 3.5	-3.6 / 3.7
Signal Generator	-4.7 / 5.4	-4.6 / 5.4	-4.7 / 5.3	-4.7 / 5.3
Cross-Sections	-0.3 / 0.3	-0.3 / 0.3	-0.3 / 0.3	-0.3 / 0.3
Drell Yan	-1.4 / 1.3	-2.2 / 2.2	-0.5 / 0.5	-0.8 / 0.9
Fake Rate	-9.7 / 9.5	-1.1 / 1.1	-6.2 / 6.2	-4.0 / 4.0

Figure 4.12: Sources of systematic uncertainty, taken from [3]. Errors quoted are asymmetric "negative/positive".

4.5.1 Relevant Uncertainties

The following remarks are based on [3] and [36].

Luminosity:

Conservative estimates of the expected error on the luminosity in the first period of data taking (up to $\sim 200\text{pb}^{-1}$) are around 20%. As data taking continues this is expected to decrease to an accuracy of around 10%. The luminosity obviously affects the cross-section measurement directly by its presence in the denominator of equation 4.6 but also through any MC based background estimates.

Trigger and Identification:

An uncertainty of 1% is expected on both the lepton trigger and I.D. efficiencies with a high level of correlation between the two. Uncertainties are expected to arise when estimating efficiencies from data due to the limited sample size and measurement systematics. Full correlation between both sources is conservatively estimated.

Missing Transverse Energy (MET):

The uncertainty on MET is more difficult to estimate for a couple of reasons. Firstly, the effect of the jet energy scale uncertainties on the MET uncertainty is not 100% correlated since the calibration of MET reconstruction takes place between levels of jet reconstruction and calibration (more precisely between the cell-level calibration and the jet-level calibration). This is somewhat mitigated by using an object based MET algorithm with object level corrections to improve measurement. An additional factor in MET errors comes from pile-up and underlying event effects which contribute through cells which are not clustered into jets but are included in the MET calculation. Since neither of these contributions is well understood a quantified estimation of MET uncertainty is not yet possible and so not included.

Lepton Energy Scale (LES):

The LES was varied by 1% and the effect calculated using the predicted number of background events together with the selection efficiency from the LES varied events and the total number of observed events from the nominal sample. The MET was rescaled and any overlap between reconstructed jets and electron objects removed as both contribute to MET at the electro-magnetic scale.

Jet Energy Scale (JES):

The JES was assessed by varying the 4-vectors of all reconstructed objects by 10% for all signal and background samples. In addition the JES variation was double for jets with $\mid \eta \mid > 3.2$. As with the LES the effect was calculated using the prediction of the number of background events and the selection efficiency with the JES varied events along with the total number of observed events from the nominal sample. Variations in JES are more complicated than a simple rescaling of selection efficiencies. For example, in $Z \rightarrow ll$ events, changing the JES down leads to an increase in MET, which can increase selection. In addition, an increase in JES increases the $\mathrm{p_T}$ distribution of the jets, which also improves selection. The interplay between competing factors mean JES variations must be understood on a process by process level.

Parton Distribution Functions (PDFs):

A re-weighting process is used to evaluate the effect of PDF on acceptance and hence the measured cross-section. This involves calculating the probability of an event with hard partons of flavors f_1 and f_2 and momentum fractions x_1 and x_2 with momentum transfer Q using two different PDF sets (or variation of PDF error sets). A weight is then defined using the ratio of the two. The weight is used in the production of histograms to scale the contribution of each event such that the resulting histograms of summed re-weighted events is consistent with the new PDFs. The greatest discrepancy between results is taken to be the bounds of the uncertainty from PDFs.

Initial State / Final State Radiation (ISR/FSR):

Here the relevant parameters (Λ_{QCD} and $\mathrm{p_T}$) of a signal shower model were varied in such a way so as to maximise and minimise the measured top mass. The signal acceptance was then calculated with direct impact on the measured cross-section. Although the mass of the top does not have a direct impact on the cross-section measurement it is strongly correlated with the jet multiplicity, which in turn affects the selection efficiency. See chapter 5 for a more detailed investigation of this source of systematic uncertainty.

Monte Carlo (MC) model:

The predictions from different MC generators were compared in order to assess any model dependencies. The largest discrepancies in selection due to disagreement in gener-

ation rates or kinematic distributions are quoted as the resulting uncertainty on the cross-section.

Theoretical cross-section:

In cases where it is not possible to isolate a control sample of background from data MC studies must be relied upon to investigate background rates and shapes. Comparison of MC models, as mentioned previously, can be used to investigate shape variations; however, rate variations require separate investigation. Studies suggest that MC production for di-boson channels should be varied by 5% and Wt single top production by 8%. For a conservative estimate of the uncertainty due to these backgrounds, the processes are varied in a fully correlated manner.

Drell-Yann (DY) background:

Both the $\not\!\!E_T$ and Z-mass veto are varied (individually and in tandem) to assess the DY background. Since DY processes only produce same flavor leptons, this background results in a systematic uncertainty of 15% for ee and $\mu\mu$ channels only, for $200\mathrm{pb}^{-1}$.

Jet Misidentification:

This systematic is based on calculating the cross-section variation between the fake rate (jets misidentified as leptons) in two different control regions (low-$\not\!\!E_T$ and high-$\not\!\!E_T$ regions) and then conservatively extrapolating twice the difference to the signal region. Also conservatively, the uncertainties of jet misidentification are estimated to be 100% for early data ($\leq 50\mathrm{pb}^{-1}$) for both electrons and muons and $\sim 50\%$ for muons and 100% from electrons up to $200\mathrm{pb}^{-1}$.

Pile-up:

Assuming optimum conditions in the early data taking period ($\mathcal{L} = 10^{32} cm^{-2} s^{-1}$ and bunch spacings of $450\mathrm{ns}$) the average number of proton-proton collisions expected per bunch crossing is four. Studies suggest pile-up has several distinct effects. Firstly, a decrease in acceptance for opposite-sign lepton selection in both $\mu\mu$ and $e\mu$ truth channels. This is an effect of the cavern background on the muon spectrometer. Another effect is increased isolation energy from all leptons, which decreases the lepton selection. However, this is not seen in the electron selection due to an increased fake rate from increased jet multiplicity, which increases the jet acceptance. An increased electron fake rate is also seen in the trigger acceptance. The overall effect of the pile-up cancels such that the combined acceptance across channels remains unchanged. In contrast there are some significant increases in background acceptance, in the Z-backgrounds case the selection is tripled. This effect can be removed at the expense of selection efficiency if an increased $\mathrm{p_T}$-cut is applied.

4.6 Pseudo-analysis Conclusion

An analysis of centrally produced datasets for fully-leptonic $t\bar{t}$ signal and background simulated events was performed. The selection was based on the three decay channels of the $t\bar{t}$ system. The resulting signal and background yields after selection were found and the corresponding kinematic distributions plotted. These are consistent with the results of [3].

From the selected events a calculation of the non-hadronic $t\bar{t}$ cross-section was made and the result found to be consistent with the quoted value. Table 4.6 shows the calculated non-hadronic $t\bar{t}$ cross-sections with relative statistical and systematic errors.

	$\sigma_{t\bar{t},calc.}(pb)$	stat. (%)	syst.(-ve/+ve) (%)
ee	217.1	$\pm$6.4	-21.7 / 29.6
$\mu\mu$	217.1	$\pm$4.9	-19.5 / 28.1
$e\mu$	217.1	$\pm$5.6	-19.9 / 28.0
combined	217.1	$\pm$3.7	-19.3 / 27.7

Table 4.17: Results of di-lepton analysis with relative statistical and systematic (inc. luminosity) errors for $\mathcal{L} = 200\mathrm{pb}^{-1}$, from table 4.12.

Chapter 5

Top Physics ISR/FSR Systematics Study

This chapter looks into one of the sources of systematic error in more detail, namely, initial and final state radiation. This is in greater detail than the signal only study included in [35] and the signal and background study in [3] and quoted in chapter 4. For each di-leptonic $t\bar{t}$ channel an evaluation of the effects of varying the initial and final state contributions to the signal and main background are investigated. The study is based on event samples which were generated using Pythia and the ATLFAST [37] detector simulation.

5.1 Motivation

The motivation for this study was to quantify any systematic effects arising from initial and final state radiation estimates of Monte Carlo event generators used to simulate signal and background processes. This was done by generating separated event samples where the generator parameters which dictate radiative effects are varied. A set of these parameters with specific values is called a tune. Specific tunes themselves are usually well-motivated from previous experimental results. However, until predictions are compared to present data there may be ambiguity in how past results should be interpreted to generate future predictions, or disagreement between earlier observations. This allows some choice in tuning pseudo-events for novel experiments such as those at the LHC. For the signal and main background processes, as found in the previous chapter, different event samples were generated using various tunes and then analysed. The variation in results can then be used as an estimation of errors in predictions originating from initial and final state radiation uncertainty.

5.1.1 Processes

For each process a sample of $100,000$ events was generated and analysed both at the hadron level and after fast simulation using ATLFAST software to mimic detector effects. The signal

process of fully leptonic $t\bar{t}$ events was generated with the phase-space constraint that the W-bosons decay only to electron or muon final states. The background processes generated were $Z + jets$, $W + jets$, $di - W$ events. In the Z-boson case, only decays to di-electron or di-muon final states were considered. In the single W case, only decays to electronic or muonic final states were allowed. Since it was unlikely that such events would contribute to the cross-section measurement, due to the selection cuts, the events were manipulated to include pseudo-fake leptons. Finally, in the the di-boson case, electron, muon or hadronic final states are allowed for either W-boson but fully hadronic events were prohibited.

5.1.2 Tunable Parameters

Although the hard interaction is the most important factor in producing absolute jet rates (tuned by parameters controlling the parton distribution functions, k-factors and renormalisation and factorisation cut-offs) other aspects of the event can have important effects. Radiative corrections are important in simulating jet rate shapes, i.e. jets produced over some kinematic range. Further effects can come from the perturbative/non-perturbative interface where models and calculations attempt to describe the semi-hard momentum space, and hadronisation. This study focuses on radiative contributions to event signatures. Parameters controlling this include shower renormalisation scale, affecting the number of partons produced, the parton shower scale, affecting the kinematics of the partons produced, coherence effects, altering multi-parton correlations, and energy-momentum conservation. Also important is the "primordial" region, between the λ_{QCD} scale and the perturbative calculations for initial state radiation, where the transverse energy of initial state partons is modelled. All of these tune variables are QCD parameters, hence there was no explicit change of parameter to vary electro-weak effects.

5.1.3 Tunes

Pseudo-events for each process were generated using Pythia [38] version 6.4.20 for 10 TeV $p\bar{p}$ collisions using ATLAS standard parameters. The initial and final state parameters were varied using the Perugia[39] group of tunes. Perugia-0 (P_0) was used as the benchmark tune. A harder variation (P_{hard}) has higher perturbative activity but less non-perturbative particle production. It also has a slightly larger phase-space for ISR and FSR, with relatively high values of FSR and harder hadronisation. This is off-set by less primordial k_t, higher IR cut-off for MPIs and more color reconnections. A softer variation was also used (P_{soft}), with a comparatively lower perturbative activity but more non-perturbative particle production. It also has a slightly smaller phase-space for ISR and FSR, with lower values for FSR and softer hadronisation. This is off-set by a sharper proton mass distribution, lower IR cut-off

for MPI, more active BR, and fewer color reconnections. Table 5.1 shows the Pythia code for each tune.

Perugia tune	P_0	P_{hard}	P_{soft}
Tune code	320	321	322

Table 5.1: Perugia tunes used in ISR study and corresponding code.

5.2 Signal Effects of Tunes

The effects of variation in tune are shown for the signal process below in figures 5.1 to 5.5 and table 5.3. These include the top decay chain at hadron level and the fast simulated event objects and selection.

5.2.1 Signal ISR chain

For heavy particles such as top quarks the decay chain after the initial hard scatter tends to wash-out much of the parameter dependence of the production conditions. Figure 5.1 shows the effect of varying the initial state radiation parameters on the decay chain particles as a function of $\mathrm{p_T}$ at the hadron-level, from the $t\bar{t}$-system to the leptons from the following W-boson decays. It shows how the divergences between tunes on the $t\bar{t}$-system, especially in the high $\mathrm{p_T}$ region is soon lost through subsequent decays. Hence, the final state particles (b-quarks and leptons) show little divergence between tunes.

5.2.2 Fast Simulated Event Objects

The event and object selection were chosen to follow closely the parameters used in the previous chapter. ATLAS Cone algorithm with radius $R = 0.4$ was used for jet construction, see 3.2.3.4. Table 5.2 shows the cuts used for object selection. No matching between hadron-level and simulated objects was required. Event selection for each channel was based on two oppositely charged leptons with two or more jets. A $E_{\mathrm{T}}^{\mathrm{miss}}$ requirement of $35GeV$ for same flavor channels and $20GeV$ for the mixed channels was also used. And an invariant mass veto of $86GeV < m_{inv} < 96GeV$ for the same flavor channels was implemented to cut background contamination from Z events. No electron quality cuts could be added using fast simulation software.

5.2.2.1 Hadron-level partons to Simulated Jets

Figures 5.2 and 5.3 show the multiplicity and $\mathrm{p_T}$ distributions for selected hadron-level particles and ATLFAST jets, respectively. There is a change in shape and relative order of the

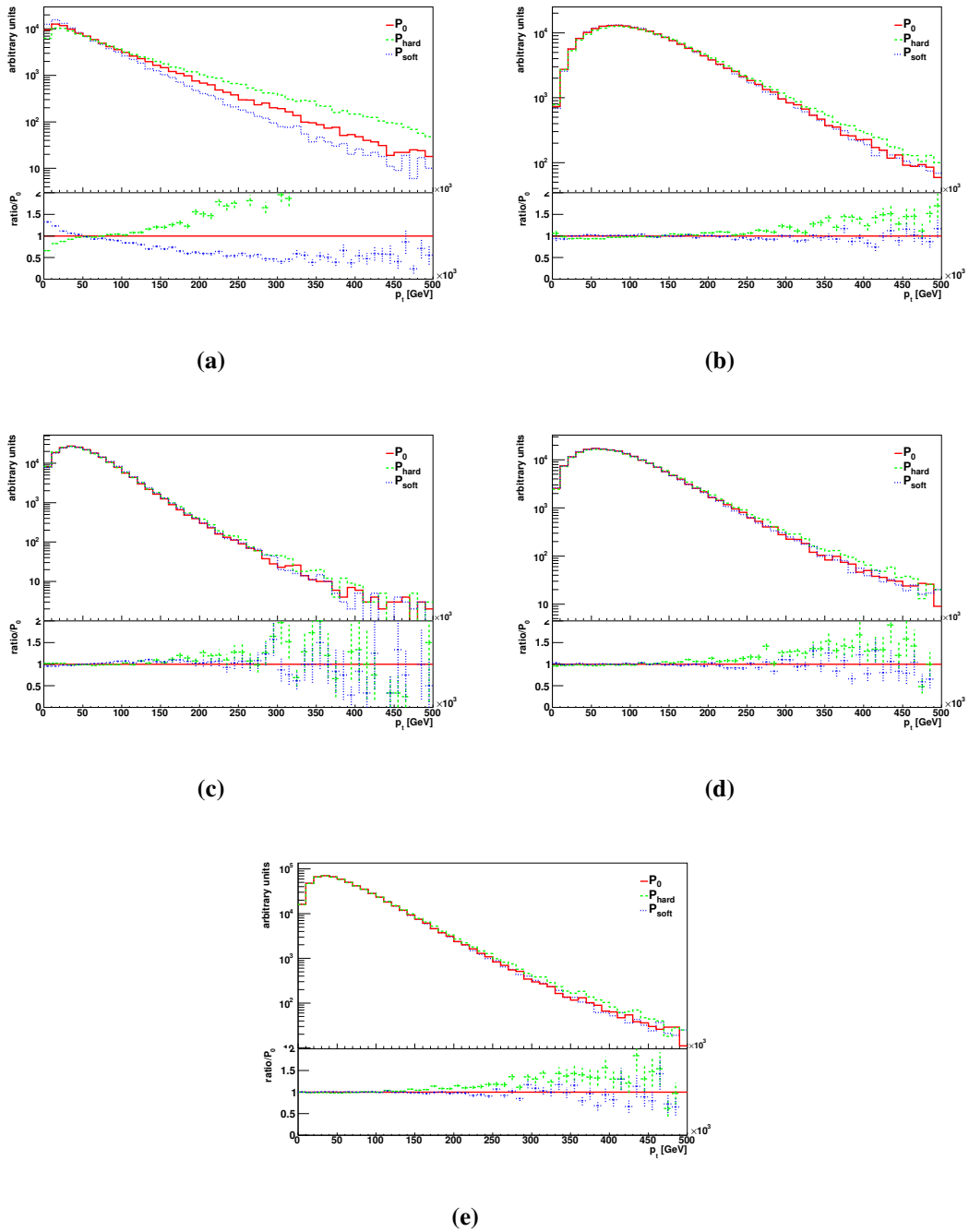

Figure 5.1: Hadron-level $\mathrm{p_T}$-spectra of a)$t\bar{t}$-system, b)top quarks, c)b-quarks, d)W-bosons and e)leptons from the top decay chain for default, soft and hard Perugia tunes (see table 5.1).

multiplicity distribution once the detector effects and jet algorithm have been applied to the generated particles. At the hadron-level the P_{soft} tune has the highest multiplicity events but the particles produced have lower $\mathrm{p_T}$. P_0 and P_{hard} have a similar lower multiplicity distribution than P_{soft} but diverge in $\mathrm{p_T}$ where P_{hard} is unsurprisingly harder. When the material simulation is applied to these hadrons many of the lower $\mathrm{p_T}$ particles will be lost.

object	p_T	$\|\eta\|$
electrons	> 20 GeV	$0 < \|\eta\| < 1.37$ and $1.52 < \|\eta\| < 2.47$
muon	> 20 GeV	< 2.5
jets	> 20 GeV	< 2.5

Table 5.2: Kinematic cuts used in reconstructed object selection.

A further complication is the application of the jet algorithm, which will be seeded on the hardest particles and neglect particles outside of the radius. The jet will then be discarded if the summed p_T is below the cut-off. These effects combined lead to a relatively reduced multiplicity distribution for P_{soft}, while P_{hard} is relatively enhanced. The order of p_T distribution remains unchanged, however the divergences are exacerbated by the material and jet algorithm effects.

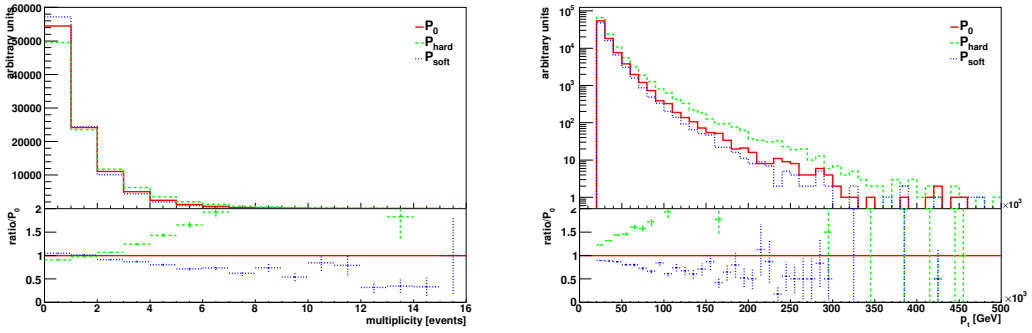

Figure 5.2: Multiplicity (left) and p_T (right) distributions of hadron-level final state hadrons for various Pythia tunes.

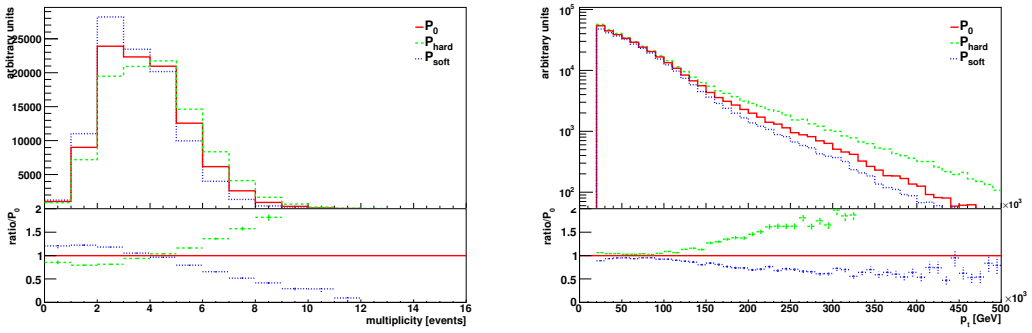

Figure 5.3: Multiplicity (left) and p_T (right) distributions of ATLFAST simulated ATLAS cone jets (R=0.4) for various Pythia tunes.

5.2.2.2 Simulated Leptons

Figures 5.4 and 5.5 show the multiplicity and p_T distributions for selected ATLFAST simulated electrons and muons, respectively. There is little difference in the distributions for each Perugia variation which is expected since the main differences between the tunes concerned

the QCD parameters and not electro-weak decay or radiation. Hence it is concluded that the main source of any discrepancies between tunes is QCD ISR parameters.

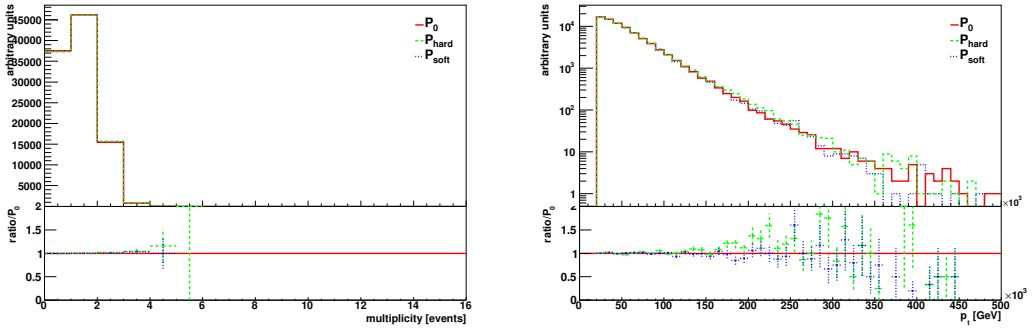

Figure 5.4: Multiplicity (left) and $\mathrm{p_T}$ (right) distributions of ATLFAST simulated ATLAS electrons for various Pythia tunes.

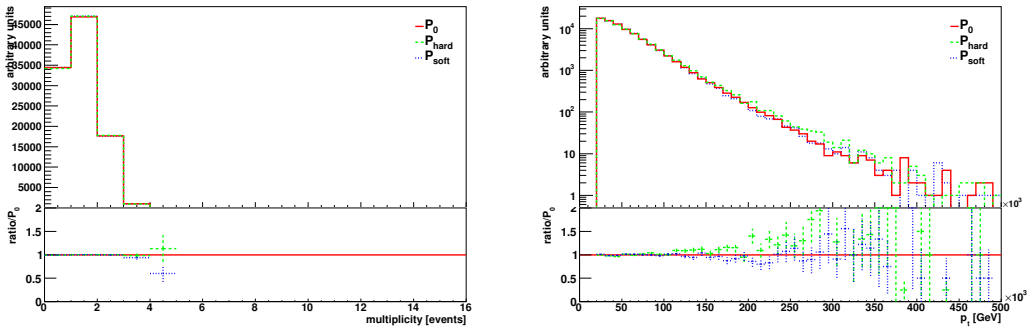

Figure 5.5: Multiplicity (left) and $\mathrm{p_T}$ (right) distributions of ATLFAST simulated ATLAS muons for various Pythia tunes.

5.2.2.3 Selected Signal Events

Table 5.3 shows the results of each channel's selection for the signal process for the P_0 along with the relative discrepancy of P_{soft} and P_{hard} tunes. Similar results are found to the fully leptonic $t\bar{t}$ study in chapter 4, with similar trends between channels, e.g. the di-electron channel is slightly less efficient than the muon. The effect of the harder initial state radiation is to enhance the selection in each channel, with the greatest increase in the di-electron channel. The softer tune diminishes the selection in each channel, with the greatest decrease in the muon channel.

5.3 Background Effects of Tunes

For each analysis channel the main background, as found in the previous chapter, was regenerated with the various Pythia tunes. For the di-electron channel this was $W + jets$ events,

tune	di-electron	di-muon	mixed
P_0	9390	10975	23631
P_{hard}	$+5.7 \pm 1.1\%$	$+3.2 \pm 1.0\%$	$+3.2 \pm 0.7\%$
P_{soft}	$-3.5 \pm 1.0\%$	$-4.2 \pm 0.9\%$	$-2.7 \pm 0.6\%$

Table 5.3: Selected signal fully leptonic di-top events for each fully leptonic analysis channel for Perugia-0 Pythia tune and the relative discrepancy of alternative tunes with statistical error. Each sample had $100,000$ events (i.e. $25,000$ ee, $25,000$ $\mu\mu$ and $50,000$ $e\mu$).

the muon channel $Z + jets$ event and di-W boson events for the mixed channel. Similar reconstructed jet and lepton trends were found between tunes for background samples as for signal, hence these are not repeated in the following sections. The only exception to this is the reconstructed electron distribution of the $W + jets$ sample where jets are included, see below. This introduces a QCD dependence to the distribution which causes further divergence between tunes.

5.3.1 W+jets

To simulate realistic detector effects which would contribute to the selection of $W + jets$ events fake electrons were added to events. Though these are included in the ATLFAST simulation to a small extent this was considered insufficient to replicate the effect in real data so jet misidentification was artificially enhanced in the sample. This was done by recording jets, chosen at random, already selected in the event as electrons. This guaranteed that one jet was misidentified in each event, a rate far higher than expected in real data. This factor can be normalised to a more realistic efficiency later.

Table 5.4 shows the selected events in the three analysis channels for P_0 tune and the relative discrepancy of the P_{hard} and P_{soft} tunes. No events are selected in the di-muon channel as there is only one W-boson to decay leptonically such that there can be at most one muon in an event. Since there is no mechanism for any object to fake a muon included in this study and a fake electron is artificially added to each event, events where the W decays muonically are found in the mixed channel. As muons are better reconstructed than electrons, the mixed channel has more events selected reflecting the superior performance of the muon filter.

The effect of the harder tune is to increase selection in the two channels, with the greatest effect in the di-electron channel. The softer tune has a greater effect on the two channels with a selection decrease of more than 25% for both. These variances must be convoluted by a realistic electron fake rate to fully appreciate the effect on $W + jets$ selection.

tune	di-electron	di-muon	mixed
P_0	629	–	947
P_{hard}	$+9.7 \pm 4.2\%$	–	$+3.5 \pm 3.3\%$
P_{soft}	$-25.6 \pm 3.4\%$	–	$-28.9 \pm 2.7\%$

Table 5.4: Selected background W+jets events for each fully leptonic analysis channel for Perugia-0 Pythia tune and the relative discrepancy of alternative tunes with statistical error. Each sample had $100,000$ events (i.e. $50,000$ $W \to e\nu$ and $50,000$ $W \to \mu\nu$). Note the di-muon channel is unpopulated, see text.

5.3.2 Z+jets

As the Z could decay to two electrons or muons only the same flavor channels are predominately populated and with a similar number of events. A very small proportion of events is found in the mixed channel due to fake electrons inherent in ATLFAST. The effect of the harder tune is to increase selection in both same flavor channels, with the greatest effect in the di-electron channel. In contrast the softer tune reduces selection in both same flavor channels, but to a much greater extent than the increase of P_{hard}. For both P_{hard} and P_{soft} the variation in the mixed flavor channel is too small to draw any meaningful conclusion.

tune	di-electron	di-muon	mixed
P_0	463	453	3
P_{hard}	$+10.6 \pm 4.9\%$	$+6.4 \pm 4.8\%$	$+100 \pm 81.6\%$
P_{soft}	$-29.2 \pm 3.9\%$	$-23.8 \pm 4.1\%$	$+33.3 \pm 66.7\%$

Table 5.5: Selected background Z+jets events for each fully leptonic analysis channel for Perugia-0 Pythia tune and the relative discrepancy of alternative tunes with statistical error. Each sample had $100,000$ events (i.e. $50,000$ $Z \to ee$ and $50,000$ $Z \to \mu\mu$).

5.3.3 di-W boson

With two W-bosons decaying electronically, muonically and hadronically all three channels are populated. The relative trends of the channels is similar to the signal case though the absolute numbers are much reduced, $25 - 29$ times smaller. The di-electron channel has fewer events than the di-muon, though the same number of events would be simulated, and the mixed channel is roughly double the leptonic channels. The effect of the harder tune is to increase selection across all channels, with the greatest increase in channels including an electron. The softer tune shows the greatest variation in the di-muon channel but in general has substantial reduction in selection across all channels.

tune	di-election	di-muon	mixed
P_0	323	451	913
P_{hard}	$+27.2 \pm 6.3\%$	$+7.1 \pm 4.9\%$	$+21.5 \pm 3.6\%$
P_{soft}	$-17.0 \pm 5.1\%$	$-22.8 \pm 4.1\%$	$-15.3 \pm 3.0\%$

Table 5.6: Selected background di-W boson events for each fully leptonic analysis channel for Perugia-0 Pythia tune and the relative discrepancy of alternative tunes with statistical error. Each sample had $100,000$ events (i.e. $25,000$ ee, $25,000$ $\mu\mu$ and $50,000$ $e\mu$).

5.4 Conclusion

The results of the Monte Carlo study of ISR/FSR shows the effect on signal selection, where the tune variance, at most 5%, is relatively small compared to the backgrounds. The effect of the change in shower parameters is considerable in each of the backgrounds. In the single boson cases, $W + jets$ and $Z + jets$, the greatest discrepancy is found when the radiative processes are softened. In contrast the harder tune has the greatest divergence in the di-boson case. Tables 5.7 and 5.8 show the resulting signal, background and various evaluations resulting from variations to the selected signal and background events, based on the P_{hard} and P_{soft} showers, respectively. A jet rejection factor of $R = 2184$ was used to scale the $W + jets$ results to a sensible fake rate, based on the *medium* electron definition, found in [35].

	S (ΔS)	B (ΔB)	S/B ($\Delta(S/B)$)
ee	241.1±5.9 (+5.7%)	47.3±16.7 (+4.4%)	5.1±1.8 (+2.0%)
$\mu\mu$	361.0±7.4 (+3.2%)	86.1±14.8 (+4.5%)	4.2±0.7 (-0.2%)
$e\mu$	763.2±10.9 (+3.2%)	107.3±40.0 (+7.8%)	7.1±2.7 (-3.8%)
combined	1365.3±14.4 (+3.6%)	242.6±45.9 (+6.7%)	5.6±1.1 (-3.0%)

Table 5.7: Signal, background and S/B using adjustments to the signal and background selection based on P_{hard} results. Numbers in brackets are the percentage change from the results of chapter 4. Quoted errors are statistical.

	S (ΔS)	B (ΔB)	S/B
ee	220.1±5.7 (-3.5%)	41.1±16.6 (-9.3%)	5.4±2.2 (+7.1%)
$\mu\mu$	335.1±7.2 (-4.2%)	69.0±14.5 (-16.3%)	4.9±1.0 (+15.7%)
$e\mu$	719.6±10.4 (-2.7%)	96.1±33.9 (-3.4%)	7.5±2.6 (+1.2%)
combined	1274.8±13.8 (-3.2%)	206.2±40.4 (-9.3%)	6.2±1.2 (+6.6%)

Table 5.8: Signal, background and S/B using adjustments to the signal and background selection based on P_{soft} results. Numbers in brackets are the percentage change from the results of chapter 4. Quoted errors are statistical.

Table 5.9 shows the systematic uncertainty on the measured fully leptonic $t\bar{t}$ cross-sections based on eqn. 4.6 in chapter 4. The greatest variation is found in the di-electron

channel. These are of the same order as the uncertainties of 4% quoted in chapter 4.

	$\sigma_{t\bar{t},meas.}(pb)$	$\Delta\sigma^{P_{hard}}_{t\bar{t},meas.}/\sigma_{t\bar{t},meas.}$	$\Delta\sigma^{P_{soft}}_{t\bar{t},meas.}/\sigma_{t\bar{t},meas.}$
ee	1.1±0.2	+6.1%	-2.0%
$\mu\mu$	1.7±0.4	+2.8%	-0.5%
$e\mu$	3.7±0.8	+2.6%	-2.5%
combined	6.6±1.3	+3.0%	-2.0%

Table 5.9: Systematic uncertainties on measured fully leptonic $t\bar{t}$ cross-sections for variations in ISR/FSR shower models based on eqn.4.6 used in chapter 4.

Table 5.10 shows the default systematic error on the calculated non-hadronic $t\bar{t}$ cross-section, from the chapter 4, along with the recalculated systematic errors on P_{hard} and P_{soft} tunes, for each channel. The effect of these adjustments in systematic uncertainty include ISR/FSR effects to both signal and background selection. Almost all of the effects arising from the variations in shower model lead to decrease in the systematics, the exception being the positive uncertainty in the di-electron channel. This is due to wider variation of tunable parameters studied and the interplay between the signal and background effects, neglected in the systematics study of chapter 4.

	default total sys.(inc.$\mathcal{L}$) (%)	new total syst. (inc.$\mathcal{L}$) (%)
ee	-13.1/13.5 (-21.7/29.6)	-12.6/14.2 (-21.4/29.9)
$\mu\mu$	-8.8/10.1 (-19.5/28.1)	-8.1/9.8 (-19.2/28.0)
$e\mu$	-9.6/10.0 (-19.9/28.0)	-9.2/9.7 (-19.7/27.9)
combined	-8.5/9.0 (-19.3/27.7)	-7.9/8.7 (-19.1/27.6)

Table 5.10: Previous and revised total systematic uncertainties on measured fully leptonic $t\bar{t}$ cross-sections for variations in ISR and FSR shower models based on eqn.4.6 used in chapter 4. For the new systematic estimate all other sources of uncertainty other than ISR and FSR are taken from table 4.12.

Chapter 6

FB-correlation $900\ \mathrm{GeV}$ Study

In this chapter the topic of investigation changes from the hard physics of di-top production to the lower energy ("soft") regime of minimum bias. The main components of minimum bias events are described from the point of view of event simulation. This is useful to distinguish the various theoretical sources of particle production in soft events. A Pythia based comparison of various generator tunings and production sources is made using a selection of observables at the hadron-level for simulated $900\ \mathrm{GeV}$ centre-of-mass proton-proton collisions. In particular, one observable is used to isolate the sources of particle production, a trait much desired by event generator developers.

The work of this chapter comes from a collaboration between the author and Peter Skands while on a MCnet studentship[1]. This chapter reiterates, with some extra detail, the work in [40].

Section 6.2, briefly introduces the Monte Carlo models used, and comments on the various sources of particle production. The very basic selection bias that was used in the analysis is described in section 6.3, to mimic a "minimal" minimum-bias selection. In section 6.4, the reference models are compared on some of the typical minimum-bias plots. In section 6.5, a more detailed study of forward-backward correlations, first inclusive, then with $\mathrm{p_T}$ dependence and ϕ dependence, is presented. Lastly, section 6.6 discusses the transverse thrust and the transverse minor of the selected models.

6.1 Introduction

Current Monte Carlo (MC) event generators for high energy collider experiments involve physics models which are primarily based upon results from the previous generation of experiments. In the case of low-energy data this includes results from UA5, LEP and underly-

[1]This research project has been supported by a Marie Curie Early Stage Research Training Studentship of the European Community's Sixth Framework Programme under contract number (MRTN-CT-2006-035606-MCnet).

ing event data from the Tevatron. Though invaluable, these datasets and the corresponding tunes are becoming outmoded by the current generation of high energy experiments, where the extrapolation of previous results to the high energies and complex collision environments incur significant uncertainties. Therefore the data set must be updated and the physics models retuned where appropriate. Hence studies of "soft" physics ensure the validity of generator tunes which are used ubiquitously over a continually expanding range of energies and intensities.

The Large Hadron Collider (LHC) offers a rich cornucopia of opportunities to test and expand the tunable dataset. The low-$\mathrm{p_T}$ results of minimum bias studies are a trial of the consistency of each generator model simulation with experiment. At higher energies, underlying event studies probe particle production mechanisms in the new energy frontier. For minimum bias (MB), event generation tunes of particle production mechanisms are of primary importance. Particle multiplicity (n-flow) and transverse momentum ($\mathrm{p_T}$-flow) components are optimised within the constraints of current experimental results. Since there are several production mechanisms (initial-, final-state radiation, beam remnants, hard process) producing overlapping distributions, several tune parameter sets may reproduce the same experimental data. In order to break this accord observables which are sensitive to various aspects of event generation must be identified and measured. Tests using several, mutually complementary, discriminating observables are essential to overcome model degeneracies.

6.2 Monte Carlo Models and Parameters

There are several features of generator models which may be tuned to effect the final state of events even when the choice of colliding particles and their kinematics have been set. For details on the modelling of hadron collisions incorporated in general-purpose event generators, see [41].

6.2.1 Models

The models investigated here are all based on Pythia's string fragmentation model [38]. In Pythia 6, there are two basic multiple parton interaction (MPI) frameworks available, here referred to as "old" [42] and "new" [43, 44]. (The latter is similar to the modelling in Pythia 8.) Briefly stated, the main differences between the old and new models are:

- **Old:** virtuality-ordered parton showers, no showers off the additional MPI, and a relatively simple description of the fragmentation of the beam remnants in which the baryon number is carried by the remnant.

- **New:** transverse-momentum-ordered parton showers, including showers off the additional MPI, and a more sophisticated treatment of the beam remnant, in which "string junctions" [45] carry the beam baryon number.

A selection of tunes using the "old" shower model (DW, ACR and Q20), which is virtuality-ordered, and "new" shower model (P0 and PT0), which is ordered by transverse-momentum, have been chosen. The ACR tune is based on Tune A, which was developed at the Tevatron, with a modified color-reconnection model such that it produces some similar results to the new shower model within the framework of the old model. It is included to make it possible to isolate whether specific features of either shower model. Tunes Q20 and PT0 come from the Professor collaboration [46] which include more recent LEP results, as does P0. All tunes were run with Pythia version 6.4.21. Table 6.1 show the tunes used along with the three digit code used to retrieve the tune parameters in Pythia with the call to `PYTUNE`.

Parameter	DW	ACR	Q20	P0	PT0
PYTUNE	103	107	129	320	329

Table 6.1: Pythia tunes and three digit Pythia code.

6.2.2 Model Parameters

Parameters controlling the hard aspect of events affect the absolute jet rates. Jet rate shapes are determined by radiation parameters. Further adjustments to the shape are made from the multi-parton interactions. For Pythia, parameters controlling the string attributes determine the final state hadron properties in the event, such as longitudinal and transverse momentum and flavor of created pairs.

In old and new shower model cases, the fundamental MPI cross sections are derived from a Sudakov-like unitarisation/resummation of perturbative QCD $2 \rightarrow 2$ scattering [42], normalised to the total inelastic non-diffractive cross-section, and regulated at low $\mathrm{p_T}$ by a smooth dampening factor. The dampening factor is interpreted as being due to color screening, and the dampening scale, $p_{\perp 0}$, represents the main tunable parameter of the model. Two other significant parameters are the assumed transverse shape of the proton (lumpy or smooth), and the strength of color reconnections (CR) in the final state, for more details see [41].

6.2.3 Sub-Process Samples

There are four minimum bias sub-processes considered: elastic scattering, single diffraction, double diffraction, low-$\mathrm{p_T}$ interactions and a mixture of each combined according to the sub-

process cross-sections. Figure 6.1 illustrates these processes and their production of particles on the $\eta - \phi$ plane. The sum of these contributions is the total hadron-hadron cross section.

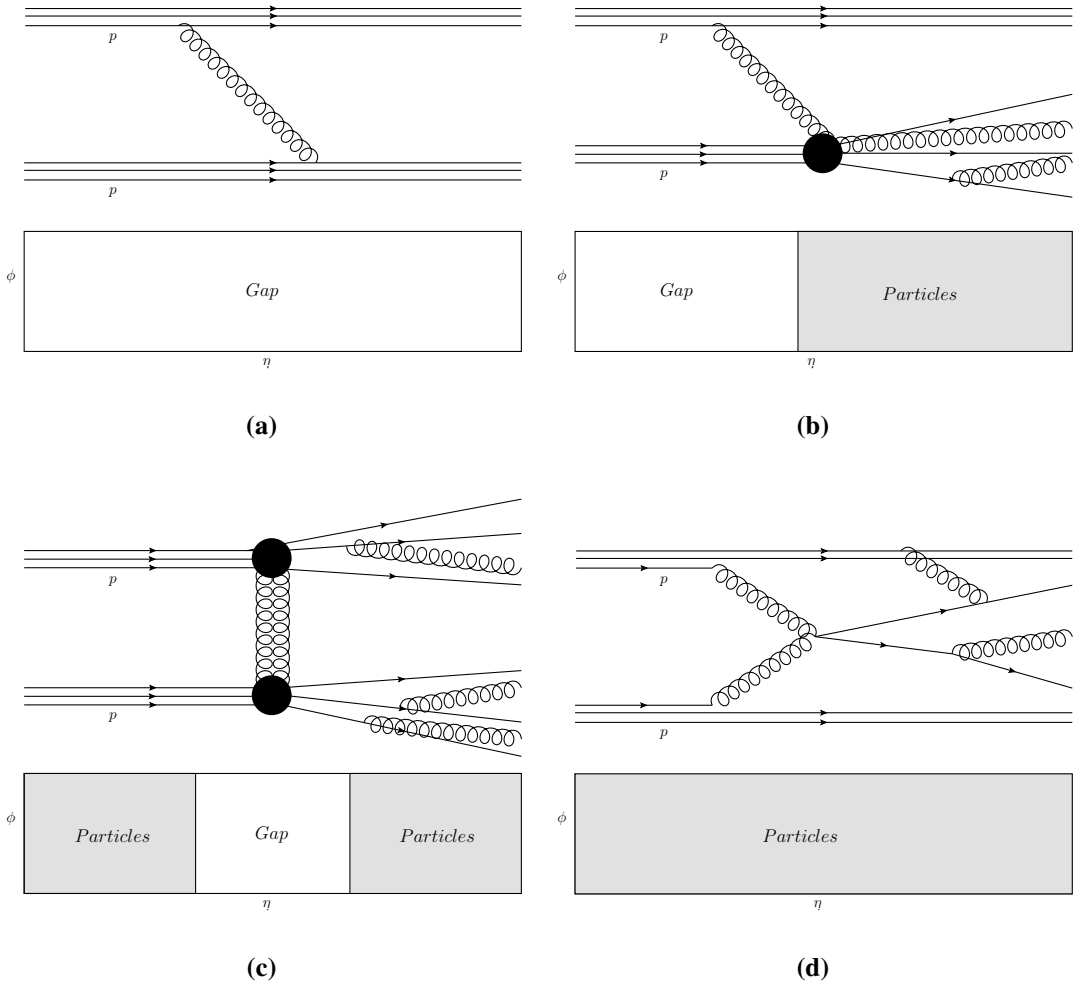

Figure 6.1: Minimum bias sub-processes: a) elastic, b) single diffractive, c) double diffractive, and d) inelastic (low-$\mathrm{p_T}$ scatterings), with illustrations of particle production on the $\eta - \phi$ plane.

The modelling of the diffractive contribution to soft-inclusive processes in Pythia 6 is more basic than the non-diffractive component. It uses parametrised cross-sections to predict the rates of single and double diffractive dissociation differentially in the mass(es) of the diffracted system(s) [47]. Each diffractively excited system is represented by a single "string" of the given mass, which is hadronised according to the Lund string fragmentation model [48, 49].

This type of diffractive modelling can be characterised as "soft" since it does not include a mechanism for hard, high-mass diffraction, such as diffractive jet production. It is included to give an idea of how the bulk of soft diffractive processes affect the distributions. It is expected that the final conclusions should not depend too crucially on the modelling of this component

as "typical" minimum-bias cuts in experiment are designed to reduce the contamination by diffractive processes.

In contrast, the modelling of inelastic, non-diffractive processes is more sophisticated and is based on a picture of multiple parton interactions (MPI). The two models available in Pythia 6 are outlined above.

Elastic scattering (fig 6.1(a)) is when the colliding protons interact but without the break up of either hadron. This process does not produce any particles at central rapidities, any reference to it is made solely for completeness. Single diffraction (SD, fig 6.1(b)) involves the break up of only one of the incoming hadrons (either proton can disintegrate). In this situation, a spread of low-$\mathrm{p_T}$ particles is expected from the disintegrated system over a limited η-region while the intact hadron continues, with modified momentum and without substantial particle production. Double diffraction (DD, fig 6.1(c)) involves the break up of both protons. Here, both systems generate significant low-$\mathrm{p_T}$ particle deposits from disintegration over η, typically with a gap between the two. Low-$\mathrm{p_T}$ or non-diffractive interaction (fig 6.1(d)) involves parton scatterings, all the way from soft to hard, with the latter mapping smoothly onto the dijet tail. Here, particle production is more localised with higher-$\mathrm{p_T}$ constituents. In this case particle production is more localised, with higher-$\mathrm{p_T}$ particles and the possibility, switched on by default, of additional perturbative activity such as parton showers and multiple parton interactions. In addition, a mixed sample of all these processes is included for comparison. The proportions of the mixture are derived from the Pythia cross-sections at 900GeV, i.e. $34.4mb$ for inelastic, $11.8mb$ for single diffractive and $6.4mb$ for double diffractive.

6.2.4 Particle Production Samples

Though many of the details involved in the calculation of particle production are not user definable, many parameters may still be varied with significant effect on the final state. The hard scatter is the core process of the event producing particles above some kinematic threshold based on the perturbative calculation up to some order N (for Pythia standalone usually N=1). Radiation from initial and final state (ISR and FSR, respectively) particles is added to the hard process. This generates particles up to a kinematic limit and is also based on a perturbative calculation. In addition, the interaction of spectator partons in the colliding hadrons, which were not involved in the initial scattering, can be added. This is known as multiple parton interaction. Models of MPI are based on perturbative $2 \rightarrow 2$ scatterings to calculate the contribution from these production mechanisms. The likelihood of MPIs occurring varies between tunes. In Pythia, radiation and MPIs can be independently activated, so it is possible to compare the contributions independently (in conjunction with the core hard process). A sample with all production mechanisms activated was also produced, this

corresponds to the low-$\mathrm{p_T}$ sample of the previous section. All variants are passed through the string fragmentation model in order to give final-state hadrons.

For all tunes, to begin there is an inclusive sample composed of the three inelastic process types, combined according to their relative cross sections, which are fixed by Pythia's default set-up [38]. Since the description of the diffractive components is quite simple, it would not make much sense to attempt to isolate individual contributions to the particle production within the two diffractive samples. However, particle production in the low-$\mathrm{p_T}$ sample receives contributions from several different algorithmic components labelled as "hard" scattering, parton showers, MPI, and remnant fragmentation, each with its own distinct behaviour. These components can be isolated ("switched off/on") and studied separately.

For each sub-process and production sample 100,000 pp collisions were generated at $\sqrt{s} = 900\ \mathrm{GeV}$, which is expected to be enough to overcome statistical fluctuations for the measurements of interest, see appendix A, and more than the data-set in [50].

6.3 Selection Procedure

Only stable charged particles within a pseudo-rapidity range of $\eta = (-5., 5.)$ are selected. This encompasses the central trackers of the ATLAS and CMS experiments, which only extend to pseudo-rapidities of ± 2.5. Stable charged particles refers to all charged particles with proper lifetimes $c\tau > 10\,\mathrm{mm}$, hence, e.g., Λ and K hadrons are stable. By default there is no $\mathrm{p_T}$-cut applied unless stated. For event selection there must be at least one charged particle in the η-range.

Table 6.2 shows the percentages of generated events passing the simple selection for each sample. The elastic sample is never selected (0%) as the scattered protons continue on "down the beam-pipe", outside the range of selection. Hence, in what follows, this sample is omitted. Of the included sub-processes, a significant fraction of SD events are rejected and about half that fraction of the events labelled DD. This is because the scattered proton(s) fail to generate particles within the fiducial region, i.e. particle trajectories are missed at high η. The double diffractive samples are more likely to be selected since they have two "chances" to produce particles in the central region. The low-$\mathrm{p_T}$ samples are selected in almost 100% of cases[2] as they generate more particles in the central η region. The mix sample has weighted effects of each sample combined according to their respective cross sections as given by Pythia . The particle production samples (hard process only, radiative, MPI and combined i.e. low-$\mathrm{p_T}$) have similar selection rates as they all include a central 'hard' interaction.

The effect of the event selection on the inclusive $\mathrm{p_T}$ distribution of the low-$\mathrm{p_T}$ samples for each tune is illustrated in figure 6.2. The top plot shows the $\mathrm{p_T}$ distribution of all generated

[2]For completeness, a few of the generated low-$\mathrm{p_T}$ events do fail, but this is below the per mille level, having produced no or only neutral particles in the central region.

tracks in black and of the selected ones in green, for the DW tune. The main effect is a reduction in the total number of accepted tracks by $10-15\%$. A secondary effect, however, is a model-dependent hardening of the spectrum. This is again found for each tune in the lower plot, which shows the ratio of selected to unselected tracks for each tune. The similarity of distributions for like-shower tunes is clear. The old shower model tunes (DW and Q20) exhibit an approximately constant value of this ratio, indicating that the shape of the $\mathrm{p_T}$ spectrum is not greatly different at high rapidities than in the central region. In contrast, the new shower tunes (P0 and PT0) exhibit a more noticeable shape, with a relatively slow curve, indicating that for these models, the spectrum of the unselected high-rapidity tracks is systematically softer than in the central region. ACR is a clear exception to the other tunes with an increase in the low-$\mathrm{p_T}$ region between the other old shower tunes and the new models followed by a further increase along with the new shower models. Hence, this suggests that the spectrum of the unselected high-rapidity tracks is related to the CR model used in the new tunes.

	mix	single	double	low-$\mathrm{p_T}$	hard	rad	MPI
DW	73%	70%	86%	100%	100%	100%	100%
ACR	73%	70%	86%	100%	100%	100%	100%
Q20	73%	69%	86%	100%	100%	100%	100%
P0	73%	68%	85%	100%	100%	100%	100%
PT0	73%	68%	85%	100%	100%	100%	100%

Table 6.2: Selection efficiencies for each tune for various Pythia sub-processes: low-$\mathrm{p_T}$, single diffractive, double diffractive and a mixed process sample; and particle production mechanisms: the hard scatter, initial state radiation and multiple parton interactions. Each sample consisted of 100,000 generated events.

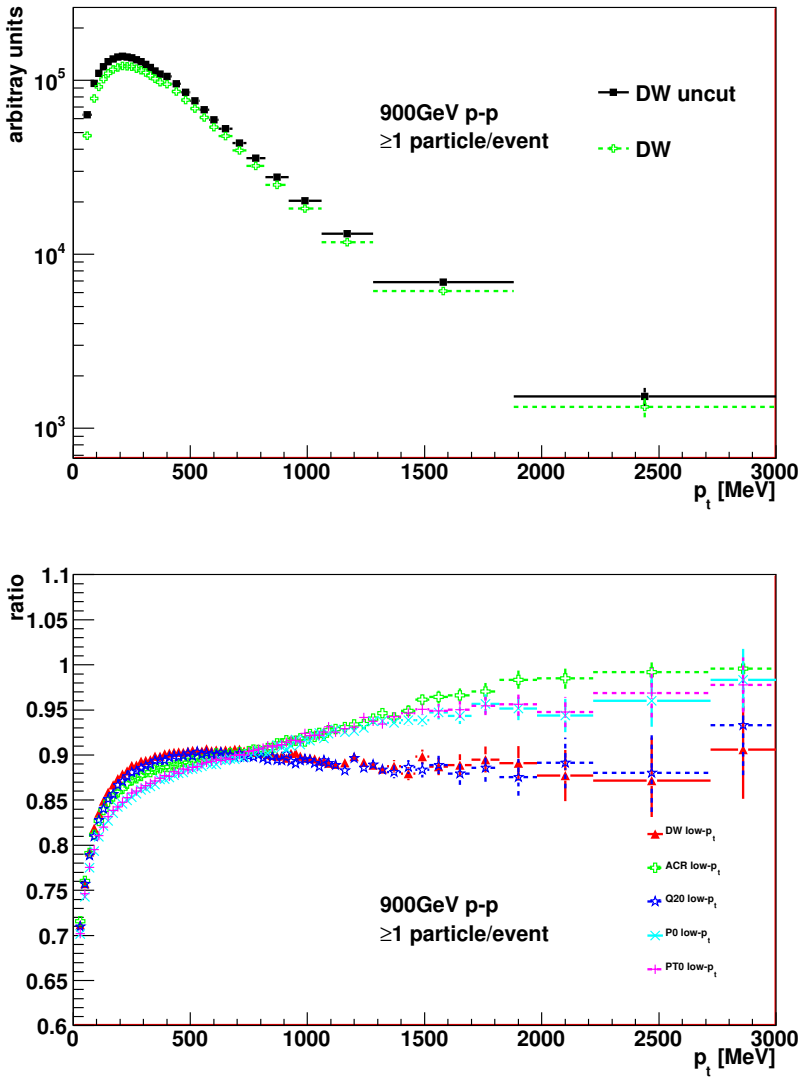

Figure 6.2: Above: Charged particle logarithmic $\mathrm{p_T}$ distribution for low-$\mathrm{p_T}$ sample of DW tune, with (red) and without (black) η selection cut. Below: Ratio of selected to unselected tracks for the low-$\mathrm{p_T}$ sample of each tune.

6.4 Current Plots

Current LHC studies of minimum bias events, e.g. [51, 52, 53, 54, 55, 56, 57, 58], have produced standard plots, focused mainly on the "basic four" charged-particle distributions: $P(n_{ch})$, $dn_{ch}/d\eta$, $dn_{ch}/d\mathrm{p_T}$, and $\langle \mathrm{p_T} \rangle$. In this section, these distributions are produced for the selected set of Monte Carlo tunes for later reference. More comments on these distributions can be found, e.g., in [39, 41].

6.4.1 Multiplicity

Tables 6.3 and 6.4 compare the average particle multiplicity, $\langle n_{ch} \rangle$, for the minimum bias production mechanisms, respectively, for each tune. Only the minimal selection requirements outlined above were used. To help illustrate the overall spread in predictions, a "range" in average values is defined as the highest average multiplicity of the tunes minus the lowest, normalised to the lowest multiplicity, i.e.

$$\text{range} = (\langle n_{ch} \rangle_{\max} - \langle n_{ch} \rangle_{\min}) / \langle n_{ch} \rangle_{\min} \ . \tag{6.1}$$

The range of $\langle n_{ch} \rangle$ predicted within $|\eta| \leq 5$ can be seen to vary between particle production mechanisms and sub-processes for each tune. In the case of the inelastic sub-processes in table 6.3 this is by $10 - 20\%$. For the diffractive processes, there is no parton showering and no MPI. Hence, the considerable differences between models must be generated by the different tunings of the hadronisation model. The new shower tunes have lower particle multiplicity than the old shower tunes, including ACR. This corresponds to the distributions shown in figure 6.2. Fewer particles produced from the same energy of collision will result in a larger proportion of high-$\mathrm{p_T}$ particles in selected events. Hence the separation in tune $\mathrm{p_T}$ distributions found above and again in figure 6.3 below. The greatest relative change between tunes in the case of sub-processes comes from the diffractive elements. Therefore, the fragmentation tuning of the new model used by PT0 and P0 produces fewer particles than the fragmentation of the old models.

In the case of the production mechanisms in table 6.4 the greatest relative change between tunes is found from radiative production. Variation between the hard process of each tune is possible due to the hadronisation differences between tunes (not investigated in this study). It is worth reiterating how variation in multiplicity from the different production sources between tunes can be be hidden in the overall multiplicity, as seen when comparing the ranges of the separate particle production processes to the combined.

Tune	single	double	low-p_T	mixed
DW	10.1	12.0	38.6	23.5
ACR	10.1	12.0	38.4	23.5
Q20	10.3	12.1	38.3	23.4
P0	9.1	10.8	35.4	21.7
PT0	9.1	10.8	36.8	22.5
range in $\langle n_{ch} \rangle$ (%)	14.1	12.8	9.0	8.4

Table 6.3: Average charged particle multiplicity for each tune for various minimum bias sub-processes: low-p_T, single diffractive, double diffractive and a mixed sample.

Tune	hard only	radiation only	MPI only	all on
DW	28.0	32.9	33.5	38.6
ACR	-	31.6	36.2	38.4
Q20	29.1	30.9	36.3	38.3
P0	23.8	26.0	29.6	35.4
PT0	24.1	26.0	31.1	36.8
range in $\langle n_{ch} \rangle$(%)	22.4	26.6	22.4	9.0

Table 6.4: Average charged particle multiplicity for each tune for various particle production mechanisms: hard-scatter only, initial state radiation only, multiple parton interaction only and all processes on. N.B. the column labelled "all on" is identical to the "low-p_T" one in table 6.3.

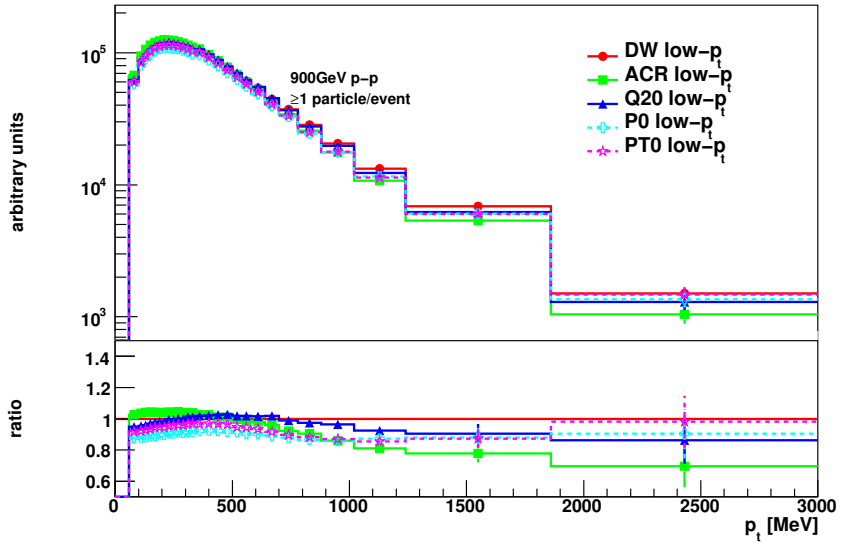

Figure 6.3: Above: Selected charged particle logarithmic p_T distribution for low-p_T sub-sample Pythia tunes. Below: Ratio is calculated with respect to the DW tune.

6.4.2 Track p_T

Figure 6.3 shows the p_T distributions for the low-p_T model samples. Some discrepancy is found between tunes across the p_T-spectrum as before. Again, the tunes exhibit differences of the order $10 - 20\%$. In the low region ($p_T < 1$ GeV) the old shower tunes DW, ACR and Q20 lie above the new shower models P0 and PT0. This is reversed in the region above 2 GeV. The ACR tune shows the greatest variation, the greatest peak in the low-p_T region and the lowest trough in the mid-region (1-2GeV). Due to limited statistics, the tail of

very high-$\mathrm{p_T}$ charged particles is omitted here, but note that the trend of the new models to generate harder $\mathrm{p_T}$ tails is illustrated in [39].

Tables 6.5 and 6.6 show the variation of the average $\langle \mathrm{p_T} \rangle$ spanned by the tunes for all the sub-samples, where "range" is defined analogously to eqn. (6.1). In the case of the low-$\mathrm{p_T}$ samples, ACR is the lowest and there is only a small variation between old and new shower models (in general, the range in $< \mathrm{p_T} >$ is less than the range in $< n_{ch} >$). Also, the Professor collaboration tunes are slightly softer on average than the others.

Tune	single	double	low-$\mathrm{p_T}$	mixed
DW	340	337	463	449
ACR	340	337	436	426
Q20	339	338	457	445
P0	330	326	463	450
PT0	330	326	459	448
range in $< \mathrm{p_T} >$ (%)	3.1	3.5	6.1	5.7

Table 6.5: Average charged particle $\mathrm{p_T}$ for each tune for various minimum bias sub-processes: low-$\mathrm{p_T}$, single diffractive, double diffractive and a mixed sample.

Tune	hard only	radiation only	MPI only	all on
DW	428	438	475	463
ACR	-	421	430	436
Q20	424	431	459	457
P0	432	440	451	463
PT0	432	437	450	459
range in $\langle \mathrm{p_T} \rangle$(%)	2.1	4.6	10.5	6.1

Table 6.6: Average charged particle $\mathrm{p_T}$ for each tune for various particle production mechanisms: hard-scatter only, initial state radiation only, multiple parton interaction only and all processes on. N.B. the column labelled "all on" is identical to the "low-$\mathrm{p_T}$" one in table 6.3.

6.4.3 Track η

Figure 6.4 shows the η distributions for the selected models. Differences are again at the $10 - 20\%$. This is not surprising as Pythia modelling is rooted in perturbative QCD. Here the processes have no hard scale and the number of charged particles is not an infrared safe observable. So although the models may be better constrained, such divergence is not excessive.

While there is clearly some sensitivity to central vs. forward production mechanisms in this distribution, its ability to discriminate between models is still limited. Indeed, there are limitations to each of these inclusive plots in differentiating between the various tunes. Agreement between each tune is generally good, especially in the case of the low-$\mathrm{p_T}$ comparison, in the region $|\eta| < 2.5$, which is most like the type of tracks selected in experiment. The experimental cuts applied in track selection will introduce systematic uncertainties which mitigate the discriminating power of these observables to discern between tunes.

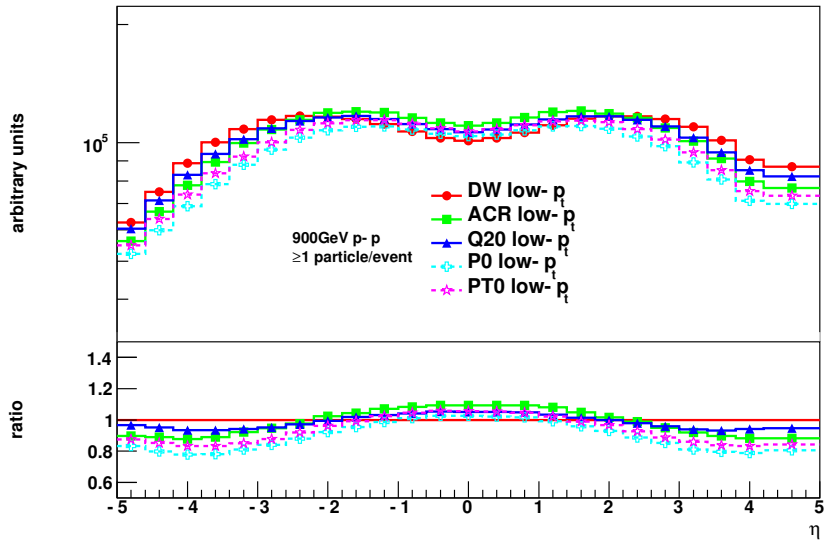

Figure 6.4: Above: Selected charged particle logarithmic η distribution for low-p_T sub-sample Pythia tunes. Below: Ratio is calculated with respect to the DW tune.

In addition, when investigating any divergence in distributions for MC tuning purposes separate observables which can isolate different particle production mechanisms would also prove useful. The above distributions do not afford such investigation. Hence, a useful addition to these plots would be a distribution, where linearly independent information on the structure of events in η, could provide valuable additional constraints.

6.5 Forward-Backward Correlations

The purpose of the proposed plots is to enhance the discriminating power between MC models and to reveal their properties more clearly, as compared to what can be achieved with the "standard" observables discussed in section 6.4. Though not unprecedented[3], these "new" plots offer important experimental data to constrain model divergences ignored so far. To this end, the proposed plots are based on forward-backward correlation of activity in the detector, also known as the b-correlation.

In this section the b-correlation will be calculated and plotted for different production mechanisms, cuts, and correlation regions.This section is divided as follows: first, a standard inclusive "minimum-bias" b-correlation is introduced in section 6.5.1 and its behaviour for the different tune samples investigated; section 6.5.2 studies the behaviour for the particle production mechanisms and section 6.5.3 for the sub-processes; then the effects of $\mathrm{p_T}$ cuts are studied in section 6.5.4. In this way, the behaviour of the correlation on various processes and in various kinematic regions is mapped out for future reference.

Further information shall be extracted by defining a set of b-correlations that are sensitive to the azimuthal structure of the events in section 6.5.5. These latter observables, which are essentially binned double-differential η-ϕ correlations, are termed "twisted" b-correlations.

6.5.1 Inclusive b-correlation

The b-correlation is defined, as in [42], as:

$$b = \frac{\sigma(n_b, n_f)}{\sigma(n_b)\sigma(n_f)} = \frac{< n_b n_f > - < n_f >^2}{< n_f^2 > - < n_f >^2}, \tag{6.2}$$

where the equality assumes $< n_f >=< n_b >$ and $< n_f^2 >=< n_b^2 >$.

$n_f(n_b)$ is the activity in the forward (backward) region of the detector. "Activity" can be one of a number of observables in the detector, e.g. energy, charged particle multiplicity (inclusively or above a given $\mathrm{p_T}$ threshold), momentum sum, etc. The forward-backward regions are defined by the η-space geometry of the detector. The pseudo-rapidity regions of the event can be divided into various bin sizes[4], ($\Delta\eta$). In the study presented, a pseudo-rapidity bin size $\Delta\eta = 0.5$ was chosen over the range $-5 < \eta < 5$. Charged particle multiplicity was chosen as the correlation variable as this has been measured previously [50] and is among the first measurements expected from LHC experiments.

The ability of the b-correlation to discern short- and long-distance production mechanisms gives it a distinguishing power between generator tunes where these mechanisms are designed and mixed with varying features and proportions. Short distance correlations are

[3] see [50]

[4] Appendix A shows a comparison of various pseudo-rapidity bin sizes.

expected to be strongest in the low-η region. In theoretical calculations these come from perturbative production mechanisms such as initial and final state radiation. These should be localised over at most a few adjacent η-bins and quickly diminish over larger distances. As the b-correlation is defined to compare opposing bins centred around $\eta_{det} = 0$, short distance correlations will only be observed in the low-η range where there is a relatively small (or no) η gap between regions used to calculate the correlation.

In contrast, long-distance correlations, originating from non-perturbative processes such as MPIs and beam remnants (BRs), involving colored exchanges, give rise to weaker correlations over longer distances. These are expected to dominate the b-correlation distribution at mid- to high-η, where the perturbative contribution has diminished. Hence, measuring the b-correlation over a wide enough η-region will probe the strength of each of these contributions at central and extreme η values, where they dominate individually. Further, an examination of the shape of the distribution across the overall η-region will probe the production mechanism proportions and interplay. This information is linearly independent from that contained in the current "standard" distributions.

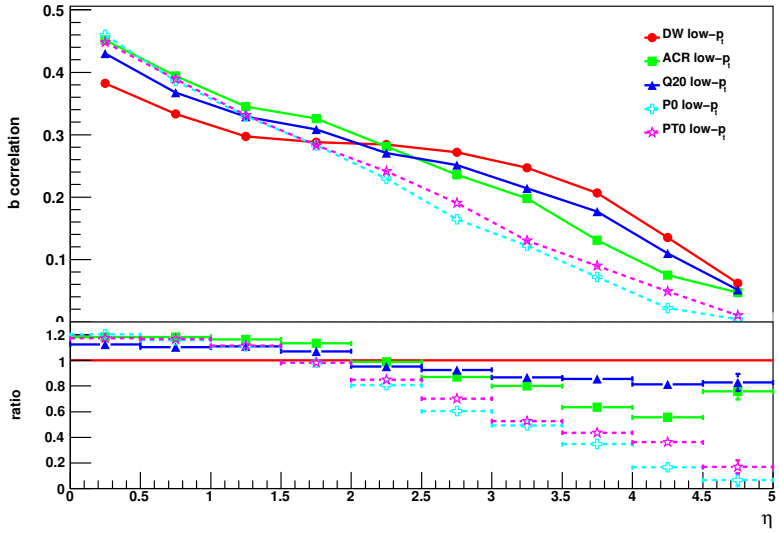

Figure 6.5: Above: Inclusive b-correlation distribution for selected low-$\mathrm{p_T}$ Pythia tunes. Below: Ratio is calculated with respect to the DW tune.

Figure 6.5 shows the inclusive b-correlation distribution for all charged particles in selected events from the low-$\mathrm{p_T}$ samples. The first difference is in the shape of the distributions between the old and new shower mechanisms. The tunes involving the new shower mechanisms (P0 and PT0) have a greater correlation at low-η and diminish across η at faster than the old shower tunes, such that there is a crossing point around the mid-η region after which the correlations of the old shower tunes lie above the new shower tunes. The new shower tunes end with almost zero correlation at $\eta = 5$, while the old shower values have small but non-zero values.

These qualitatively different shapes are interpreted as follows: due to the inclusion of showers off the MPI in the new models, more of their total particle production is driven by shower activity than was the case in the old ones, which have a larger average number of MPI [39]. The new models therefore exhibit stronger short-range correlations[5] and weaker long-range correlations than their older counterparts, with a crossover point somewhere around $|\eta| = 1 - 2$.

There are further differences in the b-correlation distributions of the like-shower tunes shown. DW has the most distinctive shape of the old shower tunes. There is a clear double curved structure where the peak at low-η is followed by a steep decline in correlation, then a plateau in the mid-η region, followed by another sharp decline. This is consistent with the $dN/d\eta$ distribution being higher for this tune for $|\eta| > 3$ than for any of the other models, cf. fig. 6.4. This suggests relatively high but localised particle production in the central region, lower and more wide reaching production in the middle section and a dearth of production at the extremes of the η-region. The Q20 distribution begins above DW but after the intermediate region drops below. As these two tunes have very similar $\langle n_{ch} \rangle$ (see section 6.4), this suggests the Q20 tune has a larger proportion of short-distance particle production mechanisms which quickly fall across η. The new shower tunes follow each other closely, while the ACR tune follows them in the low-η region before falling less steeply to follow a distribution more like the old shower models in the mid to high η region.

6.5.2 Contribution from Particle Production Mechanisms

To investigate the physical sources of particle production in the b-correlation the corresponding exclusive production samples correlations were compared. The results are shown for old and new shower tunes below. Table 6.7 shows the inclusive b-correlation values in the central ($\eta = 0 - 0.5$), mid-range ($\eta = 2.5 - 3$) and extreme ($\eta = 4.5 - 5$) bins for hard, radiative, multiple-parton interactions and combined particle production mechanisms. The general trend for all tunes is for the MPI distribution to dominate over the low- and mid-η ranges. The correlation from initial and final radiation production sources lies beneath with the hard scatter alone generating the lowest strength correlation over η. Again, this has partly to be understood as the MPI component generating the largest part of the multiplicity, see table 6.4, such that statistical fluctuations are relatively more important when that component is switched off, as in the radiation only and hard samples. The combination of all sources is the strongest as expected.

This particular ordering of correlation distributions for the production mechanisms over

[5]Note that these particular tunes of the new model have fewer average charged particles than those of the old, cf. table 6.3. Due to the dilution effect caused by statistical fluctuations, their correlation strengths are therefore intrinsically slightly lower than if they had been made to give the same average multiplicities as their older counterparts.

η is expected. The definition of the correlation, as mentioned above, focused on scatterings in the centre of the accepted geometry. The hard scatter alone will only generate particles in the central η-bins. So the correlation will be limited to this region, i.e. the low-η in the correlation plots. Particle production from initial and final state radiation extends the production region slightly out in pseudo-rapidity, coming from perturbative effects from the hard scatter. Hence, the corresponding correlation distribution is wider but also limited to the central region. The non-perturbative particle production of MPI extends across the acceptance region, producing a correlation which stretches across η.

Old shower algorithm Figures 6.6, 6.7 and 6.8 compare the particle production mechanisms for DW, ACR and Q20 tunes, respectively. In each case there is a substantial difference in the strength of correlation between the combined (labelled low-$\mathrm{p_T}$) and MPI only samples compared to the radiation only and hard process samples. Figure 6.7 shows the agreement of MPI and the combined process most acutely. These plots show that the b-correlation is dominated by MPI as the source of particle production, especially in the mid- and high-η range. Initial and final state radiation produces little correlation as η increases, while the hard process alone produces a slight anti-correlation in the mid- and high-η range.

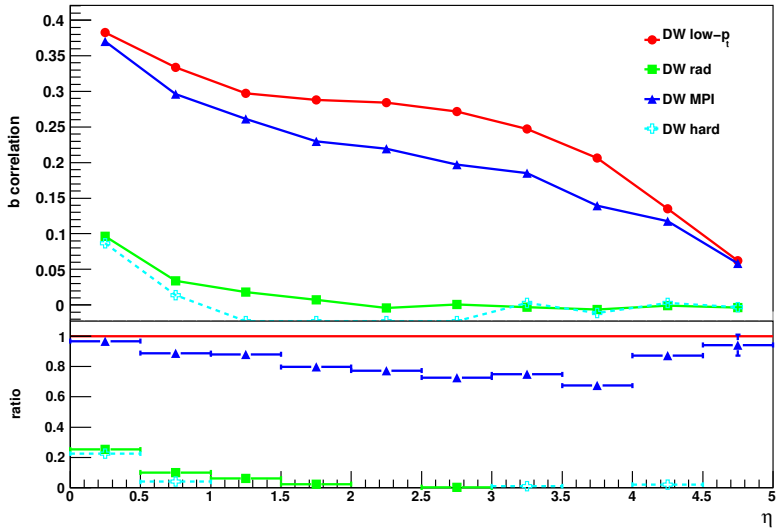

Figure 6.6: Above: Inclusive b-correlation distribution for tune DW particle production mechanisms: low-$\mathrm{p_T}$, hard process, radiative production (rad) and multi-parton interactions (MPI). Below: Ratio is calculated with respect to the low-$\mathrm{p_T}$ sample.

New shower algorithm Figures 6.9 and 6.10 compare the particle production mechanisms for P0 and PT0 tunes, respectively. Here the new shower production mechanisms give rise to more separated correlations over η, i.e. low-$\mathrm{p_T}$ and MPI distributions are more distinct, compared to the old shower tunes. MPI production remains the dominant source in the low- to mid-η ranges but at the extreme edge it falls below the plateau of the radiative and hard distributions to give an anti-correlation. This suggests the MPI production mecha-

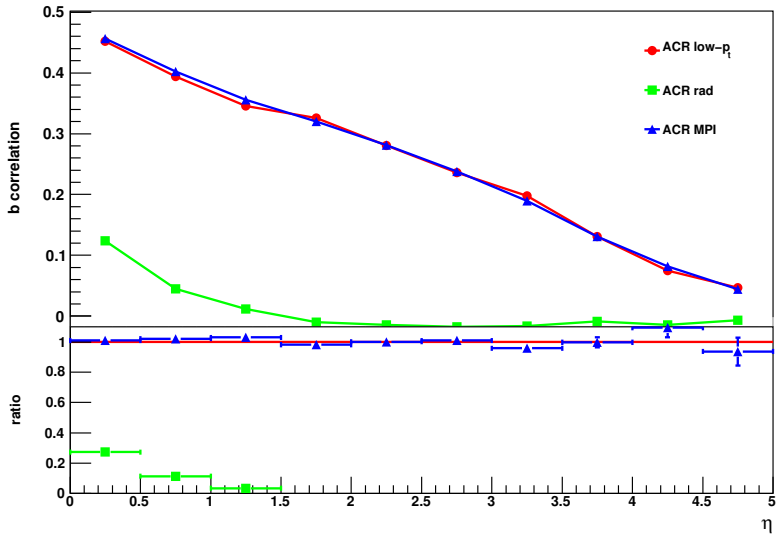

Figure 6.7: Above: Inclusive b-correlation distribution for tune ACR particle production mechanisms: low-p_T, hard process, radiative production (rad) and multi-parton interactions (MPI). Below: Ratio is calculated with respect to the low-p_T sample.

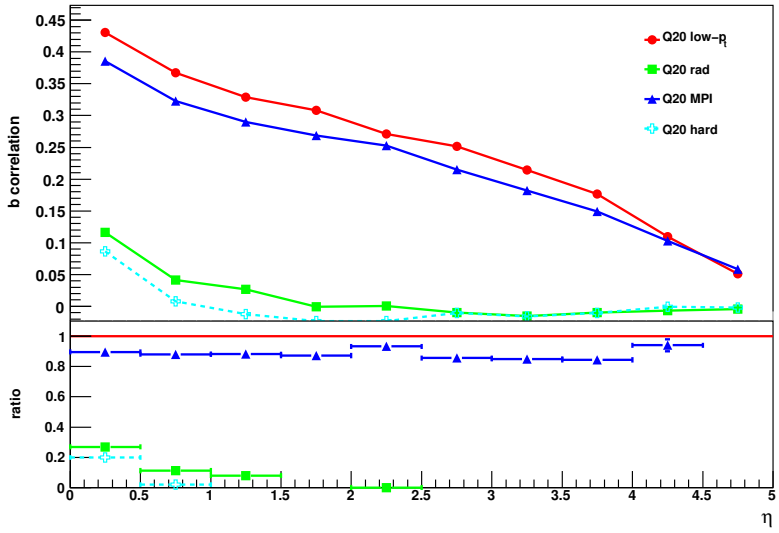

Figure 6.8: Above: Inclusive b-correlation distribution for tune Q20 particle production mechanisms: low-p_T, hard process, radiative production (rad) and multi-parton interactions (MPI). Below: Ratio is calculated with respect to the low-p_T sample.

nism for the new shower tunes is more limited to the low- and mid-η regions, than the old. This is consistent with the new model deriving more of its total particle production from shower-related activity.

In the low-η region the new shower (P0 and PT0) and ACR tunes have the highest combined correlation. In the case of ACR this seems to come from the MPI contribution. The same is true for the new tunes but to a lesser extent as the difference between the MPI

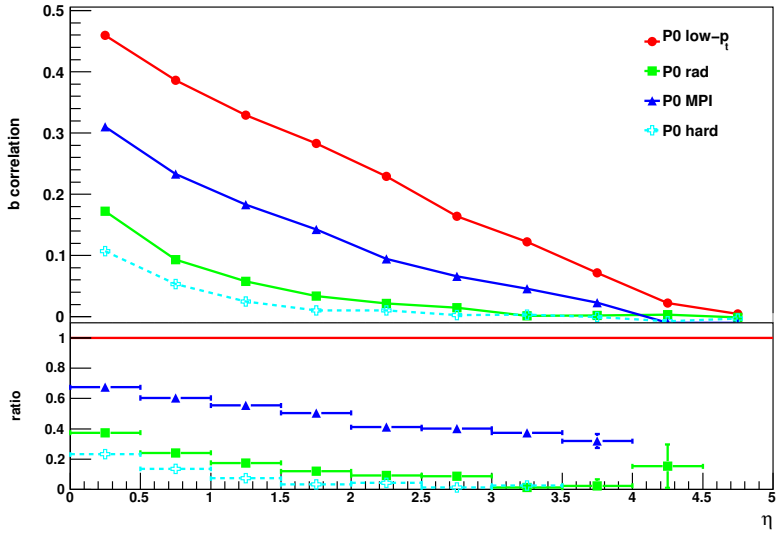

Figure 6.9: Above: Inclusive b-correlation distribution for tune P0 particle production mechanisms: low-p_T, hard process, radiative production (rad) and multi-parton interactions (MPI). Below: Ratio is calculated with respect to the low-p_T sample.

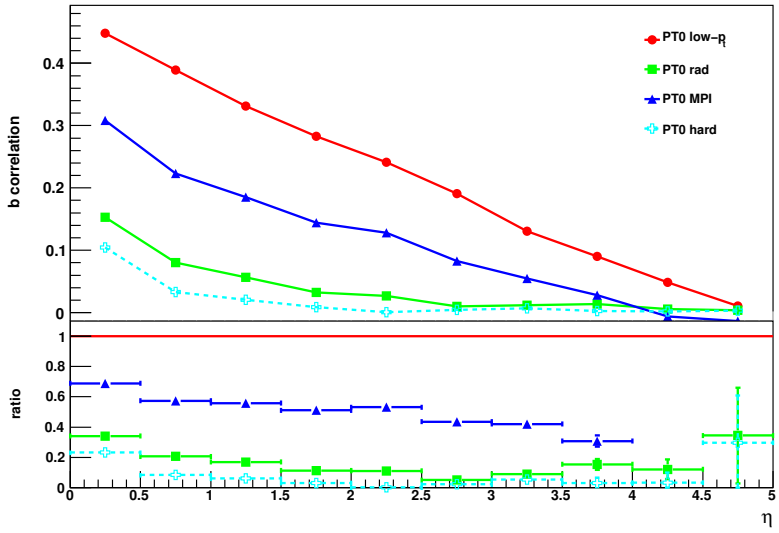

Figure 6.10: Above: Inclusive b-correlation distribution for tune PT0 particle production mechanisms: low-p_T, hard process, radiative production (rad) and multi-parton interactions (MPI). Below: Ratio is calculated with respect to the low-p_T sample.

correlation and other sources is smaller. Though the DW and Q20 old shower tunes have greater MPI correlations in this region, they do not have the same contribution from radiative sources. The combination of radiative and MPI particle production gives a combined correlation for all tunes in this region, with the exception of DW, which does not have as strong a contribution from MPI sources as the other old model tunes.

In the mid-η the correlation from radiative particle production sources decreases across

	central bin				mid-range bin				extreme bin			
Tune	hard	rad.	MPI	comb.	hard	rad.	MPI	comb.	hard	rad.	MPI	comb.
DW	0.09	0.10	0.37	0.38	-0.02	0.00	0.20	0.27	0.00	0.00	0.06	0.06
ACR	-	0.12	0.46	0.45	-	-0.02	0.24	0.24	-	-0.01	0.03	0.05
Q20	0.09	0.12	0.39	0.43	-0.01	-0.01	0.22	0.25	0.00	0.00	0.05	0.05
P0	0.11	0.17	0.31	0.46	0.00	0.01	0.07	0.16	0.00	0.00	-0.01	0.00
PT0	0.10	0.15	0.31	0.45	0.00	0.01	0.08	0.19	0.00	0.00	-0.02	0.01

Table 6.7: Central($\eta = 0 - 0.5$), mid-range ($\eta = 2.5 - 3$) and extreme ($\eta = 4.5 - 5$) b-correlation values for hard, radiative (ISR/FSR), multiple-parton interactions (MPI) and combined particle production mechanism samples for each tune at $\sqrt{s} = 900GeV$.

tunes, as the perturbative contribution is limited to low-η. However the models diverge on the strength of the MPI correlation. This entails the combined correlation is strongest in the old model tunes as these have the greatest contribution from MPI production.

In the high-η region all the tunes have low correlation strength as the limit of all particle production mechanisms has been reached in this extreme region. The old shower tunes along with ACR have some MPI particle production remaining while the new tunes are exhausted.

This investigation clearly vindicates the description of the inclusive b-correlation distributions of fig. 6.5. Firstly, the relatively high correlation strength of the new shower models in the low-η region comes at the expense of the correlation at high-η. The new tunes spend their energy on localised perturbative particle production from hard and radiative sources, while the old tunes spend a greater proportion on non-perturbative production in MPI. Secondly, the augmented shower of the ACR tune increases MPI particle production in the low and mid-η and regions to match the correlation strength of the new tunes in the central region, at the expense of particle production in other regions.

6.5.3 Comparison of minimum bias processes

To investigate the b-correlation of each minimum bias process the corresponding sub-process samples correlations were compared. The correlations in the SD and DD samples are intrinsically shorter-range than those of their non-diffractive counterparts, consistent with diffractive systems having a limited extension in rapidity. The results are shown for old and new shower tunes below. Table 6.8 shows the uncut b-correlation values in the central ($\eta = 0 - 0.5$), mid-range ($\eta = 2.5 - 3$) and extreme ($\eta = 4.5 - 5$) bins for the mixed, low-$\mathrm{p_T}$ and double diffractive processes. The general trend for the processes is for the low-$\mathrm{p_T}$ sample, which contains the hardest events, to have a higher correlation across η than the diffractive samples. Of the two diffractive samples, SD has the higher correlation distribution. The mixed sample has the combined correlation from all sub-processes and is highest over the η-region[6].

[6]It may at first seem counter-intuitive that the combined sub-processes of weaker correlated samples produce a more strongly correlated sample either of the original components, but this is sensible. See appendix B for details

Old shower algorithm Figures 6.11, 6.12 and 6.13 compare the minimum bias sub-processes for DW, ACR and Q20 tunes, respectively. Figure 6.11 shows that the correlations for single and double diffractive samples are limited to the low-η region and weaker than the low-p_T distribution. In fact the distribution shows a slight anti-correlation for these processes after $\eta \sim 2.5$. The combination of all sub-processes in the mixed distribution is flattened in the low to mid-η region, compared to the low-p_T distribution, due to the correlation of diffractive processes at low-η. This is repeated in figures 6.12 and 6.13 for ACR and Q20 tunes, respectively.

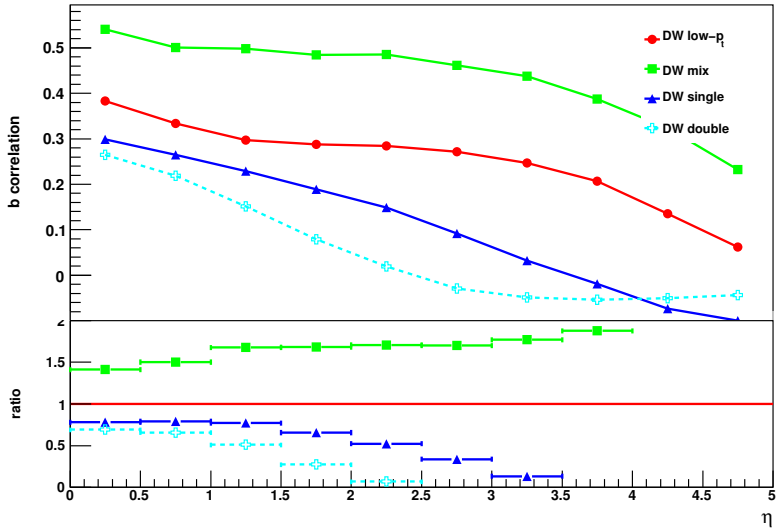

Figure 6.11: Above: Inclusive b-correlation distribution for tune DW minimum bias sub-processes. Below: Ratio is calculated with respect to the low-p_T sample.

New shower algorithm Figures 6.14 and 6.15 compare the minimum bias sub-processes for P0 and PT0 tunes, respectively. The new shower models show the same general trends as the old shower tunes. The same anti-correlation is found fin the case of the single diffractive-distribution for each tune. This is understandable as at high-η, where only side of the region is populated due to proton disintegration. The multiplicity per event will therefore be systematically different than the average multiplicity, calculated over all events, as one of the two η-bins will have a higher than average multiplicity and the other a lower than average multiplicity. This behaviour will be less obvious in more central regions due to the effects of other particle production sources will dominate. In addition, the double diffractive distribution does not have anti-correlation at the edge as the multiplicity per event and average multiplicity will not diverge in systematic way so acutely, as both sides of the η region will have similar particle populations per event.

In the low-η region the ACR tune has the highest mixed correlation with the Q20, P0, PT0 at similar values and DW slightly lower. This can be attributed to the contribution to the correlations from the low-p_T samples. This is illustrated by the DW, which tune lags behind

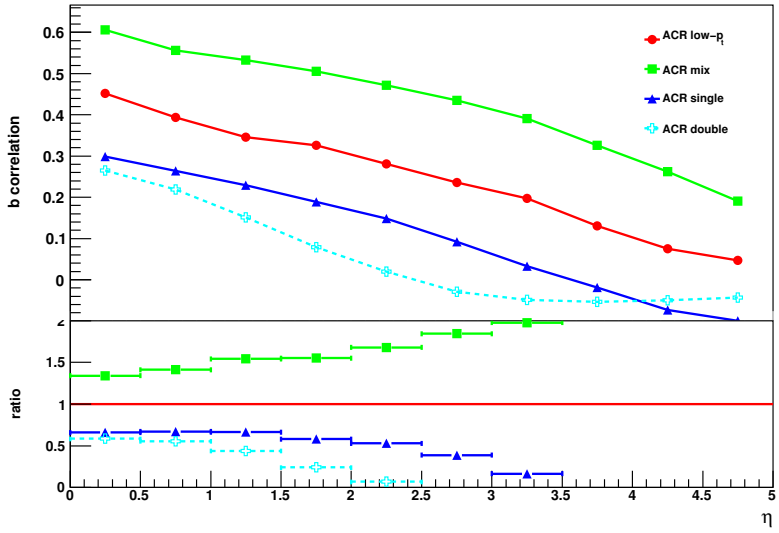

Figure 6.12: Above: Inclusive b-correlation distribution for tune ACR minimum bias sub-processes. Below: Ratio is calculated with respect to the low-p_T sample.

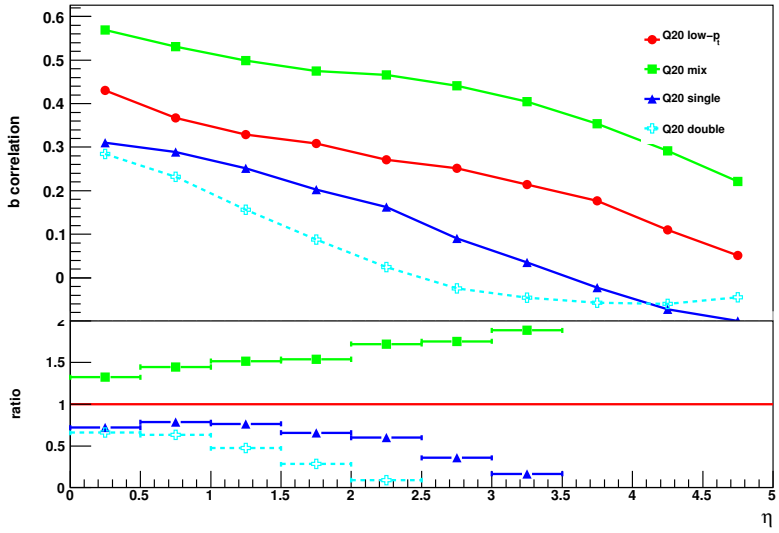

Figure 6.13: Above: Inclusive b-correlation distribution for tune Q20 minimum bias sub-processes. Below: Ratio is calculated with respect to the low-p_T sample.

the other old shower models in low-p_T but has similar diffractive correlations. ACR has the combination of the relatively strong correlations of the low-p_T contribution, shared by the new shower models, and the diffractive components, common to the old model tunes.

In the mid-η region a separation between old and new shower models can be seen. This is due to the relatively strong low-p_T correlations in the old models, while there is degeneracy of the diffractive samples across tunes.

In the high-η region the distinction between old and new shower models continues. Interestingly, in this region the ACR tune has a low-p_T correlation strength similar to the new

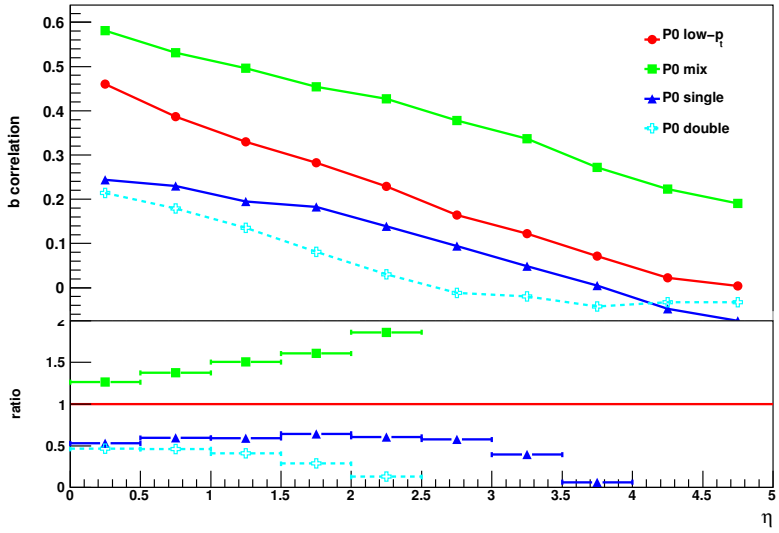

Figure 6.14: Above: Inclusive b-correlation distribution for tune P0 particle production mechanisms. Below: Ratio is calculated with respect to the low-$\mathrm{p_T}$ sample.

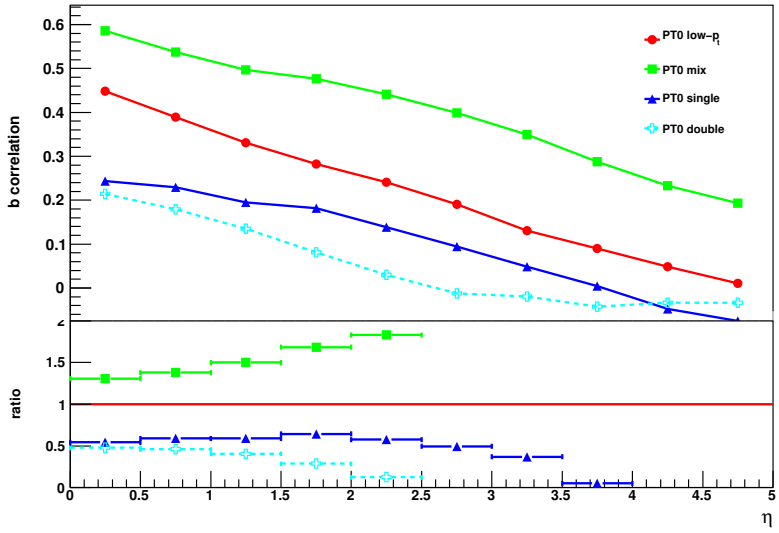

Figure 6.15: Above: Inclusive b-correlation distribution for tune PT0 particle production mechanisms. Below: Ratio is calculated with respect to the low-$\mathrm{p_T}$ sample.

shower tunes, despite the similarity of sub-process correlations to the old model tunes. This shows the effect of the production processes, outlined above, on the mixed sample. The homogeneity of the single-diffractive samples is broken as the old shower tunes are now more anti-correlated than P0 and PT0. The double-diffractive samples have correlation values remain grouped together.

These correlations show how the particle production fluctuates in each sub-process across the η-region with each tune without uniform trends. Hence it is unlikely any tune will match all data completely.

	central bin				mid-range bin				extreme bin			
Tune	mix	low-p_T	SD	DD	mix	low-p_T	SD	DD	mix	low-p_T	SD	DD
DW	0.54	0.38	0.30	0.27	0.46	0.27	0.09	-0.03	0.23	0.06	-0.11	-0.04
ACR	0.61	0.45	0.30	0.27	0.44	0.24	0.09	-0.03	0.19	0.05	-0.11	-0.04
Q20	0.57	0.43	0.31	0.28	0.44	0.25	0.09	-0.02	0.22	0.05	-0.11	-0.05
P0	0.58	0.46	0.24	0.21	0.38	0.16	0.09	-0.01	0.19	0.00	-0.08	-0.03
PT0	0.59	0.45	0.24	0.21	0.40	0.19	0.09	-0.01	0.19	0.01	-0.08	-0.03

Table 6.8: Central($\eta = 0 - 0.5$), mid-range ($\eta = 2.5 - 3$) and extreme ($\eta = 4.5 - 5$) b-correlation values for the mixed, low-p_T and single- (SD) and double-diffractive (DD) event samples for each tune at $\sqrt{s} = 900$ GeV.

6.5.4 p_T-cut b-correlation

The next series of distributions investigate the change in b-correlation with p_T. This is done by implementing various p_T-cuts on selected charged particles explicitly (i.e. in analysis rather than inside the generator) before calculating the b-distribution. This affects both the event and particle selection.The p_T-cuts used are none, 0.1, 0.2, 0.3, 0.5, 1.0, 1.5 and 2.0 GeV$/c$. How these affect the short- and long-distance contributions provides information on the kinematic make-up of these multiplicities.

Figures 6.16-6.20 show the p_T-cut distributions for selected Pythia tunes. Figures 6.16, 6.17 and 6.18 show the old shower tune distributions for DW, ACR and Q20, respectively. The new shower distributions are shown in figures 6.19 and 6.20. Note that these cuts are applied also at the level of the event selection, so only events with at least one particle harder than the given p_T cut are included, for each curve. Also, only positive correlations are expected and plotted. Any small negative correlations arise from statistical fluctuations in poorly populated bins.

Table 6.9 shows the uncut b-correlation values in the central ($\eta = 0 - 0.5$), mid-range ($\eta = 2.5 - 3$) and extreme ($\eta = 4.5 - 5$) bins, without any p_T cut, together with the reduction in the correlation strengths caused by p_T cuts of 500 MeV and 1.5 GeV.

	central bin			mid-range bin			extreme bin		
Tune	b_0	$b_{0.5}/b_0$	$b_{1.5}/b_0$	b_0	$b_{0.5}/b_0$	$b_{1.5}/b_0$	b_0	$b_{0.5}/b_0$	$b_{1.5}/b_0$
DW	0.38	0.79	0.39	0.28	0.74	0.24	0.06	0.46	-0.08
ACR	0.45	0.71	0.34	0.28	0.68	0.30	0.05	0.38	-0.03
Q20	0.43	0.74	0.29	0.27	0.68	0.17	0.05	0.42	0.16
P0	0.46	0.72	0.23	0.23	0.66	0.18	0.00	0.71	-0.39
PT0	0.45	0.73	0.23	0.24	0.65	0.18	0.01	0.15	-0.05

Table 6.9: Central($\eta = 0 - 0.5$), mid-range ($\eta = 2.5 - 3$) and extreme ($\eta = 4.5 - 5$) correlation values with fraction of correlation remaining after p_T-cut= 0.5GeV and 1.5 GeV for various Pythia tunes at $\sqrt{s} = 900GeV$. b_0 is the correlation value for p_T-cut=0.0GeV, $b_{0.5}$ the value with p_T-cut=0.5GeV and $b_{1.5}$ the value p_T-cut=1.5GeV.

In the central η-region, the effect of the $p_T = 500$ MeV cut (pink in the plots) is to lower the correlation by $\sim 25\%$. The effect is slightly larger in than the new showers where the effect is $\sim 30\%$. The effect for ACR is similar to the new shower cases. When the p_T-cut is increased to 1.5 GeV (dark purple) the reduction is much more severe and more interestingly is not a simple scaling from the reduction caused by the previous cut. PT0 and the new shower tunes have similar reductions of $\sim 75\%$, while DW and ACR are reduced by $\sim 65\%$. Hence the particle-momentum distributions of the various tunes over η are not generic and the difference between shower model is not respected.

In the middle η-range ($\eta = (2.5 - 3)$) the DW tune has the greatest proportion of its correlation coming from particles with $p_T \geq$500MeV having a decrease of $\sim 25\%$ after the

p_T-cut. The other tunes have $\sim 30\%$ reduction in correlation strength. When the p_T-cut is increased to $1.5\,\mathrm{GeV}$ DW and ACR tunes have the greatest correlation, while the new shower models have substantially lower. Again the relative order of correlation between tunes is found to fluctuate with p_T-cut in this η-region.

When the same analysis is made at the extreme end of the η-region ($\eta = (4.5 - 5)$) the low correlations are mixed with statistical fluctuations, especially when high p_T-cuts are made. However, when comparing correlation values surviving the $500\,\mathrm{MeV}$ cut between central and extreme η-bins, it can be seen that the order of these proportions is not respected as η is increased.

It is concluded that the particle-momentum distributions are found to be heterogeneous across the η-range due to the differing particle production mechanisms and parameters between tunes. Any experimental measurements should therefore by no means be restricted to the most inclusive definition possible for a given experiment. It was also shown that the long-range correlation has a much greater proportion of low-p_T particles than the central region.

Figure 6.21 shows a band plot made by combining the correlations for a given p_T-cut from each tune. The area of the band for each p_T distribution is marked out by the highest and lowest correlation values for each η-bin.

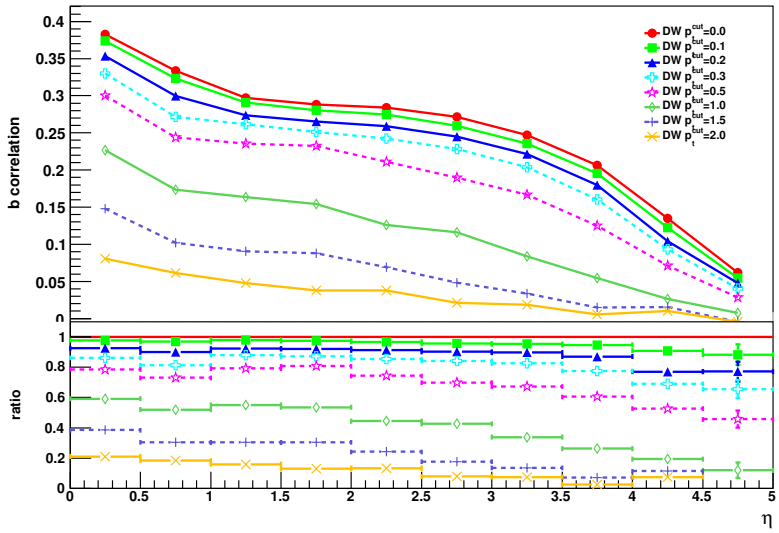

Figure 6.16: Above: b-correlation distributions for hadron-level charged particles for DW Pythia tune over various explicit p_T-cuts. Below: Ratio is calculated with respect to the non-$p_T$cut sample.

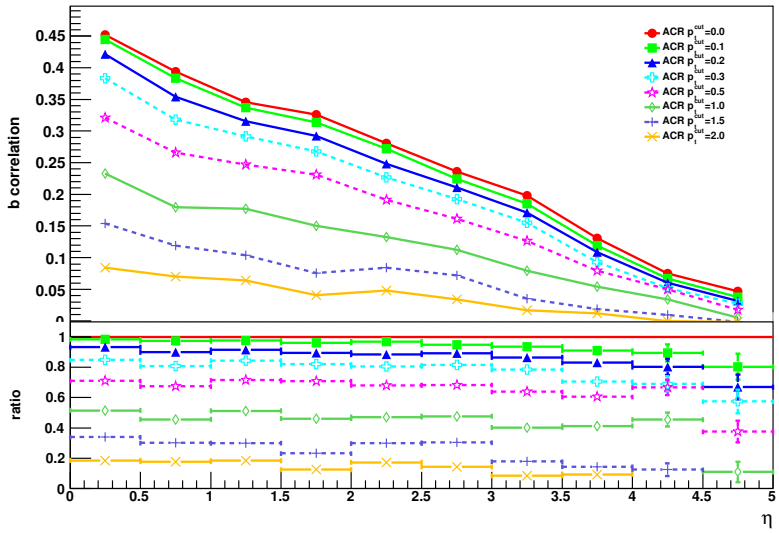

Figure 6.17: Above: b-correlation distributions for hadron-level charged particles for ACR Pythia tune over various explicit $\mathrm{p_T}$-cuts. Below: Ratio is calculated with respect to the non-$\mathrm{p_T}$cut sample.

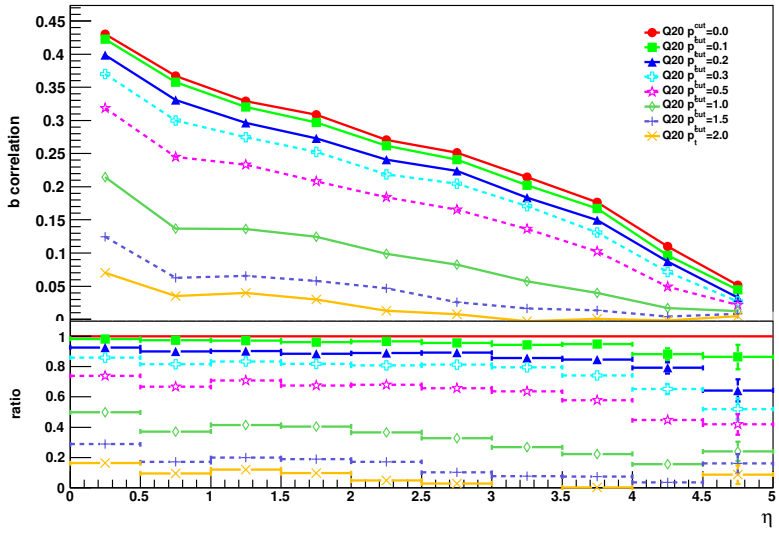

Figure 6.18: Above: b-correlation distributions for hadron-level charged particles for Q20 Pythia tune over various explicit $\mathrm{p_T}$-cuts. Below: Ratio is calculated with respect to the non-$\mathrm{p_T}$cut sample.

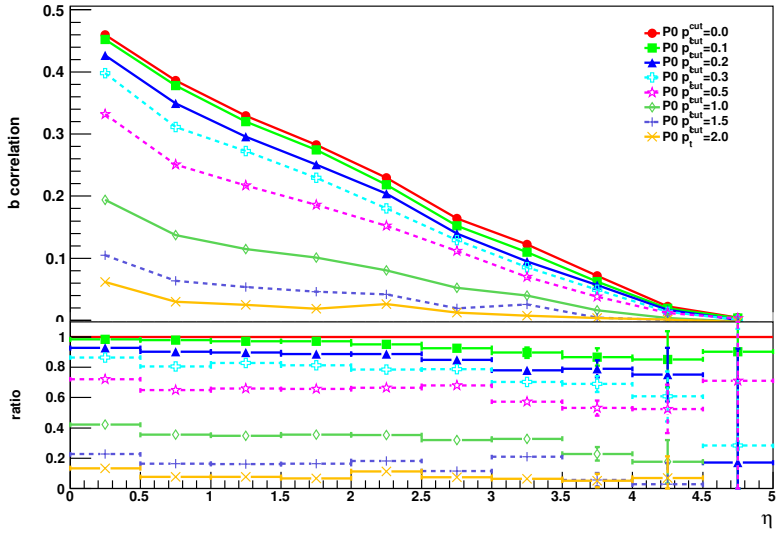

Figure 6.19: Above: b-correlation distributions for hadron-level charged particles for P0 Pythia tune over various explicit $\mathrm{p_T}$-cuts. Below: Ratio is calculated with respect to the non-$\mathrm{p_T}$cut sample.

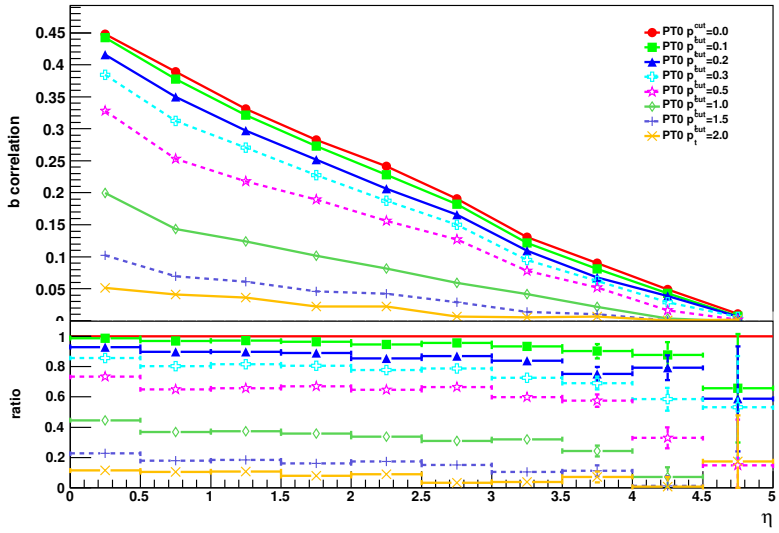

Figure 6.20: Above: b-correlation distributions for hadron-level charged particles for PT0 Pythia tune over various explicit $\mathrm{p_T}$-cuts. Below: Ratio is calculated with respect to the non-$\mathrm{p_T}$cut sample.

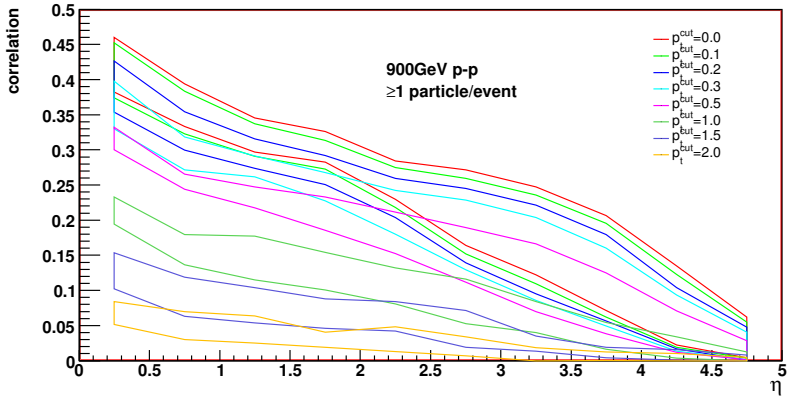

Figure 6.21: *b*-correlation distributions for hadron-level charged particles for various Pythia tunes over explicit $\mathrm{p_T}$-cuts. The area of each distribution represents the dispersion of correlation values between tunes.

6.5.5 "twisted" b-correlation: ϕ_{det}

The next series of distributions investigate the change in b-correlation over the ϕ-plane. This is studied in two ways. The first, ϕ_{det}, uses the detector geometry. In this case, no preference is given to any particular direction and hence this is expected to be independent of the event shape. The second, ϕ_{lead}, defines a privileged axis in the direction of the lead charged particle. This will bias the correlation to the most active part of the ϕ-space and hence map on to the event shape.

In each case the ϕ-plane is split into three regions of $\Delta\phi = 2\pi/3$. Only particles from a given region are used to calculate the b-correlation across η. In the case of the detector defined geometry, the *parallel*[7] region is arbitrarily defined to cover $-\pi < \phi < -\pi/3$, the *opposite* region covers $0 < \phi < 2\pi/3$, with the *transverse* region between these, i.e. over $-\pi/3 < \phi < 0$ and $2\pi/3 < \phi < \pi$. In calculating the correlation between $\eta - \phi$ regions the comparison is always to the *parallel* case on one side.

The terms of the b-correlation expression now refer to η-bins with a ϕ-dependence. Hence, the correlation expression must include this new degree of freedom. Since all regions are a priori equivalent, the normalising terms in b, $\langle n_f \rangle^2$ and $\langle n_f^2 \rangle$, are taken simply from the *parallel* region. Only the product of activity in corresponding bins of $\eta - \phi$ are sensitive to the variation in the ϕ region. The new expression, b_ϕ^{twist}, for the correlation becomes:

$$b_\phi^{\text{twist}} = \frac{\left\langle n_{b,\phi} n_{f,\|} \right\rangle - \left\langle n_{f,\|} \right\rangle^2}{\left\langle n_{f,\|}^2 \right\rangle - \left\langle n_{f,\|} \right\rangle^2} \,. \tag{6.3}$$

In general all tune correlations in the *parallel* ϕ-region dominate the central bin before falling behind the other ϕ-regions in the mid η-region, where the *opposite* correlation dominates, and finally converging with them in the extreme η-bin.

This behaviour is expected from momentum conservation. When particle production occurs in the central η-region (η=(-0.5,0.5)) a relative excess of particles can be spread over the two central bins facing the same (*parallel*) ϕ direction giving a relatively high correlation value. At the same time corresponding production occurs in the *opposite* ϕ-region to conserve momentum. Hence a relatively high correlation between the central *parallel* and *opposite* ϕ regions is also expected. This will not be as high as the *parallel* case however as the corresponding particle production can be spread over a wider ϕ or η region leading to a loss of particles in the bin of interest. Similarly if the wider particle production is found in the *parallel* region, with greater production in the *opposite* direction the mismatch in multiplicities will decrease the correlation strength. The *transverse* regions will collect particle production also but as they spread out over ϕ and perpendicular to the *parallel* region the

[7]The terminology "parallel" and "opposite" are preferred, to distinguish the geometry from Field's "towards" and "away" regions, which are taken to be defined relative to the direction of a lead particle or jet and not by the absolute detector geometry.

correlation should never lie above both other regions.

As gap between η regions is increased into the mid-η region ($1.0 < \Delta\eta < 4.0$) short-range correlations are lost in the *parallel* case and the distribution diminishes and only long-range production remains. For the same η gap, particle production in the *parallel* ϕ-region will be complemented by production in the *opposite* side of the η-range in the *opposite* ϕ-direction. Hence the *opposite* correlation remains sensitive to perturbative particle production as the η-gap expands, increasing it above the *parallel* distribution. The *transverse* correlation will also remain sensitive to any spill of particles from particle production but to less a degree than the *opposite* case.

Eventually the gap between η bins is so large ($\Delta\eta > 4.0$)that short-range production is completely lost and the *parallel* and *opposite* distributions converge at the edge of the η-range where the end of long-range production provides a small correlation value for both.

This description is further complicated by the use of detector geometry to define the ϕ-regions. As production can occur uniformly over ϕ the regions will not accurately map on to the event shape. The correlation with the *transverse* region is as close as we can come to defining an "underlying event" in an otherwise featureless minimum-bias event without a reference direction. And there is symmetry between the *parallel* and *opposite* regions. This suggests in general that the distributions for these detector defined regions will be mixtures of the descriptions above with some mitigation in the *transverse* case. Indeed, the difference in correlation strength between the three regions is not extremely large in absolute terms.

Figures 6.22-6.26 show the ϕ-cut distributions for selected Pythia tunes. Figures 6.22, 6.23 and 6.24 show the old shower tune distributions for DW, ACR and Q20, respectively. The new shower distributions are shown in figures 6.25 and 6.26. As in the inclusive ϕ cases above, the old tunes (excluding ACR) show a more gradual decline in correlation strength over η for each ϕ distribution, while the new shower models have a faster drop leading to weaker tails at high-η. Figure 6.27 shows a band plot made by combining the correlations from each tune. As above, the area of the band for each ϕ distribution is marked out by the highest and lowest correlation values for each η-bin.

Table 6.10 shows the uncut b-correlation values in the central ($\eta = 0 - 0.5$), mid-range ($\eta = 2.5 - 3$) and extreme ($\eta = 4.5 - 5$) η bins for the *parallel* ϕ-region along with the relative correlation for *opposite* and *transverse* region.

In the central η-region, there is agreement between tunes in the *parallel* ϕ-region. Comparison of correlations in the *opposite* and *transverse* regions show that, relative to the *parallel* region, sections of ϕ-space are more correlated in the case of the new model tunes and ACR. This suggests these tunes have similar activity in this η-region to the arbitrarily chosen *parallel* region. This suggests more even spread of particle production over ϕ-space in the new shower model. The agreement for each tune between *opposite* and *transverse* correlations implies there is general uniformity of production, relative to the arbitrary axis, between

	central bin			mid-range bin			extreme bin		
Tune	b_{para}	b_{oppo}/b_{para}	b_{tran}/b_{para}	b_{para}	b_{oppo}/b_{para}	b_{tran}/b_{para}	b_{para}	b_{oppo}/b_{para}	b_{tran}/b_{para}
DW	0.19	0.80	0.85	0.11	1.20	1.10	0.03	0.81	0.64
ACR	0.22	1.02	0.96	0.12	1.17	1.04	0.02	1.47	1.31
Q20	0.22	0.85	0.87	0.12	1.19	1.02	0.02	1.16	0.89
P0	0.23	0.93	0.93	0.10	1.20	0.99	0.00	0.42	0.16
PT0	0.23	0.90	0.91	0.10	1.20	1.13	0.00	3.32	4.45

Table 6.10: Central($\eta = 0 - 0.5$), mid-range ($\eta = 2.5 - 3$) and extreme ($\eta = 4.5 - 5$) correlation values for *parallel* ϕ-region (b_{para}) with relative *opposite* and *transverse* correlations for various Pythia tunes at $\sqrt{s} = 900GeV$. *Parallel* ϕ-region is $-\pi < \phi < -\pi/3$, the *opposite* region is $0 < \phi < 2\pi/3$ and *transverse* covers the two regions between, $-\pi/3 < \phi < 0$ and $2\pi/3 < \phi < \pi$. ϕ is defined by detector geometry.

these regions in each model.

In the middle η-range (η=(2.5-3)) agreement between tunes is found again in the *parallel* ϕ-region and also in the *opposite* region. However, there is now a noticeable decrease in correlation between *opposite* and *transverse* regions for each tune. As there is no tie to the event shape by this correlation definition of the correlation, this can be attributed to the geometry of the *transverse* region alone.

When the same analysis is made at the extreme end of the η-region ($\eta = (4.5 - 5)$) the differences in tunes and phi-regions are mixed with statistical fluctuations. However, the general trend across the η of decreasing correlation strength in is common to all tunes.

It is concluded that without a proper mapping to the event shape it is difficult to glean information about how particle production varies over a physically meaningful $\eta - \phi$ space. Hence, a better definition of the event geometry is required.

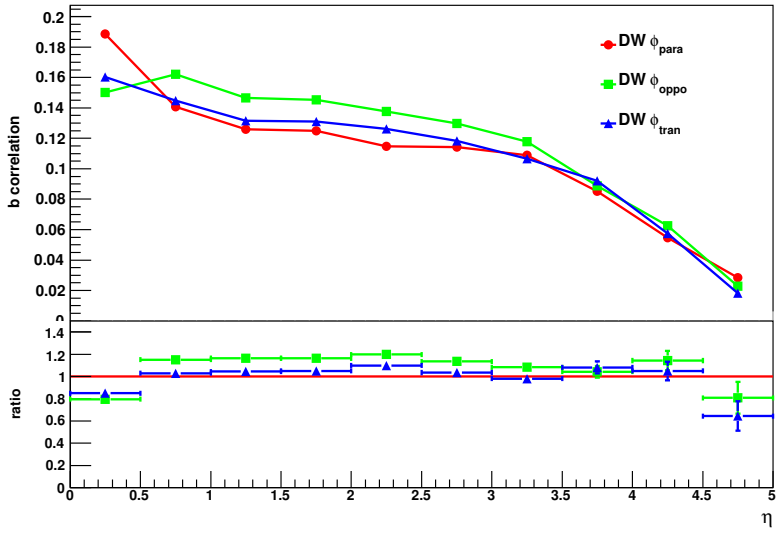

Figure 6.22: Above: b-correlation distributions for hadron-level charged particles for DW Pythia tune over various explicit ϕ-cuts based on detector geometry. Below: Ratio is calculated with respect to the *parallel* distribution.

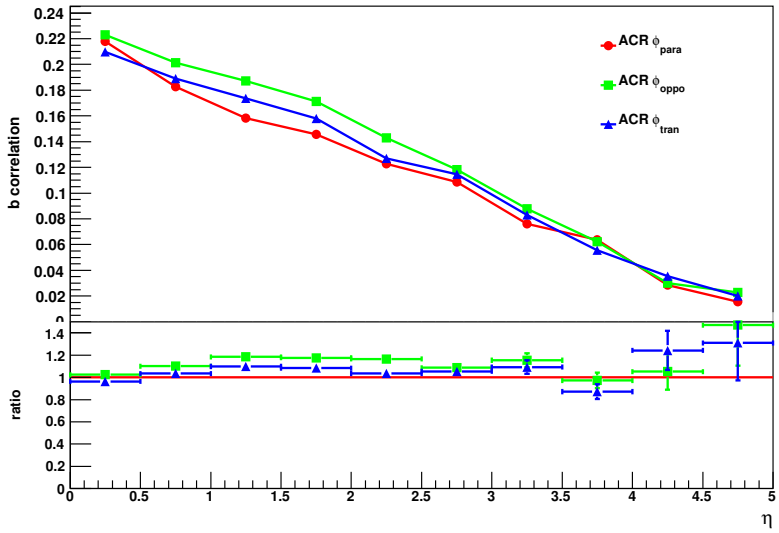

Figure 6.23: Above: b-correlation distributions for hadron-level charged particles for ACR Pythia tune over various explicit ϕ-cuts based on detector geometry. Below: Ratio is calculated with respect to the *parallel* distribution.

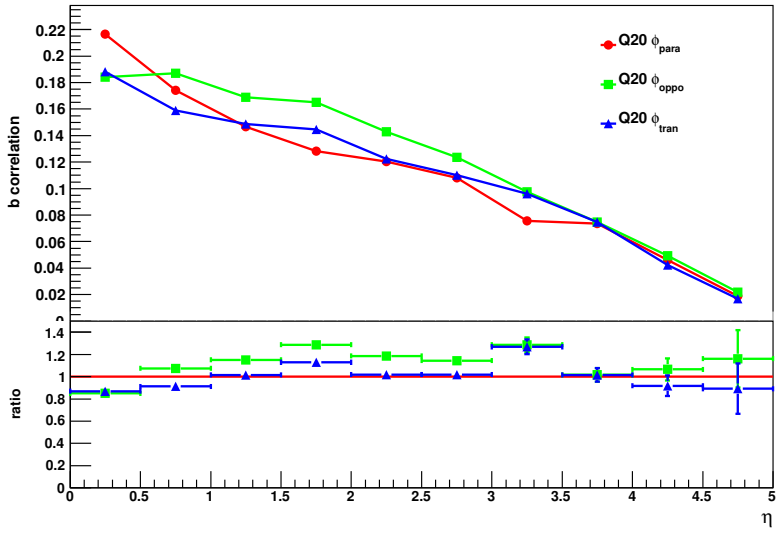

Figure 6.24: Above: b-correlation distributions for hadron-level charged particles for Q20 Pythia tune over various explicit ϕ-cuts based on detector geometry. Below: Ratio is calculated with respect to the *parallel* distribution.

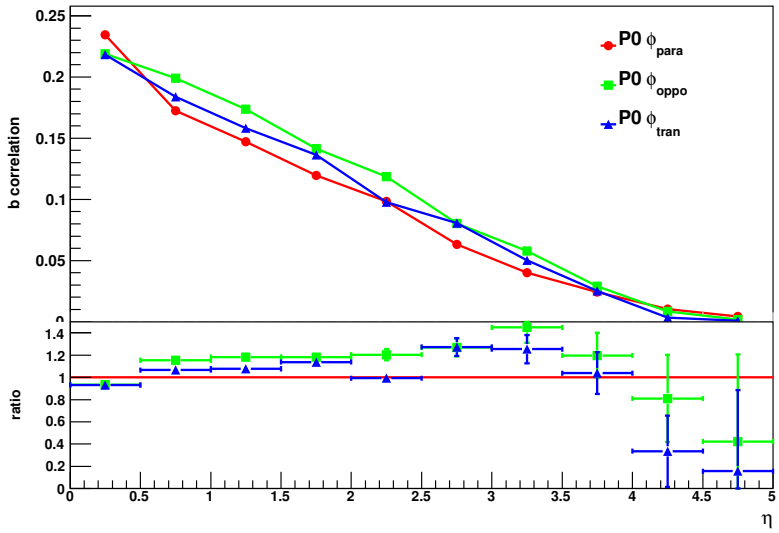

Figure 6.25: Above: b-correlation distributions for hadron-level charged particles for P0 Pythia tune over various explicit ϕ-cuts based on detector geometry. Below: Ratio is calculated with respect to the *parallel* distribution.

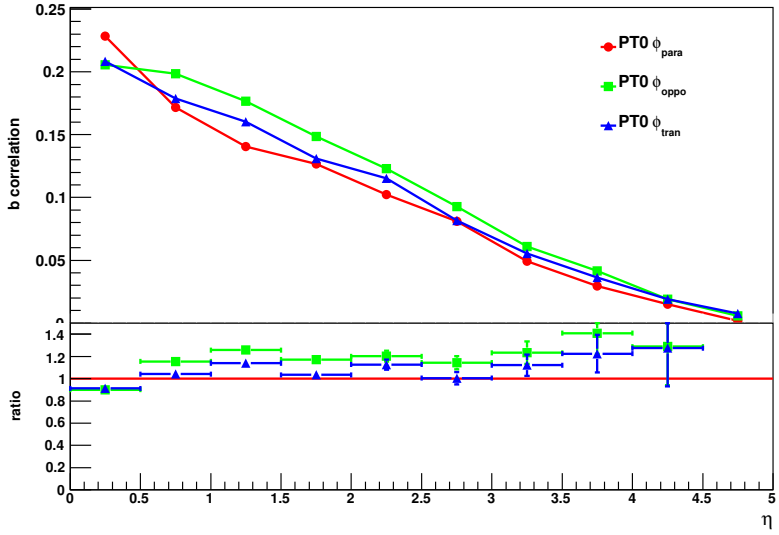

Figure 6.26: Above: b-correlation distributions for hadron-level charged particles for PT0 Pythia tune over various explicit ϕ-cuts based on detector geometry. Below: Ratio is calculated with respect to the *parallel* distribution.

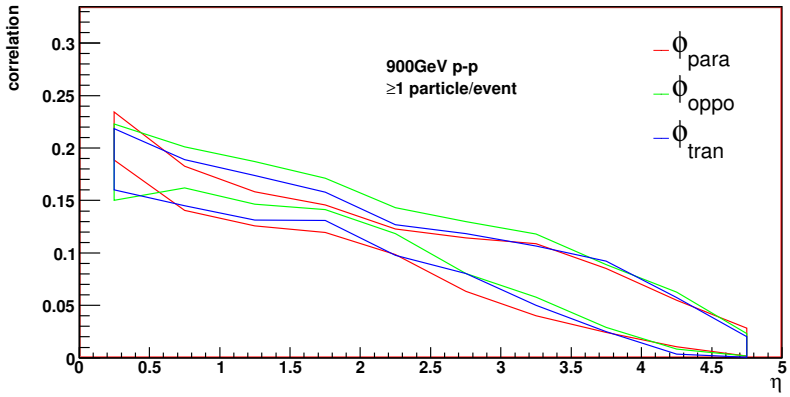

Figure 6.27: b-correlation distributions for hadron-level charged particles for various Pythia tunes over explicit ϕ-cuts based on detector geometry. The area of each distribution represents the dispersion of correlation values between tunes.

6.5.6 'twisted' b-correlation: ϕ_{lead}

In the case of the geometry defined by the lead particle, the *forward* region covers the region $\phi < \pm\pi/3$ around the lead particle, the *opposite* region covers $\pm 2\pi/3 < \phi < \pm\pi$ (where $\phi = 0$ corresponds to the lead particle) and the *transverse* region lies between, over $\pm\pi/3 < \phi < \pm 2\pi/3$. This makes most difference for events with semi-hard perturbative scattering where the particle production is back-to-back orienting the event axes to the production axis. The bias towards $\phi = 0$ as the direction of the lead particle means that the three different ϕ regions can no longer be expected to have the same averages and variances. Nonetheless, in order to define a measure comparable to the one above, the normalising terms are defined with respect to the *forward* region, so that eqn. (6.3) still holds, although its statistical interpretation is modified. Hence, although the regions have similar names and relative definitions to the detector case, their physical meaning is changed by the fact they now correspond to "event shape" (defined by the lead particle) regions rather than "detector" (i.e. arbitrary) regions.

Figures 6.28-6.32 show the ϕ-cut distributions for selected Pythia tunes based on the lead particle trajectory. Figures 6.28, 6.29 and 6.30 show the old shower tune distributions for DW, ACR and Q20, respectively. The new shower distributions are shown in figures 6.31 and 6.32. Figure 6.33 shows a band plot made by combining the correlations from each tune. As above, the area of the band for each ϕ distribution is marked out by the highest and lowest correlation values for each η-bin.

The distributions here are similar to the detector geometry correlations but emphasised by the alignment with the axis of particle production. This removes much of the effect of the uniform distribution of particle production in ϕ-space and leads to a separation of the *forward* and *opposite* distributions from the *transverse* as only the former two correlations are sensitive to perturbative particle production. Hence, in the following distributions the *transverse* correlation lies below the *forward* across the η-range, as momentum-conservation has a greater influence when the event axes converge with the direction of particle production. A similar explanation for the *forward* correlation is applicable to the dominance of the *forward* ϕ correlation in the central bin, *opposite* and in the mid-η range and the convergence at the extreme η-range.

The general remarks are similar to those for the detector-based geometry, but the differences between the distribution are more separated now that the orientation of each event is better identified. In particular, the *transverse* region can be clearly identified as lower than the others, consistent with it being an "underlying event" to the production of a "hard particle".

Table 6.11 shows the uncut b-correlation values in the central ($\eta = 0 - 0.5$), mid-range ($\eta = 2.5 - 3$) and extreme ($\eta = 4.5 - 5$) η bins for the *forward* ϕ-region along with the

relative correlation for *opposite* and *transverse* region.

	central bin			mid-range bin			extreme bin		
Tune	b_{for}	b_{oppo}/b_{for}	b_{tran}/b_{for}	b_{for}	b_{oppo}/b_{for}	b_{tran}/b_{for}	b_{for}	b_{oppo}/b_{for}	b_{tran}/b_{for}
DW	0.19	0.75	0.37	0.11	1.20	0.59	0.03	1.86	0.53
ACR	0.22	1.03	0.67	0.12	1.34	0.79	0.01	2.43	-0.02
Q20	0.20	0.79	0.45	0.09	1.28	0.56	0.01	5.07	1.24
P0	0.22	0.96	0.61	0.08	1.37	0.63	0.00	7.02	-3.78
PT0	0.22	0.94	0.60	0.08	1.49	0.67	-0.00	-25.85	13.42

Table 6.11: Central($\eta = 0 - 0.5$), mid-range ($\eta = 2.5 - 3$) and extreme ($\eta = 4.5 - 5$) correlation values for *forward* ϕ-region (b_{for}) with relative *opposite* and *transverse* correlations for various Pythia tunes at $\sqrt{s} = 900GeV$. *Forward* ϕ-region is $-\pi < \phi < -\pi/3$, the *opposite* region is $0 < \phi < 2\pi/3$ and *transverse* covers the two regions between, $-\pi/3 < \phi < 0$ and $2\pi/3 < \phi < \pi$. ϕ is defined by the highest $\mathrm{p_T}$ particle trajectory.

In the central η-region, the *forward* correlation values are similar, though there is more discrepancy in the other ϕ regions. In the *opposite* region there is a similar, though more prevalent, pattern to the detector geometry case. The old tunes, excluding ACR, have a lower correlation, compared to the *forward* region, than the new shower model tunes. There is also a large drop between in the *opposite* and *transverse* regions which was not seen in the detector geometry case. It can be seen that for all tunes most of the particle production in the central η region occurs in the axis of the hardest particle of the event. In the case of the old shower tunes without color reconnection (DW and Q20), larger proportion of the production occurs in the direction of the lead particle, compared with the new shower tunes and ACR. This is evident from the relative strengths of correlations in the DW and Q20 cases, where *opposite* and *transverse* have significantly lower correlation strengths relative to the *forward* region than the other tunes.

In the middle η-range ($\eta = 2.5 - 3$) the relative strength of correlations changes from the central trend such that the *opposite* region has the strongest correlation across all tunes. This is particularly true for the new shower models where there is a lower *forward* correlation and a higher relative *opposite* correlation than the DW and Q20 tunes. This, along with the relative strength of the *transverse* correlation, suggests particle production is more uniformly spread relative to the hardest particle in the event for the tunes involving color reconnection. The substantial drop between *opposite* and *transverse*, seen to a lesser extent in the detector geometry case, can now be attributed to particle production across the event shape.

As above, when the same analysis is made at the extreme end of the η-region the tune and ϕ-space differences are mixed with statistical fluctuations. However, the general trend across the η of decreasing correlation strength in is common to all tunes.

It is concluded that the orientation of the ϕ-regions about the hardest particle in the event maps the correlation to particle production across the event. With this orientation physically meaningful changes in particle production across $\eta - \phi$ can be measured.

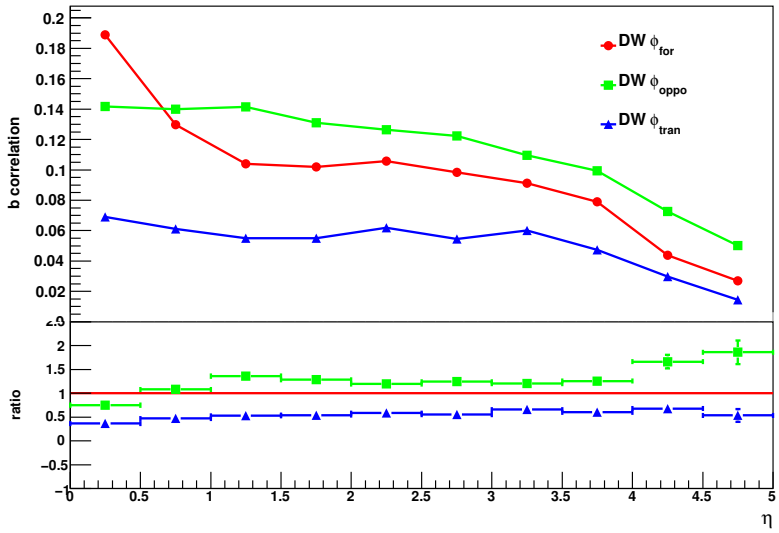

Figure 6.28: Above: b-correlation distributions for hadron-level charged particles for DW Pythia tune over various explicit ϕ-cuts based on the lead particle trajectory. Below: Ratio comparison to *forward* distribution.

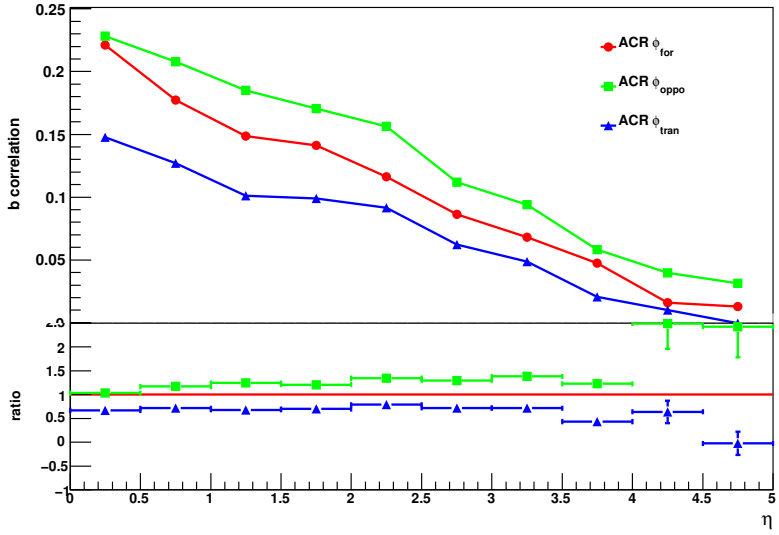

Figure 6.29: Above: b-correlation distributions for hadron-level charged particles for ACR Pythia tune over various explicit ϕ-cuts based on the lead particle trajectory. Below: Ratio comparison to *forward* distribution.

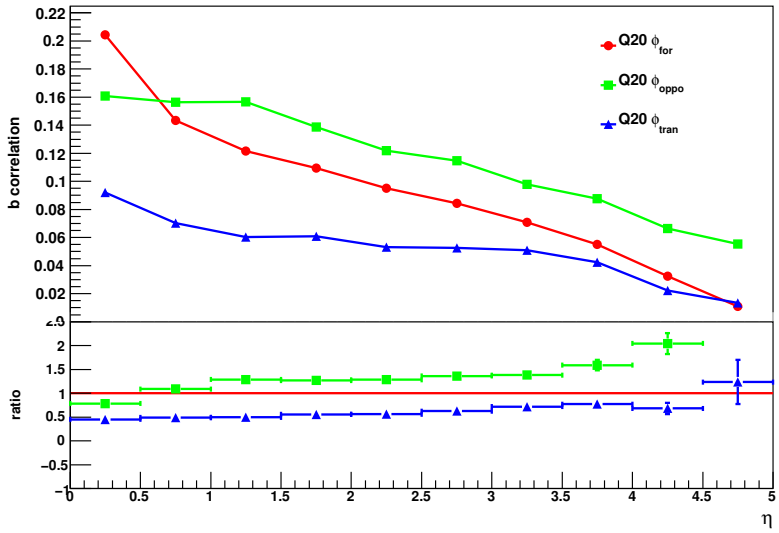

Figure 6.30: Above: b-correlation distributions for hadron-level charged particles for Q20 Pythia tune over various explicit ϕ-cuts based on the lead particle trajectory. Below: Ratio comparison to *forward* distribution.

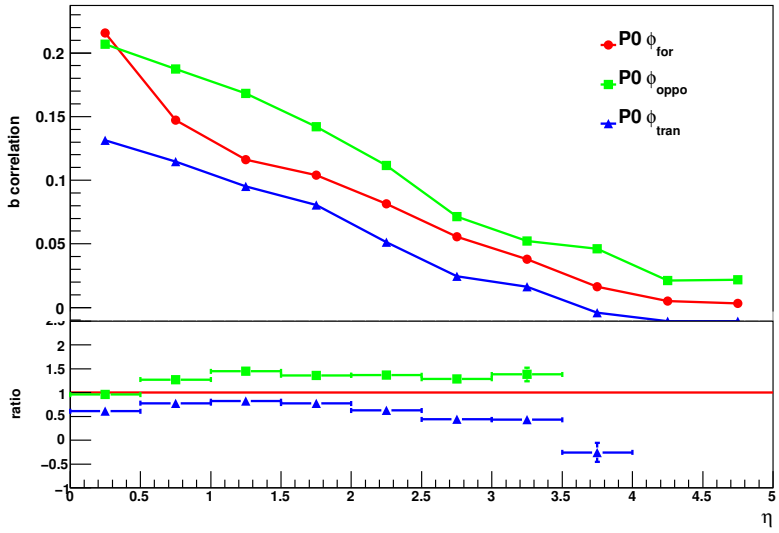

Figure 6.31: Above: b-correlation distributions for hadron-level charged particles for P0 Pythia tune over various explicit ϕ-cuts based on the lead particle trajectory. Below: Ratio comparison to *forward* distribution.

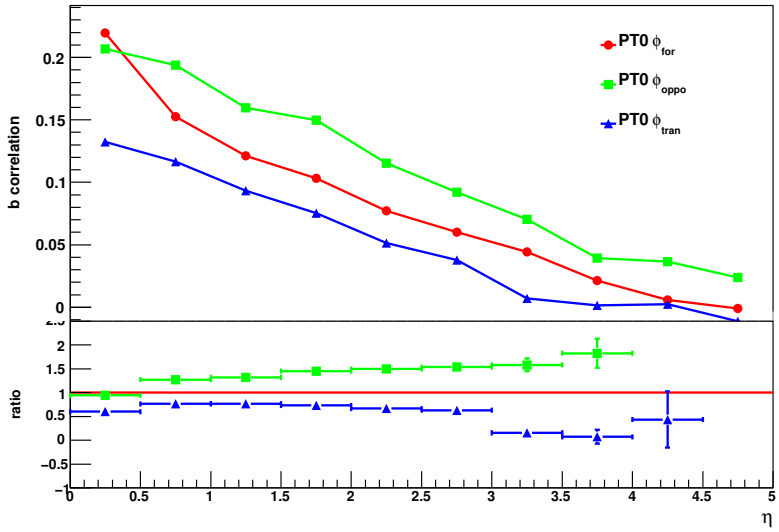

Figure 6.32: Above: b-correlation distributions for hadron-level charged particles for PT0 Pythia tune over various explicit ϕ-cuts based on the lead particle trajectory. Below: Ratio comparison to *forward* distribution.

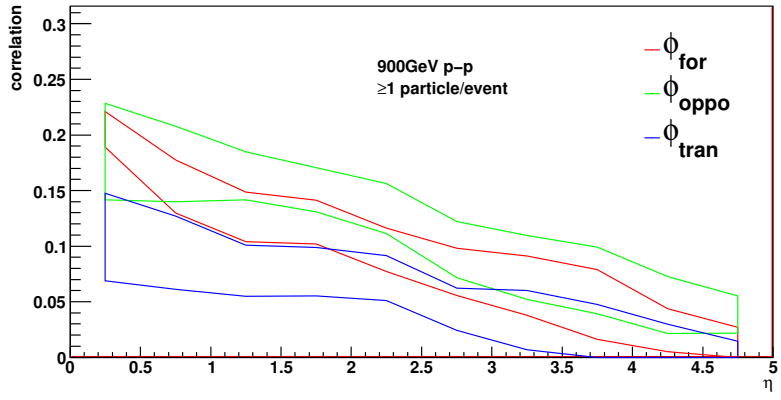

Figure 6.33: b-correlation distributions for hadron-level charged particles for various Pythia tunes over explicit ϕ-cuts based on the lead particle trajectory. The area of each distribution represents the dispersion of correlation values between tunes.

6.6 Event-shapes

Having probed the η particle distribution of events using the inclusive b-correlation, and the $\eta - \phi$ correlations, the next characteristic of events to investigate is their event-shape properties. For early data, where only charge particle multiplicity is considered in the central region of an experiment, event-shapes in the transverse plane will be the most easily analysed. Event shapes are characterised by the transverse thrust ($T_\perp$) and transverse minor ($M_\perp$) values and axes of each event[59].

6.6.1 Transverse Thrust

The transverse thrust axis can be found by maximising the coincidence of an arbitrary vector with the dominant direction of particle flow in an event in ϕ. The thrust value is then defined as:

$$T_\perp = max_{|\mathbf{n_t}|=\mathbf{1}} \frac{\Sigma_i |\mathbf{n_t}.\mathbf{p_t^i}|}{\Sigma_i |\mathbf{p_t^i}|} \, , \tag{6.4}$$

where i runs over the charged tracks in the event, $\mathbf{n_t}$ is the transverse thrust axis unit vector and $\mathbf{p_t^i}$ is the track transverse momentum vector. Thrust values lie between $0.5 < T_\perp < 1.0$ for di-jet- like events, where the highest momentum particles are produced back-to-back. These events have a pencil-like shape in ϕ, with particle production aligned predominantly along a single axis. Such events have high transverse thrust values ~ 1, which is expected for particle production dominated by perturbative processes. In contrast, events where non-perturbative and/or MPI production is predominant more particles will lie off a production axis, giving a more circular distribution of tracks in ϕ, for which the transverse thrust value will lie closer to 0.5. The effect of ISR and FSR should be to smear the orientation of particle production in events.

Fig.6.34 shows the transverse thrust distributions of the low-$\mathrm{p_T}$ sub-samples of the selected tunes. There is clear agreement between tunes to $10-20\%$ over most of the range. This presumably reflects the fundamental similarity between the MPI-based perturbative modelling in these tunes.

Fig.6.35 shows the transverse thrust distributions for model sub-processes for each individual tune. For the hard samples (i.e., before showering and MPI), the distributions are more pencil-like, peaking at higher values of $T_\perp$ (illustrated light blue curves). It is interesting that, for the old model tunes, the MPI component by itself (blue) only reduces the peak value very slightly, whereas the addition of radiation (green) produces a much larger shift. However, in the new model tunes the MPI and radiation only samples each appear to give a similar-size shift. Despite their apparent similarities, there are therefore still interesting differences underlying these distributions, which, as was shown in the previous section, the

measurement of b-correlations can help resolve.

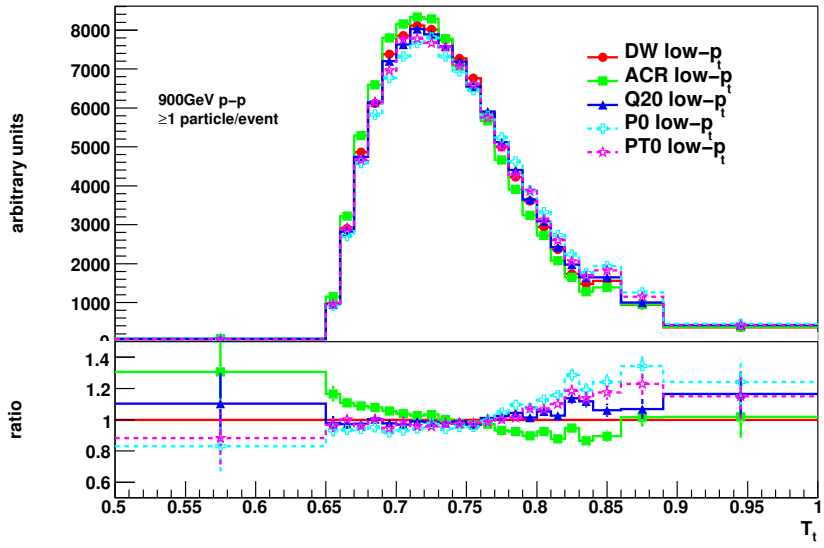

Figure 6.34: Above: Transverse thrust distributions for low-$\mathrm{p_T}$ sub-sample of selected tunes. Plots have been area-normalised. Below: Ratio is calculated with respect to the DW tune.

6.6.2 Transverse Minor

The transverse minor axis lies perpendicular to the thrust axis in ϕ. It is defined as:

$$M_{\perp} = max_{|\mathbf{n_t}|=1} \frac{\Sigma_i |\mathbf{n_t} \times \mathbf{p_t^i}|}{\Sigma_i |\mathbf{p_t^i}|} \,, \tag{6.5}$$

with similar definitions as before. Fig.6.34 shows the transverse minor distributions of the low-$\mathrm{p_T}$ sub-samples of the selected tunes. As before there is clear agreement between tunes. Also as before, as fig.6.37 shows, contributions from each model component exhibiting similar differences as for $T_{\perp}$.

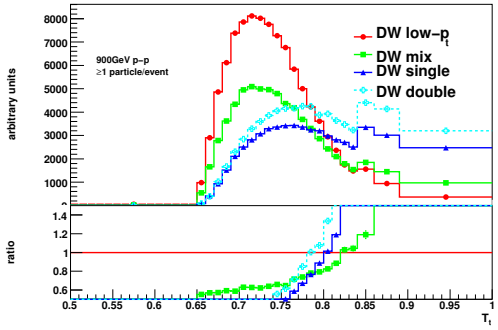

(a)

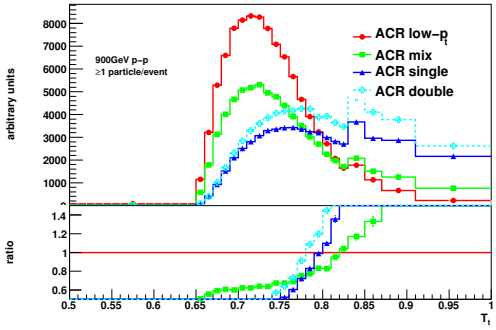

(b)

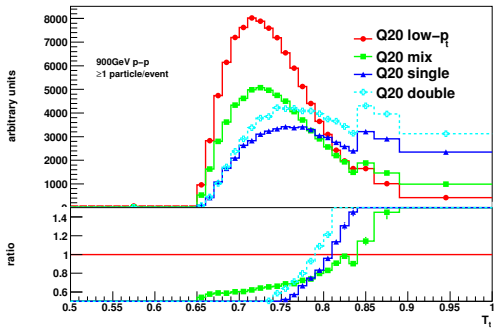

(c)

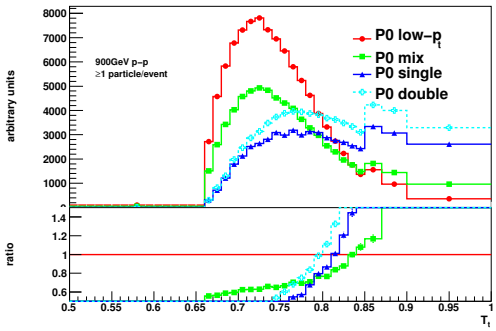

(d)

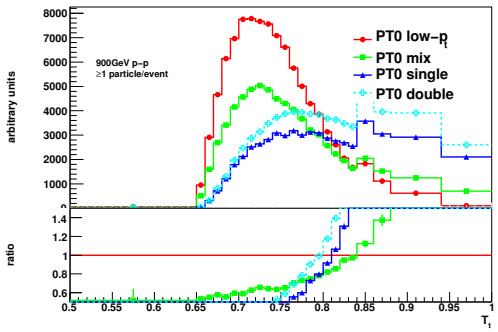

(e)

Figure 6.35: Transverse thrust distributions for low-p_T, ND, DD, elastic and mixed sub-samples of a) DW, b) ACR, c)Q20 , d) P0 & e) PT0. Plots have been area-normalised. Ratios are calculated with respect to the low-p_T sample

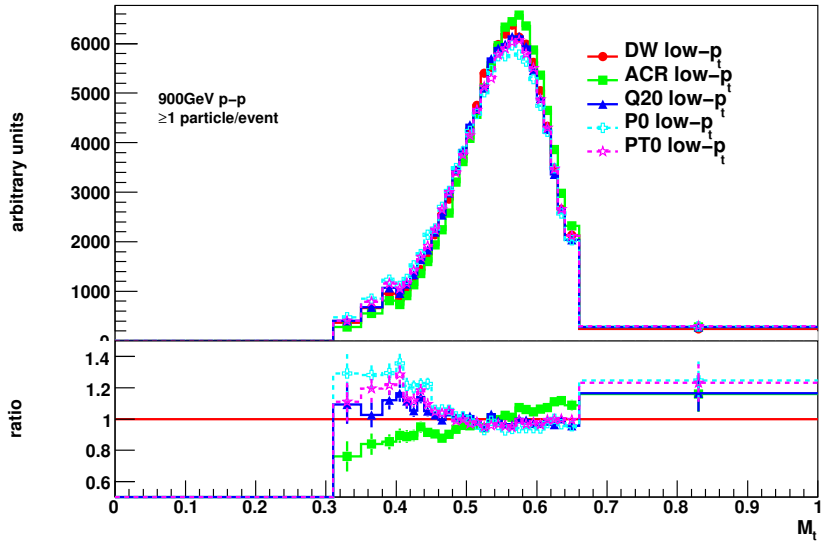

Figure 6.36: Above: Transverse minor distributions for low-p_T sub-samples of selected tunes. Plots have been area-normalised. Below: Ratio is calculated with respect to the DW tune.

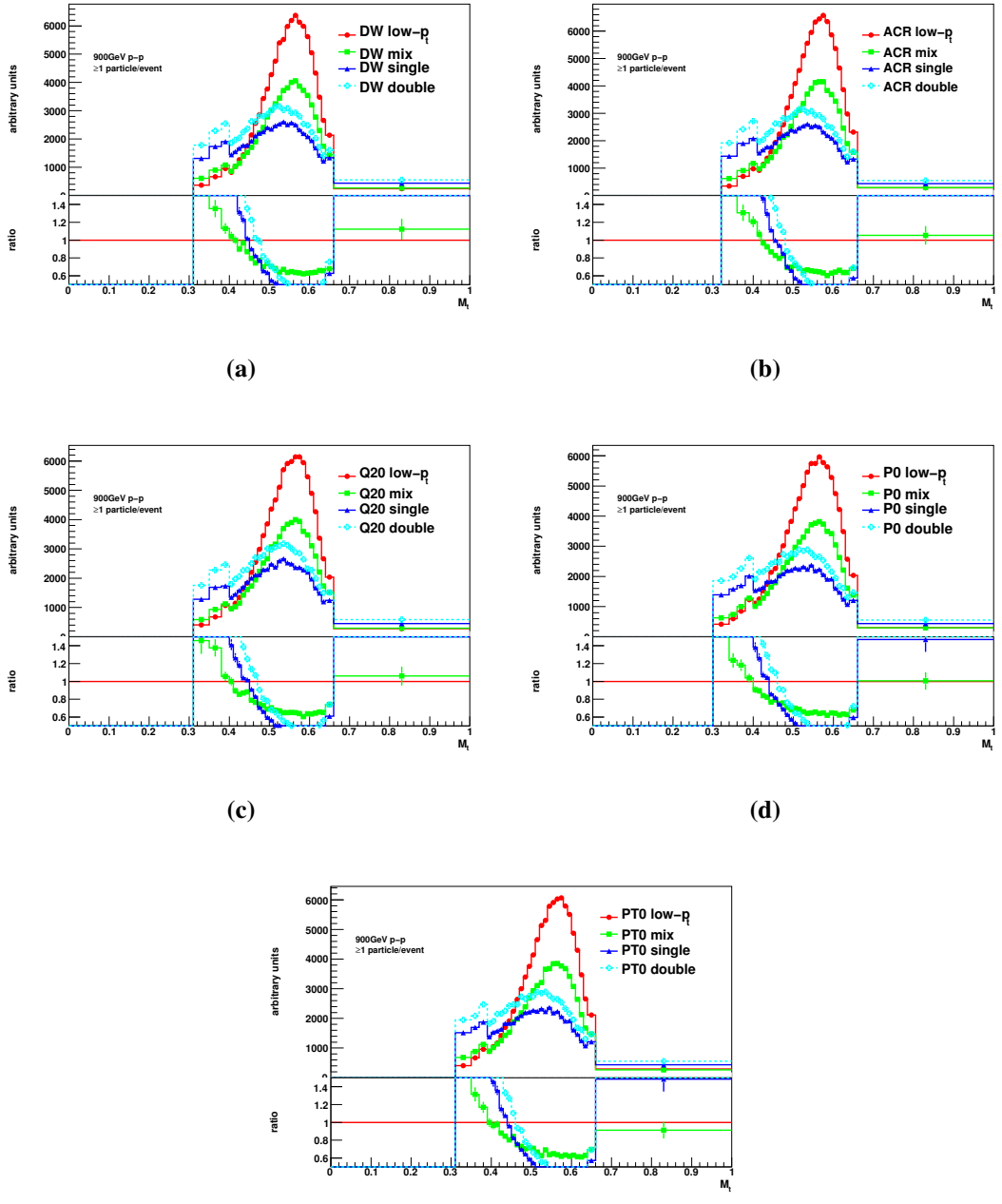

(a) **(b)** **(c)** **(d)** **(e)**

Figure 6.37: Transverse minor distributions for low-p_T, ND, DD, elastic and mixed subsamples of a) DW, b) ACR, c) Q20, d) P0 & e) PT0. Plots have been area-normalised. Ratios are calculated with respect to the low-p_T sample.

6.7 Conclusion

Forward-backward correlations can be used to extract information on the relative strengths of different sources of particle production in minimum-bias events: models dominated by a single hard (dijet) interaction exhibit strong short-range correlations and weak long-range ones, while models with a larger component of soft production between the remnants generate stronger long-range correlations. This has been illustrated by comparing a small set of recent tunes of the Pythia 6 Monte Carlo model. Although they share a common phenomenological framework for the calculation of multiple parton interactions interfaced to the Lund string fragmentation model, they differ qualitatively in the shower and remnant modelling, and quantitatively in the fragmentation tuning and amount of showering vs. MPI.

It was shown that forward-backward can discern between physical regions of particle production over various kinematic regions. Correlations were investigated which involved η, $\mathrm{p_T}$ and ϕ dependence. Particle-momentum distributions were found to be heterogeneous across the η-range due to the differing particle production mechanisms and parameters between tunes. It was also shown that the long-range correlation is dominated by non-perturbative (low-$\mathrm{p_T}$) particles. In the case of ϕ-dependence the importance of proper mapping to the event shapes was shown to be crucial to discern how particle production varies over a physically meaningful $\eta - \phi$ space. With this orientation changes in particle production across $\eta - \phi$ can be measured. In each case, b-correlations show how the particle production fluctuates in each sub-process across the η-region with each tune without uniform trends. Hence it is unlikely any tune will match all data completely.

These correlations are further complemented by measurements of event shapes, such as transverse thrust and transverse minor. Together they can help shed light on the overall properties and structure of minimum-bias events. For instance, a model with a strong dominance of perturbative (mini-)jet production should also predict event shapes closer to equivalent perturbative QCD ones in dijet events, while models characterised by other particle production mechanisms should exhibit spectra further from the factorised perturbative QCD prediction.

Hence, this investigation clearly motivates the measurement of these observables at the LHC and their inclusion to the "standard" set of distributions for future colliders in order to develop and improve event generator predictions.

Chapter 7

FB-correlation $7\ \mathrm{TeV}$ and $900\ \mathrm{GeV}$ Measurement

Given the argument for the addition of forward-backward correlation based observables to the "standard" minimum bias plots, the following chapter documents work done measuring the forward-backward (or b) correlation in the ATLAS experiment at the LHC. This chapter compares data taken in the first year of LHC operation at $900\ \mathrm{GeV}$ and $7\ \mathrm{TeV}$ collision energies to Monte Carlo predictions for the same energies. ATLAS produced fully simulated minimum bias events of various tunings are calculated and compared to measured data. The data measurements are then corrected, using a multi-variable technique, and compared to hadron-level generator predictions.

Much of this chapter is based upon [60]. The work was done in collaboration with Craig Buttar, Samir Ferrag and Peter Bussey. In particular the section on Multiple Regression Theory was developed by Samir Ferrag, all other sections are combined work.

The chapter is structured as follows: first the b-correlation is reformulated in 7.1; the Monte Carlo and data samples, event selection and cut-flow are described in section 7.2; section 7.3 describes the method for correcting the measured FB-correlation which is validated in section 7.4; the systematic effects are discussed in section 7.5 and the results are presented in section 7.6; finally 7.7 has some concluding remarks.

7.1 Reformulated forward-backward correlation

The FB-correlation, denoted ρ_{fb}, between two charged-particle-multiplicities n_b and n_f is defined by:

$$\rho_{fb} = \frac{cov(n_f, n_b)}{\sigma(n_f)\sigma(n_b)}, \tag{7.1}$$

$$\rho_{fb} = \frac{\langle (n_f - \langle n_f \rangle)(n_b - \langle n_b \rangle) \rangle}{\sqrt{\langle (n_f - \langle n_f \rangle)^2 \rangle \langle (n_b - \langle n_b \rangle)^2 \rangle}}, \tag{7.2}$$

where $\langle n_f \rangle$ is the mean of the multiplicity-distribution of n_f as estimated in the pseudo-rapidity bin $\eta_1 < \eta < \eta_2$ and $\langle n_b \rangle$ is the mean of the multiplicity-distribution of n_b as estimated in the pseudo-rapidity bin $-\eta_2 > \eta > -\eta_1$. $\sigma(n_f)$ and $cov(n_f, n_b)$ are the variance of the multiplicity distribution of n_f and the covariance between n_f and n_b multiplicities, respectively.

The FB-correlation can be derived from a linear regression of n_b on n_f, full details are given in section 7.3:

$$\langle n_f \rangle = a + b \cdot n_b, \tag{7.3}$$

where the gradient of the fit b is equal to:

$$b = \frac{cov(n_f, n_b)}{\sigma(n_b)^2}. \tag{7.4}$$

The gradient of the fit b is related to the FB-correlation by:

$$\rho_{fb} = b\frac{\sigma(n_b)}{\sigma(n_f)}. \tag{7.5}$$

As we are dealing with symmetric pseudo-rapidity bins, it is expected that $\sigma(n_f) = \sigma(n_b)$ and so b can be taken as a measurement of the FB-correlation ρ_{fb}.

In the study presented, a pseudo-rapidty bin-size of $\delta\eta = 0.5$ was chosen[1] over the range $-2.5 < \eta < 2.5$. The multiplicity-pairs are estimated in the following pairs of forward and backward pseudo-rapidty bins: $0 \leq |\eta| < 0.5$, $0.5 \leq |\eta| < 1$, $1 \leq |\eta| < 1.5$, $1.5 \leq |\eta| < 2$ and $2 \leq |\eta| < 2.5$. For convenience, those five pairs of pseudo-rapidity bins are referred to as: bin_0, bin_1, bin_2, bin_3 and bin_4. The hadron-level (true) multiplicities in the forward and backward regions are respectively denoted n_f and n_b and the observed (measured) multiplicities in the forward and backward region are respectively denoted m_f and m_b .

7.2 Correlations in Monte Carlo and Selection

This section documents the data and Monte Carlo samples used in the analysis. Details of event and object selection are given. It ends with initial reconstructed distributions of FB-correlations for data and MC events.

[1] See Appendix A for a study of the impact of the pseudo-rapidity bin size.

7.2.1 Monte Carlo Models

All the samples used in this analysis were produced by the ATLAS collaboration[2]. In the case of the 7 TeV analysis, five Monte Carlo (MC) models were used to determine the factors required to correct the observed forward-backward (FB) correlation to obtain the hadronic-level FB-correlation. They are also compared to the hadronic level FB-correlation results obtained from the data. Three Pythia based tunes were used: MC09, DW, Perugia0, which are based on Pythia version 6.4.21 in addition to an untuned Pythia 8 sample. A Phojet 6.1.35 sample was included to contrast with the low-p_T model of Pythia , although it has a similar particle hadronisation model to Pythia . Each sample consists of a mixture of non-diffractive, single-diffractive and double-diffractive events, as well as a central diffractive component in the case of Phojet. The relevant proportions are shown in Table 7.1.

	Non-Diffractive	Single-Diffractive	Double-Diffractive	Central-Diffractive
Pythia (900 GeV)	34.4 mb	11.8 mb	6.4 mb	-
Pythia (7 TeV)	48.5 mb	13.7 mb	9.2 mb	-
Phojet (7 TeV)	61.6 mb	10.7 mb	3.9 mb	1.1 mb

Table 7.1: MC sub-process cross-sections at $\sqrt{s} = 900$ GeV and 7 TeV.

Tune MC09 [61] was created by ATLAS to mimic the higher particle production rates seen in other experiments. Tune DW [62] was created to describe underlying event data at the Tevatron. Tune Perugia0 [39] was created using the p_T-ordered shower of Pythia , in contrast to the Q^2-ordering of MC09 and DW, and tuned using minimum bias data from previous experiments. The Pythia8 [63] uses several different physics models to previous Pythia tunes and has not yet been tuned to data yet. The Phojet model [64] uses a dual parton event description and has not been tuned to recent experiments.

For the 900 GeV analysis, only events generated using the MC09 tune were available with low-p_T track reconstruction.

The MC samples used for 900 GeV and 7 TeV analyses are given in tables C.1 and C.2 of appendix C. The data samples used for 900 GeV and 7 TeV are given in table C.3. Around 1 million Monte Carlo events for each tune were used to determine the correction factors and study the systematic uncertainties at 7 TeV and around 15 million data events were used for the analysis. Full details of the MC samples can be found in reference[58].

Figure 7.1 shows the values of FB-correlations for various tunes at $\sqrt{s} = 7$ TeV for generated charged particles with $p_T > 100$ MeV. There is a disagreement between the various predictions of the FB-correlation values. The corresponding spread is around 25% at high $\Delta\eta$. However, it should be reiterated that none of the models used in this study has been tuned to the measurements of the FB-correlation by previous experiments.

[2] See appendix C for a complete list of the ATLAS data samples used in this analysis

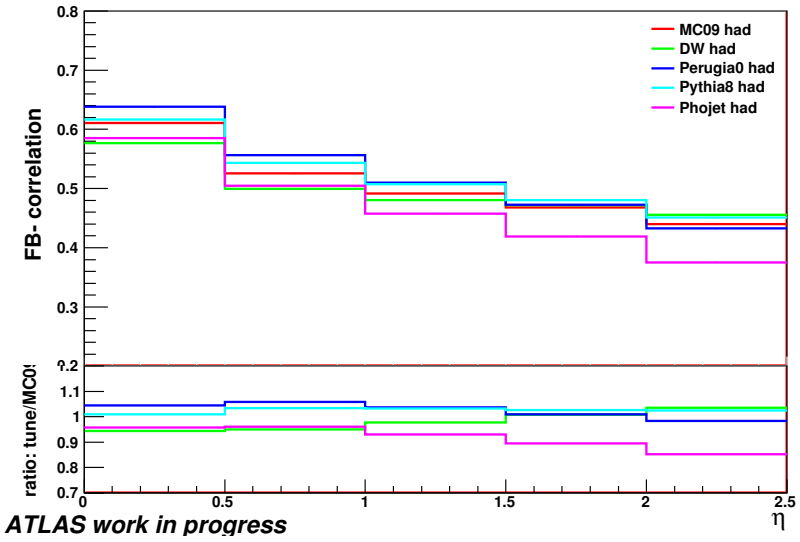

Figure 7.1: Above: Forward-backward correlation in charged particle multiplicity for generated charged particles with $\mathrm{p_T} > 100$ MeV in symmetrically opposite η-bins for events with two charged tracks within the kinematic range $\mathrm{p_T} > 100\,\mathrm{MeV}$ and $|\eta| < 2.5$ at $\sqrt{s} = 7\,\mathrm{TeV}$ for various MC tunes. Below: Ratios comparing the generated correlation from each MC tune to that from the MC09 tune.

7.2.2 Event Selection

The event and track selections for the standard minimum bias (MB2.0) analysis [58] were also used for this analysis. In addition to some basic run number, beam crossing and data quality checks, an event is selected if it satisfies the following requirements:

- Level 1 minimum bias trigger (`L1_MBTS_1`)
- At least one **primary vertex** per event, reconstructed as follows:
  - vertex built with tracks of $\mathrm{p_T} > 100$ MeV
  - transverse distance of closest approach to beam spot $d_0^{BS} > 4\mathrm{mm}$
  - transverse and longitudinal errors $\sigma(d_0^{BS}) < 5\mathrm{mm}$ and $\sigma(z_0^{BS}) < 10\mathrm{mm}$, respectively
  - at least one pixel layer and 4 SCT layer hits
  - at least 6 pixel layer and SCT layer hits combined
  - the vertex with the highest $\Sigma \mathrm{p_T}$ is selected as the primary vertex
- Pile-up removal: events with non-primary vertices with 4 or more tracks are rejected
- At least two selected tracks per event

The tracks are selected according to the following quality criteria:

- tracks are reconstructed using $inside-out$ or low-$\mathrm{p_T}$ tracking algorithms
- pixel layer: at least one pixel hit and a hit in the inner pixel layer if one is expected[3]
- SCT layer: at least 2, 4 or 6 SCT hits for $\mathrm{p_T} > 100$, 200 or 300 MeV tracks, respectively
- for tracks with $\mathrm{p_T} > 10$ GeV, the track-fitting probability must be ≥ 0.01
- kinematics: $\mathrm{p_T} > 100$ MeV, $|\eta| < 2.5$
- trajectory: $|d_0| < 1.5\mathrm{mm}$, $|z_0| \cdot \sin(\theta) < 1.5\mathrm{mm}$

For MC generated events, as in the reconstructed case, two charged particles are required per event. Accepted hadron-level charged particles are defined as:

- kinematics: $\mathrm{p_T} > 100$ MeV, $|\eta| < 2.5$
- stable: $0 < \mathrm{barcode} < 200,000$ (equivalent to proper-lifetime cut)

Tables 7.2 and 7.3 show the number of selected events and selected tracks obtained using the above selection.

[3] This means that the track is not so close to the edge of the outer pixel layers that its trajectory would miss the inner layer.

Tune	data	MC09	DW	Perugia0	Pythia8	Phojet
sample	15518295	1000937	1000940	999996	1000929	999282
luminosity	12848036	1000937	1000940	999996	1000929	999282
trigger	11307065	928705	929143	928922	928218	964237
vertex	10168544	836544	831968	825802	859764	910984
pile-up	10140813	836500	831914	825753	859684	910893
selected events	10066072	827112	821334	814366	854996	905466
selected tracks	209809408	14570440	12230701	12683910	16394322	14628282

Table 7.2: Size of the samples and number of events and tracks selected using the MB2.0 cuts for the 7 TeV data & MC samples. N.B. the luminosity cut only has an effect on real data as it is an experimental data quality cut.

Tune	data	MC
sample	1016395	999974
luminosity	530255	999974
trigger	521660	918077
vertex	371061	799155
pile-up	370961	799118
selected events	366919	787655
selected tracks	4650625	8736742

Table 7.3: Size of the samples and number of events and tracks selected using the MB2.0 cuts for the 900 GeV data & MC samples. N.B. the luminosity cut only has an effect on real data as it is an experimental data quality cut.

7.2.3 The Observed Correlation

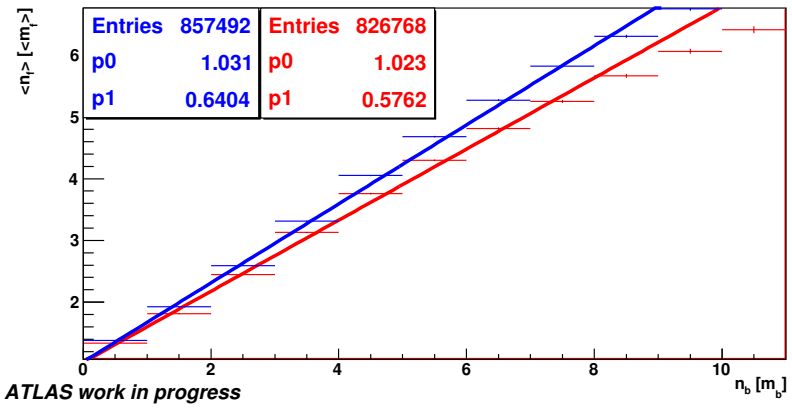

Figure 7.2: Linear regression of n_f on n_b for generated charged particles (blue) and reconstructed charged tracks (red) with $\mathrm{p_T} > 100$ MeV in the central η region ($|\eta| < 0.5$)) for events with two charged tracks within the kinematic range $\mathrm{p_T} > 100$ MeV and $|\eta| < 2.5$ at $\sqrt{s} = 7$ TeV generated with Pythia MC09 tune. The vertical error bar is the RMS of the $n_f(m_f)$ distributions.

In this analysis, the FB-correlations are calculated using the multiplicity of charged tracks with $\mathrm{p_T} > 100$ MeV. Figure 7.2 shows the hadron-level regression line of n_f on n_b fitted

to extract the ρ_{had} and the observed-level regression line of m_f on m_b fitted to extract ρ_{obs}. This figure was produced from the simulated charged particle multiplicities in the central pair of pseudo-rapidity bins, i.e. bin_0 in the 7.3, using the MC09 tune sample. The measured central charged particle density is 5.6, giving an average of 2.8 charged particles for the pseudo-rapidity bin-width of $\delta\eta = 0.5$ used in this analysis.

There is a deviation from linearity at high multiplicities greater around 10. This is due to the low statistics at high multiplicities in the sample (the error bars in this profile plot reflect the spread around the central mean of a bin and not number of entries in the bin). If the statistics of the sample are increased, the linearity is then observed for higher values of multiplicities.

The FB-correlation at the hadron-level, ρ_{had}, between n_f and n_b is diluted at the observed-level resulting in a smaller measured correlation, ρ_{obs}. This is primarily due to tracking efficiency that reduces the track multiplicity in each pseudo-rapidity bin in an independent way, i.e. the number of lost tracks that results in n_f being observed as m_f, is independent of the number of lost tracks that results in n_b being observed as m_b. This results in a reduction of the interdependence between m_f and m_b and hence the measured correlation is lower than that of the hadron-level.

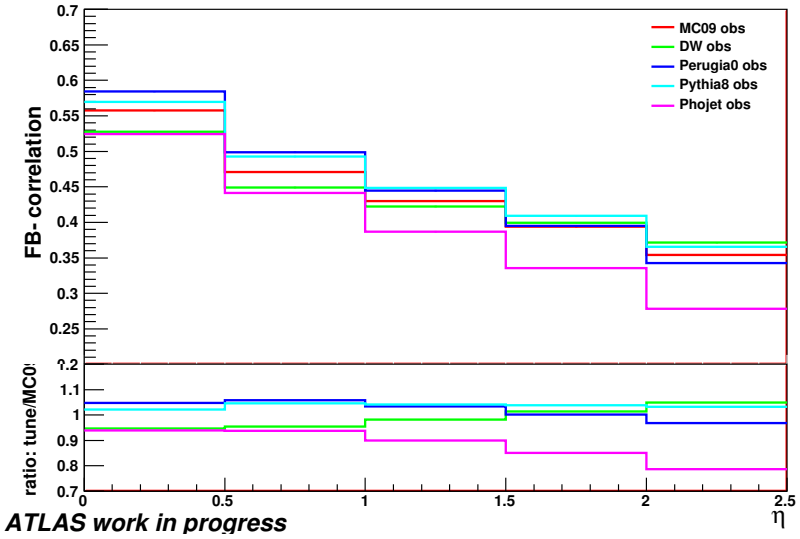

Figure 7.3: Above: Forward-backward multiplicity correlation for reconstructed charged tracks with $\mathrm{p_T} > 100$ MeV in symmetrically opposite η-bins for events with two charged tracks within the kinematic range $\mathrm{p_T} > 100$ MeV and $|\eta| < 2.5$ at $\sqrt{s} = 7$ TeV for various MC tunes. Below: Ratio of observed FB-correlations.

Figure 7.3 shows the observed FB-correlations over the pseudo-rapidity bins for various Monte Carlo tunes. Though the relative ordering of the correlation strengths of the tunes stays constant, their relative strengths fluctuate compared to the hadron-level. Figure 7.4 shows the ratio of observed-level FB-correlations to the hadron-level values, ρ_{obs}/ρ_{had}. The

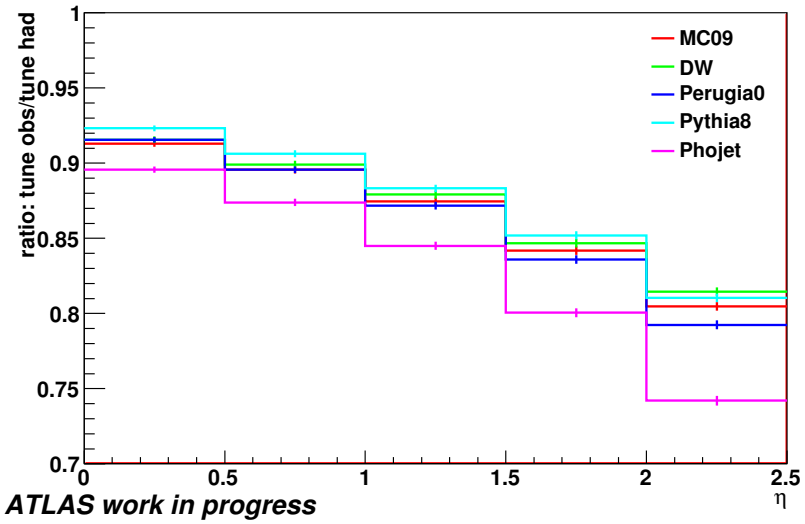

Figure 7.4: Ratio of observed FB-correlations to hadron-level FB-correlations.

observed-level FB-correlations are clearly smaller than those at hadron-level. For example, the FB-correlation values found in the hadron-level case were between $0.576 \pm 0.15\%$ and $0.638 \pm 0.13\%$ for the central pairs of pseudo-rapidity bins, while the values lie between $0.524 \pm 0.17\%$ and $0.584 \pm 0.15\%$ at the observed-level. The ratio ρ_{obs}/ρ_{had} decreases with increasing pseudo-rapidity gap, $\Delta\eta$, as expected from the decreasing tracking efficiency at high pseudo-rapidities.

It is clear from figure 7.4 that the reduction in the measured FB-correlation depends on the rapidity bin and on the tune of the MC sample simultaneously. In the case of Phojet, it is varying from $\sim$ 10% in bin_0 to $\sim$ 25% in bin_4. In the case of the extreme pair of pseudo-rapidity bins, bin_4, the FB-correlation decreases $\sim 7\%$ more for the Phojet tune than for MC09 tune. This is due to the differing parameters and the models used for particle production in each tune. Hence, it is important to develop a correction method that is able to correct for each tune and at the same time is independent of the tune. This will be the goal of the section 7.3 of this note.

7.3 Corrections

In this section, we develop the correction method to be applied on the measured data. The corrections are based on Multiple Regression Theory(MRT) [65]. This section begins with an overview and a brief summary of multiple regression theory. Correction methods are then derived to link the reconstructed to the hadron-level FB-correlations.

7.3.1 Overview

As a first attempt to correct the measured FB-correlations for detector effects, the observed multiplicities in the forward and the backward $|\eta|$ bins were unfolded individually using a Bayesian method [66]. Then the FB-correlation was calculated using the corrected multiplicities. This was found to reduce the correlation of forward and backward regions resulting in the corrected correlation being smaller than the measured correlation. This is believed to be due to the fact that the forward and backward multiplicities should be unfolded using two different matrices which are built simultaneously. One matrix accounts for the detector effects. It is used to unfold one of the two multiplicities. The other matrix accounts for both detector effects and physical correlations between the forward and backward multiplicities. It is used to unfold the other multiplicity.

An alternative method based on multiple regression theory[65] was developed. It takes account of all the interdependencies between the multiplicities n_f, n_b, m_f and m_b. This includes the correlations between n_f and m_f and between n_b and m_b due to experimental effects, and the physical correlation between n_f and n_b. This allows the relative contribution of the two effects to be evaluated. The correction factors derived using the multiple regression method in section 7.3.2.2 agree with those derived from comparing the MC reconstructed to MC generated correlations in section 7.4.3. The method is validated in section 7.4 and is shown to be model independent in section 7.5.

7.3.2 Introduction to Linear Regressions

Probability Density Functions of one variable can be summarised using constants such as mean, variance, etc. In the same way, the relationship between two or more variables can be summarised using constants such as correlations. Finding the relationship between variables is done using regressions. When only two variables are involved, we speak about a simple regression or a simple correlation. When more variables are involved, we speak about multiple regressions or multiple correlations.

7.3.2.1 Simple Regressions

If X and Y denote the two variables under consideration and they are distributed as shown in figure 7.5, then for a particular value of $X = X_i$, Y follows a conditional distribution $(Y|X_i)$. This conditional distribution has a mean which can be written as:

$$\langle Y_{X_i} \rangle = E(Y|X_i) \, . \tag{7.6}$$

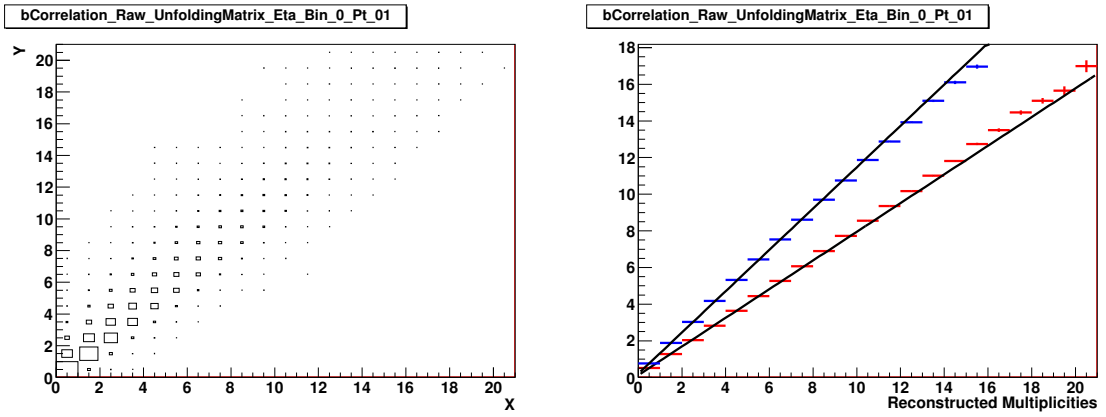

Figure 7.5: Left: scatter-plot X vs Y. Right: linear regressions of X on Y (red) and of Y on X (blue).

Similarly, by considering the conditional distribution, $(X|Y_i)$, of X given a particular value of $Y = Y_i$, we have:

$$\langle X_{Y_i} \rangle = E(X|Y_i) \; . \tag{7.7}$$

Equations (7.6) and (7.7) are called regression curves, or regressions of Y on X and of X on Y respectively. The regression curves of Y on X and X on Y are shown in Figure 7.5.

If all the points $(X, \langle Y_{X_i} \rangle)$ and the points $(Y, \langle X_{Y_i} \rangle)$ lie on straight lines as in figure 7.5, then the equations (7.6) and (7.7) can be approximated by linear regression equations given by:

$$\langle Y_{X_i} \rangle = \langle Y \rangle = a + b \cdot X, \tag{7.8}$$

$$\langle X_{Y_i} \rangle = \langle X \rangle = a' + b' \cdot Y \; . \tag{7.9}$$

Where the coefficients a and b are called linear regression coefficients and can be determined using the method of least squares. Applying the least squares method to N data points (X,Y) gives the coefficient of the slope of the linear regression of Y on X[65]:

$$\begin{aligned} b = \frac{N \cdot (\sum XY - (\sum X)(\sum Y))}{N \cdot (\sum X^2 - (\sum X)^2)}, \\ = \frac{Cov(X,Y)}{Var(X)} \; , \end{aligned} \tag{7.10}$$

where $Cov(X,Y)$ and $Var(X)$ are respectively the covariance of X, Y and the variance of X.

To simplify the notation, we can define the variables $x = X - \langle X \rangle$ and $y = Y - \langle Y \rangle$.

Equations (7.8) and (7.10) then simplify to:

$$y = b \cdot x, \qquad b = \frac{\sum xy}{\sum x^2} = \frac{\sum xy}{N \cdot \sigma_X^2} \,. \tag{7.11}$$

$$\tag{7.12}$$

Similarly, for the regression of x on y, equations (7.9) and (7.10) then simplify to:

$$x = b' \cdot y, \qquad b' = \frac{\sum xy}{\sum y^2} = \frac{\sum xy}{N \cdot \sigma_Y^2} \,. \tag{7.13}$$

$$\tag{7.14}$$

σ_x and σ_y are respectively the standard deviations of the variables X and Y (i.e. x and y).

The Correlation coefficient between the two variables X and Y is defined as:

$$\rho = \frac{\sum xy}{N \cdot \sigma_x \sigma_y}. \tag{7.15}$$

The correlation between two variables is a measure of how well they can be described by a defined relationship between them. For the linear regression case discussed here, the correlation describes how well x and y can be described by the linear relationships of equations (7.8) or (7.9).

ρ can be related to slope of the regression lines through the following relationships:

$$\begin{aligned} \rho = b \cdot \frac{\sigma_x}{\sigma_y} &= b' \cdot \frac{\sigma_y}{\sigma_x} \\ &= \sqrt{b \cdot b'} \,. \end{aligned} \tag{7.16}$$

The slopes of the regression lines from the regression of X on Y and of Y on X are not necessarily the same but the correlation coefficient is the same regardless of whether the regression is for X on Y or Y on X.

7.3.2.2 Multiple and Partial Regression

The case of simple regressions of two variables can be generalised to multiple regressions of three or more variables, allowing their interdependence to be characterised. In multiple regressions, the equation for estimating a dependent variable, say, X_1 from the independent variables $X_2, X_3, ...$ is called the regression equation of X_1 on $X_2, X_3, ...$ and can be written as $X_1 = F(X_2, X_3, ...)$.

For the case of four variables, the linear regression equation of X_1 on X_2, X_3 and X_4 has

the form:

$$X_1 = b_{1.234} + b_{12.34}\, X_2 + b_{13.24}\, X_3 + b_{14.23}\, X_4 \,, \tag{7.17}$$

where $b_{1.234}, b_{12.34}, b_{13.24}$ and $b_{14.23}$ are constants. If we keep X_3 and X_4 constant in equation (7.17), the graph of X_1 versus X_2 is a straight line with a slope $b_{12.34}$. Similarly, if we keep X_2 and X_3 constant, the graph of X_1 versus X_4 is a straight line with a slope $b_{14.23}$. Here, the subscripts after the dot indicate the variables held constant in each case.

The constant $b_{12.34}$ is called the partial regression coefficient of the regression of X_1 on X_2 keeping X_3 and X_4 constant. Similarly $b_{13.24}$ and $b_{14.23}$ are partial regression coefficients of the regression of X_1 on X_3 keeping X_2 and X_4 constant and of X_1 on X_4 keeping X_2 and X_3 constant, respectively.

To compute the partial regression coefficients $b_{1.234}, b_{12.34}, b_{13.24}$ and $b_{14.23}$, we use the following matrix notation: for 4 random variables estimated in N events, we define the $N \times 4$ matrix $X = (1, X_2, X_3, X_4)$, the 4-vector $B = (b_{1.234}, b_{12.34}, b_{13.24}, b_{14.23})$ and the N-vector $Y = X_1$. The linear regression equation (7.17) is then written as:

$$Y = X \cdot B \,. \tag{7.18}$$

By multiplying both sides by the transposed matrix X^T, one obtains the normal equation system:

$$X^T \cdot Y = (X^T X) \cdot B \,. \tag{7.19}$$

The vector B is then calculated by solving the equation above to obtain:

$$B = (X^T X)^{-1} \cdot X^T \cdot Y \,. \tag{7.20}$$

This corresponds to calculating $b_{1.234}, b_{12.34}, b_{13.24}$ and $b_{14.23}$ from the system of normal equations (7.19), which can be expressed as:

$$\begin{aligned}
\sum X_1 &= b_{1.234} + b_{12.34} \sum X_2 + b_{13.24} \sum X_3 + b_{14.23} \sum X_4 \\
\sum X_2 X_1 &= b_{1.234} \sum X_2 + b_{12.34} \sum X_2^2 + b_{13.24} \sum X_2 X_3 + b_{14.23} \sum X_2 X_4 \\
\sum X_3 X_1 &= b_{1.234} \sum X_3 + b_{12.34} \sum X_2 X_3 + b_{13.24} \sum X_3^2 + b_{14.23} \sum X_3 X_4 \\
\sum X_4 X_1 &= b_{1.234} \sum X_4 + b_{12.34} \sum X_2 X_4 + b_{13.24} \sum X_3 X_4 + b_{14.23} \sum X_4^2 \,.
\end{aligned} \tag{7.21}$$

Note that in the case of a simple regression involving 2 random variables, the vector B defined above is reduced to $B = (a, b)$, where a and b are the simple regression coefficients defined in equation (7.8). The expression of the coefficient of the slope b in equation (7.11)

is therefore the solution to the 2-dimensional system of normal equations, equivalent to the system in equation (7.21).

7.3.3 Application of Multiple Regression to correcting the correlation

7.3.3.1 Multiple Regression

The forward and backward particle multiplicities in respectively symmetric pseudo-rapidity bins are n_f and n_b at the hadron-level and m_f and m_b for the observed multiplicities. There are two kinds of correlations to be treated in the FB-correlation measurement: the physical correlation between n_f and n_b at the hadron-level, and the apparatus correlation that links the hadron-level multiplicities to the observed multiplicities, i.e. n_f to m_f and n_b to m_b. The observed correlation between m_f and m_b includes a mixture of both correlations. When we perform the corrections on the observed correlation, we should take into account both apparatus and physical correlations. The problem is treated as a four variable problem (n_f,n_b,m_f,m_b) and uses the multiple regression technique to separate between the physical and apparatus correlations and identify their contribution in a given correlation between two variables.

To apply the multiple regression method developed in section 7.3.2.2, let the 4 variables (X_1, X_2, X_3, X_4) correspond to (n_f,n_b,m_f,m_b), and simplify the equations by using the variables $x_i = X_i - \langle X_i \rangle$, with $i = 1, 2, 3, 4$. Applying a linear regression of each variable on the three others, we obtain the following system of equations:

$$\begin{aligned} x_1 &= b_{12.34}\, x_2 + b_{13.24}\, x_3 + b_{14.23}\, x_4 \\ x_2 &= b_{21.34}\, x_1 + b_{23.14}\, x_3 + b_{24.13}\, x_4 \\ x_3 &= b_{31.24}\, x_1 + b_{32.14}\, x_2 + b_{34.12}\, x_4 \\ x_4 &= b_{41.23}\, x_1 + b_{42.13}\, x_2 + b_{43.12}\, x_3\ . \end{aligned} \tag{7.22}$$

For each regression line in the above system, a system of equations like (7.21) can be built and solved to determine the partial regression coefficients $b_{ij.kl}$. These are reported in table 7.4 for the MC09 Monte Carlo sample at 7 TeV and for the MB2.0 selection criteria described in section 7.2.2. The multiplicities were obtained from the central η-pairs of bins. Hence, the forward multiplicities n_f and m_f are for $0 \leq \eta < 0.5$ and the backward multiplicities n_b and m_b are given for $-0.5 \leq \eta < 0$.

From the first row of table 7.4 where n_f is written as a function of n_b, m_f and m_b, the values of the partial coefficients show that the strongest interdependence is between n_f and m_f, with a corresponding partial regression coefficient of $b_{13.24} = 1.09$ (N.B. this is not a correlation, so a coefficient > 1 is acceptable). In contrast, the interdependence of n_f and n_b has a partial regression coefficient $b_{12.34} = 0.05$, and therefore is less significant in its

contribution. The correlation between n_f and $m_f$would be 100% if $b_{12.34} = 0$ and in the case of an ideal detector. From the partial coefficients of the third row, we see that the most relevant variable to predict the value of m_f is n_f. Once again it is the detector correlation which is most relevant when the 4 multiplicities are analysed simultaneously.

This analysis characterises the relationship between the predicted variable, n_f , and the predictor variables n_b, m_f, and m_b. This does not describe how the correlations between a given pair of variables is linked to the correlations between other pairs of variables. Specifically, it does not show how the physical correlation at hadron-level between n_f and n_b is linked to the observed correlations between m_f and m_b nor how the hadron-level correlation are linked to the apparatus correlations between n_f and m_f (n_b and m_b). To extract the relationship between the correlations, further analysis is required. This is presented below.

	$X_1 = n_f$	$X_2 = n_b$	$X_3 = m_f$	$X_4 = m_b$
$X_1 = n_f$	–	0.05 ± 0.006	1.09 ± 0.003	0.05 ± 0.007
$X_2 = n_b$	0.05 ± 0.006	–	0.04 ± 0.007	1.09 ± 0.003
$X_3 = m_f$	0.78 ± 0.002	0.03 ± 0.005	–	-0.03 ± 0.006
$X_4 = m_b$	0.04 ± 0.005	0.78 ± 0.002	-0.03 ± 0.006	–

Table 7.4: Partial regression coefficients $b_{ij.kl}$ for multiplicities in the central η-bins, bin_0, calculated using MC09 data at $\sqrt{s} = 7$ TeV for events with two charged tracks within the kinematic range: $\mathrm{p_T} > 100$ MeV and $|\eta| < 2.5$. n_f and n_b, and m_f and m_b are calculated for charged particles and selected tracks having $\mathrm{p_T} > 100$ MeV, respectively.

7.3.3.2 Linking the hadron-level FB-correlation to the observed FB-correlation

In this section, the FB-correlation at the hadron-level, ρ_{had}, is linked to the observed FB-correlation, ρ_{obs}. The goal is to find a function F that can be written as $\rho_{had} = F(\rho_{obs})$. The general regression equations that were stated as equation (7.22) and derive equations of the type (7.21) will be used by replacing the variables (X_1, X_2, X_3, X_4) with (n_f,n_b,m_f,m_b). To begin, take the second and third lines of (7.22):

$$x_2 = b_{21.34}\, x_1 + b_{23.14}\, x_3 + b_{24.13}\, x_4 \qquad (7.23)$$
$$x_3 = b_{31.24}\, x_1 + b_{32.14}\, x_2 + b_{34.12}\, x_4 \; .$$

These equations are multiplied by x_3 and by x_2, respectively, to give following relations, summing over all the events:

$$\sum x_2 x_3 = b_{21.34} \sum x_1 x_3 + b_{23.14} \sum x_3^2 + b_{24.13} \sum x_3 x_4 \qquad (7.24)$$
$$\sum x_2 x_3 = b_{31.24} \sum x_1 x_2 + b_{32.14} \sum x_2^2 + b_{34.12} \sum x_2 x_4 \; .$$

Using the definition of the zero-order correlation, as in equation (7.15), between two variables x_i and x_j and the definition of the standard deviation of a variable x_i, written respectively as $\sum x_i x_j = N\sigma_i\sigma_j\rho_{ij}$ and $\sum x_i^2 = N\sigma_i^2$, the following is found:

$$\sigma_2\sigma_3\rho_{23} = b_{21.34}\ \sigma_1\sigma_3\rho_{13} + b_{23.14}\ \sigma_3^2 + b_{24.13}\ \sigma_3\sigma_4\rho_{34} \tag{7.25}$$

$$\sigma_2\sigma_3\rho_{23} = b_{31.24}\ \sigma_1\sigma_2\rho_{12} + b_{32.14}\ \sigma_2^2 + b_{34.12}\ \sigma_2\sigma_4\rho_{24}. \tag{7.26}$$

These equations are multivariate equivalents of equation (7.16). Equating the two right-hand sides and rearranging, obtains:

$$\rho_{had} = \alpha + \beta \cdot \rho_{obs}, \tag{7.27}$$

where $\rho_{had} = \rho_{12}$, $\rho_{obs} = \rho_{34}$, and:

$$\alpha = \frac{b_{23.14}\sigma_3^2 - b_{32.14}\sigma_2^2 + b_{21.34}\sigma_1\sigma_3\rho_{13} - b_{34.12}\sigma_2\sigma_4\rho_{24}}{b_{31.24}\sigma_1\sigma_2}, \qquad \beta = \frac{b_{24.13}\sigma_3\sigma_4}{b_{31.24}\sigma_1\sigma_2}. \tag{7.28}$$

The relationships between n_f and m_f (X_1 and X_3), and between n_b and m_b (X_2 and X_4) are due to the apparatus, e.g. tracking efficiencies. These relationships are contained in the coefficient β. The terms $b_{14.23}$, $b_{41.23}$, $b_{12.34}$, $b_{43.12}$ contain apparatus effects such as trigger and vertex finding efficiencies, and also effects of physical correlations between n_f, m_f and n_b, m_b. These are contained within the coefficient α, where they partially cancel. The values of α and β are calculated from the different MC models, and their variation gives rise to a systematic uncertainty on the final answers, which has been reduced to a low level by this method. It is mainly contained within the coefficient α. It should be noted that a mirror-image set of equations can be formed by exchanging the forward-backward coefficients 1,3 and 2,4 in the above. For a symmetric apparatus such as ATLAS, the latter equations give identical results to those quoted.

Table 7.5 shows the values of α and β as calculated for the five pairs of η-bins and for different tunes using equation (7.28). It is found that the values of the correction factors α, β in a given bin show little variation with the MC tune used to generate them. The small variations arise from the different values of the tuning parameters in the models.

7.3.4 Statistical Uncertainties on Correction Factors

In this section the statistical uncertainties on the simple and multiple regression coefficients defined above are computed. To begin, take the case of the regression of Y on X as in equation (7.8). If we let $\hat{Y}$ represent the value of Y for given values of X as estimated from the regression equation $Y = a + b.X$, a measure of the scatter about the regression line of Y

Tune	MC09	DW	Perugia0	Pythia8	Phojet
α_0	$0.06 \pm 0.06\%$	$0.05 \pm 0.05\%$	$0.07 \pm 0.08\%$	$0.06 \pm 0.04\%$	$0.08 \pm 0.06\%$
β_0	$0.96 \pm 0.0001\%$	$0.97 \pm 0.0002\%$	$0.96 \pm 0.0001\%$	$0.96 \pm 0.0003\%$	$0.95 \pm 0.0002\%$
α_1	$0.06 \pm 0.03\%$	$0.05 \pm 0.01\%$	$0.06 \pm 0.05\%$	$0.06 \pm 0.02\%$	$0.07 \pm 0.06\%$
β_1	$0.97 \pm 0.0002\%$	$0.98 \pm 0.0003\%$	$0.96 \pm 0.0002\%$	$0.97 \pm 0.0003\%$	$0.96 \pm 0.0001\%$
α_2	$0.06 \pm 0.11\%$	$0.05 \pm 0.13\%$	$0.07 \pm 0.12\%$	$0.07 \pm 0.15\%$	$0.08 \pm 0.11\%$
β_2	$0.97 \pm 0.0002\%$	$0.98 \pm 0.0003\%$	$0.96 \pm 0.0002\%$	$0.97 \pm 0.0003\%$	$0.96 \pm 0.0001\%$
α_3	$0.07 \pm 0.07\%$	$0.07 \pm 0.11\%$	$0.08 \pm 0.10\%$	$0.08 \pm 0.12\%$	$0.09 \pm 0.09\%$
β_3	$0.97 \pm 0.0001\%$	$0.97 \pm 0.0004\%$	$0.96 \pm 0.0003\%$	$0.96 \pm 0.0005\%$	$0.96 \pm 0.0004\%$
α_4	$0.08 \pm 0.07\%$	$0.08 \pm 0.07\%$	$0.09 \pm 0.07\%$	$0.09 \pm 0.08\%$	$0.10 \pm 0.03\%$
β_4	$0.96 \pm 0.0001\%$	$0.96 \pm 0.0001\%$	$0.96 \pm 0.0001\%$	$0.96 \pm 0.0002\%$	$0.96 \pm 0.0004\%$

Table 7.5: Correction factors for minimum bias events at $\sqrt{s} = 7$ TeV having two charged particles within the kinematic range $p_{\mathrm{T}} > 100$ MeV and $|\eta| < 2.5$. The corrections are computed for charged particles with $p_{\mathrm{T}} > 100$ MeV applying equation 7.28 for each pairs of η-bins, for various MC tunes. Uncertainties on the correction factors can be $< 0.1\%$. The percentage sign applies only to the value of the uncertainties

on X is given by the expression:

$$SSR = \sum_i (Y_i - \hat{Y}_i)^2. \tag{7.29}$$

which is called the Sum of Squares of Residuals (SSR)[67]. It is also called the Sum of Errors of Estimate (SEE).

The statistical error on the b slope estimation, σ_b, in the regression of Y on X is defined as:

$$\sigma_b^2 = \frac{\sum_i (Y_i - \hat{Y}_i)^2}{(N-2)} \cdot \frac{1}{\sum_i (X_i - \langle X \rangle)^2} = \frac{SSE}{(N-2)} \cdot \frac{1}{\sum_i (X_i - \langle X \rangle)^2} \tag{7.30}$$

This can be generalised to the case of 4 random variables. If the regression of X_1 on X_2, X_3 and X_4 is considered, then the statistical error on the partial coefficients $b_{ij.kl}$ is given by:

$$\sigma^2_{b_{1j.kl}} = \frac{SSR}{(N-4)} \cdot (X^T X)^{-1}_{jj}, \text{when} j = 2,3,4 \tag{7.31}$$

$$\sigma^2_{b_{1.234}} = \frac{SSR}{(N-4)} \cdot (X^T X)^{-1}_{11}\,, \tag{7.32}$$

where $(X^T X)$ is the 4×4 matrix defined in section 7.3.2.2.

The statistical errors above have been properly propagated into the expression of the correction factors α and β in equation (7.28).

7.4 Validation of Correction Method

In this section the use of the multiple regression theory described above is validated.

7.4.1 Linearity of Physics and Apparatus Correlations

As mentioned above, the correlation can be derived from a linear regression of n_f on n_b. To ensure the validity of the statistical analysis based on multiple regression theory as developed above, it is necessary to check that a linear approach to the problem describes well all of the possible interdependencies due to the underlying physics or experimental effects. This is done by performing linear regressions on all possible variable pairs identified with the generated and measured multiplicities n_f, n_b, m_f and m_b. In figure 7.6, the linear regressions of n_f on n_b , of n_f on m_f , of n_f on m_b and of m_f on m_b are performed. n_f, n_b, m_f and m_b are computed for events from the MC09 7 TeV sample for the central pair of η-bins (with appropriate sub-process mixing). Figure 7.6 shows that both physical, apparatus and mixed correlations are linear, which validates the use of the linear multiple regression theory in this analysis.

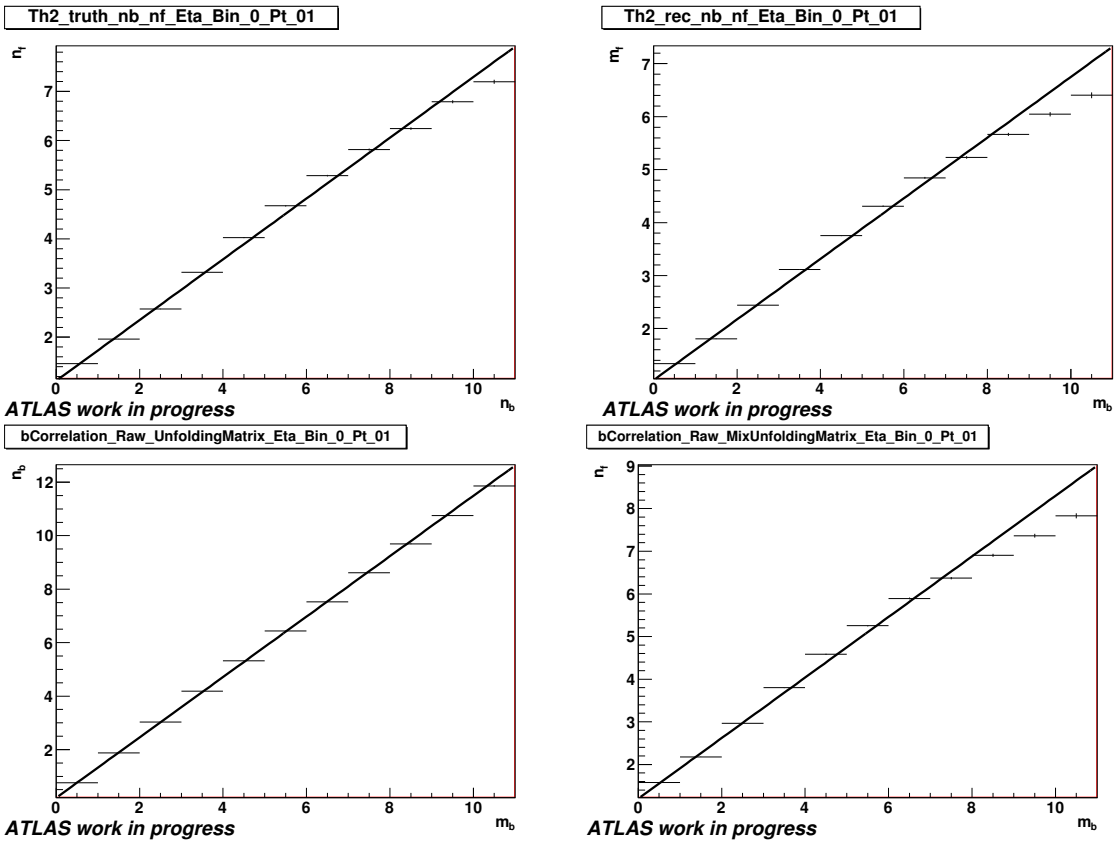

Figure 7.6: The linear regressions of n_f on n_b, of n_f on m_f, of n_f on m_b and of m_f on m_b for generated charged particles with $\mathrm{p_T} > 100$ MeV for events taken at $\sqrt{s} = 7$ TeV and having two tracks within the kinematic range $\mathrm{p_T} > 100$ MeV and $|\eta| < 2.5$.

7.4.2 Link to Unfolding Matrix

The partial regression coefficient $b_{13.24}$ in table 7.4 corresponds to the average reconstruction efficiency when we omit the effect from the physics correlations with the multiplicities n_b and m_b. In order to check the validity of the value of $\sim 78\%$ obtained, a linear regression of the unfolding matrix (n_f,m_f) is performed, i.e. a linear regression of the hadron-level multiplicity n_f on the measured multiplicity m_f is made, in order to relate $\langle n_f \rangle = a + b.m_f$. Figure 7.7 shows the linear regression of n_f on m_f. In this case, the slope coefficient, b, is interpreted as the average reconstruction efficiency and contamination. It is found to be $(78 \pm 0.3)\%$, which is in agreement with the partial coefficient $b_{31.24} = 78 \pm 0.3\%$, taking into account the partial coefficients $b_{23.14} = 3\%$ and $b_{34.12} = -3\%$.

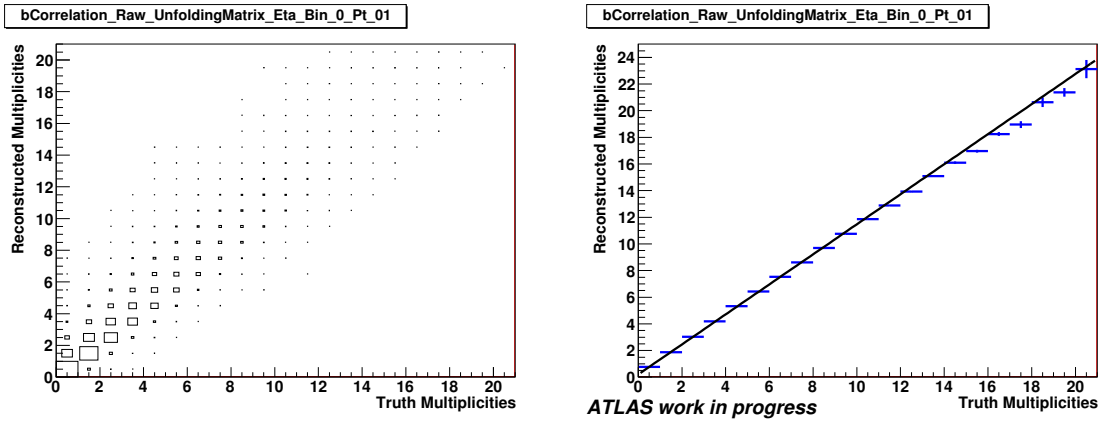

Figure 7.7: (Left) unfolding matrix (n_f vs m_f) containing contamination from secondary and fake tracks. (Right) simple regression of n_f on m_f (from the unfolding matrix) for MC09 events taken at $\sqrt{s} = 7$ TeV and having two tracks within the kinematic range $\mathrm{p_T} > 100$ MeV and $|\eta| < 2.5$.

7.4.3 Validating α and β

In order to validate the linear relationship of the correction procedure in equation (7.27), for each Monte Carlo sample ρ_{had} and ρ_{obs} are estimated for each pair of η-bins, see table 7.6. Correspondingly, in figure 7.8, for each pair η-bins, i, the points with coordinates (ρ_i^{had}, ρ_i^{obs}) are plotted in a given colour in the (ρ_{had}, ρ_{obs}) scatter-plot. For example, the FB-correlation values for the central pair of η-bins of each tune are shown in red. This figure shows that for each pair of η-bins, the points (ρ_i^{had}, ρ_i^{obs}) corresponding to various MC tunes lie on a segment of a line. This demonstrates that there is a linear relationship between ρ_{had} and ρ_{obs} as previously found in equation (7.27). Each set of points which correspond to a given pair of η-bins, is fitted with a line $\rho_i^{had} = \alpha_{fit} + \beta_{fit}.\rho_i^{obs}$ and the corresponding fit coefficients are reported in table 7.7. These coefficients are in agreement with those computed in equation (7.28) using multiple regression theory and reported in table 7.5. This validates the use of

the multiple regression theory in the correction method by demonstrating the linearity of the problem.

Note that the correction method using the multiple regression theory, allows the augmentation of statistical power from $\sqrt{5-2}$, when the 5 tunes are used to calculate the two straight line parameters α_{fit} and β_{fit}, to $\sqrt{N-4}$, where four variables are extracted from a MC sample of size N, as when α and β are calculated in equation (7.28). Thus we use the correction factor, α and β, computed from the MC09 sample to take advantage of the greater statistical accuracy.

Tune	MC09	DW	Perugia0	Pythia8	Phojet
sample	1000937	1000940	999996	1000929	999282
selected	827112	821334	814366	854996	905466
ρ_0^{had}	$0.610 \pm 0.14\%$	$0.576 \pm 0.15\%$	$0.638 \pm 0.13\%$	$0.617 \pm 0.14\%$	$0.585 \pm 0.14\%$
ρ_0^{obs}	$0.557 \pm 0.16\%$	$0.528 \pm 0.18\%$	$0.584 \pm 0.15\%$	$0.569 \pm 0.16\%$	$0.524 \pm 0.17\%$
ρ_1^{had}	$0.525 \pm 0.18\%$	$0.499 \pm 0.19\%$	$0.557 \pm 0.16\%$	$0.544 \pm 0.17\%$	$0.505 \pm 0.18\%$
ρ_1^{obs}	$0.471 \pm 0.21\%$	$0.449 \pm 0.22\%$	$0.499 \pm 0.19\%$	$0.493 \pm 0.19\%$	$0.441 \pm 0.21\%$
ρ_2^{had}	$0.492 \pm 0.19\%$	$0.480 \pm 0.20\%$	$0.510 \pm 0.18\%$	$0.507 \pm 0.18\%$	$0.458 \pm 0.20\%$
ρ_2^{obs}	$0.430 \pm 0.23\%$	$0.422 \pm 0.24\%$	$0.445 \pm 0.22\%$	$0.448 \pm 0.22\%$	$0.387 \pm 0.25\%$
ρ_3^{had}	$0.468 \pm 0.20\%$	$0.472 \pm 0.20\%$	$0.473 \pm 0.20\%$	$0.480 \pm 0.20\%$	$0.419 \pm 0.23\%$
ρ_3^{obs}	$0.394 \pm 0.26\%$	$0.400 \pm 0.25\%$	$0.395 \pm 0.26\%$	$0.409 \pm 0.24\%$	$0.335 \pm 0.30\%$
ρ_4^{had}	$0.440 \pm 0.22\%$	$0.456 \pm 0.21\%$	$0.433 \pm 0.23\%$	$0.451 \pm 0.21\%$	$0.375 \pm 0.26\%$
ρ_4^{obs}	$0.354 \pm 0.29\%$	$0.371 \pm 0.28\%$	$0.343 \pm 0.30\%$	$0.365 \pm 0.28\%$	$0.279 \pm 0.36\%$

Table 7.6: Hadron-Level (generated) and observed (reconstructed) FB-correlations for minimum bias events at $\sqrt{s} = 7$ TeV for the different MC tunes in each pair of pseudo-rapidity bin (subscript). The correlations are calculated for tracks with $\mathrm{p_T} > 100$ MeV.

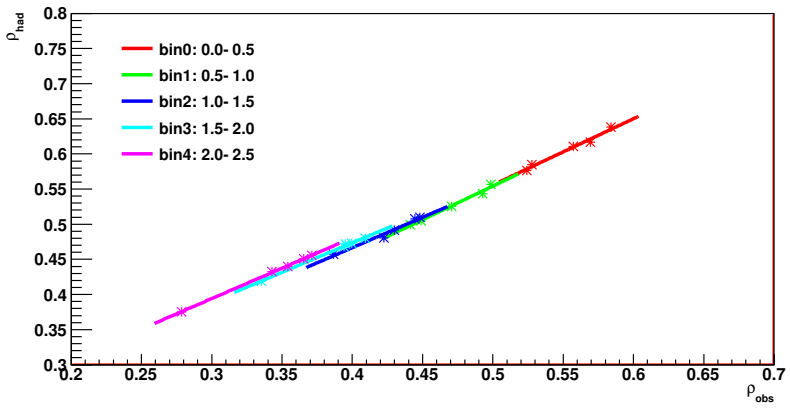

Figure 7.8: ρ_{had} vs ρ_{obs} as shown in Table 7.6. Each point corresponds to (ρ_{had}, ρ_{obs}) of a given MC Tune in a given pair of η-bins. The lines are fits to the various points in a pair of η-bins and shown in a separate colour.

Correction factors	$\text{bin}_0 : 0 - 0.5$	$\text{bin}_1 : 0.5 - 1$	$\text{bin}_2 : 1 - 1.5$	$\text{bin}_3 : 1.5 - 2$	$\text{bin}_4 : 2 - 2.5$
β_{fit}	0.96 ± 0.13	0.91 ± 0.15	0.82 ± 0.14	0.80 ± 0.07	0.88 ± 0.11
α_{fit}	0.07 ± 0.08	0.08 ± 0.07	0.13 ± 0.06	0.15 ± 0.03	0.12 ± 0.04

Table 7.7: α and β correction factors for $\sqrt{s} = 7$ TeV derived from a linear fit of the individual ρ_{had} and ρ_{obs} correction factors for the different MC tunes.

7.4.4 Linearity of Physics and Apparatus Correlations in Data

Here, the linearity of the data is investigated and shown to lie on the linear fitted segments of figure 7.8. To demonstrate this, two samples of data with two different correlation values have been mixed together to build a diluted sample. The first sample is a normal data sample with a non-zero measured ρ_{obs}. The second sample has no correlations. It is obtained by breaking the existing physical correlations by gathering a multiplicity m_f measured in one event with a multiplicity m_b measured in another event. The two samples are called *correlated* and *uncorrelated* samples, respectively. The mixture fractions in an overall diluted sample of $N = 10$ million selected events are made as follows:

- $f_{cor} \cdot N$ events from the correlated sample with $0 < f_{cor} < 1.$, where f_{cor} is the fraction of correlated events;
- $(1 - f_{cor}) \cdot N$ events from the uncorrelated sample.

50 diluted samples were built from the data by varying the fraction f_{cor} 50 times from 0 to 1. The correlation of each sample has been measured and reported in figure 7.9 for various p_T cuts. It was found that the measured FB-correlations in the diluted data samples have linear behaviour as a function of f_{cor}. This proves that the FB-correlations in the data can be modelled linearly and treated in a linear way using multiple regression theory.

Figure 7.9, can be seen as a measurement of the validity region of the FB-correlations where the correction procedure could be applied to the data. This region of validity is linear down to a few percent of the original value of the FB-correlations in the data, and covers all of the MC region in which the correction method has been tested with the closure test presented below.

7.4.5 Closure Tests at 7 TeV

A closure test, which involved using the same sample of selected MC events for analysis and correction, was performed. The upper plot of figure 7.10 shows the hadron-level, corrected and observed FB-correlations for the MC09 tune Monte Carlo sample. The lower plot of figure 7.10 shows the ratio of the corrected to hadron-level FB-correlation values, ρ_{cor}/ρ_{had}, for the various MC tunes plotted for each pair of η-bins. A value consistent with unity

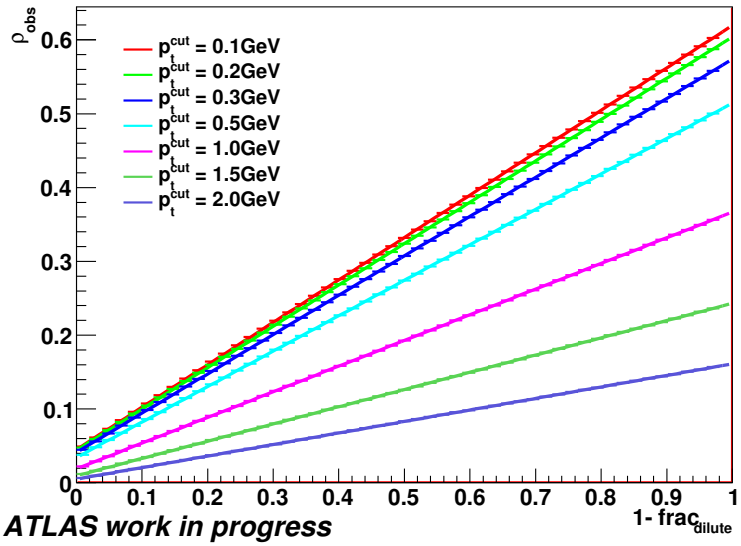

Figure 7.9: Measured correlation on various diluted data samples as a function of the fraction f_{cor} of the correlated sample in the overall sample for the following $\mathrm{p_T}$ cuts: 100, 200, 500 MeV, 1.0, 1.5 and 2.0 GeV.

is found for all the MC samples. The agreement between the corrected and hadron-level distributions shows that the input FB-correlation values can be found after corrections.

7.5 Systematics

This section investigates the correction method from the systematic uncertainties arising from the trigger, vertexing and tracking efficiencies as well as the theoretical error from the diffractive component of the diffractive cross-sections.

7.5.1 Model Dependence of the Correction Procedure

The model dependence of the analysis was evaluated for each tune by using one sample as data and another sample to determine the corrections. Specifically, the MC09 event sample was used to correct each of the other MC tune samples. The upper plot of figure 7.11 shows the hadron-level, corrected and observed FB-correlations for the DW Monte Carlo sample, where the observed FB-correlations have been corrected using an MC09 sample.

The lower plot of figure 7.11 shows the ratio distributions for the corrected to hadron-level FB-correlations, ρ_{cor}/ρ_{had}, for various MC tunes corrected using the MC09 tune. There is a small divergence between the ratios with a corresponding spread contained within the limits of order $\pm 2\%$. This corresponds to the maximum systematic uncertainty due to the model dependence of the correction procedure. The agreement between the corrected and hadron-level distributions, allowing for the statistical error, shows that the correction method

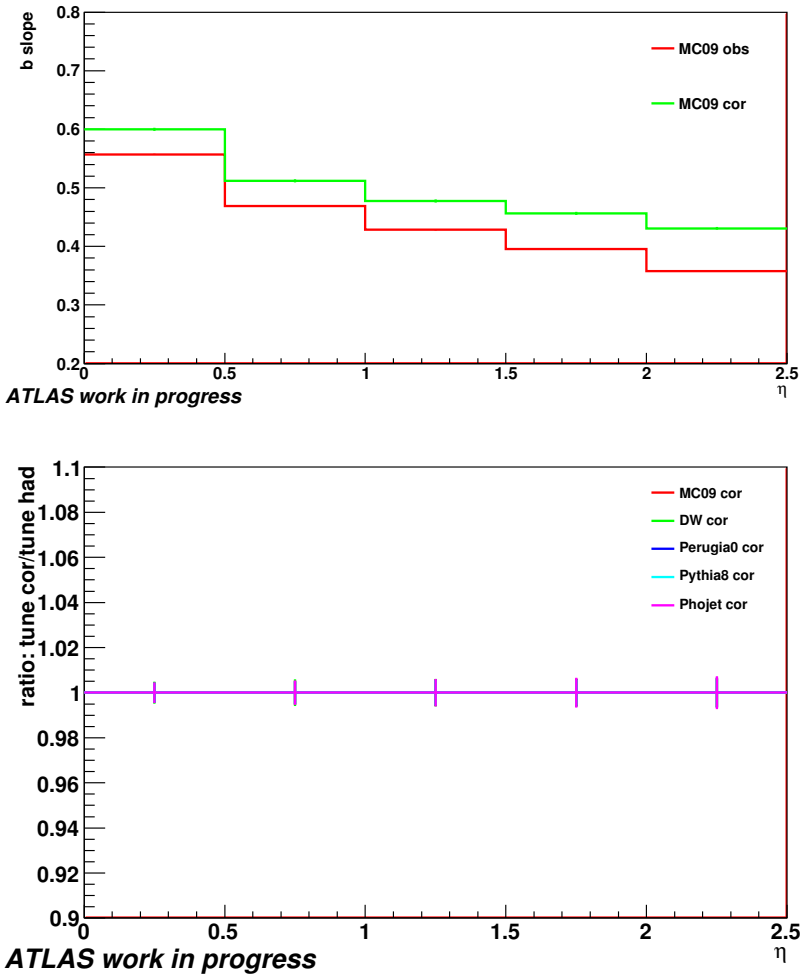

Figure 7.10: Above: Forward-backward multiplicity correlation for generated charged particles and reconstructed charged tracks with $\mathrm{p_T} > 100$ MeV in symmetrically opposite η-bins for events with two charged tracks within the kinematic range $\mathrm{p_T} > 100$ MeV and $|\eta| < 2.5$ at $\sqrt{s} = 7$ TeV for for Pythia DW tune. In addition, the corrected distribution is plotted, where the reconstructed correlation was corrected using the generator information of the analysed events from each tune. Below: Ratios comparing reconstructed to corrected correlation for each MC tune.

is only sightly sensitive to the differences between the FB-correlation values of DW and MC09 tunes.

7.5.2 Effect of Systematic Uncertainties of Efficiencies

The systematic effects on the FB-correlation due to the systematic uncertainties on the trigger, vertex and tracking efficiencies were studied. η and $\mathrm{p_T}$ dependent uncertainties on trigger, vertex and tracking efficiencies [58]. A systematic variation of the standard selection was achieved by removing or double-counting a proportion of events or of tracks in a sample according to the uncertainties on the efficiencies above. This simulates a decrease or an

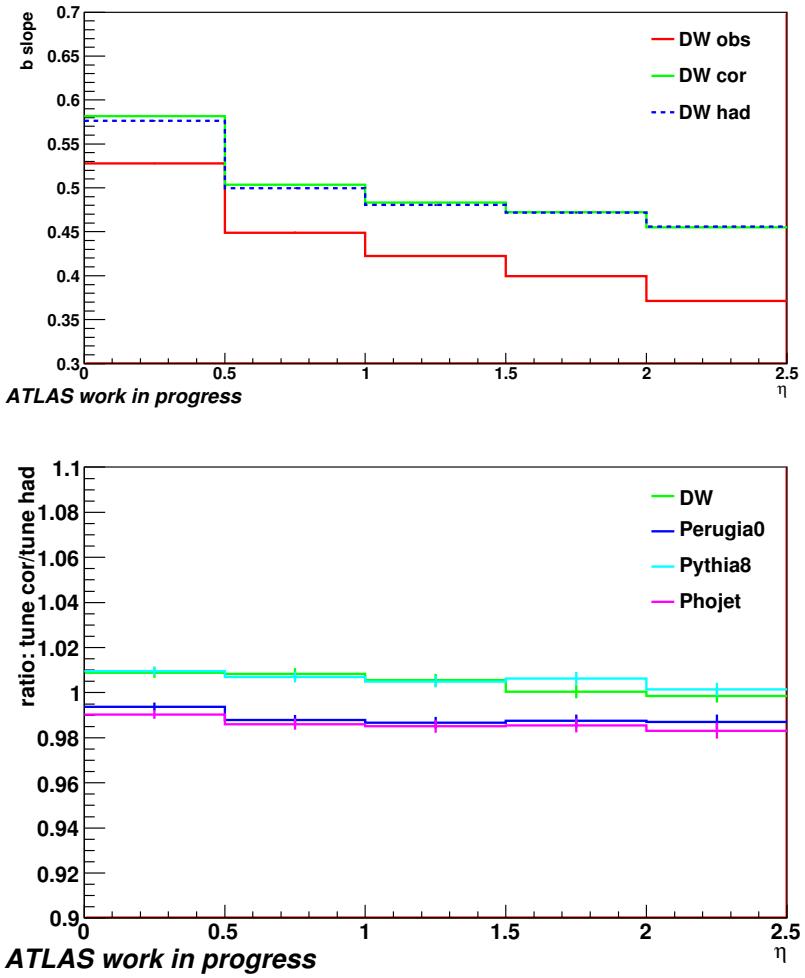

Figure 7.11: Above: Forward-backward multiplicity correlation for generated charged particles and reconstructed charged tracks with $\mathrm{p_T} > 100$ MeV in symmetrically opposite η-bins for events with two charged tracks within the kinematic range $\mathrm{p_T} > 100$ MeV and $|\eta| < 2.5$ at $\sqrt{s} = 7$ TeV for the Pythia DW tune. The corrected distribution is plotted, where the reconstructed correlation was corrected using the α and β from the MC09 tune. Below: The ratio of the generated to corrected correlation for each MC tune, where the reconstructed sample for each MC tune has been corrected using the α and β from the MC09 tune.

increase in an efficiency due to systematic uncertainty.

The effect of varying the trigger, vertex and tracking efficiency, within the uncertainties, on the observed FB-correlation is shown in figures 7.12, 7.13 and 7.14, respectively. Each figure shows the correlation distribution as a function of the pseudo-rapidity gap in the upper plot and the relative systematic variations in the lower plot. Table 7.8 shows the relative effect on the FB-correlation in each pair of η-bins.

For the case of the trigger efficiency, it can be seen as a slight deviation in the FB-correlation of a maximum of 0.2%. There is little effect on the observed FB-correlation from decreasing the trigger efficiency. In the case of the vertex, the effect on the observed FB-

correlation from varying the efficiency either up or down is negligible, it is around 0.1%. The tracking is the most dominant source of systematic uncertainties. When the fraction of tracks is removed from the events as described above, the resulting FB-correlation deviates by -1.2% in the central pair of η-bins. This deviation increases to -3.3% in the outermost pair of η-bins. When the fraction of tracks is added by the same amount, the effect is supposed to be symmetric[4] and the deviations of the observed FB-correlations are taken equal, but in the positive direction, to those observed when the fraction tracks are removed.

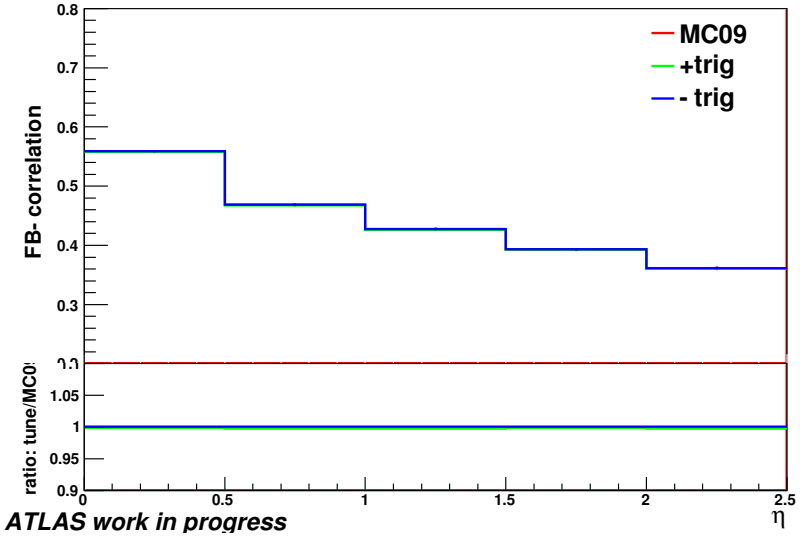

Figure 7.12: Above: Forward-backward multiplicity correlation for reconstructed charged tracks with $\mathrm{p_T} > 100$ MeV in symmetrically opposite η-bins for events with two charged tracks within the kinematic range $\mathrm{p_T} > 100\,\mathrm{MeV}$ and $|\eta| < 2.5$ at $\sqrt{s} = 900$ GeV & 7 TeV for observed tracks using MC09 tune, with trigger efficiency variations within the uncertainties. Below: Ratios comparing the upper and lower variations to the unchanged value.

In addition to these detector systematics a further systematic due to the estimate of the diffractive element of selected events was investigated. To this end, the proportion of single and double diffractive events in the MC09 events sample was increased and decreased by 10%. Figure 7.15 shows the effect of varying the diffractive component on the correlation distribution as a function of the pseudo-rapidity gap in the upper plot and the relative systematic variations in the lower plot. The systematic due to this theoretical uncertainty was found to be at most 1%.

Table 7.8 shows the relative effect of each uncertainty on the strength of the observed correlation in each η-bin for the MC09 tune. From these results, it is concluded that there is

[4]This is due to the method of estimating the systematics from the tracking. Tracks are either removed or added "randomly" to m_f or m_b respectively while varying the tracking efficiency to its lower or higher limit. In both cases the effect of the random increase or decrease of tracks in a given η-bin between m_f and m_b is to dilute the value of the FB-correlation.

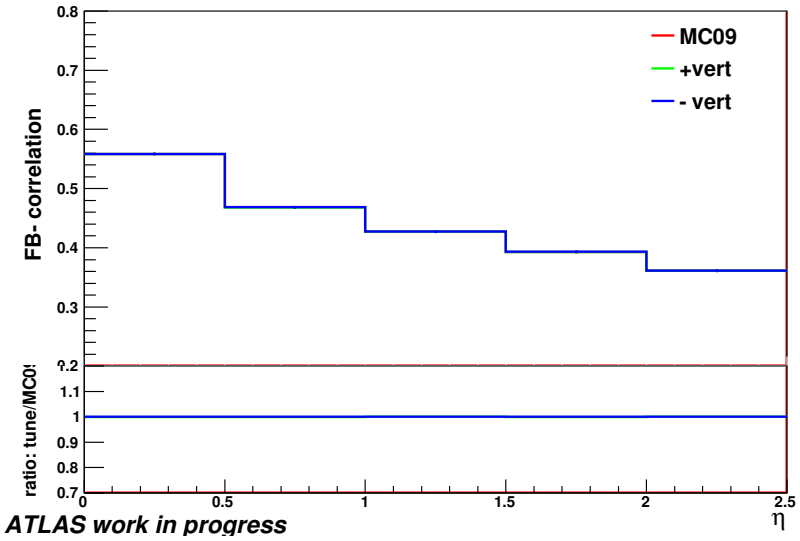

Figure 7.13: Above: Forward-backward multiplicity correlation for reconstructed charged tracks with $p_T > 100$ MeV in symmetrically opposite η-bins for events with two charged tracks within the kinematic range $p_T > 100$ MeV and $|\eta| < 2.5$ at $\sqrt{s} = 900$ GeV & 7 TeV for observed tracks using MC09 tune, with vertex efficiency variations within the uncertainties. Below: Ratios comparing the upper and lower variations to the unchanged value.

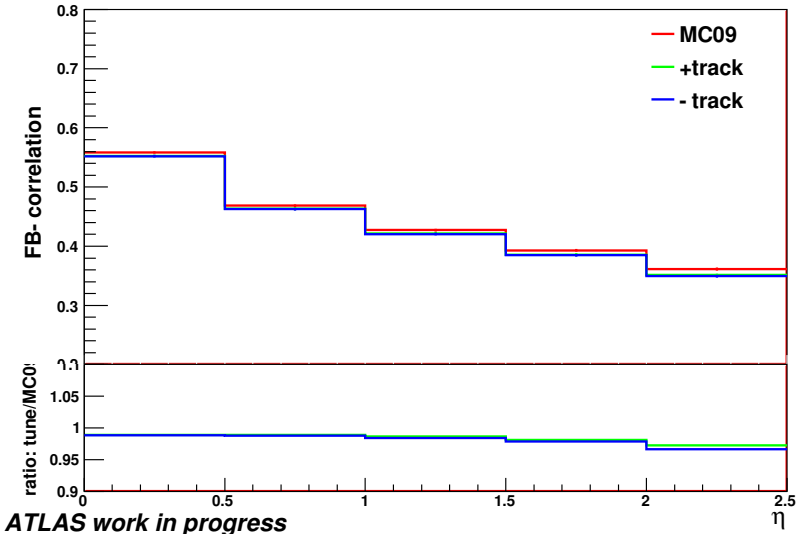

Figure 7.14: Above: Forward-backward multiplicity correlation for reconstructed charged tracks with $p_T > 100$ MeV in symmetrically opposite η-bins for events with two charged tracks within the kinematic range $p_T > 100$ MeV and $|\eta| < 2.5$ at $\sqrt{s} = 900$ GeV & 7 TeV for observed tracks using MC09 tune, with tracking efficiency variations within the uncertainties. Below: Ratios comparing the upper and lower variations to the unchanged value.

little effect on the FB-correlation in varying the efficiency of the trigger or vertex. Varying the diffractive component of the selected sample has a moderate effect on the correlation.

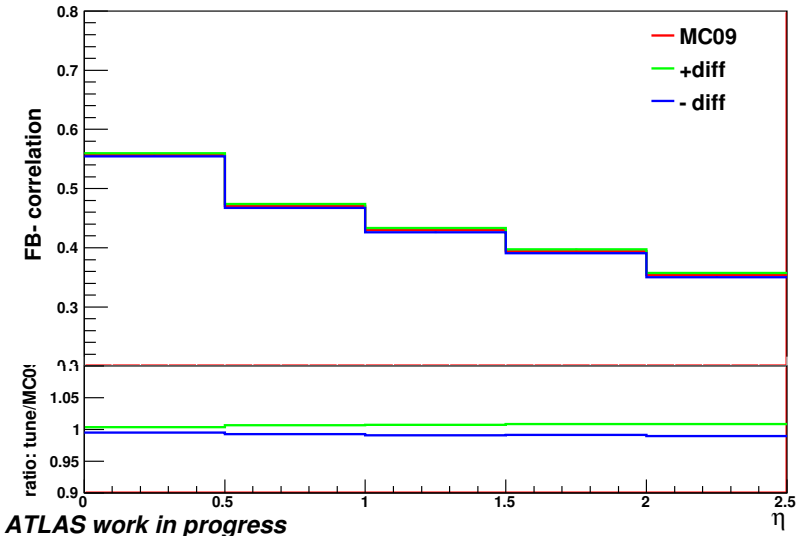

Figure 7.15: Above: Forward-backward multiplicity correlation for reconstructed charged tracks with $p_T > 100$ MeV in symmetrically opposite η-bins for events with two charged tracks within the kinematic range $p_T > 100$ MeV and $|\eta| < 2.5$ at $\sqrt{s} = 900$ GeV & 7 TeV for observed tracks using MC09 tune, with the diffractive component varied by $\pm 10\%$. Below: Ratios comparing the upper and lower variations to the unchanged value.

The tracking efficiency is the dominant source of systematic uncertainties.

bin	$0:0-0.5$	$1:0.5-1$	$2:1-1.5$	$3:1.5-2$	$4:2-2.5$
MC09(reference)	0.559	0.469	0.427	0.393	0.361
+ trig	-0.1%	-0.2%	-0.3%	-0.1%	-0.2%
- trig	0.0%	0.1%	0.1%	0.1%	0.1%
+ vert	-0.0%	-0.1%	0.0%	-0.0%	-0.0%
- vert	0.0%	0.0%	-0.0%	0.0%	0.0%
+ trac	-1.1%	-1.1%	-1.3%	-1.9%	-2.7%
- trac	-1.2%	-1.2%	-1.6%	-2.1%	-3.3%
+ 10% diff	0.4%	0.7%	0.8%	0.9%	0.9%
- 10% diff	-0.5%	-0.7%	-0.9%	-0.9%	-1.0%

Table 7.8: The variation in the forward-backward multiplicity correlation for charged tracks with $p_T > 100$ MeV in symmetrically opposite η-bins for events with two charged tracks within the kinematic range $p_T > 100$ MeV and $|\eta| < 2.5$ at $\sqrt{s} = 7$ TeV for MC09 tune MC. The sources of uncertainty are due to the efficiencies of the trigger, vertex and tracking and the diffractive component of the sample.

7.6 Results

The results of the FB-correlation analysis are documented in this section, including a comparison of the measured and corrected correlations to the set of MC tunes.

7.6.1 Observed FB-Correlation at 7 TeV

Figure 7.16 shows the observed FB-correlation for data and MC tunes at $\sqrt{s} = 7$ TeV. It is clear from the upper plot that there is a discrepancy between the MC predictions and the measured FB-correlation, where the measured correlation is consistently above the predictions of all the MC tunes. The lower plot, showing the ratio of each MC tune distribution to the correlation observed in data, $\rho_{obs}^{MC}/\rho_{obs}^{data}$, quantifies this to be between 6%, in the central pair of η-bins for the Perugia0 tune, and 35%, in the extreme pair of η-bins for Phojet, for the selected MC tunes.

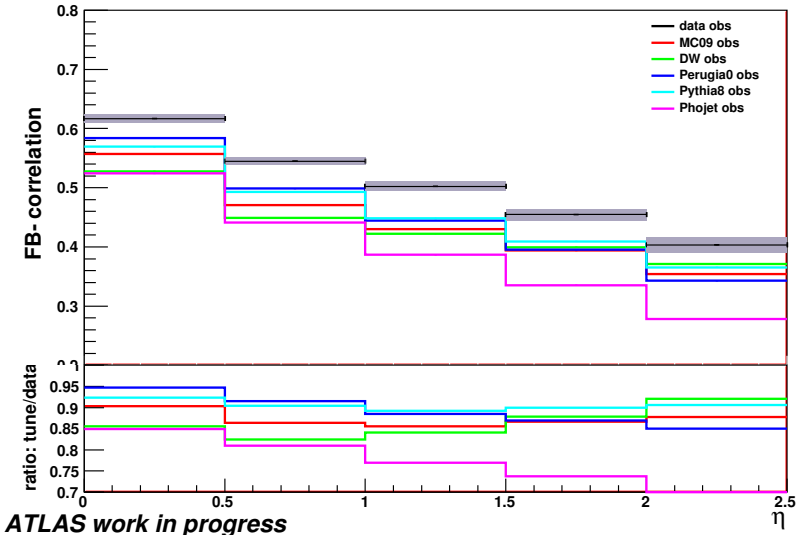

Figure 7.16: Above: Observed forward-backward multiplicity correlation for charged tracks with $\mathrm{p_T} > 100$ MeV in symmetrically opposite η-bins for events with two charged tracks within the kinematic range $\mathrm{p_T} > 100$ MeV and $|\eta| < 2.5$ at $\sqrt{s} = 7$ TeV for data and various MC tunes. Below: Ratios comparing observed FB-correlation from each MC to data.

7.6.2 Correction Systematic at 7 TeV

Figure 7.17 shows the corrected FB-correlation, using the α_i and β_i values derived from each MC tune to correct the observed FB-correlation from data. The upper plot shows the general convergence of each corrected distribution. The lower plot shows the ratio of the corrected distribution of each tune to the observed FB-correlation from data corrected using the MC09,

$\rho_{cor}^{MC}/\rho_{cor}^{data}$. Table 7.9 quantifies this discrepancy, which is used as the systematic uncertainty of the correction method. The maximum divergence above and below the MC09 tune value is quoted for each pair of η-bins.

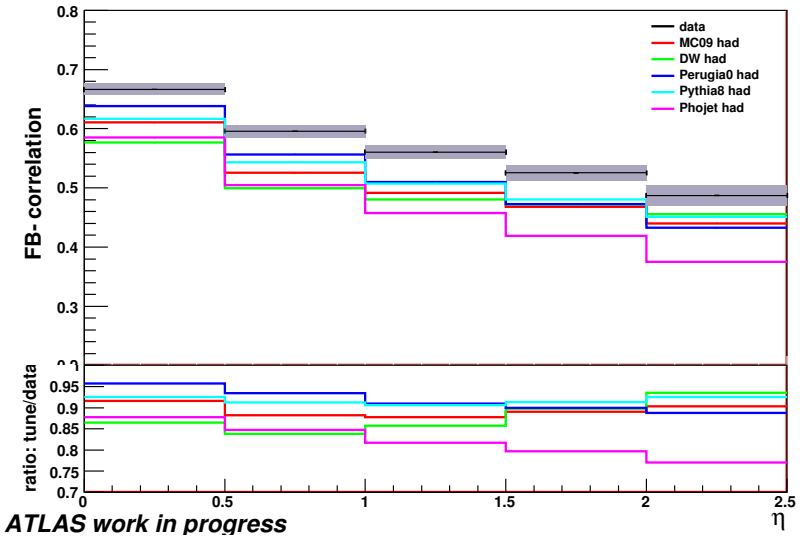

Figure 7.17: Above: Forward-backward multiplicity correlation for charged tracks with $p_T > 100$ MeV in symmetrically opposite η-bins for events with two charged tracks within the kinematic range $p_T > 100$ MeV and $|\eta| < 2.5$ at $\sqrt{s} = 7$ TeV for data corrected using various MC tunes. Below: Ratios comparing each corrected FB-correlation to that corrected with MC09 tune.

bin	$0:0-0.5$	$1:0.5-1$	$2:1-1.5$	$3:1.5-2$	$4:2-2.5$
MC09(reference)	0.666	0.596	0.560	0.526	0.487
+ variation	0.9%	1.3%	1.4%	1.4%	1.5%
- variation	-0.7%	-0.6%	-0.4%	-0.4%	-0.1%

Table 7.9: Variation in corrected forward-backward multiplicity correlation for charged tracks with $p_T > 100$ MeV in symmetrically opposite η-bins for events with two charged tracks within the kinematic range $p_T > 100$ MeV and $|\eta| < 2.5$ at $\sqrt{s} = 7$ TeV relative to those corrected with MC09.

7.6.3 Corrected FB-correlation at 7 TeV

Finally, the observed correlation from data can be corrected back to hadron-level and compared to the predictions from the MC tunes for $\sqrt{s} = 7$ TeV. The upper plot of figure 7.18 shows the corrected FB-correlation distribution from observed data, corrected using MC09, and the hadron-level distributions for each MC tune. The lower plot shows the ratio of the hadron-level FB-correlation for each MC tune to the corrected distribution from data, $\rho_{had}^{MC}/\rho_{cor}^{data}$. As in the case of the uncorrected observed FB-correlation, the corrected data distribution lies above all the MC tune predictions. The range of underestimate covers

$\sim 5\%$, in the central η-bin for Perugia0, to $\sim 25\%$, in the extreme η-bin for Phojet. Table 7.10 quantifies the FB-correlation value for corrected data and each MC tune for each η-bin.

In general, the shape of the data distribution is well produced though the details of discrepancies of the η-range reflect deficiencies in the particle production mechanisms for each tune. In the case of MC09, the trend is to under-estimate the correlation by $\sim 10\%$. There is a dip in correlation compared to the data as the η gap increases then an increase in the extreme bin. This suggests there is a relative drop in particle production in the intermediate η-region. The DW tune increases its correlation relative to the data over the η-range, suggesting short distance correlations are not strong enough compared to long distance correlations. The Perugia0 tune appears to have not enough long distance production as its correlation decreases across the η-gap increases compared to the data. Pythia8 has the most consistent correlation compared with data, suggesting production needs only to be increased for both long distance processes. Lastly, Phojet appears to lack long distance production mechanisms as it clearly diverges from data across the η-range and is most under-productive in the extreme η-region.

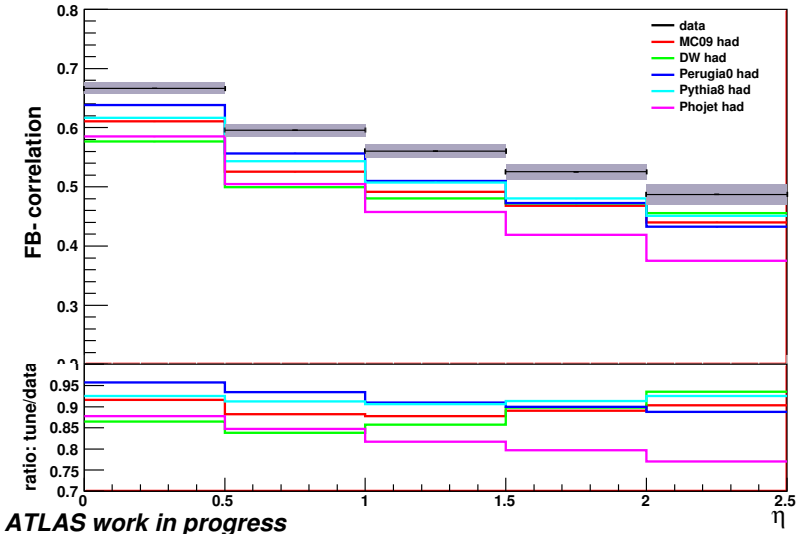

Figure 7.18: Above: Forward-backward multiplicity correlation for reconstructed charged tracks with $p_T > 100$ MeV in symmetrically opposite η-bins for events with two charged tracks within the kinematic range $p_T > 100$ MeV and $|\eta| < 2.5$ at $\sqrt{s} = 7$ TeV for data corrected using Pythia MC09 tune, and generated charged particles with $p_T > 100$ MeV from MC tunes. Below: Ratios comparing corrected correlation from data to correlations from MC tunes at generated.

7.6.4 Summed Systematic and Statistical Uncertainties

Table 7.11 shows the combined uncertainties for the FB-correlation at 7 TeV from observed data corrected using the MC09 tune. These include the summed systematic uncertainties from detector effects, uncertainties from the correction procedure and the statistical uncer-

bin	$0:0-0.5$	$1:0.5-1$	$2:1-1.5$	$3:1.5-2$	$4:2-2.5$
data	$0.666 \pm 0.1\%$	$0.596 \pm 0.1\%$	$0.560 \pm 0.1\%$	$0.526 \pm 0.1\%$	$0.487 \pm 0.1\%$
MC09	$0.610 \pm 0.1\%$	$0.525 \pm 0.2\%$	$0.492 \pm 0.2\%$	$0.468 \pm 0.2\%$	$0.440 \pm 0.2\%$
DW	$0.576 \pm 0.2\%$	$0.499 \pm 0.2\%$	$0.480 \pm 0.2\%$	$0.472 \pm 0.2\%$	$0.456 \pm 0.2\%$
Perugia0	$0.638 \pm 0.1\%$	$0.557 \pm 0.2\%$	$0.510 \pm 0.2\%$	$0.473 \pm 0.2\%$	$0.433 \pm 0.2\%$
Pythia8	$0.617 \pm 0.1\%$	$0.544 \pm 0.2\%$	$0.507 \pm 0.2\%$	$0.480 \pm 0.2\%$	$0.451 \pm 0.2\%$
Phojet	$0.585 \pm 0.1\%$	$0.505 \pm 0.2\%$	$0.458 \pm 0.2\%$	$0.419 \pm 0.2\%$	$0.375 \pm 0.3\%$

Table 7.10: Forward-backward multiplicity correlation for reconstructed charged tracks with $\mathrm{p_T} > 100\,\mathrm{MeV}$ in symmetrically opposite η-bins for events with two charged tracks within the kinematic range $\mathrm{p_T} > 100\,\mathrm{MeV}$ and $|\eta| < 2.5$ at $\sqrt{s} = 7\,\mathrm{TeV}$ for data corrected using the correction factors from the global fit values and generated MC tunes. Quoted errors are statistical errors only.

tainties from the sample size. To calculate the combined efficiency systematic, from the variations in trigger, vertex, tracking and diffraction components, a symmetries tracking efficiency is used i.e. the outer limit of the effect of variation in each bin is used. This is due to the choice of systematic strategy, see above. A similar approach is taken with the systematic coming from the choice of tune used to correct the data. As an arbitrary set of tunes was used the largest variation in each bin is symmetrised.

bin	$0:0-0.5$	$1:0.5-1$	$2:1-1.5$	$3:1.5-2$	$4:2-2.5$
+ comb. efficiency syst.	+1.3%	+1.4%	+1.8%	+2.3%	+3.4%
- comb. efficiency syst.	-1.3%	-1.4%	-1.9%	-2.3%	-3.5%
$\pm$ variation	0.9%	1.3%	1.4%	1.4%	1.5%
+ total syst.	+1.6%	+1.9%	+2.3%	+2.7%	+3.7%
- total syst.	-1.6%	-1.9%	-2.3%	-2.7%	-3.8%
$\pm$statistical(%)	$\pm$ 0.1	$\pm$ 0.1	$\pm$ 0.1	$\pm$ 0.1	$\pm$ 0.1

Table 7.11: Systematic and statistical errors for the corrected forward-backward multiplicity correlation for charged tracks with $\mathrm{p_T} > 100\,\mathrm{MeV}$ in symmetrically opposite η-bins for events with two charged tracks within the kinematic range $\mathrm{p_T} > 100\,\mathrm{MeV}$ and $|\eta| < 2.5$ at $\sqrt{s} = 7\,\mathrm{TeV}$. total syst. is quadratic sum of trigger, vertex, tracking and diffractive systematics. Total systematic error is quadratic sum of total syst. and correction systematics.

7.6.5 900 GeV Results

This section shows the results of the FB-correlation analysis for 900 GeV data. The same event and track selection of the MB2.0 analysis as above was used on a Pythia MC09 tune generated MC sample and data, both at $\sqrt{s} = 900\,\mathrm{GeV}$. The upper plot of figure 7.19 shows the observed FB-correlations for data at $\sqrt{s} = 900\,\mathrm{GeV}$ and a comparison to the prediction of MC09 MC tune. The lower plot shows the ratio of the observed FB-correlation for MC09 to the data. As for the $\sqrt{s} = 7\,\mathrm{TeV}$ case, the observed correlation lies above the MC prediction across the η-range. Figure 7.20 and table 7.12 present the corrected correlations and a comparison to the MC09 predictions. The difference between data and MC is consistent for both reconstructed and corrected distributions.

Comparison of MC to data shows a similar deficiency as in the 7 TeV case. There this a small dip in correlation with respect to data in the intermediate η-region before an increase in the extreme η-region.

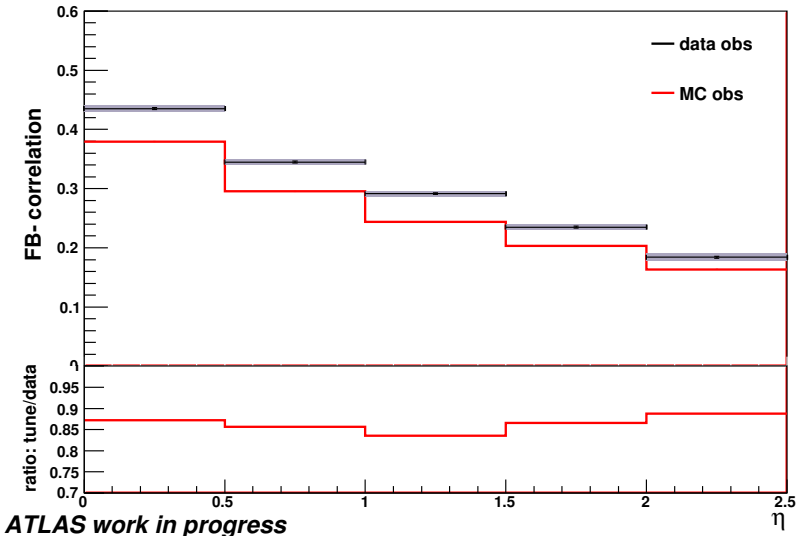

Figure 7.19: Above: Forward-backward multiplicity correlation for reconstructed charged tracks with $\mathrm{p_T} > 100\,\mathrm{MeV}$ in symmetrically opposite η-bins for events with two charged tracks within the kinematic range $\mathrm{p_T} > 100\,\mathrm{MeV}$ and $|\eta| < 2.5$ at $\sqrt{s} = 900\,\mathrm{GeV}$ for data and MC09. Below: Ratios comparing correlations from MC to data.

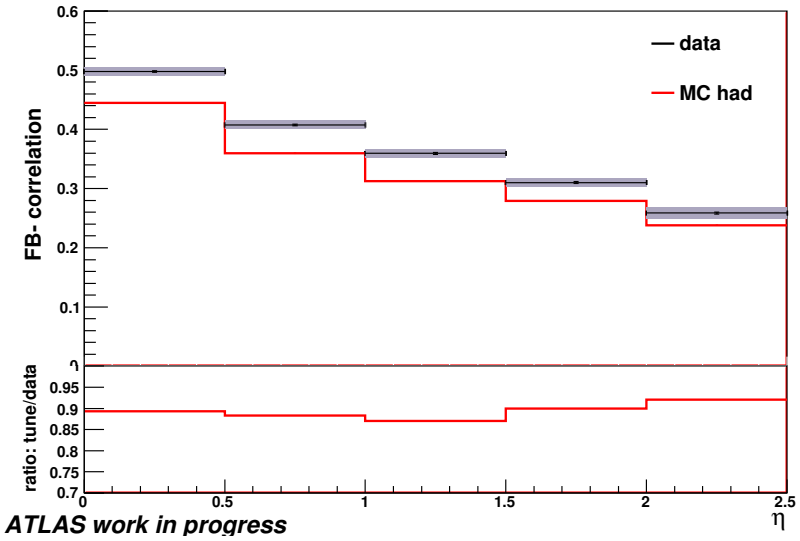

Figure 7.20: Above: Forward-backward multiplicity correlation for reconstructed charged tracks with $p_T > 100$ MeV in symmetrically opposite η-bins for events with two charged tracks within the kinematic range $p_T > 100$ MeV and $|\eta| < 2.5$ at $\sqrt{s} = 900$ GeV for data corrected using MC09 and generated charged particles with $p_T > 100$ MeV from MC09 tune. Below: Ratios comparing correlation from MC to data.

bin	$0:0-0.5$	$1:0.5-1$	$2:1-1.5$	$3:1.5-2$	$4:2-2.5$
data	$0.498 \pm 0.3\%$	$0.407 \pm 0.4\%$	$0.359 \pm 0.4\%$	$0.310 \pm 0.5\%$	$0.259 \pm 0.6\%$
MC	$0.445 \pm 0.2\%$	$0.360 \pm 0.3\%$	$0.313 \pm 0.3\%$	$0.279 \pm 0.4\%$	$0.238 \pm 0.4\%$

Table 7.12: Forward-backward multiplicity correlation for reconstructed charged tracks with $p_T > 100$ MeV in symmetrically opposite η-bins for events with two charged tracks within the kinematic range $p_T > 100$ MeV and $|\eta| < 2.5$ at $\sqrt{s} = 900$ GeV for data corrected using Pythia MC09 tune and generated charged particles with $p_T > 100$ MeV from MC09 tune. Quoted errors are statistical errors only.

bin	$0:0-0.5$	$1:0.5-1$	$2:1-1.5$	$3:1.5-2$	$4:2-2.5$
+ comb. efficiency syst.	+2.0%	+2.4%	+3.2%	+4.8%	+5.5%
- comb. efficiency syst.	-2.0%	-2.4%	-3.2%	-4.6%	-5.4%
$\pm$ variation	0.9%	1.3%	1.4%	1.4%	1.5%
+ total syst.	+2.2%	+2.7%	+3.5%	+5.0%	+5.7%
- total syst.	-2.2%	-2.7%	-3.5%	-4.7%	-5.6%
$\pm$statistical (%)	$\pm$0.3	$\pm$0.4	$\pm$0.4	$\pm$0.5	$\pm$0.6

Table 7.13: Systematic and statistical errors for the corrected forward-backward multiplicity correlation for charged tracks with $p_T > 100$ MeV in symmetrically opposite η-bins for events with two charged tracks within the kinematic range $p_T > 100$ MeV and $|\eta| < 2.5$ at $\sqrt{s} = 900$ GeV. total syst. is quadratic sum of trigger, vertex, tracking and diffractive systematics. Total systematic error is quadratic sum of total syst. and correction systematics.

7.6.6 Energy Comparison

Having corrected both the 900 GeV and 7 TeV data samples a comparison of the two can now be made, figure 7.21 and table 7.14 show the results. As expected the 900 GeV data lies below the 7 TeV across the η-range. The deficit becomes greater as the gap between bins expands, increasing from $\sim 25\%$ for the central two bins to $\sim 45\%$. This implies processes giving rise to long distance correlations are more prominent at the higher collision energy. This would suggest that in the case of Monte Carlo event simulation, non-perturbative models must vary with the interaction energy of the colliding particles. This conclusion is easily drawn using the forward-backward observable.

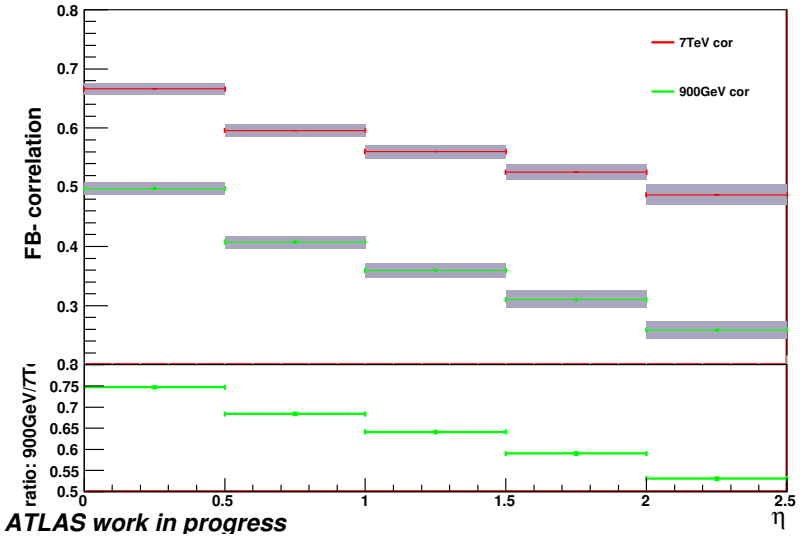

Figure 7.21: Above: Forward-backward multiplicity correlation for reconstructed charged tracks with $p_T > 100$ MeV in symmetrically opposite η-bins for events with two charged tracks within the kinematic range $p_T > 100$ MeV and $|\eta| < 2.5$ at $\sqrt{s} = 900$ GeV and 7 TeV for corrected data. Below: ratio of 900 GeV to 7 TeV correlations.

bin	$0:0-0.5$	$1:0.5-1$	$2:1-1.5$	$3:1.5-2$	$4:2-2.5$
900 GeV	0.478 $\pm 0.3\%$(stat.) $^{+2.2}_{-2.2}\%$(syst.)	0.385 $\pm 0.4\%$(stat.) $^{+2.7}_{-2.7}\%$(syst.)	0.335 $\pm 0.5\%$(stat.) $^{+3.5}_{-3.5}\%$(syst.)	0.288 $\pm 0.5\%$(stat.) $^{+5.0}_{-4.7}\%$(syst.)	0.240 $\pm 0.7\%$(stat.) $^{+5.7}_{-5.6}\%$(syst.)
900 TeV	0.654 $\pm 0.1\%$(stat.) $^{+1.6}_{-1.6}\%$(syst.)	0.581 $\pm 0.1\%$(stat.) $^{+1.9}_{-1.9}\%$(syst.)	0.544 $\pm 0.1\%$(stat.) $^{+2.3}_{-2.3}\%$(syst.)	0.508 $\pm 0.1\%$(stat.) $^{+2.7}_{-2.7}\%$(syst.)	0.469 $\pm 0.1\%$(stat.) $^{+3.7}_{-3.8}\%$(syst.)

Table 7.14: Forward-backward multiplicity correlation for charged tracks with $p_T > 100$ MeV in symmetrically opposite η-bins for events with two charged tracks within the kinematic range $p_T > 100$ MeV and $|\eta| < 2.5$ at $\sqrt{s} = 900$ GeV and 7 TeV for corrected data, with systematic and statistical errors.

7.6.7 Global Correlation

The global correlation is a forward-backward multiplicity calculated for one bin i.e. the correlation of a η-bin with $\Delta\eta$=2.5. This gives a multiplicity correlation for all of the forward region of the detector with all of the backward region. Tables 7.15 and 7.16 show the measured, hadron-level and corrected global forward-backward multiplicity correlations over the whole η-range for each 7 TeV and 900 GeV MC tunes, respectively.

Table 7.17 shows the global forward-backward multiplicity correlation over the whole η-range for $\sqrt{s} = 900$ GeV and 7 TeV data with systematic and statistical uncertainties.

	ρ_{obs}	ρ_{had}	corrected ρ_{data}
MC09	$0.729 \pm 0.1\%$	$0.760 \pm 0.1\%$	$0.801 \pm < 0.1\%$
DW	$0.741 \pm 0.1\%$	$0.774 \pm 0.1\%$	$0.803 \pm < 0.1\%$
Perugia0	$0.731 \pm 0.1\%$	$0.763 \pm 0.1\%$	$0.803 \pm < 0.1\%$
Pythia8	$0.740 \pm 0.1\%$	$0.769 \pm 0.1\%$	$0.779 \pm < 0.1\%$
Phojet	$0.685 \pm 0.1\%$	$0.725 \pm 0.1\%$	$0.806 \pm < 0.1\%$

Table 7.15: Observed and corrected global forward-backward multiplicity correlation for charged tracks with $\mathrm{p_T} > 100$ MeV for events with two charged tracks within the kinematic range $\mathrm{p_T} > 100$ MeV and $|\eta| < 2.5$ at $\sqrt{s} = 7$ TeV for selected MC tunes and correction of data.

	ρ_{obs}	ρ_{had}	corrected ρ_{data}
MC	$0.557 \pm 0.2\%$	$0.615 \pm 0.1\%$	$0.652 \pm 0.2\%$

Table 7.16: Observed and corrected global forward-backward multiplicity correlation for charged tracks with $\mathrm{p_T} > 100$ MeV for events with two charged tracks within the kinematic range $\mathrm{p_T} > 100$ MeV and $|\eta| < 2.5$ at $\sqrt{s} = 900$ GeV for selected MC tunes and correction of data.

bin	$0 < \|\eta\| < 2.5$
900 GeV	0.652 $\pm$ 0.2%(stat.) $^{+1.6}_{-1.6}$%(syst.)
7 TeV	0.801 $\pm$ 0.1%(stat.) $^{+1.0}_{-1.0}$%(syst.)

Table 7.17: Corrected global forward-backward multiplicity correlation for charged tracks with $\mathrm{p_T} > 100$ MeV for events with two charged tracks within the kinematic range $\mathrm{p_T} > 100$ MeV and $|\eta| < 2.5$ at $\sqrt{s} = 900$ GeV and 7 TeV for corrected data. Quoted errors are systematic (based on maximum of 5 bin case) and statistical.

7.7 Conclusion

The forward-backward correlation in charged particle multiplicity has been measured in minimum bias events at $\sqrt{s} = 900$ GeV and 7 TeV for symmetric $\delta\eta$ bins. A method to correct from the observed FB-correlation to the hadron-level for comparison to Monte Carlo predictions was developed using Multiple Regression Theory. The method correctly reproduced hadron-level Monte Carlo distributions from simulated data and was shown to be minimally sensitive ($\sim 2\%$) to the Monte Carlo tune used to determine the correction factors.

The principal systematic errors arise due to uncertainties on the tracking efficiencies and the sensitivity of the correction method. Systematic errors from the trigger and vertex efficiencies were found to be negligible. The systematic error arising from the theoretical uncertainty in the diffractive component of the minimum bias events was also studied and included. Statistical errors were around 0.5%.

The correlation found in data was found to lie above all MC predictions for both energies studied. In the 7 TeV case, the data was found to exceed the MC09 tune, used for correction, by $\sim 10\%$. In the 900 GeV case, the discrepancy was found to be ~ 12. At both energies the discrepancy was found to vary across the η-range. Though in general the shape of the correlation was well produced the details of the discrepancy for each tune reflect deficiencies in different particle production mechanisms. The greatest discrepancy between MC and data is found with PHOJET, whose correlation drops with increasing $\Delta\eta$. It should be noted that Monte Carlo generators have not been tuned to this variable before. The results of the comparison of MC and data suggest how particle production should be manipulated in order to reproduce experimental results.

It is hoped a further investigation into the source of divergence between data and Monte Carlo generator predictions could be undertaken in the future. This could be based on the $\mathrm{p_T}$ or ϕ sensitive observables studied in chapter 6. Sensitivity to these variables would help to isolate which aspects of event generation were under estimating the particle production rates in minimum bias measurements.

Chapter 8

Conclusions

This thesis has two main themes. The first concerned top physics measurement in the ATLAS detector at the LHC and was the subject of chapters 4 and 5. The second theme involved the study and measurement of forward-backward correlations and was the topic of chapters 6 and 7. The following remarks are based on the results of the preceding chapters.

Top Physics

A measurement of the fully-leptonic $t\bar{t}$ cross-section in the three decay channels ee, $\mu\mu$ and $e\mu$ was performed on ATLAS produced fully simulated pseudo-event data-samples, see chapter 4. The results for trigger and event selection were found to be consistent with [3]. This is not surprising as the object and event selection corresponded to those used in the preparation of the ATLAS note. The kinematic distributions of selected events were also found. From the measured cross-section a calculation of the non-hadronic $t\bar{t}$ cross-section then returned the theoretical value of $217.06pb$ used to generate the original samples. This showed the closure of the analysis technique.

A more detailed study was made of the systematic uncertainty arising from variation in the initial and final state showering models used to produce pseudo-events, see chapter 5. A default Pythia tune was compared to a harder and softer variant, all of which were consistent with previous experimental results. A fast simulation of the ATLAS detector was used with similar object and event selection to fully simulated case. The effect of ISR variations on the signal was found to be negligible as it is washed out in the subsequent decays of the $t\bar{t}$ system. In contrast, the effect of FSR was found to cause 5% uncertainty in the selected signal events. In addition, the effect of FSR was investigated in the main background of each of the selection channels. This was found to be more sensitive to the choice in shower model than the signal, with variations of up to 30% in well populated channels. The variations in signal and background measurements were used to calculate a new estimate of the systematic due to the shower model on the measured $t\bar{t}$ cross-section for each channel.

Minimum Bias

A detailed study of forward-backward correlation and events shapes on a selection of Pythia tunes

for pp collisions with $\sqrt{s} = 900$ GeV was performed, see chapter 6. This included an investigation of the various sources of particle production in generated minimum bias events as well as the component processes in generated minimum bias events. In the case of inclusive "standard" distribution the tunes were found to compare well, within $10 - 20\%$. The inclusion of forward-backward to the "standard" set was recommended as the study found this observable, and its $\mathrm{p_T}$ and ϕ sensitive variations, broke the degeneracies found in the usual inclusive distributions. Indeed, the FB-correlation was found to be sensitive to the particle production processes within the tunes, an invaluable property for the purposes of generator tuning.

A measurement of the forward-backward correlation for pp collision of $\sqrt{s} = 900$ GeV and 7 TeV at the LHC using the ATLAS detector was made, see chapter 7. The measured correlation was compared to the predicted correlation of several ATLAS produced generator tunes. A correction procedure was developed and validated on the generator samples to correct the generated correlation to the hadron-level. This was then applied to the measured correlation and a comparison of corrected data to the hadron-level predictions of the generated tunes made. The corrected correlation at the two collision energies were then compared as well as the calculation of a global correlation at both energies. The measured and corrected correlations were found to lie above the predicted distributions at both energies and across the η range. Further investigation of the strength of the correlation using the augmented FB-correlations is recommended.

Appendix A

η-bin Size Study

The optimum bin size used for equation 6.2 is a function of the statistics of the sample and the η-range observed. If the bin size is too small genuine correlations will be washed out by statistical fluctuations. Too large a bin size and the resolving power of the correlation over the limited η-range will be lost.

Figure A.1 shows the b-correlation vs. η (specifically the η value of the centre of the forward bin, with the backward one located at $-\eta$) for varying bin sizes from 0.03125 to 5 units wide, without imposing any $\mathrm{p_T}$-cuts, for the DW Pythia tune. Figure A.2 shows the same b-correlation vs. η distributions for the centrally produced DW sample at full simulation and hadron-level. A $\mathrm{p_T}$-cut of $100\ \mathrm{MeV}$ is applied in both cases with bin sizes from 0.0625 to 3 units wide.

It can be seen that bin sizes of $\Delta\eta = 5.0$ and 2.5 (and 3.0 in the centrally produced sample case) are too coarse to discern any structure in the correlation distribution. Mid-range bin sizes, $\Delta\eta = 1.0$, 0.5 and 0.25 show best the trends over the η-range. A high correlation in the low η region can be distinguished from a mid-η plateau and a drop in correlation at high η, for this particular DW Pythia tune. Smaller bin sizes, $\Delta\eta = 0.125$ and 0.0625 (and 0.03125 in the locally produced sample case), lose the structure in the distribution as statistical fluctuations begin to dominate.

Hence, the bin size $\Delta\eta = 0.5$ is reasonable for a study of the b-correlation for the sample size used. Note, however, that imposing different kinematic cuts or changing the collision energy of the particles could change this conclusion. It is the average accepted multiplicity at each η value which determines the relative size of the statistical fluctuations and hence affects the optimum bin size. As a consequence, it is not possible to directly compare b distributions taken with different cuts, or which use different-sized $\Delta\eta$ bins.

This study confirms that, for the sample size used and the η-range considered, a pseudo-rapidity bin size of 0.5 is reasonable.

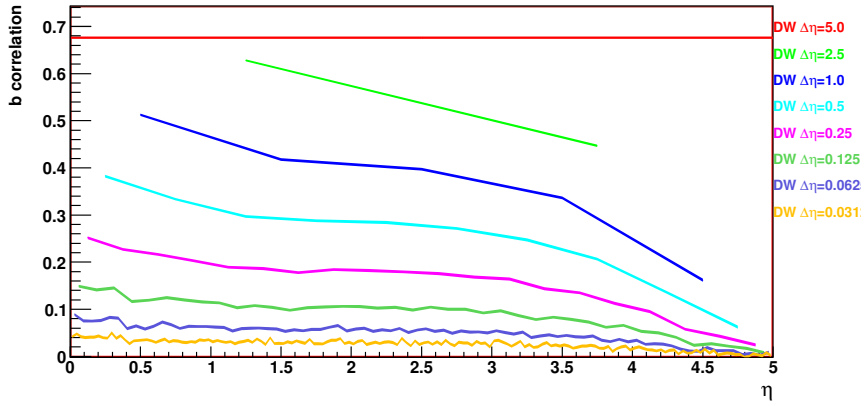

Figure A.1: b-correlation for selected events with various pseudo-rapidity bin sizes, $\Delta\eta$. The single-point correlation for a bin size of $\Delta\eta$=5.0 (red) is shown covering the whole η-region.

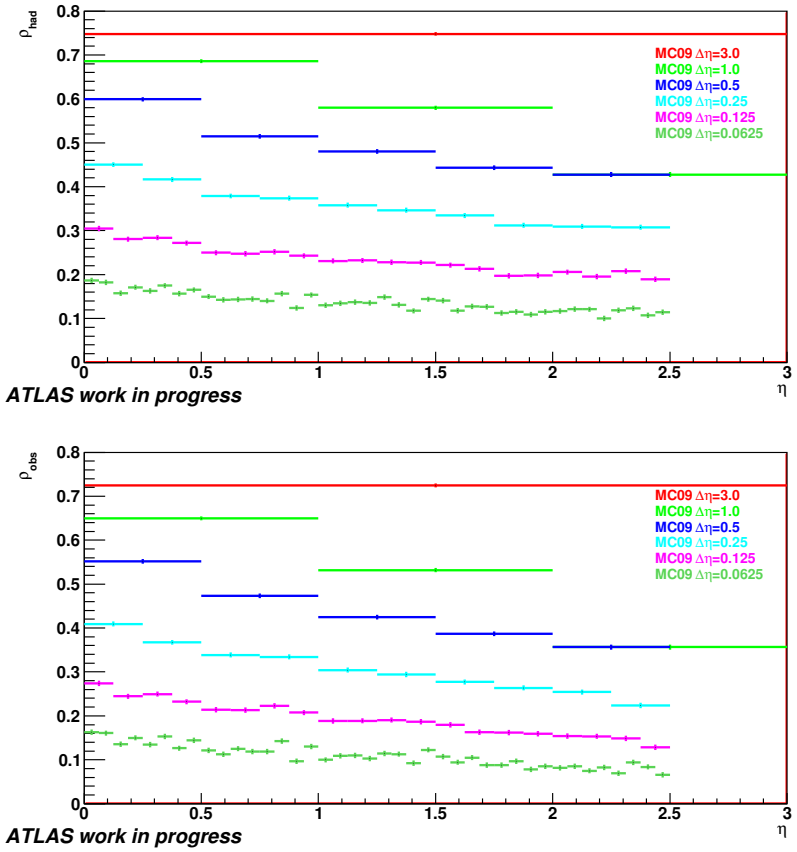

Figure A.2: Above: Forward-backward multiplicity correlation for hadron-level charged particles with $\mathrm{p_T} > 100\,\mathrm{MeV}$ in symmetrically opposite η-bins for events with two charged tracks within the kinematic range $\mathrm{p_T} > 100\,\mathrm{MeV}$ and $|\eta| < 2.5$ at $\sqrt{s} = 900\,\mathrm{GeV}$ for Pythia MC09 tune for various pseudo-rapidity bin sizes. Below: Forward-backward multiplicity correlation for reconstructed charged tracks with $\mathrm{p_T} > 100\,\mathrm{MeV}$ in symmetrically opposite η-bins for events with two charged tracks within the kinematic range $\mathrm{p_T} > 100\,\mathrm{MeV}$ and $|\eta| < 2.5$ at $\sqrt{s} = 900\,\mathrm{GeV}$ for Pythia MC09 tune for various pseudo-rapidity bin sizes.

Appendix B

Combining Correlations

An interesting effect of combining samples, namely that the correlations in the combined sample are *stronger* than in any of the individual components is explained as follows:

Imagine there are two separate distributions, A and B (representing, e.g., the diffractive and non-diffractive samples). Imagine further that the fluctuations inside each sample are purely statistical, for illustration, such that the correlation strength inside each sample is zero. What will happen when we look at the combination $A + B$?

If the mean of A is smaller than that of B, then *every* event of type A will look like it fluctuated down, systematically, from the mean of $A + B$, and conversely for the B sample. In their combination, therefore, a non-zero correlation is seen, if the mean values are different. Since the diffractive and non-diffractive event samples have very different average multiplicities (see table 6.3) this effect will lead to an increase in the correlations in the combined sample, as observed in fig. 6.11.

Alternatively:

An equivalent formulation of b (used in chapter 7):

$$\rho_{fb} = \frac{\langle (n_f - \langle n_f \rangle)(n_b - \langle n_b \rangle) \rangle}{\sqrt{\langle (n_f - \langle n_f \rangle)^2 \rangle \langle (n_b - \langle n_b \rangle)^2 \rangle}} \tag{B.1}$$

For an event,

$$\rho'_{fb} = \frac{(n_f - \langle n_f \rangle)(n_b - \langle n_b \rangle)}{\sqrt{\langle (n_f - \langle n_f \rangle)^2 \rangle \langle (n_b - \langle n_b \rangle)^2 \rangle}} \tag{B.2}$$

$$= \frac{(x)(y)}{\sqrt{\langle (x)^2 \rangle \langle (y)^2 \rangle}} \tag{B.3}$$

The magnitude and sign of the x and y terms will depend on the relative size of the $n_{f/b}$ to $\langle n_{f/b} \rangle$ and in turn to $\langle n_A \rangle$ and $\langle n_B \rangle$ and the proportions in which they are mixed. So, assume the samples don't have excessive variations from the mean value. If $\langle n_f \rangle$ for sample A and B are far enough apart then the total $\langle n_f \rangle$ when mixed will lie somewhere in between,

depending on the mixing proportions. If an event of type A(B) is chosen, then fluctuations in n_f relative to n_b, which must be quite likely since $b_A(b_B)$ is small, will make little difference as the term $\langle n_f \rangle$ is much larger(smaller). So x and y are -ve(+ve) and similar in magnitude, hence, b' is relatively large, compared to the individual b_A and b_B correlations. Therefore, the combined effect on the whole sample of A and B type events (composed of individual b's) will be to increase the correlation.

Appendix C

ATLAS Data Samples

All samples used were produced by ATLAS for the Standard Model group[68].

MC09
mc09_7TeV.105001.Pythia_minbias.merge.NTUP_MINBIAS.e517_s764_s767_r1229_p137
mc09_7TeV.105003.Pythia_sdiff.merge.NTUP_MINBIAS.e514_s764_s767_r1229_p137
mc09_7TeV.105004.Pythia_ddiff.merge.NTUP_MINBIAS.e514_s764_s767_r1229_p137
DW
mc09_7TeV.108310.Pythia_minbias_DW.merge.NTUP_MINBIAS.e514_s764_s767_r1229_p137
mc09_7TeV.108311.Pythia_sdiff_DW.merge.NTUP_MINBIAS.e514_s764_s767_r1229_p137
mc09_7TeV.108312.Pythia_ddiff_DW.merge.NTUP_MINBIAS.e514_s764_s767_r1229_p137
Perugia0
mc09_7TeV.108313.Pythia_minbias_Perugia0.merge.NTUP_MINBIAS.e514_s764_s767_r1229_p137
mc09_7TeV.108314.Pythia_sdiff_Perugia0.merge.NTUP_MINBIAS.e514_s764_s767_r1229_p137
mc09_7TeV.108315.Pythia_ddiff_Perugia0.merge.NTUP_MINBIAS.e514_s764_s767_r1229_p137
Pythia8
mc09_7TeV.108316.Pythia8_minbias_ND.merge.NTUP_MINBIAS.e533_s764_s767_r1229_p137
mc09_7TeV.108317.Pythia8_minbias_SD.merge.NTUP_MINBIAS.e533_s764_s767_r1229_p137
mc09_7TeV.108318.Pythia8_minbias_DD.merge.NTUP_MINBIAS.e533_s764_s767_r1229_p137
Phojet
mc09_7TeV.106096.PhojetNdiff.merge.NTUP_MINBIAS.e514_s764_s767_r1229_p137
mc09_7TeV.106097.PhojetSdiff.merge.NTUP_MINBIAS.e514_s764_s767_r1229_p137
mc09_7TeV.106098.PhojetDdiff.merge.NTUP_MINBIAS.e514_s764_s767_r1229_p137
mc09_7TeV.106099.PhojetCdiff.merge.NTUP_MINBIAS.e514_s764_s767_r1229_p137

Table C.1: MC sample datasets used for 7 TeV analysis.

MC09
mc09_900GeV.105001.Pythia_minbias.merge.NTUP_MINBIAS.e500_s771_s767_r1234_p137
mc09_900GeV.105003.Pythia_sdiff.merge.NTUP_MINBIAS.e466_s771_s767_r1234_p137
mc09_900GeV.105004.Pythia_ddiff.merge.NTUP_MINBIAS.e466_s771_s767_r1234_p137

Table C.2: MC sample datasets used for 900 GeV analysis.

900 GeV
data09_900GeV.00142383.physics_MinBias.merge.ESD.r1093_p101_tid120524_00
data09_900GeV.00142195.physics_MinBias.merge.ESD.r1093_p101_tid120485_00
data09_900GeV.00142193.physics_MinBias.merge.ESD.r1093_p101_tid120419_00
data09_900GeV.00142191.physics_MinBias.merge.ESD.r1093_p101_tid120365_00
data09_900GeV.00142189.physics_MinBias.merge.ESD.r1093_p101_tid120305_00
data09_900GeV.00142174.physics_MinBias.merge.ESD.r1093_p101_tid120272_00
data09_900GeV.00142171.physics_MinBias.merge.ESD.r1093_p101_tid120239_00
data09_900GeV.00142166.physics_MinBias.merge.ESD.r1093_p101_tid120206_00
data09_900GeV.00142165.physics_MinBias.merge.ESD.r1093_p101_tid120173_00
data09_900GeV.00142154.physics_MinBias.merge.ESD.r1093_p101_tid120032_00
data09_900GeV.00142149.physics_MinBias.merge.ESD.r1093_p101_tid119999_00
data09_900GeV.00141811.physics_MinBias.merge.ESD.r1093_p101_tid119768_00
data09_900GeV.00141749.physics_MinBias.merge.ESD.r1093_p101_tid119702_00
7 TeV
data10_7TeV.00152166.physics_MinBias.merge.NTUP_MINBIAS.f239_p127_tid125118_00
data10_7TeV.00152214.physics_MinBias.merge.NTUP_MINBIAS.f239_p127_tid125123_00
data10_7TeV.00152221.physics_MinBias.merge.NTUP_MINBIAS.f239_p127_tid125125_00
data10_7TeV.00152345.physics_MinBias.merge.NTUP_MINBIAS.f239_p127_tid125132_00
data10_7TeV.00152409.physics_MinBias.merge.NTUP_MINBIAS.f239_p127_tid125139_00

Table C.3: Data sample datasets used for 7 TeV and 900 GeV analysis.

Bibliography

[1] Particle Data Group. *Particle Physics Booklet*. Springer, July 2008.

[2] The ATLAS Collaboration. ATLAS TDR. Technical report, CERN, 2003.

[3] M Cristinziani, A Loginov, J Adelman, S Allwood-Spiers, B Auerbach, K Cranmer, K Gellerstedt, B Guo, B Kaplan, S Lockwitz, T Poghosyan, R Porter, S Ragajopalan, J Searcy, P Sinervo, J Sjlin, A Shibata, DB Ta, A Taffard, P Tipton, N Vlasov, D Whiteson, and K Wraight. Sensitivity of the top dilepton cross-section measurement at $\sqrt{s} = 10\ \mathrm{TeV}$. Technical Report ATL-COM-PHYS-2009-307, CERN, Geneva, June 2009.

[4] M Massimi. Exclusion Principle and the Identity of Indiscernibles: a response to Margena's argument. *Brit. J. Phil. Sci.*, 52, 2001.

[5] BR Martin and G Shaw. *Particle Physics 2nd ed.* Wiley, 2004.

[6] JC Collins and DE Soper. The Theorems of Perturbative QCD. *Ann. Rev. Nucl. Part. Sci.*, 37, 383, 1987.

[7] S Lami. Underlying Event Studies at CDF. In *11th International Workshop on Deep Inelastic Scattering*, 2003.

[8] The CDF Collaboration: F Abe et al. Observation of Top Quark Production in Pbar-P Collisions. *Phys. Rev. Lett.*, 2626, 1995.

[9] The D0 Collaboration: S Abachi et al. Observation of the Top Quark. *Phys. Rev. Lett.*, 2632, 1995.

[10] S. W. Herb, D. C. Hom, L. M. Lederman, J. C. Sens, H. D. Snyder, J. K. Yoh, J. A. Appel, B. C. Brown, C. N. Brown, W. R. Innes, K. Ueno, T. Yamanouchi, A. S. Ito, H. Jöstlein, D. M. Kaplan, and R. D. Kephart. Observation of a Dimuon Resonance at 9.5 GeV in 400-GeV Proton-Nucleus Collisions. *Phys. Rev. Lett.*, 39(5):252–255, Aug 1977.

[11] C Albajar et al. Search for New Heavy Quarks in Proton-Antiproton Collisions at sqrt s = 0.63 TeV. *Z. Phys. C*, 48(1), 1990.

[12] T Åkesson et al. Search for Top Quark Production at the CERN PPbar Collider. *Z. Phys. C*, 46(179), 1990.

[13] A Quadt. *Top Quark Physics at Hadron Colliders*. Springer, 2007.

[14] SL Glashow, I Iliopoulos, and L Maiani. Weak Interactions with Lepton-Hadron Symmetry. *Phys. Rev. D 2*, 1285, 1970.

[15] LEP Collaborations: ALEPH Collaboration, DELPHI Collaboration, L3 Collaboration, OPAL Collaboration, the LEP Electroweak Working Group, the SLD Electroweak, Heavy Flavour Groups. A Combination of Preliminary Electroweak Measurements and Constraints on the Standard Model. *CERN-PH-EP/2004-069*, 2004.

[16] LEP Collaborations: ALEPH Collaboration, DELPHI Collaboration, L3 Collaboration, OPAL Collaboration, the LEP Electroweak Working Group, the SLD Electroweak and Heavy Flavour Groups. A Combination of Preliminary Electroweak Measurements and Constraints on the Standard Model. http://www.cern.ch/LEPEWWG, 2005 update.

[17] The CDF Collaboration, the D0 Collaboration, the Tevatron Electroweak Working Group. Combination of CDF and D0 Results on the Top-Quark Mass. FERMILAB-TM-2323-E, 2005.

[18] JR Incadela et al. Status and Prospects of Top-Quark Physics. *Prog. Part. Nucl. Phys.*, 08, 001, 2009.

[19] J Pumplin et al. New Generation of Parton Distributions with Uncertainties from Global QCD Analysis. *J. High Energ. Phys.*, 07, 012, 2002.

[20] CDF Collaboration. Observation of $b_s^0 - \bar{B}_s^0$ oscillations. *Phys. Rev. Lett.*, 97, 242003, 2006.

[21] The D0 collaboration: VM Abazov et al. Direct Limits on the Bs Oscillation Frequency. *Phys. Rev. Lett. B*, 97, 021802, 2006.

[22] D0 Collaborations Tevatron Electroweak Working Group, CDF. Combination of CDF and D0 Results on the Mass of the Top Quark. Technical Report FERMILAB-TM-2466-E, TEVEWWG-TOP-2010-07, CDF-NOTE-10210, D0-NOTE-6090, Fermilab, Chicago, 2010.

[23] The ATLAS Collaboration. Expected Performance of the ATLAS Experiment - Detector, Trigger and Physics. Technical Report CERN-OPEN-2008-020, CERN, Geneva, 2008.

[24] U Baur, M Buice, and LH Orr. Direct Measurement of the Top Quark Charge at Hadron Colliders. *Phys. Rev. D*, 64, 094019, 2001.

[25] T Sjöstrand et al. High-Energy-Physics Event Generation with PYTHIA 6.1. *Comput. Phys. Commun.*, 135, 238, 2001.

[26] ML Mangano et al. ALPGEN, a generator for hard multiparton processes in hadronic collisions. *J. High Energ. Phys.*, 0307, 001, 2003.

[27] G Marchesini et al. HERWIG: A Monte Carlo event generator for simulating hadron emission reactions with interfering gluons. *Comput. Phys. Commun.*, 67, 465, 1992.

[28] S Frixione and BR Webber. Matching NLO QCD computations and parton shower simulations. *J. High Energ. Phys.*, 06, 001, 2002.

[29] S Agostinelli et al. Geant4 - a simulation toolkit. *Nucl. Instrum. Methods A*, 506, 250, 2003.

[30] V. V. Sudakov. *Sov. Phys. J.E.T.P.*, 30, 1956.

[31] S Catani, F Krauss, R Kuhn, and BR Webber. QCD Matrix Elements + Parton Showers. *J. High Energ. Phys.*, 0111, 063, 2001.

[32] F Krauss. Matrix Elements and Parton Showers in Hadronic Interactions. *J. High Energ. Phys.*, 0208, 025, 2002.

[33] S Mrenna and P Richardson. Matching Matrix Elements and Parton Showers with HERWIG and PYTHIA. *J. High Energ. Phys.*, 0405, 040, 2004.

[34] ML Mangano. A Joint Meeting of CTEQ & The Matrix Element/Monte Carlo Tuning Working Group. A Review of MLM's Prescription for Removal of DoubleCounting, April 2004.

[35] The ATLAS Collaboration: G Aad et al. *Expected performance of the ATLAS experiment: detector, trigger and physics*. CERN, Geneva, 2009.

[36] ATLAS Collaboration. *TopPubSystematics ATLAS twiki page*, Jun 2009.

[37] Elzbieta Richter-Was, D Froidevaux, and Luc Poggioli. ATLFAST 2.0 a fast simulation package for ATLAS. Technical Report ATL-PHYS-98-131, CERN, Geneva, Nov 1998.

[38] T Sjöstrand, S Mrenna, and P Skands. Pythia 6.4 Physics and Manual. *JHEP*, C66:203–214, March 2006.

[39] Peter Z. Skands. Tuning Monte Carlo Generators: The Perugia tunes. *Phys. Rev. D*, 82:074018, Oct 2010.

[40] P Skands and K Wraight. Forward-Backward Correlations and Event Shapes as probes of Minimum-Bias Event Properties. *Eur. Phys. J. C*, 71:1628, May 2011.

[41] Andy Buckley et al. General-purpose event generators for LHC physics. CERN-PH-TH-2010-298, 2011.

[42] T Sjöstrand and M van Zijl. A multiple-interaction model for the event structure in hadron collisions. *Phys. Rev. D*, 36(7):2019–2041, Oct 1987.

[43] T. Sjöstrand and Peter Z. Skands. Multiple interactions and the structure of beam remnants. *JHEP*, 0403:053, 2004.

[44] T. Sjöstrand and Peter Z. Skands. Transverse-momentum-ordered showers and interleaved multiple interactions. *Eur.Phys.J.*, C39:129–154, 2005.

[45] T. Sjöstrand and Peter Z. Skands. Baryon number violation and string topologies. *Nucl.Phys.*, B659:243, 2003.

[46] The Professor Collaboration: A Buckley, et al. Systematic event generator tuning for the lhc. *Eur.Phys.J.*, C65:331–357, 2010.

[47] Torbjorn Sjöstrand, Stephen Mrenna, and Peter Z. Skands. PYTHIA 6.4 Physics and Manual. *JHEP*, 0605:026, 2006.

[48] Bo Andersson, G. Gustafson, G. Ingelman, and T. Sjöstrand. Parton Fragmentation and String Dynamics. *Phys. Rept.*, 97:31–145, 1983.

[49] Bo Andersson. The Lund model. *Camb. Monogr. Part. Phys. Nucl. Phys. Cosmol.*, 7:1–471, 1997.

[50] UA5 Collaboration. Charged particles correlations in $p\bar{p}$ at c.m. energies of 200, 546 and 900 GeV . *Z. Phys. C, Particles and Fields*, 37:191–213, 1988.

[51] Vardan Khachatryan et al. Transverse momentum and pseudorapidity distributions of charged hadrons in pp collisions at sqrt(s) = 0.9 and 2.36 TeV. *JHEP*, 02:041, 2010.

[52] G. Aad et al. Charged-particle multiplicities in pp interactions at sqrt(s) = 900 GeV measured with the ATLAS detector at the LHC. *Phys. Lett.*, B688:21–42, 2010.

[53] K. Aamodt et al. Charged-particle multiplicity measurement in proton-proton collisions at sqrt(s) = 7 TeV with ALICE at LHC. *Eur.Phys.J.*, C68:345–354, 2010.

[54] K. Aamodt et al. Charged-particle multiplicity measurement in proton-proton collisions at sqrt(s) = 0.9 and 2.36 TeV with ALICE at LHC. *Eur.Phys.J.*, C68:89–108, 2010.

[55] Vardan Khachatryan et al. Transverse-momentum and pseudorapidity distributions of charged hadrons in pp collisions at sqrt(s) = 7 TeV. *Phys. Rev. Lett.*, 105:022002, 2010.

[56] K Aamodt et al. Transverse momentum spectra of charged particles in proton-proton collisions at $\sqrt{s} = 900$ GeV with ALICE at the LHC. *Phys.Lett.*, B693:53–68, 2010.

[57] Vardan Khachatryan et al. Charged particle multiplicities in pp interactions at sqrt(s) = 0.9, 2.36, and 7 TeV. CERN-PH-EP-2010-048, 2010.

[58] G. Aad et al. Charged-particle multiplicities in pp interactions measured with the ATLAS detector at the LHC. *New J.Phys.*, 2010.

[59] Andrea Banfi, Gavin P. Salam, and Giulia Zanderighi. Phenomenology of event shapes at hadron colliders. *JHEP*, 1006:038, 2010.

[60] C Buttar, S Ferrag, and K Wraight. Measurement of forward-backward correlations in charged particle multiplicity in pp collisions at $900\ \mathrm{GeV}$ and $7\ \mathrm{TeV}$. ATL-COM-PHYS-2010-735.

[61] A Buckley et al. ATLAS Monte Carlo Tunes for MC09. ATL-COM-PHYS-2009-631.

[62] R Field. Min-Bias and the Underlying Event at the Tevatron and the LHC. A talk presented at the Fermilab me/mc tuning workshopFermilab, 2002.

[63] T Sjöstrand and P Skands. A Brief Introduction to PYTHIA 8.1. *Comput. Phys. Comm.*, 178, 2007.

[64] R Engel. Photoproduction within the two component dual parton model. 1. Amplitudes and cross-sections. *Z. Phys.*, C66:203–214, 1995.

[65] MG Kendall and A Stuart. *The Advanced Theory of Statistics*, volume 2. London: Griffin, 3 edition, 1951.

[66] G D'Agostini. A multidimensional unfolding method based on Bayes' theorem. *Nuclear Instruments and Methods in Physics Research A*, 362:487–498, 1995.

[67] MR Spiegel and LJ Stephens. *Theory and Problems of Statistics*. Shaume's Outline Series. McGraw-Hill, 4 edition, 2008.

[68] The ATLAS Collaboration. https://svnweb.cern.ch/trac/atlasoff/browser/PhysicsAnalysis/StandardMo%delPhys/Minbias/MbAnalysis/trunk/anaMb7TeV_v20/MbXsection.h.